UNIVERSITY OF CALIFORNIA

Santa Barbara

Nanomaterials' Influences on the Emergence of Life and Their Toxic Effects on Bacteria and Protozoa

A dissertation submitted in partial satisfaction of the requirements for the degree Doctor of Philosophy in Environmental Science & Management

by

Randall Edward Mielke

Committee in charge:

Professor Patricia A. Holden, Chair

Professor Hunter S. Lenihan

Professor Galen D. Stucky

Dr. Michael J. Russell, Jet Propulsion Laboratory - NASA

Professor Jay L. Nadeau, McGill University

September 2014

The dissertation of Randall Edward Mielke is approved.

Michael J. Russell

Jay L. Nadeau

Galen D. Stucky

Hunter S. Lenihan

Patricia A. Holden, Committee Chair

August 2014

Nanomaterials' Influences on the Emergence of Life

and Their Toxic Effects on Bacteria and Protozoa

Copyright © 2014

by

Randall Edward Mielke

ACKNOWLEDGEMENTS

Thank you REMII!!!!

Randall E. Mielke - Publication participation during Bren School PhD program:

1. Mielke, R. E., J. H. Priester, R. Werlin, J. Gelb, A. M. Horst, E. Orias, P. A. Holden. Differential Growth of and Nanoscale TiO_2 Accumulation in *Tetrahymena thermophila* by Direct Feeding versus Trophic Transfer from *Pseudomonas aeruginosa*. Applied and Environmental Microbiology. Oct 2013. Vol. 79, Num. 19, Cover Image.

2. Mielke, R. E., J. H. Priester, R. Werlin, J. Gelb, A. M. Horst, E. Orias, P. A. Holden. Differential Growth of and Nanoscale TiO_2 Accumulation in *Tetrahymena thermophila* by Direct Feeding versus Trophic Transfer from *Pseudomonas aeruginosa*. Applied and Environmental Microbiology. Sep 2013. Vol. 79, Num. 18, 5616-5624.

3. Priester, J. H., Yuan Ge, R. E. Mielke, A. Horst, S. Moritz, K. Espinosa, J. Gelb, S. Walker, R. Nisbet, Y. An, J. Schimel, R. Palmer, J. Hernandez-Viezcas, L. Zhao, J. L. Gardea-Torresdey, P. A. Holden. Reply to Lombi et al.: Clear effects of manufactured nanomaterials to soybean. PNAS. Dec 2012. 109:49, 14734-14 pp. E3337.

4. Priester, J. H., Y. Ge, R. E. Mielke, A. Horst, S. Moritz, K. Espinosa, J. Gelb, S. Walker, R. Nisbet, Y. An, J. Schimel, R. Palmer, J. Hernandez-Viezcas, L. Zhao, J. L. Gardea-Torresdey, and P. A. Holden. Soybean susceptibility to manufactured nanomaterials: Evidence for food quality and soil fertility interruption. *Proceedings of the National Academy of Sciences,* 109:37:1-6 (2012).

5. Bennett S., D. Zhou, R. E. Mielke, and A. Keller. Photoinduced Disaggregation of TiO_2 nanoparticles enables transdermal penetration. *PLOS ONE,* 7:11:e48719 (2012).

6. Gleeson, D. F., R. T. Pappalardo, M. S. Anderson, S. E. Grasby, R. E. Mielke, K. E. Wright, and A. S. Templeton. Biosignature detection at an Arctic analog to Europa. *Astrobiology,* 12:2:135-150 (2012).

7. Mielke, R. E., K. J. Robinson, L. M. White, S. E. McGlynn, K. McEachem, R. Bhartia, I. Kanik and M. J. Russell. Iron-sulfide-bearing chimneys as potential energy traps at life's emergence. *Astrobiology*, 11:10:930-950 (2011).

8. Zhang, X., H. Chibli, R. Mielke, and J. Nadeau. Ultrasmall gold-doxorubicin conjugates rapidly kill apoptosis-resistant cancer cells. *Bioconjugate Chemistry*, 16:22:2:235-243 (2011).

9. Werlin, R., J. H. Priester, R. E. Mielke, S. Krämer, S. Jackson, P. K. Stoimenov, G. D. Stucky, G. N. Cherr, E. Orias, and P. A. Holden. Biomagnification of cadmium selenide quantum dots in a simple experimental microbial food chain. *Nature Nanotechnology*, 6:65-71 (2011).

10. Horst, A., A. C. Neal, R. E. Mielke, P. R. Sislian, W. H. Suh, L. Mädler, G. D. Stucky, and P. A. Holden. Dispersion of TiO_2 nanoparticle agglomerates by *Pseudomonas aeruginosa*. *Applied and Environmental Microbiology*, 76:21:7292-7298 (2010).

11. Mielke, R. E., P. R. Wilson, M. Coleman, I. Kanik and M. J. Russell. Design, fabrication and test of a hydrothermal reactor for origin-of life experiments. *Astrobiology*, 10:8:799-810 (2010).

12. Clarke, S., R. E. Mielke, A. Aneal, P. A. Holden, and J. L. Nadeau. Bacterial and mineral elements in an Arctic biofilm: a correlative study using fluorescence and electron microscopy. *Microscopy & Microanalysis,* 16:2:99133:1-13 (2010).

13. Bair, E. H., J. Dozier, R. E. Davis, T. U. Kaempfer, M. T. Colee, R. Mielke, and J. R. Blackford. Observations of two seasons of sintering in a mountain snowpack. *International Snow Science Workshop, Davos 2009, Proceedings.* http://arc.lib.montana.edu/snow-science/item/207 (2009).

14. Nadeau, J., R. E. Mielke, and S. Clarke. Quantum dot conjugates for SEM of bacterial communities. *Scanning Microscopy,* 73781Y:1-10 (2009).

15. Dumas, E-M, V. Ozenne, R. E. Mielke, and J. L. Nadeau. Toxicity of CdTe quantum dots in bacterial strains. *Institute of Electrical and Electronics Engineers,* 8:1:58-64 (2009).

16. Niederberger, T. D., N. N. Perreault, J. R. Lawrence, J. L. Nadeau, R. E. Mielke, C. W. Greer, D. T. Andersen, and L. G. Whyte. Novel sulfur-oxidizing streamers thriving in perennial cold saline springs of the Canadian High Arctic. *Environmental Microbiology*, 11:3:616-629 (2009).

17. Priester J. H., P. K. Stoimenov, R. E. Mielke, S. M. Webb, C. Ehrhardt, J. P. Zhang, G. D. Stucky, and P. A. Holden. Effects of soluble cadmium salts versus CdSe quantum dots on the growth of planktonic *Pseudomonas aeruginosa*. *Environmental Science & Technology,* 43:7:2589-2594 (2009).

Publication Contributed and Acknowledged Imaging by R. E. Mielke:

1. Chowdhury I., D. M. Cwiertny and S. L. Walker. Combined factors influencing the aggregation and deposition of nano-TiO2 in the presence of humic acid and bacteria. Environmental Science and Technology 46:13:6869-6976 (2012). ESEM images by REM.

VITA OF RANDALL EDWARD MIELKE
JUNE 2013

EDUCATION:

August 2014 – Doctor of Philosophy in Environmental Science & Management, Bren School, University of California, Santa Barbara.

December 2001: Masters of Science in Biology (Geomicrobiology), Northern Arizona University, Flagstaff, AZ. Advisor: Gordon Southam, Ph.D.

May 1998: Masters of Science in Chemistry (Phytoremediation), Northern Arizona University, Flagstaff, AZ. Advisor: Christine Kelley, Ph.D.

May 1992: Bachelor of Arts in Biology & Bachelor of Arts in Chemistry, Point Loma Nazarene University, San Diego, CA.

PROFESSIONAL EMPLOYMENT:

04/10 to Present – Director of Imaging Technologies. Blue Ocean Sciences, Not-for-Profit/for Profit

07/09 to 06/13 – Graduate Student Researcher, Earth Research Institute, University of California, Santa Barbara.

03/06 to 06/09 – University of California, Santa Barbara, MEIAF Technical Support/Lab Manager.

06/01 to 01/14 – Astrobiology Research Element, Geomicrobiologist/Electron Microscopist. JPL - NASA, Astrobiology – Planetary Sciences (Ices Group; Paul Johnson, Ph.D.)

08/98 to 06/01 – Research Assistant. Northern Arizona University, Biology Dept., Gordon Southam, Ph.D.

01/98 to 08/98 – Research Assistant. Northern Arizona University, Geology Dept., Michael Ort, Ph.D.

06/98 to 07/98 – Instructor/Mentor. Northern Arizona University, Four-Corners Math/Science Program.

08/96 to 05/98 – Graduate Assistant/Instructor. Northern Arizona University, Chemistry Dept., John Nauman.

09/93 to 06/98 – Associate Faculty. Northland Pioneer College, Biology and Chemistry Dept., Show Low, AZ.

09/88 to10/92 – Environmental Biology Assistant. Sweetwater Environmental Biologist, San Diego, CA, Susan Brownlee.

01/88 to 01/89 – Laboratory Technician. Multiple Peptide Systems, La Jolla, CA, General Atomic Center.

PUBLICATIONS:

1. Mielke, R. E., J. H. Priester, R. Werlin, J. Gelb, A. M. Horst, E. Orias, P. A. Holden. Differential Growth of and Nanoscale TiO_2 Accumulation in *Tetrahymena thermophila* by Direct Feeding versus Trophic Transfer from *Pseudomonas aeruginosa*. Applied and Environmental Microbiology. Oct 2013. Vol. 79, Num. 19, Cover Image.

2. Mielke, R. E., J. H. Priester, R. Werlin, J. Gelb, A. M. Horst, E. Orias, P. A. Holden. Differential Growth of and Nanoscale TiO_2 Accumulation in *Tetrahymena thermophila* by Direct Feeding versus Trophic Transfer from *Pseudomonas aeruginosa*. Applied and Environmental Microbiology. Sep 2013. Vol. 79, Num. 18, 5616-5624.

3. Priester, J. H., Yuan Ge, R. E. Mielke, A. Horst, S. Moritz, K. Espinosa, J. Gelb, S. Walker, R. Nisbet, Y. An, J. Schimel, R. Palmer, J. Hernandez-Viezcas, L. Zhao, J. L. Gardea-Torresdey, P. A. Holden. Reply to Lombi et al.: Clear effects of manufactured nanomaterials to soybean. PNAS. Dec 2012. 109:49, 14734-14 pp. E3337.

4. Priester, J. H., Y. Ge, R. E. Mielke, A. Horst, S. Moritz, K. Espinosa, J. Gelb, S. Walker, R. Nisbet, Y. An, J. Schimel, R. Palmer, J. Hernandez-Viezcas, L. Zhao, J. L. Gardea-Torresdey, and P. A. Holden. Soybean susceptibility to manufactured nanomaterials: Evidence for food quality and soil fertility interruption. *Proceedings of the National Academy of Sciences,* 109:37:1-6 (2012).

5. Bennett S., D. Zhou, R. E. Mielke, and A. Keller. Photoinduced Disaggregation of TiO_2 nanoparticles enables transdermal penetration. *PLOS ONE,* 7:11:e48719 (2012).

6. Gleeson, D. F., R. T. Pappalardo, M. S. Anderson, S. E. Grasby, R. E. Mielke, K. E. Wright, and A. S. Templeton. Biosignature detection at an Arctic analog to Europa. *Astrobiology,* 12:2:135-150 (2012).

7. Mielke, R. E., K. J. Robinson, L. M. White, S. E. McGlynn, K. McEachem, R. Bhartia, I. Kanik and M. J. Russell. Iron-sulfide-bearing chimneys as potential energy traps at life's emergence. *Astrobiology*, 11:10:930-950 (2011).

8. Zhang, X., H. Chibli, R. Mielke, and J. Nadeau. Ultrasmall gold-doxorubicin conjugates rapidly kill apoptosis-resistant cancer cells. *Bioconjugate Chemistry*, 16:22:2:235-243 (2011).

9. Werlin, R., J. H. Priester, R. E. Mielke, S. Krämer, S. Jackson, P. K. Stoimenov, G. D. Stucky, G. N. Cherr, E. Orias, and P. A. Holden. Biomagnification of cadmium selenide quantum dots in a simple experimental microbial food chain. *Nature Nanotechnology*, 6:65-71 (2011).

10. Horst, A., A. C. Neal, R. E. Mielke, P. R. Sislian, W. H. Suh, L. Mädler, G. D. Stucky, and P. A. Holden. Dispersion of TiO_2 nanoparticle agglomerates by *Pseudomonas aeruginosa*. *Applied and Environmental Microbiology*, 76:21:7292-7298 (2010).

11. Mielke, R. E., P. R. Wilson, M. Coleman, I. Kanik and M. J. Russell. Design, fabrication and test of a hydrothermal reactor for origin-of life experiments. *Astrobiology*, 10:8:799-810 (2010).

12. Clarke, S., R. E. Mielke, A. Aneal, P. A. Holden, and J. L. Nadeau. Bacterial and mineral elements in an Arctic biofilm: a correlative study using fluorescence and electron microscopy. *Microscopy & Microanalysis,* 16:2:99133:1-13 (2010).

13. Bair, E. H., J. Dozier, R. E. Davis, T. U. Kaempfer, M. T. Colee, R. Mielke, and J. R. Blackford. Observations of two seasons of sintering in a mountain snowpack. *International Snow Science Workshop, Davos 2009, Proceedings.* http://arc.lib.montana.edu/snow-science/item/207 (2009).

14. Nadeau, J., R. E. Mielke, and S. Clarke. Quantum dot conjugates for SEM of bacterial communities. *Scanning Microscopy,* 73781Y:1-10 (2009).

15. Dumas, E-M, V. Ozenne, R. E. Mielke, and J. L. Nadeau. Toxicity of CdTe quantum dots in bacterial strains. *Institute of Electrical and Electronics Engineers,* 8:1:58-64 (2009).

16. Niederberger, T. D., N. N. Perreault, J. R. Lawrence, J. L. Nadeau, R. E. Mielke, C. W. Greer, D. T. Andersen, and L. G. Whyte. Novel sulfur-oxidizing streamers thriving in perennial cold saline springs of the Canadian High Arctic. *Environmental Microbiology*, 11:3:616-629 (2009).

17. Priester J. H., P. K. Stoimenov, R. E. Mielke, S. M. Webb, C. Ehrhardt, J. P. Zhang, G. D. Stucky, and P. A. Holden. Effects of soluble cadmium salts versus CdSe quantum dots on the growth of planktonic Pseudomonas aeruginosa. Environmental Science & Technology, 43:7:2589-2594 (2009).

17. Rohrssen, M., R. E. Mielke, B. Brunner, and M. Coleman. A method for simultaneous oxygen and hydrogen isotope analysis of water of crystallization in hydrated minerals. *Analytical Chemistry*, 80:7084-7089 (2008).

18. Brunner, B., J-Y. Yu, R. E. Mielke, J. A. MacAskill, S. Madzunkov, T. J. McGenity, and M. Coleman. Different isotope and chemical patterns of pyrite oxidation related to lag and exponential growth phases of *Acidithiobacillus ferrooxidans* reveal a microbial growth strategy. *Earth and Planetary Science Letters,* EPSL-270:63-72 (2008).

19. Douglas, S., W. Abbey, R. Mielke, P. Conrad, and I. Kanik. Textural and mineralogical biosignatures in an unusual microbialite from Death Valley, California. *Icarus,* 193:620–636 (2008).

20. Jae-Young Yu, Y. Park, R. E. Mielke, and M. L. Coleman. Sulfur and oxygen isotopic compositions of the dissolved sulphate in the meteoric water in Chuncheon, Korea. *Geosciences Journal*, 11:4:357 − 367 (2007).

21. Christensen, L. E., B. Brunner, K. N. Truong, R. E. Mielke, C. R. Webster, and M. Coleman. Measurement of sulfur isotope compositions by tunable laser spectroscopy of SO_2. *Analytical Chemistry*, 79:24:9261-9268 (2007).

22. Lies, D. P., M. E. Hernandez, A. Kappler, R. E. Mielke, J. A. Gralnick, and D. K. Newman. *Shewanella oneidensis* MR-1 uses overlapping pathways for iron reduction at a distance and by direct contact under conditions relevant for biofilms. *Applied and Environmental Microbiology,* 71:8:4414-4426 (2005).

23. Pace, D. L., R. E. Mielke, G. Southam, and T. L. Porter. Scanning force microscopy studies of the colonization and growth of *Acidithiobacillus ferrooxidans* on the surface of pyrite minerals. *Scanning,* 27:3:136-140 (2005).

24. Kloepfer, J. A., R. E. Mielke, and J. L. Nadeau. Uptake of CdSe and CdSe/ZnS quantum dots into bacteria via purine-dependent mechanisms. *Applied and Environmental Microbiology,* 71:5:2548-2557 (2005).

25. Kloepfer, J. A., R. E. Mielke, and J. L. Nadeau. CdSe quantum dot internalization by *Bacillus subtilis* and *Escherichia coli*. *Proceedings of International Society for Optics and Photonics,* 5361:133-141, (2004) Invited Paper.

26. Gorlenko, V., A. Tsapin, Z. Namsaraev, T. Teal, T. Tourova, D. Engler, R. E. Mielke and K. Nealson. *Anaerobranca californiensis* sp. nov. an anaerobic alkalithermophilic fermentative bacterium, isolated from hot spring on Mono Lake. *International Journal of Systematic and Evolutionary Microbiology,* (029009) 54:Pt 3:739-743 (2004).

27. Kloepfer, J. A., R. E. Mielke, M. S. Wong, K. H Nealson, G. Stucky, and J. L Nadeau. Quantum dots as strain- and metabolism- specific microbiological labels. *Applied and Environmental Microbiology,* 69:7:4205-4213 (2003).

28. Mielke, R. E., D. L. Pace, T. Porter, and G. Southam. A critical stage in the formation of acid mine drainage: Colonization of pyrite by *Acidithiobacillus ferrooxidans* under pH-neutral conditions. *Geobiology,* 1:81-90 (2003).

29. Mielke, R. E. The colonization of pyrite by *Thiobacillus ferrooxidans* under pH neutral conditions. *Master of Science in Biology,* Northern Arizona University, December (2001).

30. Kelley, C., R. E. Mielke, D. Dimaquibo, A. J. Curtis, and J. G. Dewitt. Adsorption of Eu(III) onto roots of Water Hyacinth. *Environmental Science and Technology,* 33:1439-1443 (1999).

31. Mielke, R. E. Adsorption of Europium Ions by Water Hyacinth. *Master of Science in Chemistry,* Northern Arizona University, May (1998).

Publication Contributed and Acknowledged Imaging by R. E. Mielke:

32. Chowdhury I., D. M. Cwiertny and S. L. Walker. Combined factors influencing the aggregation and deposition of nano-TiO_2 in the presence of humic acid and bacteria. Environmental Science and Technology 46:13:6869-6976 (2012). ESEM images by R. E. Mielke.

33. Kappler, A., B. Schink, and D. K. Newman. Fe(III) mineral formation and cell encrustation by the nitrate-dependent Fe(II)-oxidizer strain BoFeN1. *Geobiology*, 3:235-245 (2005). TEM & ESEM images produced by R. E. Mielke.

34. Jiao, Y., A. Kappler, L. R. Croal, and D. K. Newman. Isolation and characterization of a genetically tractable photoautotrophic Fe(II)-oxidizing bacterium, *Rhodopseudomonas palustris* strain TIE-1. *Applied and Environmental Microbiology,* 71:8:4487-4496 (2005). TEM images produced by R. E. Mielke.

35. Kappler, A. and D. K. Newman. Formation of Fe(III)-minerals by Fe(II)-oxidizing photoautotrophic bacteria. *Geochimica et Cosmochimica Acta,* 68:6:1217-1226 (2004). TEM images produced by R. E. Mielke.

36. ENGenious. Cover Image, Bacteria nests: micro scale pattern formation of desiccated carbon nanotube carpets, after immersion in solutions containing bacterial spores (*Bacillus pumilus*). Spring (2002). ESEM image by R .E. Mielke.

ABSTRACT

Nanomaterials' Influences on the Emergence of Life

and Their Toxic Effects on Bacteria and Protozoa

BY

RANDALL EDWARD MIELKE

This research investigates the unique properties of nanomaterials (NMs) with highly catalytic surfaces that make them ideal for the production of organic molecules but also confer toxic properties of some NMs. Iron-sulphide NMs were used in a hydrothermal reactor that released hydrogen sulphide and other metal ions in the effluent, as analyzed by inductively-coupled plasma (ICP) spectrometry. Using an environmental scanning electron microscope (ESEM), iron sulphide NM surfaces indicate severe weathering as a result of environmental conditions including high pressure (100 bar H_2) and moderate temperatures (130°C). The effluent's chemical properties from the reactor experiment generated chimney structures from newly formed iron-sulphide NMs in a ferrous rich 'Hadean Ocean' solution. Using ESEM,

we show that structural changes occur under different pHs, temperatures, and silicate concentrations. The presence of 5-mer peptides also shows distinct structural differences during the formation of iron-sulphide NM chimneys.

Nano-titanium dioxide NMs ($nTiO_2$) were used to show the toxicity of $nTiO_2$ encrusted *Pseudomonas aeruginosa* (PA) fed to *Tetrahymena thermophila* (TT) protozoa under aerobic conditions. The control TT showed limited toxicity when grown in the presence of $nTiO_2$, and scanning transmission electron microscopy (STEM) revealed the initial accumulation of $nTiO_2$ in food vacuoles (FVs) of control TT cells that were not observed in the TT grown with $nTiO_2$-encrusted PA. After 22 h, very little $nTiO_2$ is observed in the control TT FVs as compared with the TT grown with $nTiO_2$-encrusted PA FVs which had about 30% of the FV filled with $nTiO_2$. Toxicity to $nTiO_2$ was observed as reduced growth yields for both the control and the PA fed TT, but also as a reduction in growth rate for TT grown with $nTiO_2$-encrusted PA.

To understand biological weathering of NMs, the use of STEM energy dispersive spectroscopy (EDS) was enhanced to analyze single nano-sized particles. Contamination studies using cadmium selenide (CdSe) and cadmium telluride (CdTe) NMs with PA showed that CdSe weathering occurred in the cytoplasm while CdTe weathering predominantly occurred when associated with the PA cell wall. PA was shown to produce CdSe NMs in the cytoplasm when grown with cadmium and selenite salts as revealed by STEM-EDS. The use of STEM-EDS on embedded

samples makes it possible to analyze NM structures while in their experimental location.

TABLE OF CONTENTS

ACKNOWLEDGEMENTS –……..…..…….iv

Publication participation during Bren School PhD program –..……..……v

VITA OF RANDALL EDWARD MIELKE –……..…….……..viii

ABSTRACT –……..……...…..xiv

TABLE OF CONTENT –…..……..…….xvii

LIST OF FIGURES –…..……..…….....…xx

I. INTRODUCTION –……..……..……....1

II. Design, Fabrication, and Test of a Hydrothermal Reactor for Origin-of-Life Experiments –.....19

Abstract –…….…..……...……..19
1. Introduction –…….…….….……..20
2. Materials and Methods –.....……...…….…….....26
   2.1. Reactor design and construction
   2.2. Preparation of solutions
   2.3. Operation and experimental test
   2.4. Investigation of precipitates
3. Results –……..……...……32
   3.1. Solution chemistry
   3.2. Mineralogy
   3.3. Chimney and geodic growth
4. Discussion –……...…….…...…35
   Acknowledgments
   Disclosure Statement
   Abbreviations
   Figures –……...…..…..…...39

III. Iron-Sulfide-Bearing Chimneys as Potential Energy Catalytic Traps at Life's Emergence –.....49

Abstract –……...……...……..49
1. Introduction –……...…..……50

2. Methods –…….....……....…….57
3. Results and Interpretation –……...……63
3.1. Basic iron sulfide chimney structure
3.2. Varying injection solution pH
3.3. Varying sodium orthosilicate concentrations and temperature
3.4. Effects of pentameric peptides on structure
4. Discussion –…….....…69
5. Conclusions –……....…...…73
Acknowledgments
Authors Disclosure Statement
Abbreviations
Figures –……..….....79

IV. Differential growth of and nanoscale TiO2 accumulation in Tetrahymena thermophile by direct feeding versus trophic transfer from Pseudomonas aeruginosa –…….....90

Abstract –…….....….....91
1. Introduction –…….....92
2. Materials and Methods –…….....94
2.1. Strains, media, and nanomaterials
2.2. Preparation of *P. aeruginosa* and *T. thermophila* inocula
2.3. *P. aeruginosa* cultivation in liquid medium
2.4. *T. thermophila* growth without *P. aeruginosa* prey
2.5. *T. thermophila* growth with *P. aeruginosa* prey
2.6. Cell counts by light microcopy
2.7. Electron microscopy and X-ray microanalysis
2.8. X-ray microscopy
2.9. Calculation of TiO_2 mass adsorbed to *P. aeruginosa*
2.10. Quantitative analysis of *T. thermophila* food vacuoles
2.11. Bioconcentration and biomagnification calculations
2.12. Quantitative assessment of TiO_2 within *T. thermophila* populations
2.13. Additional data and statistical analyses
3. Results and Interpretation –…….....108
3.1. Growth and morphology of *P. aeruginosa*
3.2. *T. thermophila* growth and motility
3.3. *T. thermophila* uptake of TiO_2 from rich medium
3.4. *T. thermophila* uptake of TiO_2 from *P. aeruginosa* prey
3.5. Quantitative assessment of TiO_2 bioconcentration and biomagnification
4. Discussion –…….....…116
Acknowledgments
Figures –…….....121

5. Supplemental Materials –…… 126
5.1. Estimation of the average amount of TiO_2 adsorbed to *P. aeruginosa*
1. Background.
2. Amount nanoscale TiO_2 adsorbed onto *P. aeruginosa* cells, as confirmed by ESEM image**s**
3. Volume- and mass-basis concentration of nanoscale TiO_2 per *P. aeruginosa* cell
5.2. Mass of TiO_2 delivered with *P. aeruginosa* in the trophic transfer experiment
5.3. Mass of nTiO2 delivered with PA in the trophic transfer experiment.
Supplemental Materials Figures –……...131

V. Dark-field Scanning Transmission Electron Microscopy – Energy Dispersive X-ray Spectroscopic (STEM-EDS) analysis of manufactured nanomaterial alterations …….….146

Abstract –……..…..…..146
1. Introduction –……..……...148
2. Materials and Methods –……...153
2.1. Strains, media, and nanomaterials
2.2. Preparation of bacterial and protozoan inocula
2.3. Bacterial cultivation in aqueous media with QDs, cadmium, or selenite salts
2.4. Protozoan growth with QD contaminated bacterial prey
2.5. Specimen preparation, and electron microscopy and x-ray microanalysis
2.6. Quantitative assessment of theoretical EDS spectral penetration depth for specific minerals
2.7. Quantitative assessment of EDS spectra to analyze quantum dot weathering
2.8.Additional Data and Statistical Analyses
3. Results and Interpretation –……..……....171
3.1. QD weathering by bacteria
3.2. Quantification of bacterial formed QD by STEM-EDS
3.3. Quantification of QD weathering by protozoa with STEM-EDS
3.4. Evaluation of x-rays generation depth profile
4. Discussion –……...……..…….182
Acknowledgments
Figures –……..……..……...188

VI. CONCLUSION –…….....206

REFERENCES –……..…210

LIST OF FIGURES

Figure II-1. A scenario for the emergence of life whereby the first organic building components are generated in a natural hydrothermal reactor (the iron sulfide–bearing mound figured here) produced over an unforced convection cell operating at hydrostatic pressure on the Hadean Ocean floor (cf. Figs. II-8 and II-9). A reactor simulating these conditions is described in the text and shown in Fig. II-2. Key to catalysis and electron transfer in the natural reactor is a supply of hydrogen sulfide anion (HS^-, dissolved from the iron sulfides beneath) to react with the ferrous (and minor ferric) iron in the early ocean, a concern of the test experiment. Occasional iron sulfide veins and pods within ocean floor sequences of komatiitic lavas would have been a source of soluble hydrogen sulfide ion (e.g., Lesher and Stone, 1997), and gabbros, cherts, or quartz veins as the source of silica (Barnes *et al.*, 1972; Fallick *et al.*, 1991). Serpentinization is the process of hydration, carbonation, and oxidation of komatiites and other mineralogically comparable rocks thought to be an initial requirement for life's emergence (Russell *et al.*, 1989).

Figure II-2. Top: CAD drawing of the reactor design with inset photograph of the reactor before lagging with thermoelectric coil. Two-way or three-way valves are shown in green, and non-return ball valves are in red. Gasses are purged into solutions through the bottom port to ensure adequate gas/solution interface time. The reactor on the right illustrates placement of temperature sensors on the external reactor surface and the distribution inside the reactor of iron sulfide (FeS) and rock

wool. Bottom: the lagged system. PG, pressure gauge. Color images available online at www.liebertonline.com/ast.

Figure II-3. Inductively coupled plasma optical emission spectrometry analysis of effluent for the time-dependent samples. Graph II-3A shows the results of 60 samples collected over the first 4000min, and graph A3B shows the complete experimental time period (250 samples). The initial few samples contained over 50 ppm of sulfur determined to be sulfate ions that dropped to zero after 240 min. Initially the pH of the hydrothermal solution dropped almost one unit before rising again after 10 hours to stabilize around pH 12.3. The operating reactor temperature was reached within 120 min, whereas the maximum sulfur concentration (as HS^-) was reached at 360 min, indicating that major dissolution of sulfide occurs only after the operating temperature is reached. The hydrothermal solution was open to the reactor for the first 1440 min followed by alternating ocean/hydrothermal solutions opened every 15 min for another 1440 min. For the remainder of the experiment both solutions were opened to the reactor. The heaters were shut off at 13,200 min, and the system was at ambient temperature by 14,000 min. At this time the concentrations of sulfur, calcium, silicon, potassium, and magnesium were below the detection limits. Color images available online at www.liebertonline.com/ast.

Figure II-4. (A) Environmental scanning electron microscope image of basalt rock wool prior to alteration; (B) the same rock wool comprising Layer 1, the image revealing severe surface alteration and loss of calcium (cf. Fig. II-5). (C) Calcite precipitates on basalt rock wool from Layers 1–3. (D) Clumps of iron- and sulfide-

rich minerals cover portions of the basalt rock wool of Layer 15, demonstrating local mobility of these two elements.

Figure II-5. The graph shows the ESEM-EDX analyses of several of the basalt rock wool layers and the basalt rock wool control (n = 50). The most drastic changes occurred in the amount of calcium dissolved from the surface material at the bottom of the reactor (Layer 1, n = 44) and in the hot zone above the iron sulfide layer (Layer 15, n = 67). Aluminum was also removed from Layer 1. In contrast, the top, cool portion of the reactor (Layer 25, n = 50) shows surface atomic ratio composition at levels equivalent to the control basalt rock wool, except for a slight enrichment of silicon. However, some of the calcium now resides in a carbonate phase in Layer 25. Color images available online at www.liebertonline.com/ast.

Figure II-6. Sketch of hydrothermal reactor with range of atomic S:Fe ratios on the surface of altered FeS as analyzed by ESEM (numbers of analyses in parentheses): Pristine FeS=1.07, 1σ±0.17; Layer 3=0.50–0.21, 1σ±0.17 (2); Layer 6=0.71–0.21, 1σ±0.19 (3); Layer 9=0.42–0.33, 1σ±0.21 (2); Layer 12=0.83–0.15, 1σ±0.19 (5); Layer 14=0.62–0.01, 1σ±0.18 (6). Color images available online at www.liebertonline.com/ast.

Figure II-7. Photomicrographs demonstrating the iron-rich minerals (probably green rust) precipitated on the surfaces of the iron sulfide. The S:Fe ratios of these minerals were invariably less than 1, and in many cases much less, as to be expected as sulfide was lost to solution (Fig. II-3). Images (A) and (B) are from Layer 3 and show various sizes of flakey ball structures. There were other larger aluminosilicate crystals

present in the iron sulfide layers (arrow) as shown in image (C). Image (D) is from Layer 14 with similar characteristic morphologies but had the largest diversity and included phases with aluminum: silicon ratio close to ~2 (possibly vermiculite) and only minor iron content.

Figure II-8. Injection of the reactor effluent taken after 5 hours (Fig. II-3) into the simulacrum of the Hadean Ocean containing 10mM/L ferrous iron. When injection rate is rapid, a chimney grows to ~35mm in 8 min before the top spalls off and settles (white arrow) (A). Geodic growth is favored when injection rate is slow [pictured after 12 hours in (B) and detailed in Fig. II-9]. Color images available online at www.liebertonline.com/ast.

Figure II-9. Environmental scanning electron microscope images of a cross section near the base of the inflated geode figured in A and B shown to comprise an outer mixed iron hydroxide, silicate, carbonate, and sulfide wall (A and B) and a hollow interior containing a collection of smaller well-defined geodes. One of these microgeodes is revealed as partly filled with fluffy nanocrysts of iron-bearing minerals (C). Compare with Fig. II-1.

Figure III-1. The experimental apparatus used for the production of metal-bearing chimneys. The crimp-top Wheaton bottle (125 mL) was cut open to more easily harvest the chimneys from the ‘‘Ocean’’ receptacle. Parafilm was tightly wrapped around the receptacle’s open top, and a gaseous nitrogen purge line was used to create an oxygen-depleted headspace. All solutions were purged with gaseous nitrogen before use in experiments. A 10 mL syringe connected with Teflon tubing to a 1/16-

inch (1.59 mm outer diameter) stainless steel tube was used to inject the ‘‘Hydrothermal’’ solution into the ‘‘Ocean’’ receptacle through the Teflon septa. Specially designed devices were used to minimize structural damage to the chimneys during harvesting and transport to the particular analytical instruments.

Figure III-2. (a) Video image sequence of a growing iron-sulfide chimney as a 10 millimolar alkaline sulfide solution is injected into a slightly acidic 10 millimolar iron (II) solution at a rate of 0.2 mL/h. The stream of effluent-bearing precipitate (white arrow) can be seen emerging from the top of the chimney, indicating a hollow structure. Over time the stream becomes paler. Through to the first 100 min the chimney appears smooth, but thereafter becomes increasingly covered in fibrous strands and globules of precipitate. The chimney growing from the 1/16-inch (1.59 mm outer diameter) stainless steel tubing is itself about 1 mm in diameter (3 mm scale bar). (b) Environmental scanning electron microscope (ESEM) micrographs seamed together of an FeS chimney showing the top opening at lower magnification. (c and d) ESEM images of increasing magnifications showing the morphologies of the FeS minerals comprising the chimney (compared with figure 1h of Pagano *et al.*, 2008). (e) Scanning transmission electron micrographs of the FeS chimney cross section showing the variety of morphologies that support the intricate channels comprising the semipermeable membrane. All solutions contain 600 millimoles/liter of sodium chloride. Color images available online at www.liebertonline.com/ast.

Figure III-3. ESEM micrographs (a) showing a cross section of chimney wall produced as a sodium sulfide solution is injected into a solution of iron (II) chloride at 50°C. The iron:sulfur ratio of the shards (arrow) that comprise this outer membrane is ~6.5 (indicative of iron hydroxides dominating over FeS); (a) and (b) illustrate the contrasting overgrowths on the interior and exterior of the membrane; (c) and (d) show spherical morphologies that resemble framboids (cf. Wilkin and Barnes, 1997; Ohfuji and Rickard, 2005). The latter have iron:sulfur ratios of between 1.2 and 1.5, indicative of a mixture of mackinawite, greigite, or pyrite with minor iron hydroxide (cf. Sawlowicz, 1993, 2000; Ariztegui and Dobson, 1996). They also bear comparison with framboids found in fossil hydrothermal chimneys (Larter *et al.*, 1981; Boyce *et al.*, 1983). Framboids are produced as aggregates of magnetic iron sulfides (generally ferromagnetic greigite) in far-from-equilibrium conditions (Wilkin and Barnes, 1997; Sawlowicz, 2000). Note that this experiment was run at 50°C, with the standard reagent concentrations specified in the Methods section.

Figure III-4. ESEM micrographs of the flanged walls to iron sulfide/hydroxide chimneys produced when 5 millimolar alkaline sulfide solution is injected into a slightly acidic 10 millimolar iron (II) chloride solution. Experiments were conducted at a rate of 7.2 mL/h with a peristaltic pump. Micrographs (a) and (b) are from separate experiments. Both exhibit flange growth normal to the apparent growth axis with a periodicity (wavelength) of ~4 μm. The exterior flanges are composed of iron hydroxide flocculent (Fe/S = 5.42 – 0.48 for the mean of three EDX analyses). The polarity of growth in (b) might indicate the direction of diffusive flow.

Figure III-5. Series of frames (top) captured from video of separate experiments with varying injection solution pH (i.e., sodium sulfide solution). Notice the increasing bulbous appearance and eventual deterioration of the FeS precipitate as pH is lowered and the lack of chimney formation that occurs at pH 8.03. Above pH 11 the exterior membrane surfaces comprise green rust (iron oxyhydroxides), and chimneys are characteristically taller and often branched. The graph (bottom) shows the ESEM–energy dispersive X-ray spectroscopy (EDX) analytical results for iron:sulfur atomic ratios of multiple analyses per chimney cross section and multiple chimneys at the various pHs. Note that this experiment was run under ambient laboratory conditions with reactant concentrations specified in the Methods section. For a scale of reference, the stainless steel tubing possesses an outer diameter of 1/16 inch (1.59 mm) (3 mm scale bar). Color images available online at www.liebertonline.com/ast

Figure III-6. Series of frames (top) captured from video of separate experiments involving various concentrations of sodium orthosilicate added to the sodium sulfide solution at an unadjusted pH of ~11.7 and injected into a solution of iron (II) chloride. The left-hand data point here is equivalent to right-hand data point in Fig. III-5. The precipitate structures become more bulbous with increasing sodium orthosilicate concentrations. The graph (bottom) of ESEM-EDX analyses of iron:sulfur atomic ratio indicates that the highest sulfur content relative to iron is found in these structures when the concentration of sodium orthosilicate in the sodium sulfide injection solution is ~7.15 millimoles/liter. For a scale of reference, the stainless steel

tubing possesses an outer diameter of 1/16 inch (1.59 mm) (3 mm scale bar). Color images available online at www.liebertonline.com/ast.

Figure III-7. X-ray diffraction spectra of a precipitate formed via the injection of 2.0 millimolar sodium orthosilicate and 10.0 millimolar of sodium sulfide solution into a receptacle solution of 10 millimolar iron (II) chloride at STP. The main mineral phase was found to be mackinawite. The two strong peaks at ~32° and ~46° are associated with unknown minerals that may be forms of ferrous silicate (cf. Bourdoiseau *et al.*, 2008; Rémazeilles *et al.*, 2010). All solutions contain 600 millimoles/liter sodium chloride. Color images available online at www.liebertonline.com/ast.

Figure III-8. Raman spectrographic analysis shows evidence for partially oxidized mackinawite (iron (III)-containing mackinawite) in iron sulfide chimney grown at 70°C. The small shoulder peak at ~309 cm^{-1} and the broad hump centered around ~354 cm^{-1} are similar to the spectral peaks identified by Bourdoiseau *et al.* (2008) as representing partial oxidation of iron (II) in mackinawite to iron (III). The partial oxidation of iron (II) is demonstrated to lead to the formation of greigite (Rickard *et al.*, 2001, and see Fig. 9). Color images available online at www.liebertonline.com/ast.

Figure III-9. Raman spectrographic analysis shows evidence for greigite and native sulfur in iron sulfide chimneys grown at 70°C. Greigite is expected at higher temperatures through the loss of iron to solution, and the native sulfur is possibly produced by the same process, though we cannot rule out the production of sulfur by

oxidation occurring during transfer of the sample to the Raman system. The large greigite peak around 350 cm^{-1} is separated into two bands occurring at ~351 and ~352 cm^{-1}, closely resembling the greigite Raman spectrum of Rémazeilles *et al.* (2010, and see Wei and Osseo-Asare, 1995; Benning *et al.*, 2000; Rickard *et al.*, 2001.) Color images available online at www.liebertonline.com/ast.

Figure III-10. ESEM images of flanged walls on ferrous sulfide/hydroxide chimneys grown by the injection of a 5 millimolar alkaline sodium sulfide (pH ~11.7) solution bearing 100 micromolar pentameric peptides into a 10 millimolar slightly acidic iron (II) chloride solution. The chimneys were produced at an injection rate of 7.2 mL/h, and the different pentameric peptides are identified below the ball-and-stick illustrations. All three peptide experiments formed flanged walls that had a similar periodicity (wavelength) of ~4 μm. The three peptides gave structures topographically unique from one another as judged by ESEM. All solutions contained 600 millimolar sodium chloride and no sodium orthosilicate. Ball-and-stick images produced with BALLView 1.4.

Figure III-11. Composite selection of micrographs illustrating the regular flanges that comprise ferrous hydroxide microdendrites (see Fig. III-B & III-D for detail) on the exterior of an iron sulfide–bearing membrane (left), a cross section (middle), and framboidal iron sulfides from the interior of a chimney (right). We speculate that flange growth results from the escape of alkaline solution through the membrane along subcompartments oriented normal to growth. Where this solution meets the

ferrous iron, ferrous hydroxide is precipitated as ribs, also normal to growth. A counterflow of protons down-gradient to the alkaline interior takes place in the neighboring subcompartments. Platelets of ferrous minerals are spontaneously precipitated at the interface of the two solutions. This is where we imagine the potential exists for carbon dioxide reduction/hydrogenation under the higher pressures obtaining early in the history of wet, rocky worlds—an idea amenable to testing through microfluidics.

Figure IV-1. Growth curves of *T. thermophila* cultured in rich (SSP) medium without bacterial prey (open symbols, dashed lines) or in Dryl's medium with bacterial prey (closed symbols, solid lines). Triangles (Δ, ▲) and circles (○, ●) represent control (without TiO_2) and treatments with TiO_2, respectively. Each point is the average of three independent replicates. Standard error bars are smaller than the symbols and thus not visible. The inset graph shows the individual replicate growth curves for the six Dryl's medium (with prey) cultures. The symbols in the inset represent the same treatments as in the main graph.

Figure IV-2. Dark-field STEM micrographs of unstained thin sections of *T. thermophila* cells grown in rich medium (SSP) in the presence of TiO_2 (0.1 mg ml/L) without (w/o) bacteria (left column) or in Dryl's medium with (w) TiO_2-encrusted *P. aeruginosa* prey (right column). *T. thermophila* cells are shown after 2 h (a, b), 8 h (c, d), 16 h (e, f), and 22 h (g, h) of growth, where 16 and 22 h were during rapid growth (Fig. IV-1). Food vacuoles (FV) are indicated. The brighter spots are indicative of

higher-molecular-weight elements, in this case, Ti associated with TiO_2. Scale bars, 2 μm.

Figure IV-3. Time course during *T. thermophila* growth (Fig. IV-1) of mean food vacuole (FV) volume (○, dashed lines), measured average percent food vacuole volume filled with TiO2 (◊, dotted lines), and TiO_2 mass per *T. thermophila* cell (●, solid lines). (a) *T. thermophila* grown in rich (SSP) medium with 0.1 mg ml/L TiO_2 but without *P. aeruginosa* bacterial prey. (b) *T. thermophila* grown by feeding exclusively on TiO_2-encrusted *P. aeruginosa* cells. The patterns are consistent with those observed in electron micrographs (Fig. IV-2). The plotted values are tabulated in Tables IV-S2 to IV-S5 in the supplemental material.

Figure IV-4. Total TiO_2 mass (a) and percentage of total administered TiO_2 (b) within whole *T. thermophila* populations at each time point during growth. Dashed line (○), SSP-grown population; solid line (●), population grown in Dryl's medium with *P. aeruginosa*. Points are average values (n = 3). Error bars are the result of propagating errors according to standard methods.

Table IV-S1. Tabulation of the methods used to measure and calculate characteristics of *T. thermophila*, including food vacuole (FV) sizes, FV filling with TiO_2, and TiO_2 mass and mass concentration per *T. thermophila* cell. The measurement approaches, using quantitative analysis of STEM images, are described in the IV-Methods; results are tabulated in Tables IV-S2 through IV-S5, and described in the main manuscript.

Table IV-S2. Characteristics of individual food vacuoles (FVs) over time, during TT growth in rich media without PA, and with/ $nTiO_2$. Shown are the total number of FVs measured (across several individual TT cells), and the means, plus or minus standard error of the mean, of measured and calculated FV characteristics. In the table, "Meas." indicates that the characteristic was measured directly from electron micrographs, as per the Methods. "Calc." indicates that the characteristic was calculated from measurements with stated assumptions herein and as per the Methods.

Table IV-S3. Characteristics of individual food vacuoles (FVs) over time, during TT growth in starvation media with $nTiO_2$-encrusted PA. Shown are the total number of FVs measured (across several individual TT cells), and the means, plus or minus standard error of the mean, of measured and calculated FV characteristics. In the table, "Meas." indicates that the characteristic was measured directly from electron micrographs, as per the Methods. "Calc." indicates that the characteristic was calculated from measurements with stated assumptions herein and as per the Methods.

Table IV-S4. Calculated values of TiO_2 volume- and mass-based concentrations in *T. thermophila* cells, and calculated values of Bioconcentration Factor (BCF) for the *T. thermophila* growth condition of rich medium with TiO_2.

Table IV-S5. Calculated values of TiO_2 volume- and mass-based concentrations in *T. thermophila* cells, and calculated values of Biomagnification Factor (BMF) for the *T. thermophila* growth condition of Dryl's medium with TiO_2-encrusted *P. aeruginosa* as the food source.

Figure IV-S1. Schematic/flow diagram and sample calculations for the *T. thermophila* trophic transfer experiment. TiO_2-exposed *P. aeruginosa* cells were fed to *T. thermophila* (a), resulting in food vacuole (FV) filling by TiO_2-encrusted bacteria. TiO_2 in FVs was clearly visible in STEM micrographs of *T. thermophila*, and the FV and TiO_2 areas (A_v and A_{Ti}, respectively) were measured for each FV (b). The diameter (D_{Ti}) of a circle, whose area (A_{Ti}) was equivalent to the measured TiO_2 area within the FV, was calculated (c). The calculated diameter D_{Ti} derived from the circular area was then used to calculate the spherical volume ($Vol._{Ti}$) of TiO_2 in the FV (c). The volume percent FV filling was calculated by dividing $Vol._{Ti}$ into the FV volume ($Vol._v$), then multiplying by 100 (d). The mass of TiO_2 contained in each FV (d) was calculated by multiplying $Vol._{Ti}$ by the density of TiO_2 (3.97×10^{-12} g μm^{-3}).

Figure IV-S2. Growth curves for planktonic *P. aeruginosa* in the absence (○) or presence (▲) of nanoscale TiO_2 (0.1 mg ml^{-1}). Mean optical density (OD_{600}; n = 3) is plotted. Error bars represent the standard errors of the means, but are not visible due to their low values.

Figure IV-S3. Representative ESEM micrographs of nanoscale TiO_2-encrusted *P. aeruginosa*. Arrows indicate individual cells. The scale bar in each image represents 2 μm.

Figure IV-S4. Linearity of natural log-transformed *T. thermophila* cell counts (mL^{-1}) over 22 hours of growth in Dryls' medium with *P. aerginosa* as the exclusive food source. Symbols are as per Figure IV-1 in the main manuscript, where filled triangles are the averaged triplicate measures for the treatment with control *P. aeruginosa* (no TiO_2), and filled circles are the averaged triplicate measures for the treatment w/ TiO_2 pre-adsorbed to *P. aeruginosa* before feeding to *T. thermophila* as prey. Regression lines are calculated from the average data (n=3) at each time point, within each data series. Slopes of the regression lines are the specific growth rates (h^{-1}), as reported in the main manuscript. Error bars are not shown, but the low variation is indicated by overlapping growth curves in the Figure IV-1 inset. Note that, in the calculation of specific growth rates (see main manuscript, IV-Methods) slopes of individual lines of regression from individual replicate growth curves were calculated, then the slopes averaged to compute mean specific growth rate constants.

Figure IV-S5. Dark field STEM micrograph of an unstained thin section of embedded *T. thermophila* culture grown in rich (SSP) medium with TiO_2 for 2 h. There are no *T. thermophila* cells in the image, which is expected given the early stage in the population growth (Figure IV-1). Rich medium components are visible as gray microspheres (arrow). The bright spots are TiO_2 agglomerates.

Figure IV-S6. Electron micrograph acquired by backscatter detection (BSD) of a single 16-h *T. thermophila* food vacuole (FV, a), with an associated X-ray microanalysis spectra (b, by energy dispersive spectrometry or EDS). The food vacuole (a) contains *P. aeruginosa* cells that were TiO_2-encrusted when fed as prey for *T. thermophila* growth in minimal (Dryl's) medium (Figure IV-1). The spectrum (b) was collected from one region (white square) shown in (a). The black arrow in (b) is above the Ti peak of the spectrum, confirming the presence of Ti. The brightness of the *P. aeruginosa* cells in the image is atomic weight-dependent, illustrating that these cells are coated with non-agglomerated TiO_2. Agglomerates separate from *P. aeruginosa* cells are evidenced by bright white speckles (bottom right).

Figure IV-S7. Artificial color X-ray microscope image of a whole *T. thermophila* protozoan cell, harvested from a population grown for 22 h in minimal (Dryl's) medium with TiO_2-encrusted *P. aeruginosa* bacteria as prey. TiO_2 filled food vacuoles (FV) are visible in the anterior region of the cell. The scale bar represents 25 μm. Thin sections of such FVs are shown in high magnification in Figure IV-2h.

Figure IV-S8. Nomarski images of *T. thermophila* cells cultured in Dryl's medium with TiO_2-encrusted *P. aeruginosa* after 0 h (a) and 22 h (b). Extracellular TiO_2 agglomerates (stars) and *P. aeruginosa* cells (triangles) are visible. The oral apparatus is well outlined in one cell (thin arrow). At 22 h, TiO_2-filled food vacuoles (thick arrows) are also visible (b). *T. thermophila* in these 22-h cultures showed normal motility.

Movie IV-S1.

http://www.bren.ucsb.edu/~holden/AEM_SI_2013_movie/UXRM029_UCSB_Protozoa_TiO2NP_VRT.mpg

3D volume rendering of X-ray microscopy reconstruction of *T. thermophila* grown for 22 hours with TiO_2-encrusted *P. aeruginosa* as prey. This volume rendering is represented by the 2D virtual slice in Figure IV-S7 in this IV-supplemental material.

Table V-1. The central core and first shell has a diameter of 1.450 nm (Kasuva et al. 2004) and is built on by addition of tetrahedral structures (0.3548 nm total height). The addition of 11 shells to the central core will develop a ~8.5 nm CdSe QD. The shells elemental content can be calculated through the volume and density of CdSe. The enumeration of Cd and Se atoms present in each shell will allow further investigation into understanding the influence of weathering surface atoms the STEM-EDS analyses. This table was generated with Microsoft Excel.

Table V-2. When x-rays are generated from only the outer most shell of the CdSe crystal. The weathering of the surface atoms would produce a Cd:Se atomic ratio of 2:1 if 50% of the Se atoms were removed. For shell 11 with 1,349 CdSe molecules in the outer most shell and a central core with 4,611 CdSe molecules, since we have equal numbers of Cd as Se atoms there are 1,349 atoms of Cd and 1,369 atoms of Se located in the 11th shell. If there is 50% weathering of the Se atoms there will be 1,369 atoms of Cd and 684.5 atoms of Se producing and x-ray atomic ratio of 1,369/684.5 = 2.0 Cd:Se.

Figure V-1. Diagramed CdSe Quantum dots with the 11 shells of an ~8.55 nm size (not to scale). The red shell, in this case shell 11, illustrates that the EDS x-ray signal is being only generated by atoms in the very most outer shell of an ~8.55 nm QD. This results in a Cd:Se atomic ratio of 2.0 for all size QDs and it is unlikely that non-of the atoms from the interior core of the QDs will not influence the EDS analytical results.

Table V-3. When x-rays are generated from only the two outer most shell CdSe molecules of the CdSe crystal and only weathering is occurring on the outer shell Cd or Se atoms. The weathering of the surface atoms would produce a Cd:Se atomic ratio of above 2 for the extreme weathering of 70% of the Se atoms were removed. For shell 11 with 1,349 CdSe molecules in the outer most shell and a central core with 4,611 CdSe molecules, since we have equal numbers of Cd as Se atoms there are 1,349 atoms of Cd and 1,369 atoms of Se located in the 11th shell. If there is 70% weathering of the Se atoms there will be 1,369 atoms of Cd and 410 atoms of Se resulting in producing x-ray being produced from;

= 1,369 (shell 11) Cd + 1,142 (shell 10) Cd /

/410 (shell 11; weathered) Se + 1,142 (shell 10) Se

= 2,511 Cd atoms / 1,552 Se atoms = 1.618 Cd:Se atomic ratio

(This is the atomic ratios 7.84 & 8.55 (70%) in circle)

Figure V-2. Diagramed CdSe QD that shows the 11 shells of an ~8.55 nm size (not to scale). The red shell, in this case shell 6 (5.00 nm QD), illustrates that the EDS x-ray signal is being generated from atoms in shell 6 and the adjacent shell of atoms in green (shell 5 4.29 nm). This results in a Cd:Se atomic ratio up to only 2.36 with 100% weathering of all Se atoms from the surface. This is an unlikely theoretical model since the experimental EDS analyses produce Cd:Se atomic ratios up to 2.8 and even some of the analyses are as much as 4.0:1.0 Cd:Se atomic ratio.

Table V-4. When x-rays are generated from only the outer most shell CdSe molecules and 25% of the adjacent inner shell of the CdSe crystal with only weathering occurring on the outer shell of Cd or Se atoms. The weathering of the surface atoms would produce a Cd:Se atomic ratio of about 2.46 for extreme weathering of 70% of the Se atoms removed for a 5.00 nm QD. The number of atoms influencing the x-ray signal is more in line with the experimental EDS analyses generating the range between Cd:Se 2.8 to Se:Cd 1.3.

Figure V-3. Diagramed CdSe QD that shows the 11 shells of an ~8.55 nm size (not to scale). The red shell, in this case shell 6 (5.00 nm QD), illustrates that the EDS x-ray signal is being generated from atoms in shell 6 and the adjacent shell of atoms in blue (shell 5, 4.29 nm) is only influencing the EDS with 25% of the shell atoms. This results in a possible Cd:Se atomic ratio of 6.22 when 100% weathering of all Se atoms from the QD surface. The theoretical model is more likely and fits the

experimental EDS analyses that produces Cd:Se atomic ratios over 2.8 when below 80% weathering of Se atom from the surface has occurred.

Figure V-4. PA contaminated with CdSe Quantum dots for 24 hours. The STEM images show the progression of cell internal structural deformation (white star). The CdSe QDs are located in the PA cytoplasm and associated with the PA cell wall (white arrows). The dark-field STEM imaging technique is atomic mass dependent that produces brighter contrast where larger atomic masses of CdSe QDs are located.

Figure V-5. STEM-EDS analyses for CdSe QDs (filled circle) starting material, PA cytoplasm QDs (diamond), PA cell wall QDs (triangle), and QDs located away from PA cells (blue-filled circle). A total of ~50 EDS analyses were acquired for each of the three specific region for each time point. The replicate (n=x) is for the number of replicates for either Cd:Se or Se:Cd. Whole numbers were maintained in determining appropriate atomic ratio placement in graph to visually maintain similar spacing for Cd-enriched (pink region, Cd-QDs) or Se-enriched (green region, Se-QDs) QDs. The EDS analyses that calculated atomic percentage for only Cd or only Se are indicated by the lower (n=x) in the respective Cd (pink) region or Se (green) region. These EDS results could be from CdSe QDs with selenium concentrations below the detectable level or are bright cellular location where only cadmium is present and visa versa for bright spots with only Se having a calculated atomic percentage.

Figure V-6. STEM-EDS analyses were taken of QDs located in PA cytoplasm, QDs associated with PA cell wall and QDs outside PA in the medium. The starting

material (SM-QDs) QDs was also analyzed to determine how weathering of QDs progress for during the 24 h contamination study. A total of ~50 EDS replicates were determined to be either Cd enriched QDs (Cd-QDs) or Se enriched QDs (Se-QDs) by the respective Cd:Se (<1.0) or Cd:Se (>1.0; Se:Cd greater than 1). The SM-CdSe QDs resulted in 82% showing Cd-QDs and SM-CdTe QDs had 52% of the EDS analyses showing Cd-QDs. The PA CdSe QD study had Cd-QDs in the cytoplasm being reduced to 50% showing the QDs were becoming Se-QDs. The PA CdTe QD study showed the Cd-QDs associated with the PA cell wall was reduced to 18% indicating the trend toward Se-QDs.

Figure V-7. PA contaminated with CdTe Quantum dots for 24 hours. The STEM images show the progression of cell internal structural deformation (white star). The CdTe QDs are located in the PA cytoplasm and associated with the PA cell wall (white arrows). The dark-field STEM imaging technique is atomic mass dependent that produces brighter contrast where larger atomic masses of CdTe QDs are located.

Figure V-8. STEM-EDS analyses for CdTe QDs (filled circle) starting material, PA cytoplasm QDs (diamond), PA cell wall QDs (triangle), and QDs located away from PA cells (black-filled circle). A total of ~50 EDS analyses were acquired for each of the three specific region for each time point. The replicate (n=x) is for the number of replicates for either Cd:Te or Te:Cd. Whole numbers were maintained in determining appropriate atomic ratio placement in graph to visually maintain similar spacing for Cd-enriched (pink region, Cd-QDs) or Te-enriched (green region, Te-QDs) QDs. The

EDS analyses that calculated atomic percentage for only Cd or only Te are indicated by the lower (n=x) in the respective Cd (pink) region or Te (green) region. These EDS results could be from CdTe QDs with tellurium concentrations below the detectable level or are bright cellular location where only cadmium is present and visa versa for bright spots with only Te having a calculated atomic percentage.

Figure V-9. STEM images of PA contaminated with 0.075 mg mL^{-1} Cd^{+2}, 0.075 mg mL^{-1} Cd^{+2} and 0.2 mg mL^{+2} SeO_3^{-2} in LB broth for 24 hours. The STEM images show Cd^{+2} bright spots within the periplasmic space cell. The Cd^{+2} and SeO_3^{-2} contaminated PA STEM images show distinct bright spots located in the cytoplasm and associated with the PA cell wall. The scale bars are 1 μm for all images.

Figure V-10. STEM-EDS analyses were taken of QDs located in PA cytoplasm, QDs associated with PA cell wall and QDs outside PA in the medium. The starting material (SM-QDs) QDs was also analyzed to determine how weathering of QDs progress for during the 24 h contamination study. A total of ~50 EDS replicates were determined to be either Cd enriched QDs (Cd-QDs) or Se enriched QDs (Se-QDs) by the respective Cd:Se (<1.0) or Cd:Se (>1.0; Se:Cd greater than 1). The SM-CdSe QDs resulted in 82% showing Cd-QDs and SM-CdTe QDs had 52% of the EDS analyses showing Cd-QDs. The PA Cd^{+2} and SeO_3^{-2} salt study had Cd-QDs in the cytoplasm being 50% showing the QDs were becoming Se-QDs enriched. The QDs associated with the PA cell wall had 16 analyses resulting in Cd-CdSe QD and 20 that

showed only Cd which could indicated either Cd-enriched QDs that Se is below the detection limit or build up of Cd^{+2} ions.

Figure V-11. STEM-EDS analyses were taken of QDs located in TT contaminated with CdSe QDs PA after 8 h contamination. The TT cell membrane had 10 replicates of CdSe atomic ratios similar to the starting materials QDs (Figure V-2). The TT cellular organelles show the presence of CdSe QDs located throughout the TT cell.

Figure V-12. STEM-EDS analyses were taken of QDs located in TT contaminated with CdSe QDs PA after 24 h contamination. The TT cell membrane had 9 replicates of CdSe atomic ratios similar to the starting materials QDs (Figure V-2). The TT cellular organelles show the presence of CdSe QDs located throughout the TT cell. The greatest potential use of STEM-EDS is determining how the QDs are weathering in the different chemical environments that are present in the different TT organelles.

INTRODUCTION

Nanomaterials on Earth are both natural and anthropogenic. Whether from volcanic eruptions or interstellar dust from outer space, nanomaterials (NMs) have been raining down on Earth since the beginning of geological time (Krueger and Kissel, 2000). NMs are formed in deep sea hydrothermal seeps where they provide a huge reactive surface area for the generation and accumulation of pre-biotic organics in the relative calmness of the bottom of the putative Hadean Ocean (Russell and Kanik, 2010; Mielke *et al.*, 2011). Clusters of iron sulfides, some dosed with nickel, may have been sequestered by short peptides and acted as the first hydrogenases, and metabolic catalysts. Similar structures are involved in modern coded enzymes. A hypothesis affirms that the emergence of life is a direct result of NMs' catalytic surfaces aiding in synthesis of the first organic compounds essential for the generation of life.

The introduction of Manufactured NMs (MNMs) into the food supply and the environment is of increasing concern. Highly reactive NM surfaces are currently being utilized for their catalytic and other properties in man-made products (Villota *et al.*, 1986; Mueller & Nowack 2010). Specifically, carbon-based NMs and metal-based NMs are found in seasoning salts, milk, cosmetics, pharmaceuticals, and electronics (Boxall *et al*. 2007; Castro *et al*. 2006; Choksi *et al.*, 2010; Phillips *et al.*, 1997; Royal Commission Report 2008; Villota *et al.*, 1986). When these products are used in everyday practices, the small amounts of NMs contained within products can

be released into the environment (Gottschalk and Nowack, 2011) contributing to environmental pollution upon their release (Rico *et al*. 2011) which could affect the long-term health of the consumer (Maynard and Michelson, 2007).

The first section of this dissertation investigates the emergence of life using NMs as potential catalytic energy traps, as well as the use of NMs in a hydrothermal reactor to better understand whether simple organic compounds can be formed in an early Earth putative Hadean Ocean environment. This involves the study of hydrothermal interactions at high pressure and subsequent experiments reacting the effluent with simulated cold ancient ocean water. The second section addresses the development of techniques for visualizing MNMs at high resolution in order to better understand both MNM compartmentalization and environmental impacts due to weathering in specific organismal locations.

Following are the four research questions and related hypotheses that are addressed in this dissertation. Questions I and II relate to the influence of NMs on the emergence of life; Questions III and IV address the issue of nanotoxicity of MNMs to bacteria and higher life forms.

I. When using a hydrothermal reactor simulating Hadean ocean conditions, how do iron-nickel sulfide NMs react and what environmental changes produce the characteristic mineral alteration products? Results of hydrothermal alteration under specific temperature, fluid flow, solution chemistry, and pressure conditions were

investigated, in the presence of carbon dioxide and hydrogen gases. It is expected that NM surfaces of the iron-nickel sulfides in an ultra-mafic rock matrix will produce simple organic molecules as byproducts. In the event, we found no such reductions took place. This is in line with the results from work reported recently from other laboratories (McCollom and Seewald, 2001; Fu *et al*., 2007).

II. Injecting the effluent form the hydrothermal reactor as a simulant of earlymost submarine hydrothermal solution into simulated Hadean ocean water produces chemical garden like structures. What are the mineralogical characteristics and morphologies of the precipitated chimney structures? Iron-sulfide NMs formed into chimney structures with highly defined compartmentalization and large catalytic surface areas vary structurally depending on pH, silicate concentrations, temperature, and assorted 5-mer peptides.

III. What is the toxicity to *Tetrahymena thermophila* protozoa of P25 industrial Titanium dioxide NMs ($nTiO_2$) bound to *Pseudomonas aeruginosa* bacteria prey during protozoan feeding, as observed by electron microscopy? Using electron microscopy, trophic transfer of $nTiO_2$ from bacteria into protozoa is observable and quantifiable, and is related to protozoan population growth effects.

IV. When using dark-field scanning transmission electron microscopy – energy dispersive x-ray spectroscopy (STEM-EDS), what are the relationships between environmental exposure conditions and the varied elemental compositions of weathered surfaces of quantum dots (QDs) associated with *Pseudomonas aeruginosa* (PA) bacteria and with *Tetrahymena thermophila* (TT) protozoans? Using STEM-EDS, it can be observed that intracellular weathering of QDs varies with QD elemental composition and the time course of internalization of QDs by either PA or TT.

Nanomaterials' influence on the emergence of life. The emergence of life on early Earth was fed from energy-(electron)-rich hydrothermal hydrogen and methane which, on meeting the surfaces of the iron nickel sulfides and oxyhydroxides comprising the concomitantly precipitated compartments, reacted with carbon dioxide, and perhaps other volatile oxides in the Hadean Ocean to produce the first building blocks of life. Catalytic energy traps are comprised of inorganic membranes separated by interconnected compartments where chemiosmotic forces and electron bifurcations fuel the formation of complex organic molecules (Russell *et al.*, 1994; Russell and Hall, 1997; Nitschke and Russell, 2009, 2011; Lane *et al.*, 2010; Michalkova *et al.*, 2011). During an eruption, oceanic hydrothermal systems release an enormous amount of energy at extreme temperatures during the subsequent redistribution of the earth's mantle (Turcotte *et al.*, 1977; Russell and Kanik, 2010).

However, these are too energetic to have given rise to life. Smaller, less energetic hydrothermal vents form initially on the ocean floor, where faults in the bedrock result in mineral alteration at elevated temperatures, redox reactions, and pH-dependent leaching (Russell, 1978; Lowell and Rona, 2002; Kelley *et al.*, 2005; Ludwig *et al.*, 2005; Emmanuel and Berkowitz, 2006; Russell *et al.*, 2010). Hydrothermal systems located 'off-axis' from the main eruption centers will derive heat from the bedrock, augmented by exothermic reaction. In such hydrothermal systems, temperatures are lower, and organic compounds persist and accumulate (Russell *et al*., 1988, Lane *et al*., 2010; Mast and Braun, 2010). The continuous flow of fluid in off-axis hydrothermal systems generate serpentinite through the partial dissolution, hydration, carbonation and oxidation of the iron magnesium and calcium silicates and sulfide minerals comprising the ocean floor. The result is the generation of calcium hydroxide (high pH) fluids bearing milli-molar concentrations of hydrogen and methane to the ocean floor. Such an off-axis hydrothermal system produces of a mound of precipitates comprising clays, silicates, carbonates, iron sulfide and oxyhydroxide compounds (Brock 2009, Figure 14.4). These mounds have precipitates with large surface areas with varied catalytic potential for the reduction of carbon dioxide with the concomitant oxidation of methane to produce organic compounds (Nitschke and Russell, 2013).

Deep-sea submarine mounds have central fluid-filled channels filled with hydrothermally heated alkaline spring water driven through the ultra-mafic komatiitic ocean floor crust (Martin *et al.*, 2008; Mielke *et al.*, 2010; Proskurowski *et al.*, 2008;

Russell *et al.*, 2010; Seewald *et al.*, 2006). Ultra-mafic komatiitic, or ultrabasic high magnesium content, rock was formed from igneous intrusions and the tectonic exposure of the mantle throughout Earth's history. The ultrabasic-high magnesium rock (MgO >18%) imagined to have comprised the floor of the earliest ocean is similar to the bedrock of present day hydrothermal fields of Lost City. The highest temperatures of the hydrothermal solutions feeding Lost City are ~100°C (Proskurowski *et al.*, 2008), 270°C for white smokers and ~400°C for black smokers These latter two hydrothermal systems exceed the moderate temperature of up to 100°C promoting the generation of simple organic compounds used as the building blocks of early life (Russell *et al.*, 1989; Köhler *et al.*, 1994).

This research develops and tests a continuous flow-through hydrothermal reactor that simulates early Earth by introducing hydrogen and carbon dioxide gases to iron-sulfide minerals (nano- to micron-size particles) at high pressure and moderate temperature. The reactor maintained a 100 bar pressure of hydrogen gas at 100°C over a 10 to 14 day experimental period. The structural integrity of the experimental hydrothermal reactor is critical to insure that no atmospheric oxygen is introduced, or that a possibly fatal structural catastrophic failure occurs by an internal explosion. Safety features, including shrapnel curtains in place around the reactor system and a blast shield were erected with adequate room to work on the reactor system while isolating it from researchers monitoring the experimental progress 24 hour per day during the reactor running period. Through separate temperature-controlled fluid reservoirs, the composition of the central fluid was switched periodically during the

experiment to deliver either the alkaline hydrothermal solution (pH 12) or the model acidic Hadean Ocean solution (pH 5.3) (Mielke *et al.*, 2010). Continuous sampling was required to understand the progression of mineral weathering and the mobile inorganic compounds being developed and subsequently released into the effluent.

The effluent containing mg/L of hydrothermally generated mineral weathering byproducts, including magnesium, calcium, sulfur, and silicates, was used to determine the effluents' capability of developing chimney structures when injected into a reduced iron, simulated Hadean Ocean, solution. The chimney structures varied in chemical composition depending on reactor bedrock mineral composition and the time period over which the effluent was produced during a reactor experiment. These simulated chimney structures will help to identify how a naturally formed hydrothermal mound was produced by identifying the chemical composition of the hydrothermal solution during its migration through the host bedrock before reaching the ocean floor surface. The hydrothermal mounds (or chimney structures) act as porous inorganic membranes that would have been essential to the emergence of life during the turbulent early Earth (Russell 1978). The development of optimal "membranous" compartments was likely one initial requirement to form large chemical gradients across a small distance. In an Earth model hydrothermal system, the hydrogen gas is generated by hydrothermal serpentinization (Figure II-1). Serpentinization occurs in the hydrothermal convection cells in the oceanic crust, made up of komatiitic lavas and ultramafic rocks, with ocean waters releasing soluble hydroxides during the dissolution of calcium and minor quantities of magnesium and

the formation of hydrogen gas (Russell *et al.*, 1989, 2010; Macleod *et al.*, 1994). The hydrogen gas is a source of energy (electrons) in a redox reaction that reduces carbon dioxide; hydronium ions are products of the oxidized hydrogen gas that traverse the iron-sulfide NM-compartmentalized membrane toward the acidic Hadean ocean (Nitschke & Russell 2009; Russell & Martin 2004; Russell *et al.*, 2010).

The iron-sulfide mineral surfaces produced in precipitates on these interactions of the reactor effluent with a simulant of the earliest ocean are highly reactive and their large surface areas make them ideal for mediating chemiosmotic forces and electron bifurcations across the inorganic membranes. These experiments set the stage for further experiments given to the synthesis of organic compounds and their take-over from minerals to provide structure for emerging life.

The importance of compartmentalization is evident when considering the similarity of an electrochemical gradient of an iron-sulfide chimney to the proton motive force observed in biological cells (Mitchell 1961). The alkaline interior (pH 11) interfaces the acidic Hadean ocean (pH ~5.5) so that hydroxide ions (OH^-) are simultaneously diffuse outwards while hydronium ions (H_3O^+) are being forced into the interior compartments through a disequilibrium amounting to five logs of pH, producing a natural, ambient a proton motive force. Understanding how hydrothermal chimneys are formed and what organic compounds might be produced under simulated Hadean Ocean conditions could enable researchers to better understand the key players in the emergence of life's story, which will then lead to a better grasp of

how life potentially began or where life could exist on other planets in our solar system or elsewhere. NMs have played an extensive role in the emergence of life and are inevitably a part of everyday life, including synthetic NMs that are – ironically considering their place at life's birth – under scrutiny for their potential to harm humans and the environment.

Nanomaterials' toxicity to bacteria and protozoa. Materials with sizes below ~100 nm are considered NMs and can arise from environmental or from man-made sources. During the formation of early Earth, the Hadean oceans produced massive amounts of NMs in hydrothermal vent chimney structures. Present-day MNNs come from a variety of environmental source minerals produced through the chloride or sulphate process route (McNulty 2007), resulting in nano-sized materials like titanium dioxide ($nTiO_2$) that are later processed into essential consumer products. Other MNMs like cadmium selenide quantum dots (CdSe QDs) are formed through chemical precipitate reactions and used in electronic devices due to their reactive surfaces (Nicoll 1958, Firth *et al.*, 2004, Patel *et al.*, 2006).

An MNM that is in particularly high production for use in consumer goods is $nTiO_2$. The use of affordable micron-scale TiO_2 in commercial grade paints was first adopted when lead was banned in 1978. Lead poisoning, from ingestion of lead paint dust by children under six, was resulting in delayed development, stunted growth, kidney and nervous systems problems, while adults' ingestion resulted in

reproductive problems for both men and women (Jacobs *et al.*, 2002). Over the past 20 years, 'nano'-TiO_2 has been developed to replace micron-scale TiO_2, to reduce the amount of paint required to mask over darker colored surfaces (Kaegi *et al.*, 2008; Weir *et al.*, 2012). What is disturbing is the adopted use of $nTiO_2$ in everyday products for human use on skin and even for consumption without proper understanding of its toxicity on microscopic organisms, humans, and the environment. $nTiO_2$ in cosmetics (Nohynek *et al.*, 2010), medical ointments (Choksi *et al.*, 2010) and food products (Philips *et al.*, 1997) that have direct human contact are increasingly researched to understand its toxicity to not just larger organisms (rabbits or mice used for testing) but to the microbes present in the human intestinal tract and environmental systems into which the $nTiO_2$ will ultimately be released (Boxall *et al.*, 2007, Klaine *et al.*, 2008).

The release of $nTiO_2$ MNMs into the environment occurs each time you jump into a lake or river while wearing sunscreen that contains $nTiO_2$ as a base material used for its ability to block the sun's rays from reaching your skin. Additionally, even before being released into the environment, $nTiO_2$ presents a problem for the user. When a user of $nTiO_2$ sunscreen goes into the sun, the excitation of the $nTiO_2$ by light causes a small amount of the MNMs to be driven past the skin's dermal layers and into the capillary beds of the skin (Bennett *et al.*, 2012). Along with other MNMs (Suresh *et al.*, 2013), it has been shown that $nTiO_2$ causes cellular membrane damage and reduced bacterial population growth (Mileyeva-Biebesheimer *et al.*, 2010).

Another type of NM are Quantum Dots (QDs), increasingly proposed for use

in photovoltaic cells, and in medical imaging. Studies with CdSe QDs and cadmium telluride (CdTe) QDs report that production of Reactive Oxygen Species (ROS) causes the disruption of cell walls, allowing the QDs to enter the cytoplasm, i.e. the interior of the bacterial cell (Kloepfer *et al.*, 2003, Dumas *et al.*, 2009, Priester *et al.*, 2009). In contrast, $nTiO_2$ is generally a larger NM than the QD MNMs and will become attached to the bacterial cell wall, with minimal penetration into the cytoplasm. The comparative findings make it possible to label bacteria for trophic transfer research by two methods that are representative of likely 'natural" associations of NMs with bacteria: 1) CdSe QDs located in the cytoplasm encapsulated by bacterial cells and 2) $nTiO_2$ adsorbed to the external membrane of bacterial cells.

Trophic transfer of NMs occurs when an organism consumes prey contaminated with NMs, resulting in the net transfer and accumulation of NMs into the organism host. Trophic transfer experiments have used CdSe QDs internalized by planktonic *Pseudomonas aeruginosa* (PA) to feed the protozoan *Tetrahymena thermophila* (TT) (Werlin *et al.*, 2011). The bioaccumulation of CdSe QDs was 5 times greater in the protozoa than what was initially located in the bacterial source, and was considered to be biomagnified in the higher trophic level organism. Similar trophic transfer experiments used PA with $nTiO_2$ adsorbed to external membrane and fed to TT (Mielke *et al.*, 2013). The presence of $nTiO_2$ on PA cell walls resulted in slightly slower TT growth during the 22 hour experiments. The reduced growth was apparently related to food displacement due to excessive amounts of accumulated

$nTiO_2$ in the food vacuoles (FVs). Our trophic transfer and NM toxicity research extensively used Electron Microscopy (EM) techniques to visualize and analyze the presence of NMs in protozoan organelles and the NMs associated with bacteria. The ability to view inside a single cell, while also observing the stages of NM migration throughout a cell, then to ultimately determine how the NMs are weathered in their resident locations, make the STEM-EDS technique invaluable for the investigation of NMs' weathering and toxicity in experimental organisms.

STEM-EDS imaging and analysis of nanomaterials inside bacteria and protozoa. Imaging with a microscope can be done using a wide variety of light wavelengths, including the use of a flood of electrons on or through a sample as utilized in EM techniques (Goldstein 2003). Imaging through a thin-section of sample is done with a bright field-transmission electron microscope (TEM) where the detector is directly below the sample, producing a dark area of scattered electrons due to the presence of electronically dense atoms. This physical scattering of electrons to some angle can also be imaged in what is called dark field-TEM, for example to visualize atomically heavy molecules in a matrix of organic carbon similar to what is found in a bacterial cell. The STEM has one main difference in that STEM images are generated by computer software that reconstructs images from data as the detector rasters back and forth across a sample. This is in contrast to TEM imaging that utilizes a single flood of electrons onto photo-activated silver droplets, producing negative images used to generate the photographic positive TEM image (Goldstein 2003). Conventional TEM imaging with negatives is a time-consuming process for the generation of research

images, and a whole day's work is easily wasted if at the end of the complete process the resulting images are unusable (e.g. from contaminated chemical reagents). With computerized imaging systems reaching similar levels of resolution as those observed with negatives, imaging by EM techniques has become routine in many types of research.

EM techniques have become essential for research investigations in the study of the physical location of NMs and how NMs interact with organisms. The EM's ability to reveal the physical location of NMs on, or within, organisms directly indicates NM bioavailability and where biological damage is likely occurring. While EM images display NM spatial relationships only at discrete time points, such relationships may nonetheless reveal locations of process (e.g. toxicity) end points as influenced by NMs. Further, if collected at time intervals during NM-biological interaction processes, EM images could reveal intermediate spatial relationships that contribute to process endpoints.

STEM-EDS is a non-destructive research tool that enables us to investigate the atomic composition of NMs. Normally, to understand atomic composition of NMs, bulk sample analysis is accomplished by a destructive method called Inductively Coupled Plasma - Mass Spectroscopy (ICP-MS). For example, the ICP analysis of CdSe QDs is achieved only after complete destruction of surrounding cellular material and dissolution of the minerals with strong acids to release Cd and Se atoms into solution (Priester *et al.*, 2009). Similar results as ICP-MS should be

observed by STEM-EDS of the (1:1) Cd:Se atomic ratio when the x-ray signal is generated from surface and interior atoms. A space filled theoretical 8 nm CdSe QD is illustrated in Rosenthal *et al.* (2007; see Figure 13) showing flat crystal facets composed of either Cd or Se atoms in a uniform manner. Facets have similarly-sized mated surfaces that have Cd or Se facing opposite directions. The crystalline surface atoms of this theoretical CdSe QD will have approximately equal numbers of Cd atoms on the exposed surfaces as Se atoms. Thus we could conclude that for this theoretical unweathered QD, an EDS analysis should have a 1:1 Cd:Se atomic ratio and any weathering of surface atoms will cause a change in observed Cd:Se atomic ratios. When all QD crystal atom constituents are accounted for, the loss of weathered atoms will be significant enough to detect. This can only be accomplished by building theoretical CdSe QDs from the central core outward with the addition of tetrahedron shells until reaching a ~8.5 nm diameter ideal crystal.

The theoretical research here developed the ~8.5 nm CdSe crystal which required 11 shells around a central core-shell (Kasuya *et al.*, 2010) with the surface atoms comprising 22% of all atoms in the single QD (Table V-1). The surface atoms' percentages increases as the QD size gets smaller due to the principal that surface area is inversely proportional to size. This is clearly illustrated with the 5.0 nm CdSe QD surface atoms comprising 36.8% of the total QD atoms (Table V-1) and since CdSe are 1:1, we can then assume that 36.8% of the Cd atoms are located on the surface facets. Previous research by Priester *et al.* (2009) with 5 nm diameter CdSe QDs followed the predicted model using Noyes – Whitney relation that plateaued

dissolved Cd(II) at approximately 0.023 mg mL^{-1} when the starting solution contained 0.075 mg mL^{-1} of Cd(II) equivalent. This is approximately 31% of the total Cd in the QDs and as described above 36.8% of the surface atoms are comprised of Cd atoms (Table V-1). What we could conclude from these findings is that de-ionized water (with a pH probably slightly acidic) had favorable environmental conditions for the leaching or weathering of surface Cd atoms and not the Se atoms from the CdSe QDs (Priester *et al.*, 2009). Additional information about Se concentration would be helpful to fully understand the implications derived from the theoretically developed CdSe QD analytical value.

The theoretical STEM-EDS CdSe QD can be used as an analytical tool to investigate previous research results using elements within similar core crystals. Research investigating CdSe QDs interactions with PA has shown extensive cellular damage by generation of ROS that produced holes in cell walls allowing QDs to enter the cytoplasm (Cho *et al.*, 2007; Priester *et al.*, 2009; Aruguete *et al.*, 2010; Werlin *et al.*, 2011). The STEM-EDS analysis at 30.0 kV accelerating voltage showed that whole QDs had entered the cytoplasm of PA with Cd:Se atomic ratios ranging from 2.8:1.0 (Cd:Se) to 1.0:2.1 (Cd:Se) after 24 hour (Priester *et al.*, 2009; Werlin *et al.*, 2011). These results show weathering of Cd and Se from NMs to varying degrees. Evaluating the atoms from the entire first interior shell and exterior surface atoms the 2.8:1.0 Cd:Se atomic ratio is theoretically unattainable for a 5.0 nm QD (Table V-2, Figure V-1). The removal of 99% of Se from the exterior surface will result in an atomic ratio of 2.36:1.0 Cd:Se (Table V-3, Figure V-2). When considering only one

element being weathered from the exterior surface the range for 2.8:1.0 Cd:Se could be attained at approximately 75% of the Cd atoms weathered (Table V-4, Figure V-3). The Se weathering requires only ~60% removal of Se atoms from the exterior surface to reach the Cd:Se ratio of 1.0 : 2.1 (Table V-4, Figure V-3).

We further investigate the application of the same theoretical 5 nm CdSe QD data and apply it to higher accelerating voltage EDS data to determine the change in depth of x-rays generated at the higher voltages. TEM-EDS analysis at 100kV accelerating voltage conducted on similar crystalline core CdSe QDs produced a 1.42±0.01:1.0 (Cd:Se) (n=100) atomic ratio with an overall range of 1.2:1 to 1.8:1 for QDs located in the cytoplasm of *Bacillus subtilus* (BS) bacteria (Kloepfer *et al*., 2005). Before being introduced to BS, the CdSe QDs were labeled with adenosine monophosphate (AMP) and had a Cd:Se atomic ratio of 2.0±0.02 (n=21). The authors' interpreted the change in Cd:Se atomic ratios from 2.0 to 1.4 as an indicator of surface alterations in the elemental composition of the QD-AMP. Additionally, QD-AMP surfaces were enriched with Cd atoms initially before weathering 264 Cd atoms from the surface as the QD traversed the cell wall. The AMPs bound to the QD surface are likely stripped in a very short time to be used as an energy source for the bacterium and could be an indicator of the surface atoms the AMP was bound to and dislodged from. The AMP with a single negative charge bound to Cd atoms could account for 264 molecules of AMP, initially all that could be physically and chemically arranged on the QD surface (Table V-1). When considering all the third and second interior shell atoms along with surface weathered atoms, it would require

99% removal of Se atoms from the surface to reach a Cd:Se atomic ratio of 1.82:1.0 (Table V-4, Figure V-3).

To study whether the STEM EDS theoretical model of a QD is applicable to research-generated data, the dissertation research further investigates weathering of CdSe and CdTe QDs with PA bacteria over longer exposure times than observed in previous studies and at multiple points during the experiment (Priester *et al.*, 2009; Clarke *et al.*, 2010). The gradual weathering is evident in the time course series (Figure V-7); the CdSe QDs internalized by the PA become Se enriched QDs over the 24 hour, the CdTe QDs associated with the PA cell wall become Te enriched QDs (Figure V-10). The EDS atomic ratio range for Cd:Se was 4.8:1.0 to 1.0:3.2 (Table V-4, Figure V-3). The trophically transferred CdSe Qds with PA into the TT cellular organelles showed weathering of the QDs towards the Cd enriched region reaching 1.8 ± 0.8:1.0 Cd:Se (n=39) from the starting QDs with Cd:Se of 1.5 ± 0.5:1.0 (n=50) after 24 hour (Figure V-14). These results can be interpreted to show that 50% of the surface atoms are Se at 24 hour, indicating that approximately 132 atoms of Se were weathered from the exterior surface during the travel time and residence time at the specific organelle (Table V-1). The 8 hour time point had even more Se weathered from the surface with a Cd:Se of 1.9 ± 0.8:1.0 leading to the conclusion that Cd is being weathered from the QD surface since it is unlikely that Se would be at a high enough concentration to re-adsorb back onto a QD (Figure V-13).

In summary, the variety of potential NMs is vast, and thus NM uses will continue to grow. From an environmental and long-term health perspective, a question is at which point will toxic consequences of engineered NMs outweigh their benefits? This research regards NMs being used presently in electronic devices (CdSe QDs) and in cosmetic products (TiO_2) as potentially biologically toxic; it also regards NMs as having potentially life generating catalytic surfaces ((Fe/Ni)S NMs). In all cases, because the surfaces of NMs are directly interacting with the environment, the understanding of their surface composition is essential to further the research goals involved in explaining both biological compartmentalization and toxicity, and NM mineral processing during organic molecule genesis. In both research directions, electron microscopy is a scientific tool available to image biological ultra-structures approximately 1 billion times smaller than a human, and to analyze surfaces of highly reactive nano-sized materials. In my dissertation research, I expand the understanding of electron microscopy techniques and their essential role in understanding a wide spectrum of scientific topics including nanotoxicity and the emergence of life.

II. Design, fabrication, and test of a hydrothermal reactor for origin-of-life experiments

Astrobiology, Volume 10, Number 8, pp. 799-810 (2010).

Randall E. Mielke,[1] Michael J. Russell,[1,2] Philip R. Wilson,[1] Shawn E. McGlynn,[1,2,*] Max Coleman,[1,2] Richard Kidd,[1] and Isik Kanik[1,2]

[1] Jet Propulsion Laboratory, California Institute of Technology, Pasadena, California.

[2] NASA Astrobiology Institute.

*Present address: Department of Chemistry and Biochemistry and the Astrobiology Biogeocatalysis Research Center, Montana State, University, Bozeman, Montana.

ABSTRACT

We describe a continuous high-pressure flow reactor designed to simulate the unforced convective interaction of hydrothermal solutions and ocean waters with submarine crust on early Earth—conditions appropriate to those that may have led to the onset of life. The experimental operating conditions are appropriate for investigating kinetic hydrothermal processes in the early history of any sizable wet, rocky planet. Beyond the description of the fabrication, we report an initial experiment that tested the design and investigated the feasibility of sulfide and silica

dissolution in alkaline solution from iron sulfide and basaltic rock, and their possible subsequent transport as HS^- and $H_2SiO^{2-}_4$ in hot alkaline solutions. Delivery of hydrogen sulfide and dihydrogen silicate ions would have led to the precipitation of ferrous hydroxide, hydroxysilicates, and iron sulfides as integral mineral components of an off-ridge compartmentalized hydrothermal mound in the Hadean. Such a mound could, we contend, have acted as a natural chemical and electrochemical reactor and, ultimately, as the source of all biochemistry on our planet. In the event, we show that an average of ~1 mM/kg of both sulfide and silica were released throughout, though over 10 mM/kg of HS^- was recorded for ~100 minutes in the early stages of the experiment. This alkaline effluent from the reactor was injected into a reservoir of a simulacrum of ferrous iron-bearing ‘‘Hadean Ocean’’ water in an experiment that demonstrated the capacity of such fluids to generate hydrothermal chimneys and a variety of contiguous inorganic microgeode precipitates bearing disseminations of discrete metal sulfides. Comparable natural composite structures may have acted as hatcheries for emergent life in the Hadean. Key Words: Hydrothermal reactor—Hydrothermal mound—Hydrothermal chimneys— Geodes—Transition-metal sulfides—Hadean Ocean. Astrobiology 10, 799–810.

1. INTRODUCTION

One hypothesis for the origin of life posits that its prebiotic building components were synthesized within moderate temperature (≤130°C) hydrothermal

chimneys and mounds on the floor of the most ancient (Hadean) ocean before the unambiguous geological record began on Earth (Russell *et al.*, 1989). Mounds like these—precipitated where off-ridge alkaline, calcium-, silica-, sulfide-, and H_2-bearing spring waters met with carbonic ocean water that contained ferrous iron and photo-oxidized iron colloids—would have acted as natural electrochemical flow reactors whereby hydrogen, derived through serpentinization, could reduce carbon oxides to produce simple organic molecules, driven by ambient redox and proton gradients acting across inorganic precipitate membranes (Russell *et al.*, 1994; Russell and Martin, 2004; Nitschke and Russell, 2010, Fig. 6), notionally:

$$2\ CO_2 + 4\ H_2 \rightarrow CH_3COO^- + H^+ + 2\ H_2O$$

The catalytic pores in these ancient mounds are envisaged to consist of iron-nickel sulfide clusters and nanocrystals dosed with cobalt, molybdenum, and tungsten embedded in clays, amorphous silica, and carbonate. Such compartments have been considered to comprise the hatchery of life (Russell and Hall, 2006). The hydrothermal fluids that fed the mounds would have been rendered alkaline as ocean waters convected within the oceanic crust through the dissolution of calcium, along with a minor portion of the magnesium from komatiitic lavas or ultramafic crust, during serpentinization to produce soluble hydroxides (Russell *et al.*, 1989, 2010; Macleod *et al.*, 1994).

$$(MO)_{pyroxene} + H_2O \rightarrow M^{2+} + 2\ OH^-$$

The conditions pertinent to the emergence of life, which we attempted to reproduce in this study, stand in strong contrast to the acidic hydrothermal fluids that likely were exhaled from ocean ridges and volcanoes and favored for biosynthesis by Corliss (1986) and Wächtershäuser (2006). Since the formulation of the alkaline hydrothermal scenario, a broadly comparable alkaline (pH ≤12.1) hydrothermal system was discovered at the Lost City site in the North Atlantic 15km west of the Mid-Atlantic Ridge at 30°N, above serpentinized peridotites (Kelley *et al.*, 2001, 2005; Martin *et al.*, 2008). Recorded temperatures of the effluent there reach ~94°C (Kelley *et al.*, 2005; Charlou *et al.*, 2010). Another submarine alkaline system (pH ~10), which consists mainly of clays and is fed largely with 11,000-year-old fresh water, was discovered exhaling from basaltic lavas in Eyjafjordur, northern Iceland, at temperatures up to 78°C (Marteinsson *et al.*, 2001; Gautason *et al.*, 2005; Hreiðar Þór Valtýsson, personal communication, 2010). The temperatures and pH values at Lost City and Eyjafjordur are comparable to some of those detected in certain subaerial springs in ophiolitic terrains (Barnes *et al.*, 1972; Neal and Stanger, 1984; Abrajano *et al.*, 1990; Fallick *et al.*, 1991). Given this information and considering the hydrogen isotopic results of Proskurowski *et al.* (2006) from Lost City, we deem the temperature of the fluids at the base of the open system hydrothermal cells that feed such submarine mounds to be thermostated around 130°C (Russell *et al.*, 2010). Though at odds with the interpretations of Foustoukos *et al.* (2008) and our own

earlier estimates (Russell and Hall, 1997), we take this view with the presumption that above 130°C serpentinite becomes too plastic—in the absence of magmatic intrusion— to force convection, which thereby renders portions of the crust impermeable to waters under hydrostatic pressure. In contrast to the assumption that the Lost City system is magma driven (Allen and Seyfried, 2004), we have argued, as have others, that the continual heating of the aqueous fluids is partly a result of the geothermal gradient, partly the downward migration of the base of the hydrothermal cell, and partly a result of exothermic reactions (Russell, 1978; Lowell and Rona, 2002; Kelley *et al.*, 2005; Ludwig *et al.*, 2005; Emmanuel and Berkowitz, 2006; Russell *et al.*, 2010). While such physical constraints are generally invariant between the Hadean and the present day, the same cannot be said for the chemistry in that, given the ambient oxygenated seawater and the waste products from populations of archaea and bacteria, along with differences in crustal mineralogy and structure, neither Lost City nor Eyjafjordur can be considered directly analogous to a lifeless Hadean hydrothermal system and its submarine springs.

Thus, because of these uncertainties there is a need to address the hypothesis in the laboratory in oxygen-free and sterile conditions. To this end and to test our expectations as to the effects of mixing a simulacrum of ancient carbonic ocean water with alkaline hydrothermal solution, we describe the design, fabrication, and operation of the hydrothermal reactor built to reproduce the relevant conditions on early Earth or any other wet and rocky world with a carbonic ocean, such as Europa (Hand *et al.*, 2007, 2010; Vance *et al.*, 2007). Specifically, the reactor was built to (i)

reproduce chemical interactions as hydrothermal waters flow in a conduit through rocks just beneath the ancient ocean floor at ~100 bar H_2 pressure and up to 130°C; (ii) assess the chemical interactions between the hydrothermal solution and carbonic ocean water that might give rise to a freshly precipitated carbonate-, silica-, and sulfide-bearing hydrothermal mound; and (iii) test the potential of such a hydrothermal system of synthesizing particular organic molecules, if any, through the hydrogenation of carbon oxides.

In this contribution, we describe the construction and testing of such a reactor and then report results of our first experiment, which addressed silica and sulfide dissolution from iron sulfides and basaltic rock wool in a representation of a Hadean Ocean crust (Fig. II-1). While there is some geological evidence for the dissolution of sulfides in the ocean crust under non-equilibrium alkaline hydrothermal conditions (Delacour *et al.*, 2008), the absence of a rock record of early Earth and a lack of a modern example of sulfide delivery in alkaline springs dictated that this would be our first experimental test. Indeed, the known chambered alkaline hydrothermal precipitate mounds at Lost City consist mainly of carbonates with minor brucite (Kelley *et al.*, 2001), whereas at Eyjafjordur, North Iceland, they are composed of sepiolite (Marteinsson *et al.*, 2001). Sepiolites mixed with poorly crystalline Fe-Mn hydroxides at the Owen fracture zone (a transform fault) in the Indian Ocean at ~12°N, ~58°E, also appear to be the vestiges of precipitates from alkaline springs (Bonatti *et al.*, 1983). This (almost) complete lack of sulfide in modern alkaline springs is a potential threat to the ‘‘alkaline hydrothermal hypothesis,’’ as we have

argued that metal sulfides, as constituents of inorganic membranes, are central to redox catalysis and the transfer of protons from the ocean to the porous interiors required of chemiosmosis (Russell *et al.*, 1994; Martin and Russell, 2007; Nitschke and Russell, 2009). Silica activities too are generally low in fluids that interact with ultramafic rock (Palandri and Reed, 2004). Nevertheless, silica veins and subaerial precipitates are common in serpentinized terrains, where gabbros, cherts, or other siliceous rocks occur in the footwall (Barnes *et al.*, 1972; Fallick *et al.*, 1991; Zedef *et al.*, 2000). Moreover, the submarine alkaline springs emanating from basalt rather than ultramafic rock at Eyjafjordur contain ~1.6 mM/L SiO_2 (Marteinsson *et al.*, 2001), and in any case silica concentrations in the Hadean Ocean could have reached 5 mM/L (Knauth and Lowe, 2003).

In the origin-of-life model considered here, the silica and hydrogen sulfide anions are expected to bring about the precipitation of catalytic sulfide-bearing (cobalt- and tungsten-doped-FeS > Fe(Ni)S >> $NiFe_5S_8$ >> MoS_2) compartments through interaction with ‘‘oceanic’’ iron (Fe^{2+} >> Fe^{III}), nickel, and cobalt (Fig. II-1). These transition metals, dissolved as clusters or occurring as nanoparticles in the early oxygen-free carbonic ocean, were ultimately derived from much hotter (360–400°C) acidic submarine springs (Douville *et al.*, 2002; Kump and Seyfried, 2005). At the pressures and moderate temperatures indicated by the model, the alkaline fluids also had the theoretical propensity to dissolve calcium and minor magnesium from silicates (Palandri and Reed, 2004), and silica from cherts or quartz veins (Kehew, 2001). Thus, the effluent from this first experiment might be expected to

produce chimneys or compartments, or both, on injection into a ferrous iron-bearing solution representing the Hadean Ocean. Such inorganic compartments are expected to hold a redox and proton tension between simulacra of the hydrogen-bearing alkaline hydrothermal interior of the mound and the mildly acidic carbonic ocean bathing the exterior. Oxidized entities apart from CO_2 in the Hadean Ocean would be phosphate, nitric oxides and nitrate, and photolytically generated ferric iron particles (Braterman *et al.*, 1983; Yamagata *et al.*, 1991; Martin *et al.*, 2007). In the event, the reactor operated to plan; some sulfide, silica, and calcium were dissolved in the solution, which, on exhalation into the ferrous solution, did produce sturdy chimneys and compartments dosed with iron sulfide and ferrous hydroxide.

2. MATERIALS and METHODS

2.1. Reactor design and construction. Two 3.8 L, pressure-tested 316 electro-polished alloy stainless steel (316 epSS) cylinders were employed as solution reservoirs, one for the hydrothermal solution and one for the simulated Hadean Ocean. Heating coils allow the fluids to be subjected to temperatures of up to 140°C. Each of the two reservoirs has two access ports, one at the top for pumping out headspace gases and for the introduction of liquids, and the other at the base so that the gases may be bubbled through the solution to ensure full gas/water exchange prior to each run. The vessels are connected through high-pressure 316SS non-return and two-way ball valves to the lagged central tee connector to the reactor (Fig. II-2). The reactor itself was fabricated, assembled, and operated in the Jet Propulsion

Laboratories, California Institute of Technology. The requirements for high-pressure hydrogen (~100 bars), weldable material, and a minimum of catalytic activity dictated the use of a chrome steel barrel with an electro-polished chromium oxide interior for the reactor. For safety, it was built and tested to tolerate at least 400 atmospheres. It is 508.0 mm long and has an outer diameter of 25.4 mm and an internal diameter of 19.1 mm. The feed to the reactor from both the hydrothermal vessel and the ocean vessel is driven by hydrogen overpressure and controlled by 316SS non-return ball valves and high-pressure needle valves. A screw connection is placed at the T-joint to allow retrieval of the packing material and catalyst for analysis and also for the cleaning of the barrel. Heating of the vessels and reactor is by rheostatically controlled thermoelectric coils, and the temperature is measured electronically by DT-670D-SD temperature sensors. At this central location, the two fluids may be alternately introduced to the reactor barrel that stands slanted 10° from the vertical to simulate the hydrothermal conduit and the hydrothermal mound (Figs. II-1 and II-2).

Before operations, the reactor was flushed with 4% HCl/ 4% HNO_3 solution (15 min) followed by three Milli-Q (18.2MΩ) water washes (15 min each), and baked out at 300°C under helium. The reactor was then packed with basaltic rock wool (or crysotile asbestos if health and safety conditions allow), which acts as a crustal (or mantle) rock analogue and support for crushed sulfide minerals or as a substrate for freshly precipitated iron (nickel) sulfide catalyst. Temperatures can be controlled up to 140°C over the lower 258 mm—the remaining 254 mm simulates the natural cooling of hydrothermal fluids as they interface colder Hadean Ocean waters at the

base of the mound. To relieve pressure, the reactor feeds into 3 m long, 1.59 mm (1/16 inch) 316SS tubing and terminates in a three-way valve for sample distribution through 1m of 0.075 mm silica capillary lines. The capillary lines are fed into helium-purged, acid-washed 20 mL or 120 mL crimp-top vials. The effluent delivery rate approximates 3 μL/s.

2.2. Preparation of solutions. For the first hydrothermal vent experiment, 3.5 L of both ocean water simulant and the hydrothermal solution (derived from the same ocean water simulant) were charged with sodium chloride at 35 g/L to mimic present-day ocean and alkaline hydrothermal solutions. This value was chosen on the assumption that the Hadean Ocean was largely sourced from high-temperature springs exhaling from ultramafic crust (Wetzel and Shock, 2000). It is noteworthy that there is little contrast between the sodium content of hydrothermal fluids at Lost City and that of the ocean (Charlou *et al.*, 2010). In addition, 10 mM/L of sodium bicarbonate was introduced to the hydrothermal solution, which was adjusted with ~1 mL of dilute sodium hydroxide to pH 12.0—comparable to peak pH in submarine serpentinite pore waters and the Lost City effluent (Macleod *et al.*, 1994; Salisbury, 2002; Charlou *et al.*, 2010). The ocean solution was prepared at pH 5.3, and ammonium bicarbonate was added to the level of 0.5 mM/L. This solution was then readjusted to pH 5.3 with ~1 mL dilute hydrochloric acid to maintain a final volume of 3.5 L (Macleod *et al.*, 1994).

The two electro-polished stainless steel cylinders, previously baked out and

washed with deionized water, were filled with 3.5 L of each of the solutions. Prior to the experimental run, helium was bubbled through the lower ports into the filled cylinders at 100 psi and ambient temperatures for a 15 min flush to remove any last vestiges of oxygen and nitrogen. Three consecutive flushings and head-space pumping removed all air from fluids and in head space prior to the introduction of hydrogen gas. Following the final pumping sequence, hydrogen was introduced through the bottom of both reservoirs at a pressure of 1500 psi (~100 bar) equivalent to 160 mM/L of hydrogen (Wiebe and Gaddy, 1934). The base of the reactor was packed with 50 mm of basalt rock wool (Minwood 1200, Industrial Insulation Group, Al, USA). In atomic percentage it comprises SiO_2 51.7; CaO 17.2; MgO 16.2; Al_2O_3 9.0; FeO 2.5; Na_2O 2.7; K_2O <0.1; P_2O_5 0.5 (ESEM-EDAX), in the compositional range of a calc-alkaline basalt. The next 180 mm of the reactor (above the rock wool) were packed with reagent-grade iron monosulfide (FeS) (Argos Organics, Geel, Belgium; crushed to ~1 mm fragments to increase reactive surface area and promote mineral/water interaction without clogging the effluent capillary lines). The remaining (upper) 280 mm was also packed with basalt rock wool. (The calcium content of the rock wool is high compared to mafic rock; however, health and safety decreed that chrysotile, our preferred crustal simulant but a carcinogen, not be used.) The reactor barrel was heated to a maximum of 130°C, with temperature cooling to near 30°C downstream to reproduce the kind of gradient to be expected as off-ridge hydrothermal solutions infuse the base of the mound. After 290 mL of the hydrothermal fluid (pH 12.0) was passed through the reactor barrel for the first 24

hours, the mildly acidic ocean simulant (pH 5.3) was introduced in equal and alternating measure, switching from vessel A to vessel B.

Almost immediately upon introduction of the hydrogen gas, at the specified 100 bar pressure, the hydrothermal vent solution began flowing into the sample acquisition bottles previously purged with helium. For the first 48 hours, samples were taken at 1-hour intervals. Over the remaining experimental time, samples were taken at intervals of several hours. The hydrothermal vent solution sample containers were stored at 4°C prior to processing. Approximately 3 μL/s of hydrothermal vent solution samples were acquired and subsequently analyzed for pH and elemental composition by a Thermo Scientific, iCAP 6300a inductively coupled plasma optical emission spectrometer (ICP-OES). The hydrothermal vent reactor was disassembled at the end of the experiment, and layers of rock wool and sulfides were immediately separated and stored at 4°C in crimp-top vials purged with helium. The helium minimizes alteration prior to imaging and analysis by environmental scanning electron microscopy (ESEM).

2.3. Operation and experimental test. As a first test of the reactor as well as a test of one aspect of the alkaline-hydrothermal hypothesis, we investigated whether anionic hydrogen sulfide (HS^-) could be dissolved from iron monosulfide and transported in the hot alkaline solution of the chemistry we predicted for such a system. Thus, the reactor was used to simulate the effect of passing the hydrothermal fluid through sulfides in veins or pods under the seafloor with the expectation that the

resulting solution would contain dissolved sulfide (Fig. II-1). We also expected the FeS in the lower portion of the reactor to be partly stripped of its sulfur, which would leave a patina of ferrous hydroxide. Further up in the cooler portion of the reactor, we expected white and green rust [i.e., $Fe(OH)_2$ or $\sim Fe^{II}_4Fe^{III}_2(OH)_{12}CO_3(H_2O)_2$)] and metal sulfides to precipitate on the rock wool where they might have a role as potential catalysts (Russell and Hall, 2006).

$$FeS + H_2O + OH^- \rightarrow Fe(OH)_2 + HS^-$$

Here, we have assumed (and adopted) temperatures of up to ~130°C based on (i) the hydrogen isotopic analyses of Lost City effluent (Proskurowski *et al.*, 2006), (ii) the absence of evidence for higher temperatures in land-based alkaline (pH ≤12.4) hydrothermal systems in ultramafic rocks (Fallick *et al.*, 1991; Zedef *et al.*, 2000), and (iii) the highest temperature of fluids recorded at Lost City (94°C) and Eskjaldamur (79°C). A pressure limited to 100 bars for reasons of safety only corresponds to an overall hydrostatic depth of a kilometer, so the reactor only has the capacity to reproduce conditions to be expected where the most ancient ocean was relatively shallow. It falls short of addressing the very high pressures expected at the bottom of Europa's ocean (Vance *et al.*, 2007).

2.4. Investigation of precipitates. To investigate the effects of injecting the effluent emanating from the hydrothermal reactor into a simulacrum of the Hadean

Ocean water, a batch collected after 5 hours was introduced through a 0.5 mm hole at the bottom of an inverted glass bottle into a mildly acidic solution that contained 10 mM/L ferrous iron (Russell and Hall, 2006). Two injection rates were employed, the first at 7.2 mL/hour and the second at 0.04 mL/hour. The time from removal of the precipitated structures from the aqueous solution to their placement in the freeze-drier was about 2 min. A portion of the precipitate was attached to a specimen stub by means of a carbon tab. ESEM was used to investigate the resulting structures precipitated during the experiments.

3. RESULTS

3.1. Solution chemistry. An arresting result was the immediate conversion of the acidic ocean water to a highly alkaline solution through the dissolution of Ca from the pristine rock wool (Fig. II-3). Also, a surge of hydrogen sulfide ion (as HS^-) began about 4 hours after the beginning of operations and peaked at 460 ppm (≤14 mM/L) at around 6 hours as measured by ICP-OES (Fig. II-3). Sulfide concentrations of 330 ppm (10 mM/L) or more were maintained for ~100 min during interaction with the hydrothermal solution before dropping to ~50 ppm (1.5 mM/L) at 12 hours and oscillated around 25–50 ppm (~1 mM/L) thereafter until the heaters were switched off after 9 days. Calcium also surged with the sulfide, though to a lesser degree. Calcium concentrations also then dropped, perhaps as a result of calcite precipitation in the upper section of the reactor where the fluids became more alkaline (Figs. II-3 and II-4C). Silicon concentrations correlated inversely with calcium and increased

more slowly than sulfide to reach a constant 50 ppm (2 mM/L) after 2 days (Fig. II-3). Iron, as expected from its minimal solubility in alkaline solution, was constantly below the detection limit of 0.1 ppm.

The delivery of calcium in the hydrothermal solution is mirrored by the alteration of the basalt rock wool that is shown prior to reaction (Fig. II-4A) and after reaction (Fig. II-4B). Figure II-4C demonstrates the direct re-precipitation of calcium as the carbonate upon rock wool in the hottest, lowest section of the reactor. The dissolution of calcium from the rock wool in the hottest section of the reactor as analyzed by environmental scanning electron microscopy–energy dispersive X-ray spectroscopy (ESEM-EDX) is particularly notable (Fig. II-5, II-6).

3.2. Mineralogy. The basaltic rock wool and sulfides were investigated with an environmental scanning electron microscope prior to, and following, the experiment. Precipitates on the rock wool in the lower layers in the reactor consisted of calcite, whereas clumps of iron- and sulfide-rich minerals were seen to cover portions of the rock wool high up in the reactor (Layer 15) (Figs. II-4D and II-7). ESEM-EDX analyses of the rock wool revealed a significant loss of calcium from the rock wool surface material at the bottom of the reactor (Layer 1, n = 44) as well as in the hot zone above the iron sulfide layer (Layer 15, n = 67) (Figs. II-4B and II-5). Aluminum was also lost from Layer 1. The rock wool comprising the highest, coolest level of the reactor (Layer 25, n = 50) was largely unaffected beyond a slight enrichment of silicon. The main change here was in the addition of calcium as calcite in Layer 25.

Iron-rich mineral overgrowth on the iron sulfide surface exhibited low to very low S:Fe ratios; values decayed from 0.94 in the relatively unaltered sulfide to ~0.2, which reflects the insolubility of the iron while sulfide was lost to the alkaline solution (Fig. II-6). The overgrowths were probably a form of green rust. Aluminosilicate crystals (possibly vermiculite) also occurred sparsely in the iron sulfide layers, revealing minor aluminum transport.

3.3. Chimney and geodic growth. By taking the solution eluted from the hydrothermal experiment, which contained several millimoles per liter of sulfide, and injecting it from below and into inverted glass bottles of simulated, mildly acidic ferric chloride-bearing Hadean Ocean water (pH ~5.3 and 10 mM $FeCl_2$), we found chimney morphology to be dependent on injection rate. At a rate of 7.2 mL/hour, a fibrous hollow chimney morphology was produced that had affinities to chemical garden structures (Russell and Hall, 2006) (Fig. II-8A). Structures produced during low injection rates (0.04 mL/hour), as illustrated in Figs. II-8B and II-9, were bulbous and contained similar geodic structures within them at a much smaller scale (Russell *et al.*, 1994). The geodes and chimneys comprised an outer wall of iron hydroxide, silicate, carbonate and sulfide, and a hollow interior containing a collection of smaller well-defined geodes. One of these micro-geodes was partly filled with iron-bearing nanocrysts (cf. Fig. II-1 and Larter *et al.*, 1981, plate 2).

4. DISCUSSION

Conditions throughout the operation of the reactor were easy to control, and the first experiment, apart from being a technical success, delivered useful data on the likely evolution of hydrothermal fluids in conditions we imagine for early Earth. The delivery rate of effluent from the reactor was limited to ~0.2mL/min. As might be expected, the simulacrum of the acidic ocean water was rendered highly alkaline as it traversed the basalt rock wool at temperatures at or below 130°C (Macleod *et al.*, 1994). In fact, the pH oscillated between 11 and 12.3 as measured at standard temperature and pressure regardless of the pH of the introduced solution. This is the kind of pH met with in many cool to warm springs operating in ultramafic oceanic rocks, and pH values of up to 12.5 have been recorded in pore waters in serpentinite seamounts at a depth of 4km in the Southern Mariana Forearc (Salisbury, 2002). Nevertheless, chrysotile asbestos wool would obviously furnish a more realistic substrate than the rock wool used in this experiment, but it was precluded for reasons of health and safety. Calcium, generally oscillating around 25 ppm and partly responsible for the high pH, appears to have been leached out of the rock wool after 27 hours or was reprecipitating higher in the reactor (Figs. II-3 and II-4).

At a peak of 14 mM/L, sulfide concentrations approached the theoretical maxima calculated for alkaline hydrothermal solutions (Macleod *et al.*, 1994, p 36), before falling back to around 1 mM/L. Even at this level, the concentration is quite enough to ensure some sulfide precipitation in a putative hydrothermal mound. The sulfur values correlate positively with calcium and negatively with pH and silicon.

The concentration of silica approaches 2 mM/L, which is to be expected in such alkaline hydrothermal solutions where there is a source of free silica (Marteinsson *et al.*, 2001). Thereafter, sulfur values oscillate between 1 and 2 mM/L and silica between 0.5 and 2 mM/L. Why there should be a peak concentration of 14 mmol/kg of hydrogen sulfide ion around 6 hours is puzzling and could be the result of the dissolution of free sulfur from the commercial FeS used here. However, these results speak against the possibility that the first compartments of life consisted purely of sulfides (cf. Russell *et al.*, 1994). Nevertheless, there would be enough sulfide to ensure a component of (catalytic) iron-nickel-cobalt sulfide within the walls of compartments that otherwise would be composed of carbonate, green rust, silicates, or silica itself. Indeed, an effluent solution sample taken from the reactor after 5 hours was introduced through the base of inverted glass bottles into a ferrous chloride solution that simulated the heavy metal–rich Hadean Ocean, and a complex of chimneys and geodes were produced as expected, which consisted mainly of silica or silicate, ferrous hydroxide, and minor sulfide (Fig. II-9A, II-9B). At the high pH conditions maintained by the reacted fluid, a major stable phase for iron in the chimneys was probably white or green rust [~$Fe(OH)_2$], as indicated by the ESEM-EDX analysis, though with scattered ferrous sulfide (Fig. II-7A). Such transition-metal sulfide catalysts would thereby be ripe for participation in the growing network of reactions requisite for the onset of metabolism (McGlynn *et al.*, 2009; Berg *et al.*, 2010; Haydon *et al.*, 2010; Say and Fuchs, 2010).

Both types of hollow structure may have been significant in the emergence of life. The microgeodes may have harbored the simple organic molecules synthesized through the hydrogenation of carbon dioxide as CO_2 seeped through the inorganic walls to the chambers where it met H_2 on the catalytic sulfides that comprised portions of the interior—a focus for our future experiments. The energy to drive the hydrogenation could have been supplied by an ambient chemiosmotic gradient that acted across the inorganic membrane via suitable variable valence metal catalysts (Nitschke and Russell, 2009; Lane *et al.*, 2010). At a more advanced state of metabolic evolution, the thin cylindrical structures might have supported a convective polymerase chain reaction and a thermal diffusive concentration reaction of charged polymers such as RNA (Baaske *et al.*, 2007; Mast and Braun, 2010). We suggest that it is in such inhibiting circumstances that life would have emerged.

We envisage the next experimental step as using the reactor in an attempt to synthesize methane and other organic intermediates while an alkaline hydrothermal solution that bears sulfide and hydrogen, as well as molybdenum and tungsten ions, is introduced to a simulacrum of the early ocean that bears carbon dioxide, ferrous iron, and minor nickel in solution. In these future experiments, natural sulfide minerals will be introduced to, or precipitated in, the reactor; and a safe protocol to use fibrous serpentinite minerals as packing and substrate will be developed. Carbon dioxide will be introduced to the ocean simulacrum to investigate the power of the system to reduce this gas, as occurs in the Lost City serpentinizing system (Proskurowski *et al.*, 2008; Konn *et al.*, 2009).

ACKNOWLEDGMENTS

We thank Lawrence Wade for help with fabrication; Grazyna Orzechowska for support; and Bill Martin, Steven Vance, and Hreiŭar pór Valtýsson for discussions. Anonymous referees gave helpful critiques. S.E.M was supported by the Marine Biological Laboratories NASA Planetary Biology Internship Program and acknowledges support by a NSF IGERT Fellowship by the MSU Program in Geobiological Systems (DGE 0654336). The research described in this publication was carried out at the Jet Propulsion Laboratory, California Institute of Technology, under a contract with the National Aeronautics and Space Administration: with initial support by JPL grant (R.06.021.071) and subsequently by NASA Exobiology and Evolutionary Biology award (NNH06ZDA001N) and supported by the NASA Astrobiology Institute (Icy Worlds).

DISCLOSURE STATEMENT

There are no competing interests.

ABBREVIATIONS

EDX, energy dispersive X-ray spectroscopy; ESEM, environmental scanning electron microscopy; ICP-OES, inductively coupled plasma optical emission spectrometer.

FIGURES

Figure II-1. A scenario for the emergence of life whereby the first organic building components are generated in a natural hydrothermal reactor (the iron sulfide–bearing mound figured here) produced over an unforced convection cell operating at hydrostatic pressure on the Hadean Ocean floor (cf. Figs. II-8 and II-9). A reactor simulating these conditions is described in the text and shown in Fig. II-2. Key to catalysis and electron transfer in the natural reactor is a supply of hydrogen sulfide anion (HS^-, dissolved from the iron sulfides beneath) to react with the ferrous (and minor ferric) iron in the early ocean, a concern of the test experiment. Occasional iron sulfide veins and pods within ocean floor sequences of komatiitic lavas would have been a source of soluble hydrogen sulfide ion (e.g., Lesher and Stone, 1997), and gabbros, cherts, or quartz veins as the source of silica (Barnes *et al.*, 1972; Fallick *et al.*, 1991). Serpentinization is the process of hydration, carbonation, and oxidation of komatiites and other mineralogically comparable rocks thought to be an initial requirement for life's emergence (Russell *et al.*, 1989).

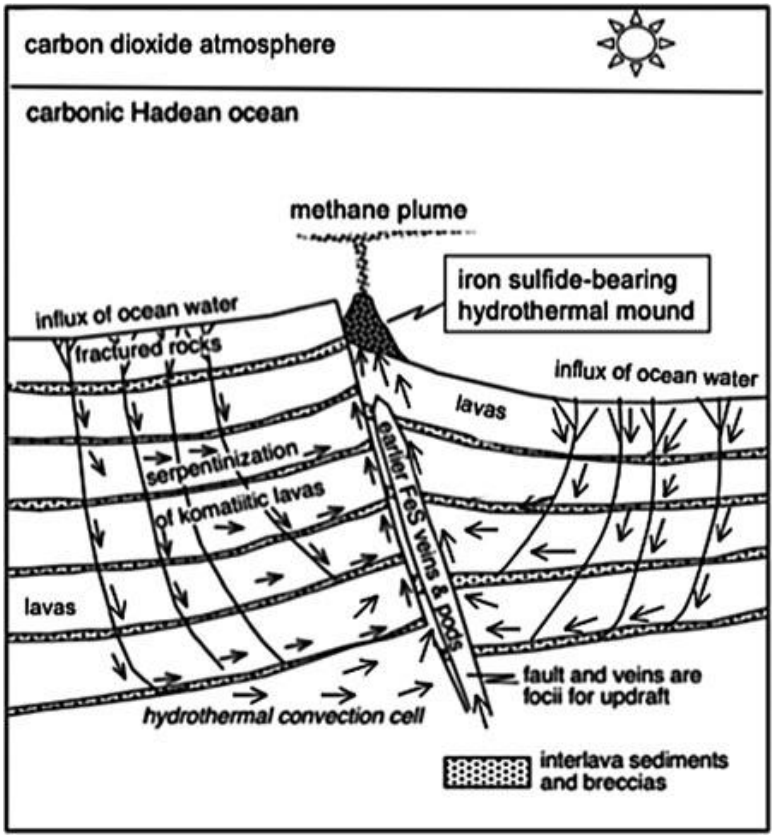

Figure II-2. Top: CAD drawing of the reactor design with inset photograph of the reactor before lagging with thermoelectric coil. Two-way or three-way valves are shown in green, and non-return ball valves are in red. Gasses are purged into solutions through the bottom port to ensure adequate gas/solution interface time. The reactor on the right illustrates placement of temperature sensors on the external reactor surface and the distribution inside the reactor of iron sulfide (FeS) and rock wool. Bottom: the lagged system. PG, pressure gauge. Color images available online at www.liebertonline.com/ast.

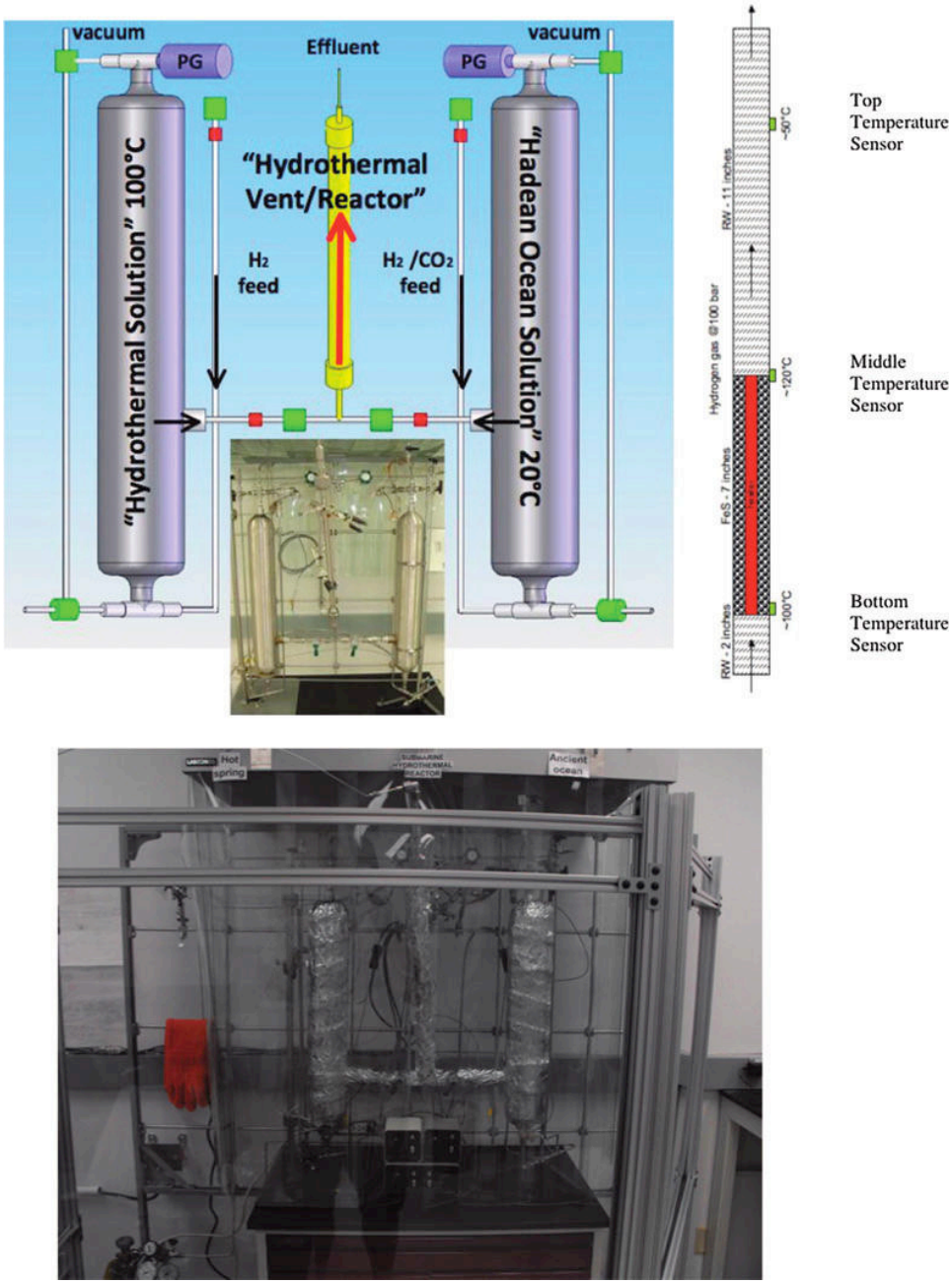

Figure II-3. Inductively coupled plasma optical emission spectrometry analysis of effluent for the time-dependent samples. Graph II-3A shows the results of 60 samples collected over the first 4000min, and graph II-3B shows the complete experimental time period (250 samples). The initial few samples contained over 50 ppm of sulfur determined to be sulfate ions that dropped to zero after 240 min. Initially the pH of the hydrothermal solution dropped almost one unit before rising again after 10 hours to stabilize around pH 12.3. The operating reactor temperature was reached within 120 min, whereas the maximum sulfur concentration (as HS^-) was reached at 360 min, indicating that major dissolution of sulfide occurs only after the operating temperature is reached. The hydrothermal solution was open to the reactor for the first 1440 min followed by alternating ocean/hydrothermal solutions opened every 15 min for another 1440 min. For the remainder of the experiment both solutions were opened to the reactor. The heaters were shut off at 13,200 min, and the system was at ambient temperature by 14,000 min. At this time the concentrations of sulfur, calcium, silicon, potassium, and magnesium were below the detection limits. Color images available online at www.liebertonline.com/ast.

A

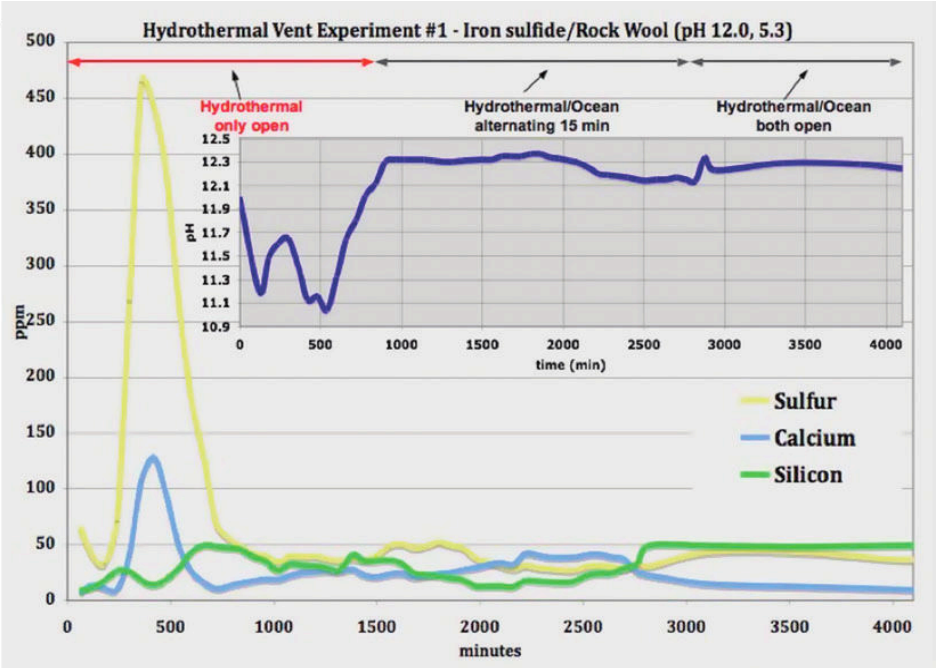
Hydrothermal Vent Experiment #1 - Iron sulfide/Rock Wool (pH 12.0, 5.3)
Hydrothermal only open
Hydrothermal/Ocean alternating 15 min
Hydrothermal/Ocean both open
pH
time (min)
ppm
minutes
Sulfur
Calcium
Silicon

B

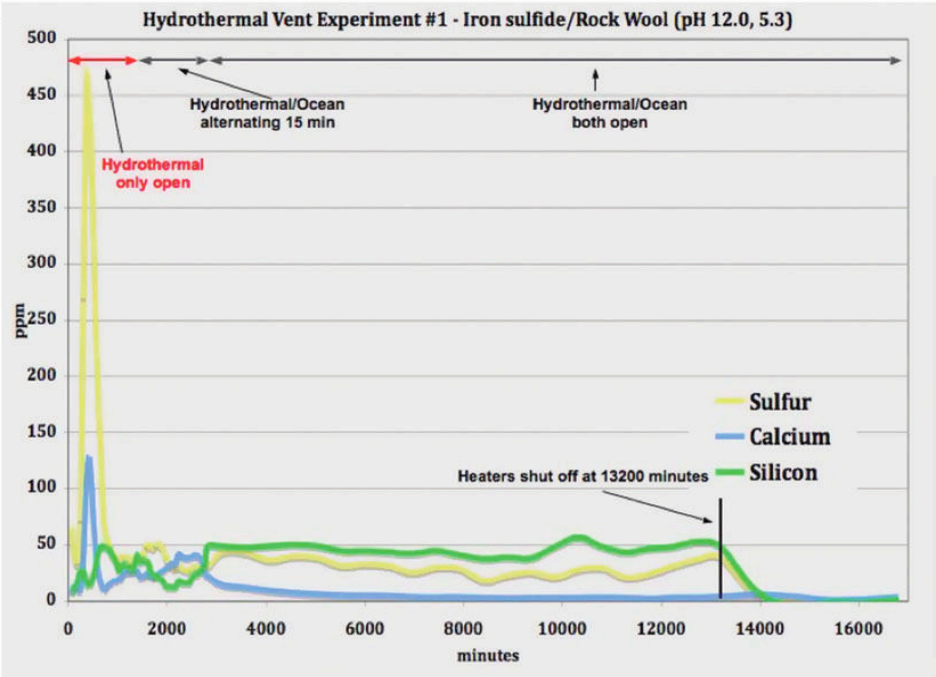
Hydrothermal Vent Experiment #1 - Iron sulfide/Rock Wool (pH 12.0, 5.3)
Hydrothermal only open
Hydrothermal/Ocean alternating 15 min
Hydrothermal/Ocean both open
Heaters shut off at 13200 minutes
ppm
minutes
Sulfur
Calcium
Silicon

Figure II-4. (A) Environmental scanning electron microscope image of basalt rock wool prior to alteration; (B) the same rock wool comprising Layer 1, the image revealing severe surface alteration and loss of calcium (cf. Fig. II-5). (C) Calcite precipitates on basalt rock wool from Layers 1–3. (D) Clumps of iron- and sulfide-rich minerals cover portions of the basalt rock wool of Layer 15, demonstrating local mobility of these two elements.

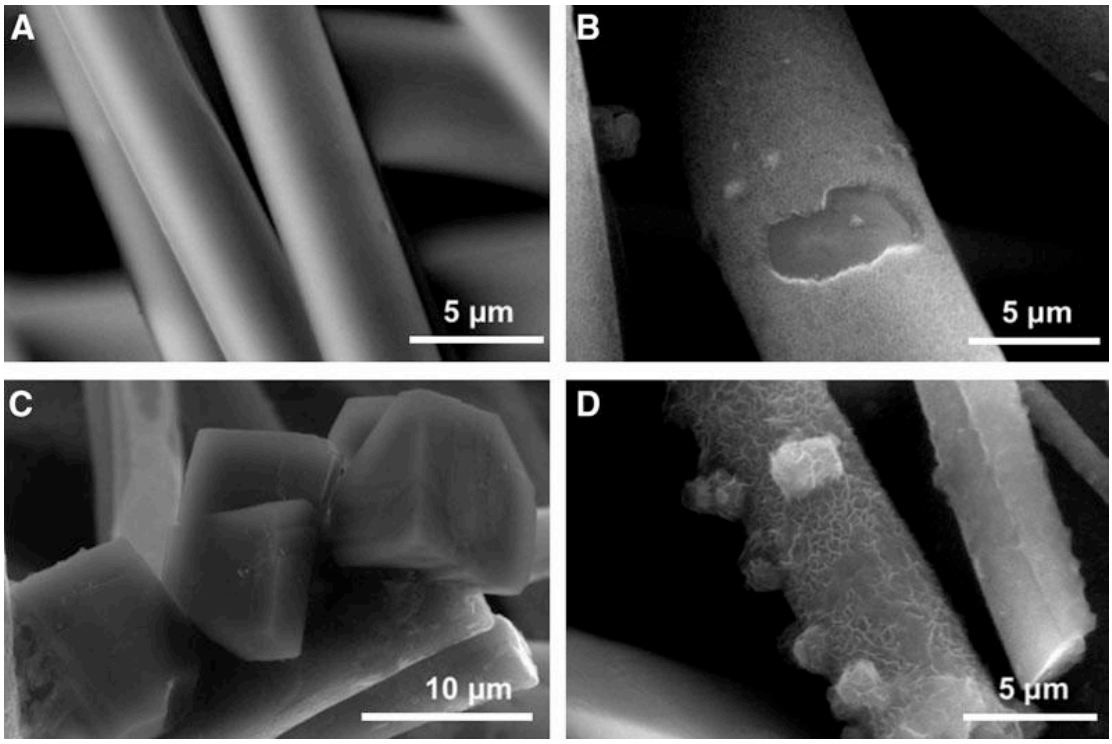

Figure II-5. The graph shows the ESEM-EDX analyses of several of the basalt rock wool layers and the basalt rock wool control (n = 50). The most drastic changes occurred in the amount of calcium dissolved from the surface material at the bottom of the reactor (Layer 1, n = 44) and in the hot zone above the iron sulfide layer (Layer 15, n = 67). Aluminum was also removed from Layer 1. In contrast, the top, cool portion of the reactor (Layer 25, n = 50) shows surface atomic ratio composition at levels equivalent to the control basalt rock wool, except for a slight enrichment of silicon. However, some of the calcium now resides in a carbonate phase in Layer 25. Color images available online at www.liebertonline.com/ast.

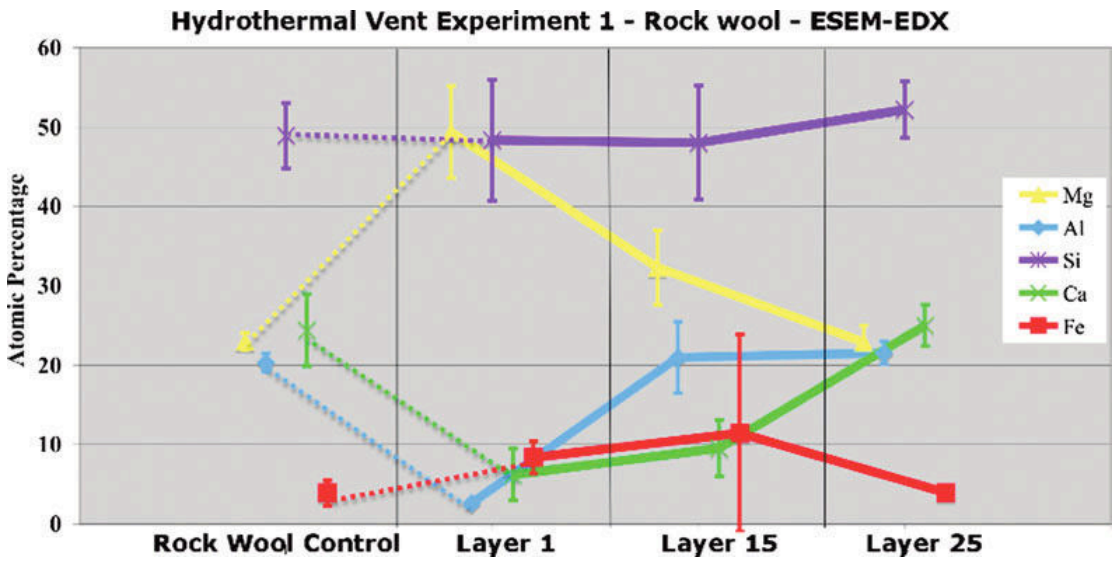

Figure II-6. Sketch of hydrothermal reactor with range of atomic S:Fe ratios on the surface of altered FeS as analyzed by ESEM (numbers of analyses in parentheses): Pristine FeS=1.07, 1σ±0.17; Layer 3=0.50–0.21, 1σ±0.17 (2); Layer 6=0.71–0.21, 1σ±0.19 (3); Layer 9=0.42–0.33, 1σ±0.21 (2); Layer 12=0.83–0.15, 1σ±0.19 (5); Layer 14=0.62–0.01, 1σ±0.18 (6). Color images available online at www.liebertonline.com/ast.

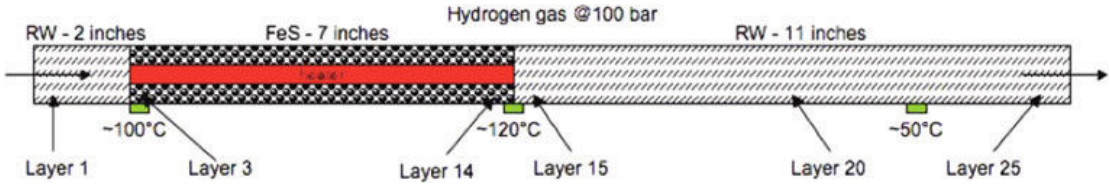

Figure II-7. Photomicrographs demonstrating the iron-rich minerals (probably green rust) precipitated on the surfaces of the iron sulfide. The S:Fe ratios of these minerals were invariably less than 1, and in many cases much less, as to be expected as sulfide was lost to solution (Fig. II-3). Images (A) and (B) are from Layer 3 and show various sizes of flakey ball structures. There were other larger aluminosilicate crystals present in the iron sulfide layers (arrow) as shown in image (C). Image (D) is from Layer 14 with similar characteristic morphologies but had the largest diversity and included phases with aluminum: silicon ratio close to ~2 (possibly vermiculite) and only minor iron content.

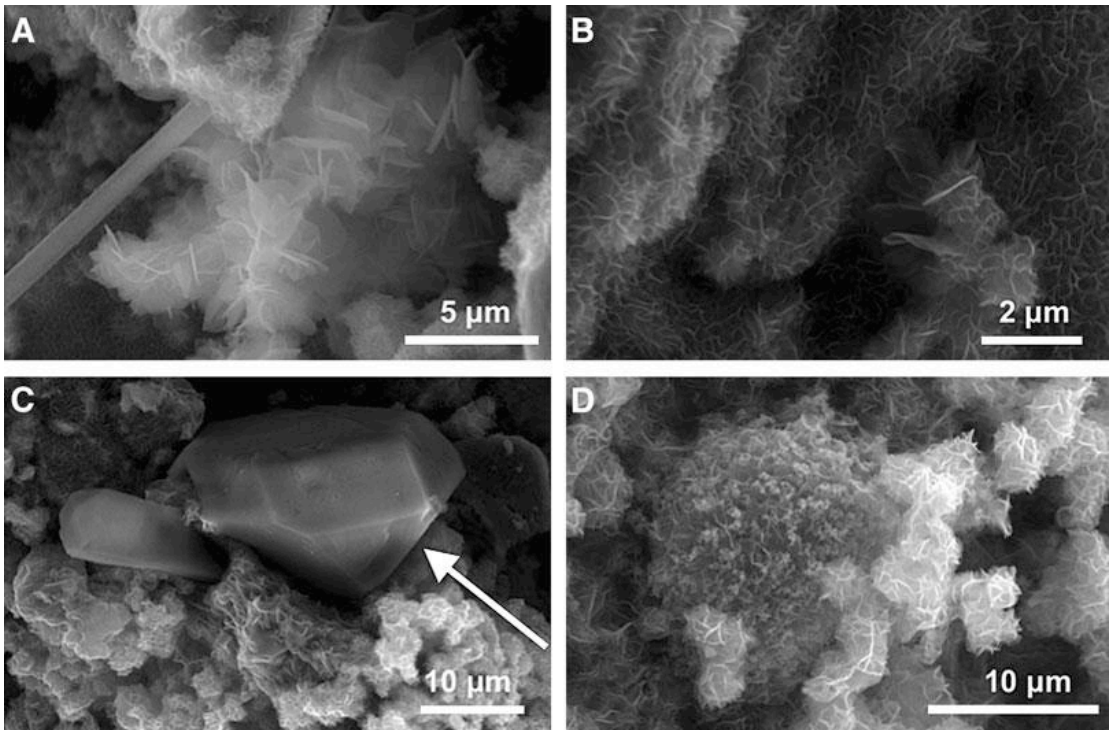

Figure II-8. Injection of the reactor effluent taken after 5 hours (Fig. II-3) into the simulacrum of the Hadean Ocean containing 10 mM/L ferrous iron. When injection rate is rapid, a chimney grows to ~35 mm in 8 min before the top spalls off and settles (white arrow) (A). Geodic growth is favored when injection rate is slow [pictured after 12 hours in (B) and detailed in Fig. II-9]. Color images available online at www.liebertonline.com/ast.

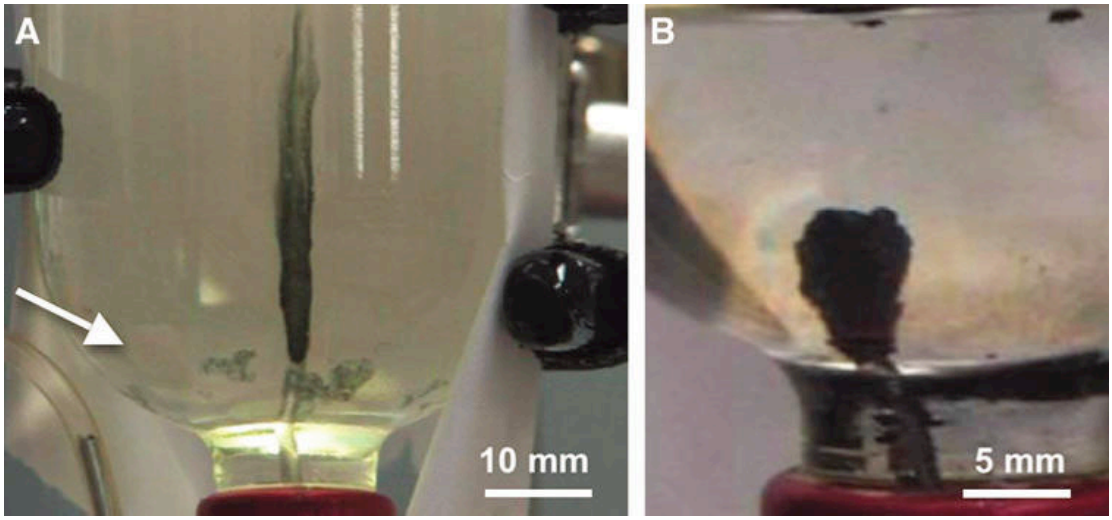

Figure II-9. Environmental scanning electron microscope images of a cross section near the base of the inflated geode figured in II-8B shown to comprise an outer mixed iron hydroxide, silicate, carbonate, and sulfide wall (A and B) and a hollow interior containing a collection of smaller well-defined geodes. One of these microgeodes is revealed as partly filled with fluffy nanocrysts of iron-bearing minerals (C). Compare with Fig. II-1.

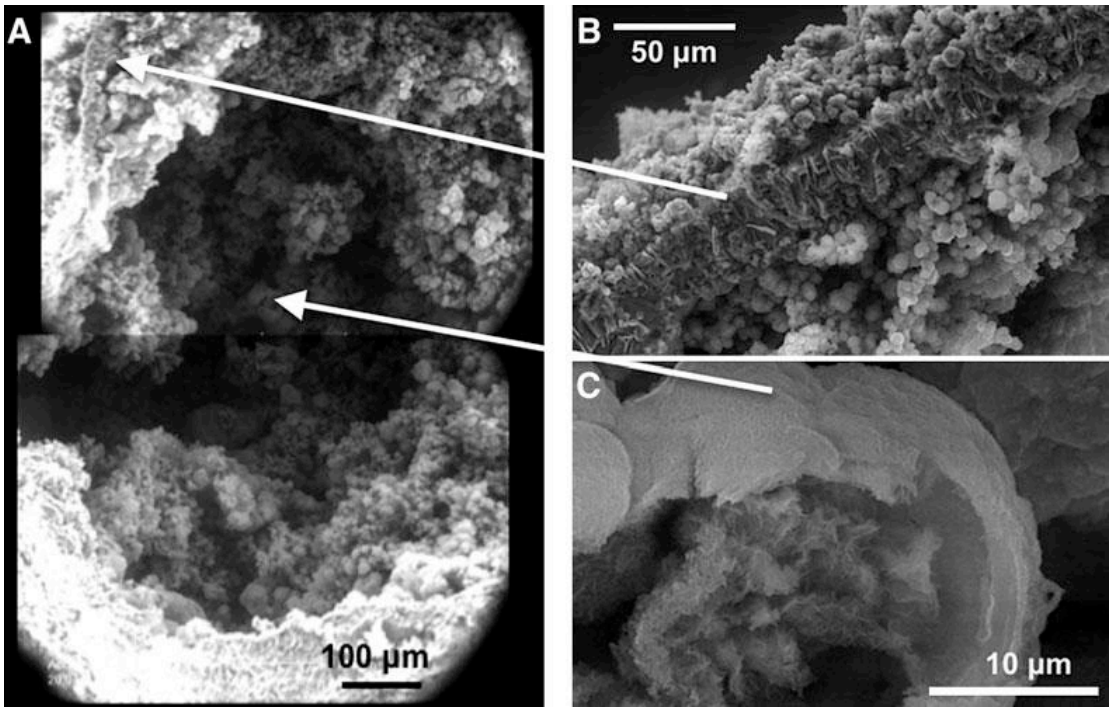

III. Iron-Sulfide-Bearing Chimneys as Potential Catalytic Energy Traps at Life's Emergence

Astrobiology, Volume 11, Number 10, pp. 1-18 (2011).

Randall E. Mielke,[1] Kirtland J. Robinson,[1] Lauren M. White,[1] Shawn E. McGlynn,* Kavan McEachern,[1] Rohit Bhartia,[1] Isik Kanik,[1,] and Michael J. Russell[1,]

[1]Jet Propulsion Laboratory, California Institute of Technology, Pasadena, California.

*NASA NAI Astrobiology Biogeocatalysis Research Center, Montana State University, Bozeman, Montana.

ABSTRACT

The concept that life emerged where alkaline hydrogen-bearing submarine hot springs exhaled into the most ancient acidulous ocean was used as a working hypothesis to investigate the nature of precipitate membranes. Alkaline solutions at 25–70°C and pH between 8 and 12, bearing HS^- ±silicate, were injected slowly into visi-jars containing ferrous chloride to partially simulate the early ocean on this or any other wet and icy, geologically active rocky world. Dependent on pH and sulfide content, fine tubular chimneys and geodal bubbles were generated with semipermeable walls 4–100 μm thick that comprised radial platelets of nanometric mackinawite [FeS] ± ferrous hydroxide [~$Fe(OH)_2$], accompanied by silica and, at the higher temperature, greigite [Fe_3S_4]. Within the chimney walls, these platelets define a myriad of

micropores. The interior walls of the chimneys host iron sulfide framboids, while, in cases where the alkaline solution has a pH > 11 or relatively low sulfide content, their exteriors exhibit radial flanges with a spacing of ~4 μm that comprise microdendrites of ferrous hydroxide. We speculate that this pattern results from outward and inward radial flow through the chimney walls. The outer $Fe(OH)_2$ flanges perhaps precipitate where the highly alkaline flow meets the ambient ferrous iron-bearing fluid, while the intervening troughs signal where the acidulous iron-bearing solutions could gain access to the sulfidic and alkaline interior of the chimneys, thereby leading to the precipitation of the framboids. Addition of soluble pentameric peptides enhances membrane durability and accentuates the crenulations on the chimney exteriors. These dynamic patterns may have implications for acid-base catalysis and the natural proton motive force acting through the matrix of the porous inorganic membrane. Thus, within such membranes, steep redox and pH gradients would bear across the nanometric platelets and separate the two counter-flowing solutions, a condition that may have led to the onset of an autotrophic metabolism through the reduction of carbon dioxide. Key Words: Dendrites—Framboids—Greigite—Hydrothermal chimneys—Mackinawite—Origin of life. Astrobiology 11, 1–18.

1. INTRODUCTION

Because there is no autonomous metabolism outside of cells, compartmentation of some kind has been recognized as essential to the emergence of

life (Traube, 1867; Leduc, 1911; Cairns-Smith, 1982; Russell *et al.*, 1989; Cartwright *et al.*, 2002; Martin and Russell, 2003; Koonin and Martin, 2005; Baaske *et al.*, 2007; Allen, 2010). That such compartments must have been inorganic is forced on us by the difficulty of imagining how appropriate organic molecules from disparate sources could be selected and continuously delivered to the site of the emergence of autogenic metabolism in an atmosphere dominated by CO_2 and N_2 on a turbulent water world subject to high tides, hard UV, and cosmic radiation (Turcotte *et al.*, 1977; Canuto *et al.*, 1982; Wood *et al.*, 1990, 2006; Kasting *et al.*, 1993; Bahcall *et al.*, 2001; Elkins-Tanton, 2008; Russell and Kanik, 2010). In the alkaline hydrothermal (chemiosmotic) theory for the emergence of life, such compartments were considered to have comprised iron monosulfide botryoids, geodes, and chimneys comparable to those discovered at the Silvermines and Tynagh base metal sulfide deposits in the Lower Carboniferous rocks of Ireland (Larter *et al.*, 1981; Boyce *et al.*, 1983; Banks, 1985; Russell *et al.*, 1989, 1994). However, the study of these and other mineralizing systems has taught us that the ratio between hydrothermal metal sulfide ore deposits and hydrothermal convection cells that could potentially generate such deposits was remarkably low and depended not only on conditions at the potential site of deposition but also on the makeup of the source rock (Hunt, 1991; Russell and Skauli, 1991; Fallick *et al.*, 2001). In addition, there is little or no record of sulfide being transported in extant or ancient alkaline springs, though we have reasoned this might reflect the absence of sulfide in the crust beneath. On early Earth, however, much of the volcanic overplating was komatiitic, lavas well known to host massive sulfide

lenses and dykes (Barnes, 2004; Bekker *et al.*, 2009; Houlé *et al.*, 2010). This gave us the impetus to investigate, using a hydrothermal flow reactor built at the Jet Propulsion Laboratory, whether alkaline hydrothermal fluids of moderate temperature produced by serpentinization might release enough sulfur from such sulfides and generate the kind of porous compartmentalized mound we envisaged, which would comprise disseminated sulfide clusters with or without silica. Our results support such a supposition (Mielke *et al.*, 2010). Of course, it could still be argued that sulfidic alkaline springs may have been relatively rare even on early Earth. However, given the thousands of off-ridge springs that must have operated in the past and produced mounds that comprised trillions of compartments and their continual generation over the hundreds of millions of years between the condensation of the first ocean and signs of life at 3.8 Ga (Mojzsis *et al.*, 1996; Rosing, 1999; Abramov and Mojzsis, 2009), there was an abundance of opportunity for such springs to precipitate sulfidic compartments of the kind we envisage as likely candidates for supporting the emergence of biological systems.

Presuming such a scenario, flow reactor experiments were undertaken that involved the interaction (serpentinization) of mafic rock in the presence of iron monosulfide at 100 bar pressure and temperatures up to 120°C. These produced sulfidic and siliceous alkaline effluent (Mielke *et al.*, 2010). As expected, both chimneys and geodes were generated on passing these solutions into a simulacrum of the ferrous iron rich Hadean Ocean (Kump and Seyfried, 2005; Russell and Hall, 2006). Comparable membranes or walls to such compartments hold a potential of

more than half a volt for several hours (Filtness *et al.*, 2003; Russell and Hall, 2006). Such exothermic serpentinization also generates the fuels and some of the materials required for the onset of metabolism: H_2, CH_4, NH_3, HS^-, Mo, and W (Russell *et al.*, 1994, 2010; Kelley *et al.*, 2001, 2005; Proskurowski *et al.*, 2006, 2008); and would deliver them in alkaline solutions to compartments at comparable temperatures to those exhaling at Lost City in the North Atlantic (average 70°C, Proskurowski *et al.*, 2006) and Eyjafjordur in northern Iceland (also inferred to average 70°C, Marteinsson *et al.*, 2001). Because the compartment walls would restrict diffusion of these hydrothermal fluids, they might be expected to focus reactions with the invasive carbonic ocean at, or within, their boundaries. Indeed, these boundaries may act as ‘‘low-entropy’’ traps whereby compatible products would be forced to interact through their proximity (Nitschke and Russell, 2010; Russell *et al.*, 2010; Simoncini *et al.*, 2010). Within limits, the smaller the compartment the more effective the trap. Crucially, without compartments there could be no focusing of the electrochemical gradients required to drive a metabolic pathway over the initial, thermodynamically unfavorable steps of carbon dioxide reduction (Maden, 2000). Nor could organic products be retained and concentrated for further interactions (Russell *et al.*, 1988, 1994; Schoonen *et al.*, 1999; Nitschke and Russell, 2009; Berg *et al.*, 2010; Lane *et al.*, 2010; Mast and Braun, 2010). Thus, the compartments are the devices that solve the thermodynamic problem met at the onset of metabolism (cf. Schrödinger, 1944; Sievers *et al.*, 2004; Russell *et al.*, 2010).

Such semipermeable and semiconducting compartment walls that comprise

ferrous hydroxide, silica gel, and a complex of iron, nickel, and cobalt sulfides with adsorbed molybdenum or tungsten, or both, and act as a multifunctional catalyst would, along with their interiors, be the most beneficial sites for emergent biochemistry. The molybdenum or tungsten atoms act as two electron transfer agents; while one electron transfers to a high potential electron acceptor such as ferric iron or nitrate, the other now has enough energy to reduce carbon dioxide in an otherwise highly endergonic reaction (Russell and Hall, 1997, Maden, 2000; Ducluzeau *et al.*, 2009; Nitschke and Russell, 2009). Although silica is not generally dissolved in alkaline spring waters exhaling from serpentinizing ultramafic terrains, it does occur to the extent of around 2 millimoles in such springs exhaling from basaltic crust and has been found at such a level in our own experiments with basalt (Kelley *et al.*, 2001; Marteinsson *et al.*, 2001; Mielke *et al.*, 2010). Moreover, silica can be extremely enriched in alkaline springs that transect previously carbonated environments (Shibuya *et al.*, 2010). Ephemeral carbonate (primarily as siderite, $FeCO_3$) is also a possible initial precipitate, though it would soon be redissolved or transformed to a hydroxide around springs issuing from the seafloor into the deep (perhaps around 8 km) and mildly acidic Hadean ocean (Macleod *et al.*, 1994; Bounama *et al.*, 2001; Elkins-Tanton, 2008). Brucite, another hydroxide [$Mg(OH)_2$], is also a likely precipitate (Kelley *et al.*, 2001). We assume, in the absence of firm evidence, that the salinity of the early ocean was much like today's, because while the absence of evaporite basins in the Hadean might suggest higher concentrations, there was probably twice as much water on the planet at that time (Bounama *et al.*, 2001;

Elkins-Tanton, 2008; Tarduno *et al.*, 2010). And given that the salinity of modern ocean water is little affected during hydrothermal circulation that feeds off-ridge springs (Kelley *et al.*, 2001), we also assume an ocean water–like salinity of similar springs in the Hadean and thus no sodium cation gradient. The alternative view, that the first ocean was magnesium sulfate–dominated rather than sodium chloride–dominated, was not acted on in these experiments (Izawa *et al.*, 2010).

It is notable that simple organic reactions of the kind that may have led to the emergence of metabolism are favored by hot alkaline conditions. For example, Huber and Wächtershäuser (1997) demonstrated the catalytic potential of entities such as NiS and $NiSO_4$ in the production of activated acetate from methyl sulfide and carbon monoxide. The same authors showed that $Fe(OH)_2$ is equally active as FeS in catalyzing the amination of other carboxylic acids to amino acids (Huber and Wächtershäuser, 2003). Yamanaka *et al.* (1988) dimerized glycines with trimetaphosphate in Mg^{2+} -bearing alkaline solution at 38°C, and 4- to 6-mer peptides have been generated at the same temperatures but at the lower pH that might have occurred at the exterior of ancient hydrothermal mounds (Rabinowitz *et al.*, 1969; Yamanaka *et al.*, 1988; Yamagata and Inomata, 1997; Gao *et al.*, 2008). In life itself, iron ± nickel sulfide clusters, along with molybdenum or tungsten, play a critical role as active centers of proteins in many biological processes (Beinert *et al.*, 1997; Adams, 1998; Hoke *et al.*, 2004; Volbeda and Fontecilla-Camps, 2006; Rothery *et al.*, 2008; McGlynn *et al.*, 2009). For example, ferredoxin derivatives and iron-(nickel)-sulfur cluster proteins can act as hydrogenases; and electron donors, acceptors, and

transfer agents in all domains of life are found even in the deepest evolutionary roots to both the bacteria and the archaea (Eck and Dayhoff, 1966; Hall *et al.*, 1971; Baymann *et al.*, 2003; Martin and Russell, 2007; Say and Fuchs, 2010). Even in the absence of organic ligands, metal sulfide clusters may have catalyzed the synthesis of simple organic molecules through reactions between the hydrogen, ammonia, and bisulfide produced from serpentinization reactions and the carbon dioxide and phosphate introduced from the Hadean ocean (Walker, 1985; Yamagata *et al.*, 1991; Hagan *et al.*, 2007; Smirnov *et al.*, 2008)—reactions possibly energized by the ambient proton motive force and redox energies that acted across the inorganic membranes (Russell *et al.*, 1994, 2010). In particular, the ambient proton motive force might have driven pyrophosphate synthesis which, in turn, drove the polymerization of amino acids within the membrane, thus improving its durability and functionality (Russell *et al.*, 1994; Milner-White and Russell, 2010). These and other organic anions so generated would tend to have been trapped within the compartments and further concentrated through thermal diffusion, driven by the ambient temperature gradient that also acted across the margins of the hydrothermal mound (Baaske *et al.*, 2007; Budin *et al.*, 2009; Mast and Braun, 2010). Such interactions between a diverse set of reactants may have led to the onset of metabolism. While the metal sulfides had the makings of proto-metalloenzymes, the silica could have trapped and even helped in the synthesis of the sugars (Lambert *et al.*, 2004, 2010). Eventually, RNA based coenzymes might have replicated and then been polymerized through a natural convective polymerase reaction and concentrated

through thermal diffusion (Baaske *et al.*, 2007; Yarus, 2010). These RNA polymers may then have infected contiguous compartments and encoded the proteins that ushered in Darwinian evolution proper (Koonin and Martin, 2005). Such an evolutionary continuum, from the mineral to the living world, was first advocated in broad terms by Leduc (1911).

It is the aim of the present study to understand the effects of varying four important chemical conditions for iron sulfide or hydroxide precipitation in such a compartmentalized hydrothermal mound: (i) addition of silica in rising concentrations, (ii) pH levels, (iii) temperature, and (iv) the addition of pentameric peptides. One variable impossible to assess was the effect of pressure. However, given that no volatiles were involved in our experiments and only hydrogen and minor amounts of methane are evolved at Lost City and Eyjafjordur, this is unlikely to compromise our conclusions. Moreover, the effect of pressure on, for example, peptide stability, increases rather than decreases at higher pressure (Shock, 1992), which again is a trend that would be expected only to improve the results of our simulation.

2. METHODS

In the laboratory simulation of alkaline seepages, aqueous alkaline solutions between 25°C and 70°C (70°C is the average temperature of submarine alkaline springs recorded so far) containing sulfide ± silicate were injected into iron (II)

solutions by way of motorized syringe pipettes or a peristaltic pump, at rates between 0.08 mL/h and 0.2 mL/h for the syringe (Fig. III-1) and at 7.2 mL/h for the peristaltic pump. Chemicals, including $FeCl_2 \bullet 4\ H_2O$ and $Na_2S \bullet 9\ H_2O$, were purchased from VWR and used without further purification. Oxygen-free water (milli grade; 18.2 MΩ) was used throughout these experiments. Four main experimental approaches were taken, as follows: (i) sodium orthosilicate concentrations in syringe solutions were varied to observe the precipitated membrane mineralogical and structural changes; (ii) the pH within the injected solution was varied, and the resulting structures again were observed and analyzed; (iii) change of temperature; (iv) the effect on membrane structure was investigated through the addition of different simple and soluble pentameric peptides that comprise residues likely to have been generated early in the development of metabolism (Eck and Dayhoff, 1966; Hennet *et al.*, 1992; Brooks *et al.*, 2002; Davis, 2002). The growth, structure, and elemental composition of the resulting iron-sulfide precipitate membranes were analyzed by environmental scanning electron microscopy (ESEM), energy dispersive X-ray spectroscopy (EDX), X-ray powder diffraction, and Raman spectroscopy.

All receptacle and injection solutions were prepared simultaneously under the same environmental conditions at standard temperature and pressure (STP). Receptacle solutions were prepared inside glass Wheaton vials that had their base removed with a wet tile saw, were stoppered and inverted, and after the newly created opening was covered with parafilm, solutions were continuously sparged with gaseous nitrogen (N_2) to create anaerobic solutions. Sparging was begun at least 30

min before any reactants were added to millipore (18.2 MΩ) water to displace dissolved oxygen. After water sparging, sodium chloride was added to each solution to achieve a 600 millimolar concentration similar to modern ocean water (see III-Introduction).

All pH values were determined with a Thermo Orion 550A pH meter. Injection solutions were pumped upward through an acid-cleaned (1% HCl; 3 x H_2O rinses) 1/16-inch stainless steel capillary tube into the receptacle solutions (Mielke *et al.*, 2010, figure 8) with a peristaltic pump at a rate of 7.2 mL/h. For slower injection rates of 0.08 to ~0.2 mL/h, a Razel Model A-99 syringe pump was used with a plastic 10 mL syringe and 16G - 1 ½ inch needle (Becton-Dickinson Medical). Experiments were duplicated or triplicated for each set of conditions. Similar runs were undertaken in a positive pressure nitrogen-filled glove box to check on any differences in product (data not shown). During the injection process, nitrogen gas was continually introduced into both solutions to ensure the exclusion of oxygen from the experimental environment and maintain positive pressure.

(i) *Varying silicate concentrations.* Primary reactants were added simultaneously to each solution to achieve a 10 millimolar iron (II) chloride receptacle solution (~pH 5.0) and a 10 millimolar sodium sulfide injection solution. The injection solutions were then slowly titrated with 4% hydrochloric acid to obtain a pH of 11 for all the silicate experiments. Once these constant reactants were completely dissolved, varying concentrations of sodium orthosilicate (Na_4SiO_4), ranging from 0.01 to 416 millimolar, were added to only the injection solution. This

alkaline injection solution was allowed to flow into the receptacle solution for approximately 20–24 h at ~0.2 mL/h.

(ii) *Varying injection solution pH.* Primary reactants were added simultaneously to each solution to achieve a 10 millimolar iron (II) chloride receptacle solution (~pH 5.0) and a 10 millimolar sodium sulfide injection solution. The injection solutions were then slowly titrated with 4% hydrochloric acid to reach a range of pHs from 7.98 to 11.7. For all values of alkaline pH tested, the sodium orthosilicate concentration was kept consistent at 0.1 millimolar.

(iii) *Heated precipitation experiments.* To better mimic the hydrothermal environment as described in the III-Introduction, receptacle solutions were heated to hydrothermal temperatures (70°C) before the injection solution was allowed to flow. An acidic salt solution (600 millimolar NaCl, 10 millimolar $FeCl_2$ at pH ~5) mimicking the Hadean ocean was prepared in a 125 mL round-bottom flask with attached condenser and purged with N_2. As described in previous experiments, an inverted glass bottle was used to prepare an oxygen-sparged alkaline hydrothermal solution containing 600 millimolar NaCl, 10 millimolar Na_2S, and 2 millimolar Na_4SiO_4. The acidic solution was heated to 70°C by a resistor-controlled electric heating jacket. Once the solution reached 70°C, the pH of the solution was recorded. The alkaline hydrothermal solution was slowly injected at two different rates, ~0.2 mL/hr over a 20–24 h period (Mielke *et al.*, 2010, figure 8) and ~0.08 mL/h over a 68–72 h period.

Upon the formation of an inorganic tube or bubble (up to 20 h, Fig. III-2a, III-

2b), injection was halted, and the precipitate sample was extracted into a glass vial via either a 1000 μL pipette whose disposable tip had been trimmed to make a large opening or a Gilson 5000 lL pipette. This was accomplished by placing the pipette tip around the chimney and simultaneously knocking the structure free while drawing the precipitate upward into the pipette, along with the surrounding solution. The resulting mixture was moved to an Eppendorf tube and allowed to settle. The majority of the solution phase was removed with a pipette, and 2.0 mL of oxygen-free water was added to rinse the precipitate. This rinsing process was performed four additional times to remove aqueous ions and minimize excess precipitation of reagent salts. The chimney was applied directly from this solution to an ESEM stub, or alternatively the vial was then sealed and purged with nitrogen gas for 10 min or until the sample was dry. Samples were then either immediately subjected to ESEM or Raman analysis or stored on the bench top for not more than 1 h under a nitrogen purge.

For ESEM analysis, samples were placed on an aluminum tab within 15 min and then inserted into the ESEM (FEI XL30 FEG) under a water vapor pressure of 3.8 torr, an accelerating voltage of 20 kV, and a working distance of 10.2 mm. The gaseous secondary electron detector was used at a chamber pressure of 3.8 torr to allow imaging without subsequent coating steps. The spot analysis feature was used for an energy dispersive X-ray spectrometer (EDAX, Inc.) to analyze X-ray signals with the Genesis program. Additional samples were washed, dehydrated, and embedded in Eponate resin before ultrathin sections of 60 nm were made and imaged with a scanning transmission electron microscope. An accelerating voltage of 30 kV

and a working distance of 6.8 mm was used on the ESEM as described above (Werlin *et al.*, 2011).

For X-ray powder diffraction analysis, the glass vials containing samples were immediately sealed after the three rinses and purged with nitrogen gas for 10 min or until the sample was dry. Samples were then placed on a sample cell between two layers of micro-thin Kapton film and placed under a Siemen's D500 diffractometer, equipped with a Cu anode tube. The energy beam was a Co-Ka Fe-filtered radiation. X-ray diffraction analysis was by a Peltier cooled Kevex Si(Li) (lithium-drifted silicon) X-ray detector. Mineral identification was made by reference to the 2009 ICDD database for organic and inorganic phases in conjunction with the JADE PLUS Version 9.1.1 XRD analysis program to identify the diffraction responses in the spectra.

Raman spectroscopy was performed on samples precipitated at both STP and 70°C. After injection, precipitated chimney structures were cut off from the steel capillary from which they grew with a steel scupula. Still intact, the chimney and remaining ocean solution were poured out into a Petri dish and rinsed six times with N_2-purged Millipore (18.2 MΩ) water to remove excess salt. After extraction and rinsing, the precipitates were placed on a 3 x 1 inch glass slide and partially crushed with a spatula to expose the interior of the chimney. The slide was placed in a nitrogen-purged cryochamber at 10°C to limit oxidation of the sample. Raman spectra were obtained on a LabRam HR (Horiba Jobin Yvon) with use of a 532 nm laser and 600 g/mm grating with a resolution of ~2 cm^{-1}. The cryochamber was placed on a 3-

axis motorized stage and the sample illuminated through a sapphire window. The instrument was calibrated by using the 520 cm^{-1} silicon line and zero order.

(iv) *Addition of pentameric peptides.* Primary reactants were added simultaneously to each solution to achieve a 10 millimolar iron (II) chloride receptacle solution (~pH 5.0) and a 5 millimolar sodium sulfide injection solution. The solutions involved in the peptide experiments were not manually buffered, and their initial pHs were measured as 4.1 and 11.7, respectively. Control experiments were performed without addition of peptide. For this series of experiments, a 5 millimolar sulfide solution was utilized in conjunction with a 10 millimolar ferrous iron solution, while concentrations of 5-mer peptides were added into the sulfide solution to obtain 100 micromolar concentration. Peptides were obtained from ANASPEC with no further purification. Peptides selected for investigation were AEGEA, EEGEE, and GGGGG on the basis of their simplicity, plausibility, and solubility (Hennet *et al.*, 1992). All solutions were at a 600 millimolar sodium chloride concentration.

3. RESULTS and INTERPRETATION

3.1. Basic iron sulfide chimney structure. Analysis by ESEM and light microscopy revealed membrane bilayers with an overall thickness of ~20 μm (though ranging between ~4 and ~100 μm). The inside is composed of globular clusters of higher sulfur content (always considered relative to iron) and the outside composed of

more rigid shards of lower sulfur content (Figs. III-2 and III-3). The outermost crystalline layer's iron:sulfur ratios are relatively high (~2.0 to 8.0), and the globular aggregations are relatively low (~0.75–2.0). These atomic ratios lead us to assume that the outermost crystalline layers are primarily composed of ferrous hydroxide [$Fe(OH)_2$] with an admixture of nanocrystalline ferrous sulfide [FeS], that is, mackinawite, whereas the globular clusters that comprise, or are attached to, the inner walls consist of mackinawite with greigite. These clusters, ~1–10 μm in diameter, resemble framboids similar in appearance to those found in the interiors of fossil hydrothermal chimneys (Fig. III-3c, III-3d) (Larter *et al.*, 1981; Boyce *et al.*, 1983). In experiments where no silica was added, ESEM revealed regular and symmetrical crenulations parallel to growth around and within the chimney walls (Fig. III-4). At first, the crenulations reminded us of ''capping and escape'' effects comparable to chemical garden growth, whereby the top of the chimney is initially capped by a precipitate membrane that, in time, bursts or is at least sloughed off to the sides, leaving the outer edges as an additional rib to the growing chimney (cf. the growth rings of Stone and Goldstein, 2004). However, the crenulations' regularity, intricate structure that comprises well-ordered microdendrites (Fig. III-4b), and sinuous appearance, along with the fact that periodicities were discerned at ~4 μm (Fig. III-11), all suggest a certain self-ordering— a physicochemical wave pertaining perhaps to the dissipation of the steep pH gradient (cf. Tóth *et al.*, 2007, figure 2C). Indeed, the orientation of these dendrites normal to banding suggests a response to inward

and outward diffusive flow through the chimney walls (cf. Jeong *et al.*, 2001) (Fig. III-2d). The crenulations were produced both at the slower and faster pump rates.

Under injection at 0.2 mL/h, chimneys were observed to completely cap off with a substantial covering of iron sulfide precipitate, which halted elongation (Fig. III-5). This process is thought to start off in the same way as the aforementioned capping and escape cycle, with the exception that the fluid pressure is dissipated through the greater area of iron sulfide membrane in longer chimneys. This pressure dispersal obviates bursting, though it causes the cover to thicken and strengthen from additional layers of precipitates. This type of permanent capping has been followed by spongiform overgrowth in some cases (Fig. III-2A). Experiments where chimneys appeared capped usually also spawned secondary chimneys branching from their sides or base (Fig. III-5). This suggests that, on fouling, the pressure once again exceeds chimney strength and causes a portion of the membrane to burst, which thereby allows further exhalation and chimney growth. We could view this phenomenon as revealing how reproduction was initiated in the mound and how organic molecules generated in one compartment could be transported to the offspring.

3.2. Varying injection solution pH. According to the ESEM-EDX data, chimneys formed from injected solution with a pH that exceeded 11 are composed of ferrous oxyhydroxide. Below pH 11, the membranous precipitates mainly comprise

stoichiometric FeS (Fig. III-5, graph), a result consistent with expected $FeS/Fe(OH)_2$ equilibria. However, the lower the pH, the weaker and more bulbous is the structure (Fig. III-5). These bulbous structures also possess more fibrous clusters of precipitate on the outside than the standard chimneys. Based on observations of broken samples and ESEM images of bulb walls, these fibers are also hollow. Because of their smaller size relative to the chimneys, it appears that the membranes of the bulbs are more permeable than the chimney membranes, or at least more fluid and less brittle, as they do not rupture from injection pressure. Under ESEM, they are visibly more permeable and spongy. Below a pH of 8.03, no precipitate formed, neither was sulfide found present in the solution mixture, having volatilized as hydrogen sulfide gas.

3.3. Varying sodium orthosilicate concentrations and temperature.

Increasing the concentration of sodium orthosilicate (Na_4SiO_4) generated more bulbous or geodic structures (Fig. III-6). It appears that a concentration of 6 millimolar Na_4SiO_4 generates Fe:S ratios that approach 1:1, which effectively facilitates iron monosulfide precipitation, whereas higher concentrations appear to facilitate ferrous hydroxide precipitation.

Under ESEM, the membranes of the silicate-induced bulbous structures are quite similar to those membranes created by lowering the injection solution pH. The mineralogy of the iron sulfide nanocrystalline precipitates was investigated with X-

ray powder diffraction spectrometry. Mackinawite was strongly indicated with some suggestion of greigite (Fig. III-7). Raman spectroscopy revealed three peaks in the spectra that correspond to crystalline mackinawite at STP, and the higher-temperature (70°C) chimneys were found to be, as expected, partially composed of greigite (Figs. III-8 and III-9) (Krupp, 1994; Lennie *et al.*, 1997; Rickard *et al.*, 2001; Bourdoiseau *et al.*, 2008, 2010; Rémazeilles *et al.*, 2010).

3.4. Effects of pentameric peptides on structure. Experiments in which peptides were added to the injected alkaline solutions were conducted to investigate their effects as metal chelating agents on growth, structure, and morphology at STP. Three contrasting pentameric peptides (AEGEA, EEGEE, or GGGGG) were added at 100 micromolar concentration to 5 millimolar sulfide-bearing alkaline solution at STP. This composite solution was then injected into a 10 millimolar ferrous iron solution at a flow rate of 7.2 mL/h. Tubular structures comprising multiple distinct iron sulfide mineralogical phases were produced as judged by ESEM contrast as well as EDX. Sulfur-rich iron sulfide spheres, again with the appearance of framboids and Fe:S ratios of ~1.5 to 3, and darker, nonspherical material of lower Fe:S ratios of around 6, were the major constituents observed. However, in examples where 5-mer glycine was added, particular locations had Fe:S ratios that approached 18 (Fig. III-10C). The other pentameric peptides induced Fe:S ratios that reached as high as ~8 and ~12 (Fig. III-10A and III-10B, respectively). Addition of these peptides also

enhanced the development of the crenulations on the outer walls of the chimneys (compare Fig. III-4 with Fig. III-10). Thus, results of these experiments indicate that iron:sulfide ratios of the mixed mineral precipitate increase with the addition of the three peptides, though the effect of the 5-mer glycine was most marked (Fig. III-10C).

The small peptides utilized in these studies comprise the simplest and earliest amino acids (Brooks *et al.*, 2002; Davis, 2002). Apart from pentaglycine, these peptides contain a number of functional groups capable—as multi-dentate carboxyl, amine, and carbonyl ligands—of coordinating metal ions. Thus, each peptide could potentially ligate to several metals or other inorganic entities with multiple bonds (Harford and Sarkar, 1999; Watson and Milner-White, 2002; Cox *et al.*, 2005; Milner-White and Russell, 2008; Torrance *et al.*, 2009).

The propensity of peptides to chelate metal ions in solution and at solution/mineral phase boundaries, together with the observed change in morphological and elemental composition of iron sulfide/hydroxide chimneys, suggests the possibility that these polymers direct epitaxial growth of particular iron-rich minerals by specific metal ion chelation. As an initial iron sulfide zone is formed, polymers present in the spring solution may be exposed at the liquid-membrane interface. In addition to this, the high porosity of these structures allows the possibility that, as the solution continues to flow, organic polymers are transported into the membrane. These processes together would make for an iron sulfide wall that bears an organic functionality capable of metal ion chelation. The presence of these

metal cation-binding sites in the form of an organic matrix increases local concentrations of iron near the outer wall, which creates a unique chemical environment that contrasts with environments where organic functionalities are absent (cf. Sikes *et al.*, 1991; Silverman *et al.*, 1995).

4. DISCUSSION

The inorganic compartments produced in these experiments appear to satisfy one of the expectations of the alkaline hydrothermal theory for the emergence of life in that they could act as chemiosmotic and semiconducting containers for organic reactions and their reactive products (Russell *et al.*, 1994; Lane *et al.*, 2010). Moreover, we know from previous studies that the compartments can hold a potential of more than half a volt for several hours, in theory quite enough to contribute to a putative autotrophic metabolism (Filtness *et al.*, 2003; Russell and Hall, 2006). However, their thicknesses, from 4 to 100 μm, are generally orders of magnitude greater than the 5–10 nm typical of the prokaryotic membrane. Thus, at first sight the pH and redox gradients would be too low to drive some of the otherwise endergonic reactions that frustrate the earliest steps in CO_2 reduction (Maden, 2000; Michalkova *et al.*, 2011). Regarding pH, it might be expected that protons find their way through the membrane to the alkaline interiors, perhaps via rotational/ translational diffusion of water/hydronium molecules that comprise the Langmuir layer on sulfide, hydroxide, or silica surfaces oriented normal to the membrane (Fig. III-2) (da Silva

and Williams, 1991, p 103). Of course, the pH gradient is logarithmic, and thus a fairly steep gradient will obtain at some locale within the membrane. Judging from comparable studies by Bähr *et al.* (1984), this is likely to be situated toward the outermost margins of the membrane. And like any response to ionic gradients, the protonic flow is likely to be as waves and as such carry packets of energy along the wave fronts (cf. Stone and Goldstein, 2004). As the membranes themselves are spatially heterogeneous at the micron level and perhaps below, the transportation of ionic species would likely be heterogeneous as well, resulting perhaps in the buildup of steep gradients at some locales. At the same time, the two electrons stemming from hydrothermal hydrogen and reducing molybdenum (or tungsten) VI to IV bifurcate and could be conducted along the iron layers (Fe-Fe = 2.6 Å) or tetrahedra that comprise the ‘‘ab’’ crystallographic plane of mackinawite (Russell and Hall, 2006; cf. Ferris *et al.*, 1992; Kwon *et al.*, 2011) from the interior, one to an electron acceptor such as ferric iron phases, sulfur, nitrate, or nitric oxide on the exterior, while the other now has the energy to reduce CO_2 (Russell and Hall, 1997; Ducluzeau *et al.*, 2009; Nitschke and Russell, 2009). In this way, molybdenum-bearing mackinawite nanocrysts—possibly ligand modified— act as a protohydrogenase (Russell and Hall, 2002; Nitschke and Russell, 2009; and see McGlynn *et al.*, 2009).

Results of these experiments also reveal patterns of precipitation of the kind normally considered to result from conditions far from thermodynamic equilibrium, that is, from supersaturation attendant upon fluid mixing. The first example is that of the framboids found within the chimney interiors, which presumably comprise

aggregates of magnetic Fe^{III}-bearing mackinawite and greigite (Sawlowicz, 2000; Mitra-Delmotte and Mitra, 2010; cf. Larter *et al.*, 1981) (Figs. III-3, III-8, and III-9). The second is the periodic equi-spacing of the crenulations that mark the exteriors and interiors of many of the chimney walls when grown from more alkaline solution or on those where peptides were added to the influx (Figs. III-4 and III-10). Given the fidelity and regularity of the crenulations and their orthogonality to flow, an early thought was that they were Chladni plates (Lévy, 2006, figure 1), that is, artifacts that respond to vibrations transmitted along the capillary tube that feeds the receptacle solution. However, because these structures were generated in experiments involving both peristaltic and syringe pumps, and because we employed different lengths of plastic tubing, all giving the same length between rill and ridge, we considered the crenulations more likely to be an outward manifestation of hidden chemical self-ordering. After all, flanges at much larger scale around hydrothermal chimneys that comprise beehive heat exchangers are clearly generated far from equilibrium (Fouquet *et al.*, 1993, figure 4; Koski *et al.*, 1994; Rickard *et al.*, 1994, figure 1; Ludwig *et al.*, 2006, figure 2b; Rickard and Luther, 2007, figure 39). Those so-called beehives consist of regularly spaced ribs of anhydrite, pyrite, and iron oxides that encircle a black smoker chimney. The conditions are imposed by the temperature, redox, and pH contrasts across the chimney walls. Fluid flow is organized radially both inward and outward. Rickard *et al.* (1994) suggested that anhydrite, being inversely soluble, is precipitated along with iron oxides as seawater—presumably drawn toward the chimney by the Venturi effect—is heated by the outgoing

hydrothermal fluids from which pyrite and chalcopyrite are precipitated. Once the pattern is set, it is reinforced by feedback effects to be expected of far-from equilibrium systems. We speculate that the regularly spaced flanges around our micro-chimneys are a result of flow and counterflow, guided and reinforced through a comparable positive feedback. In this case, the outflow of hydroxyl and hydrosulfide ions of the alkaline solution perhaps leads to the precipitation of the external ferrous hydroxide ridges that comprise the rows of microdendrites, while the inflow of hydronium may be focused in the rills between. We envisage this two-way ionic and electron transport through the chimney wall as being controlled by spontaneously precipitated central dividers 10–100 nm thick that comprise platelets of FeS or $Fe(OH)_2$, or both, and separate the permeable channels ~2 μm deep (Fig. III-11). If this tentative interpretation were to prove correct, the scene would be set for the reduction of CO_2 or hydrothermal formate and, concomitantly, a high potential electron acceptor, within the nanopores of the membrane rather than in the compartment's interior. Regarding CO_2 reduction, the simplest pathway for emerging biochemistry is via two tributaries, one the hydrogenation of carbon dioxide to a methyl entity and the other to form a carbonyl group. These components are then assembled as activated acetate at acetyl coenzyme-A synthase, the nickel iron sulfide–bearing enzyme that gives this pathway its name (Fuchs, 1989; Ljungdahl, 1994; Russell and Martin, 2004).

While inorganic compartments formed at particular hot springs on early Earth may offer a plausible site for life's emergence (Koonin, 2007), and the hypothesis

examined here requires a minimum of contingency, it must be pointed out that sulfide-rich deposition at alkaline springs would have been rare, relying as it would on extensive developments of sulfides in the oceanic crust beneath (Mielke *et al.*, 2010; Russell *et al.*, 2010). More typical would have been precipitates of silica, brucite, and ephemeral carbonates (Shibuya *et al.*, 2010). Ferrous hydroxide and green rust would have been rarer additions to the precipitate mounds, and sulfide deposits rarest of all. Nevertheless, given the thousands of such submarine springs operating at any one time, the hundreds of millions of years between the condensation of the first ocean and the Archean with its signs of life, and the billions of compartments that comprised any one mound, there was an abundance of possibilities for this kind of metabolic process to emerge and evolve into life. The same might be said for Mars and the icy wet moons of Jupiter and Saturn—Europa and Enceladus—prime targets for life-detection missions (Russell and Hall, 1999; Hand *et al.*, 2010; Postberg *et al.*, 2011).

5. CONCLUSIONS

Iron sulfide and hydroxide precipitates formed in experiments that simulated particular, and probably rare, ancient submarine alkaline hydrothermal vents occurred as chimney-like tubes and geodic bubbles. At STP, the exteriors were composed dominantly of crystalline mackinawite (FeS), often with an exterior of dendritic ferrous hydroxide, while framboidal-like iron sulfide spheres tended to coat the

interiors. In the higher-temperature chimneys, some of the mackinawite was transformed to greigite (Fe_3S_4). From a prebiotic perspective, we note that mackinawite has a similar conformation as does the active center of iron-iron hydrogenase, albeit without ligand modification, while the structure of greigite is similar to the active centers of acetyl coenzyme-A synthase and carbon monoxide dehydrogenase as well as to the ferredoxins (Russell and Hall, 1997, 2006; McGlynn *et al.*, 2009) (Fig. III-12).

Iron sulfide–bearing precipitates are influenced greatly by the overall chemical environment. Atomic sulfur ratios relative to iron increase with the decrease of injection solution pH (minimum 8.03) and also with the increase of sodium orthosilicate concentrations (maximum 6 millimolar). Moreover, observed differences in cases in which peptides were added to the alkaline solutions reveal a novel functionality for these molecules in that they may have participated as binders and modifiers to chimney structure and reactivity prior to their contemporary roles in biological processes (Milner-White and Russell, 2008; Rabone *et al.*, 2010). The diversity of structural and mineralogical morphologies and elemental stoichiometries of iron and sulfur are consistent with theories in which these elements played a fundamental role in the emergence of chemical complexity through the dissipation of physico- and electrochemical gradients (Russell and Hall, 1997, 2006; Baaske *et al.*, 2007). That is, together they provide for a scenario whereby the close proximity of a number of different mineral types and forms creates a foundry of chemical potential through which the catalysis and gradient-driven chemical condensations required for

the interconversion of chemical species could be wrought. In addition, the existence of gel-like to nanocrystalline chimney compartments allows for the sequestering and concentration of reaction products. Put another way, the hydrothermal conduits and their superposed chimneys, geodes, and gels focus and confine the kind of high enthalpy, but low entropy, hydrothermal feed that interacts with the carbonic ocean through the chemiosmotic and semiconducting inorganic membranes that could promote chemical ordering and the emergence of biochemistry through the acetyl coenzyme-A pathway—‘‘order from order’’ as Schrödinger (1944) would have it (Russell *et al.*, 1994; Nitschke and Russell, 2010; Shock and Canovas, 2010; Stockbridge *et al.*, 2010).

This work suggests that the main site for reduction and polymerization was within the porous and semipermeable membranes themselves rather than in the compartmental voids. However, the compartments may have acted as repositories for some of the products, which in turn may have been entrained and passed on upward by the hydrothermal solution to newly formed compartments, so enriching these in organic anions such as peptides. These peptides may have continued to chelate the ready-made inorganic clusters that acted as ever more effective catalysts or protoenzymes. Finally, these may have coated the inorganic interiors, so bringing about an organic takeover and the formation of budding organic cells (Milner-White and Russell, 2008).

We reiterate that geochemistry could not emerge into biochemistry without the extra energies afforded by the chemiosmotic forces and electron bifurcations that act through the kind of inorganic membranes described here (Russell *et al.*, 1994; Russell and Hall, 1997; Nitschke and Russell, 2009, 2011; Lane *et al.*, 2010; Michalkova *et al.*, 2011). Precipitating at a pH front between the injected alkaline solutions that represent a hydrothermal spring and the ocean-like solvent, there exists the potential across iron sulfide–bearing membranes for relatively steep electrochemical and thermal gradients, for the concentration and storage of organic molecules and an ambient proton motive force, which all autotrophic life appears to exploit (Kell, 1979; Baltscheffsky *et al.*, 1999; Mast and Braun, 2010). These are challenges for experimentation. Further research is also called for to examine whether protons could be put to work condensing monophosphate and acetyl phosphate to pyroor trimetaphosphate as a natural proton-motive force (Milner-White and Russell, 2010; Barge *et al.*, 2011; cf. de Zwart *et al.*, 2004).

We emphasize that, dependent as it would be upon source rock, temperature, depth, and perhaps proximity to a 400°C hydrothermal spring discharging high concentrations of the d-block elements and a subsidiary quantity of hydrogen sulfide (Douville *et al.*, 2002), the generation of iron sulfide/ hydroxide–rich chimneys would have been a rather rare, but inevitable, event at submarine alkaline springs. We say this in the knowledge that there would have been hundreds of submarine alkaline springs operating over the hundreds of millions of years that comprised the Hadean era, each one producing a complex of billions of assorted compartments over their

lifetimes of tens of thousands of years (Früh-Green *et al.*, 2003; Ludwig *et al.*, 2006), some of them reproducing and promoting the kind of protometabolic reactions that we consider to have led to the emergence of life.

ACKNOWLEDGMENTS

We thank Bill Abbey, Mathieu Choukroun, James Gleixner, and Richard Kidd for help in the laboratory. For discussions we are grateful to Wolfgang Nitschke, Laszlo Roszlo, and Professor Galen Stucky, as well as Laurie Barge, Elbert Branscomb, and Eugenio Simoncini, members of the NAI-sponsored Thermodynamics Disequilibrium and Evolution Focus Group. K.R. thanks the National Aeronautics and Space Administration New York Space Grant Consortium for financial sponsorship. L.W. is supported by the ConvEne IGERT Program (NSF-DGE 0801627). S.E.M. was supported by the Marine Biological Laboratories NASA Planetary Biology Internship Program, an NSF IGERT Fellowship by the MSU Program in Geobiological Systems (DGE 0654336) and acknowledges the NASA Astrobiology Institute–Montana State University Astrobiology Biogeocatalysis Research Center (NNA08CN85A). The research described in this publication was carried out at the Jet Propulsion Laboratory, California Institute of Technology, under a contract with the National Aeronautics and Space Administration, with support by NASA Exobiology and Evolutionary Biology award (NNH06ZDA001N) and supported by the NASA Astrobiology Institute (Icy Worlds).

Author Disclosure Statement

No competing financial interests exist.

Abbreviations.

EDX, energy dispersive X-ray spectroscopy; ESEM, environmental scanning electron microscope, environmental scanning electron microscopy; STP, standard temperature and pressure.

FIGURES

Figure III-1. The experimental apparatus used for the production of metal-bearing chimneys. The crimp-top Wheaton bottle (125 mL) was cut open to more easily harvest the chimneys from the ‘‘Ocean’’ receptacle. Parafilm was tightly wrapped around the receptacle’s open top, and a gaseous nitrogen purge line was used to create an oxygen-depleted headspace. All solutions were purged with gaseous nitrogen before use in experiments. A 10 mL syringe connected with Teflon tubing to a 1/16-inch (1.59 mm outer diameter) stainless steel tube was used to inject the ‘‘Hydrothermal’’ solution into the ‘‘Ocean’’ receptacle through the Teflon septa. Specially designed devices were used to minimize structural damage to the chimneys during harvesting and transport to the particular analytical instruments.

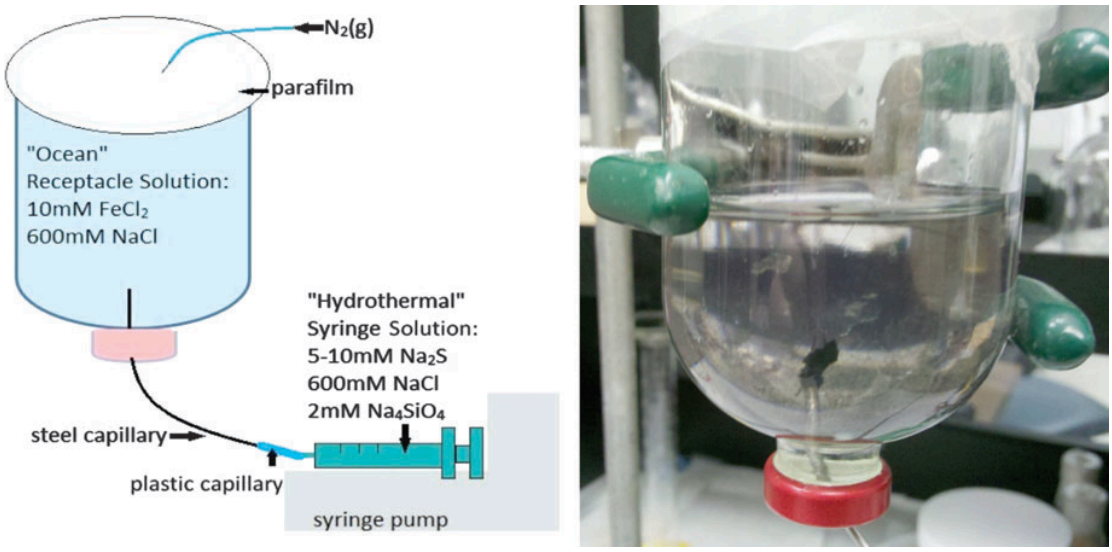

Figure III-2. (a) Video image sequence of a growing iron-sulfide chimney as a 10 millimolar alkaline sulfide solution is injected into a slightly acidic 10 millimolar iron (II) solution at a rate of 0.2 mL/h. The stream of effluent-bearing precipitate (white arrow) can be seen emerging from the top of the chimney, indicating a hollow structure. Over time the stream becomes paler. Through to the first 100 min the chimney appears smooth, but thereafter becomes increasingly covered in fibrous strands and globules of precipitate. The chimney growing from the 1/16-inch (1.59 mm outer diameter) stainless steel tubing is itself about 1 mm in diameter (3 mm scale bar). (b) Environmental scanning electron microscope (ESEM) micrographs seamed together of an FeS chimney showing the top opening at lower magnification. (c and d) ESEM images of increasing magnifications showing the morphologies of the FeS minerals comprising the chimney (compared with figure 1h of Pagano *et al.*, 2008). (e) Scanning transmission electron micrographs of the FeS chimney cross section showing the variety of morphologies that support the intricate channels comprising the semipermeable membrane. All solutions contain 600 millimoles/liter of sodium chloride. Color images available online at www.liebertonline.com/ast.

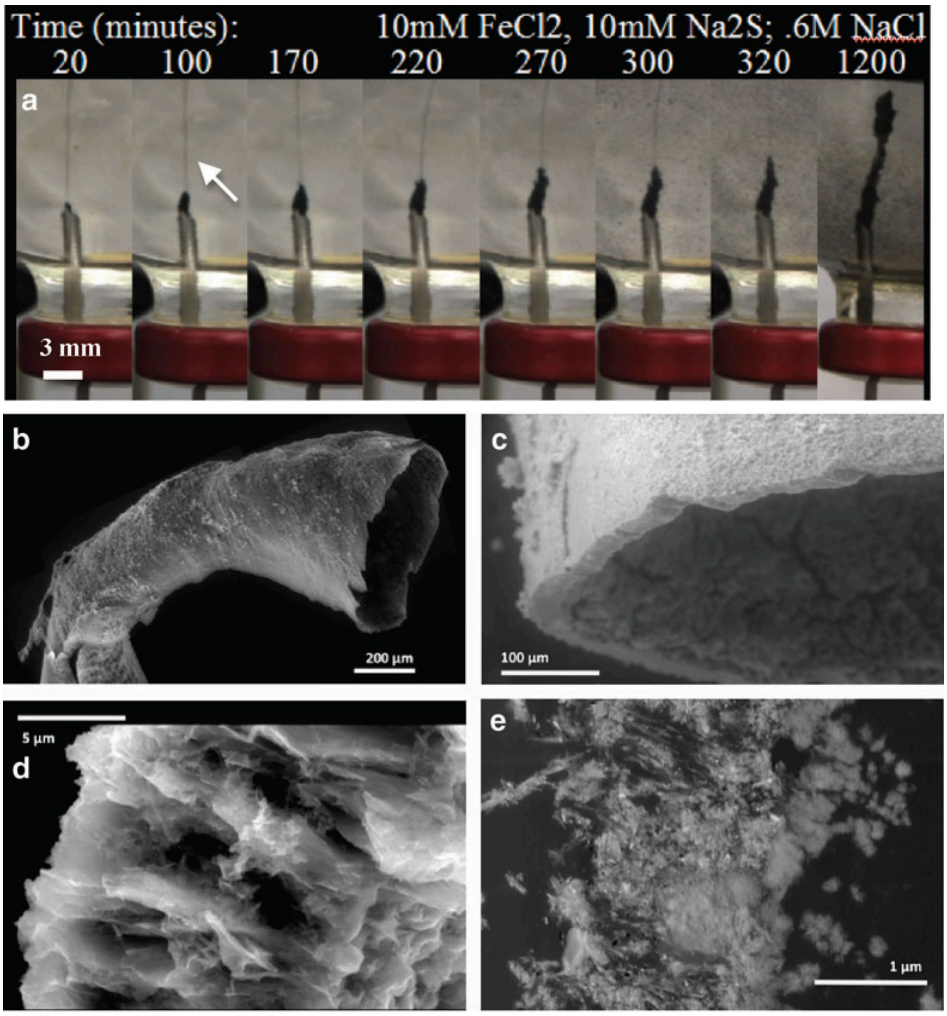

Figure III-3. ESEM micrographs (a) showing a cross section of chimney wall produced as a sodium sulfide solution is injected into a solution of iron (II) chloride at 50°C. The iron:sulfur ratio of the shards (arrow) that comprise this outer membrane is ~6.5 (indicative of iron hydroxides dominating over FeS); (a) and (b) illustrate the contrasting overgrowths on the interior and exterior of the membrane; (c) and (d) show spherical morphologies that resemble framboids (cf. Wilkin and Barnes, 1997; Ohfuji and Rickard, 2005). The latter have iron:sulfur ratios of between 1.2 and 1.5, indicative of a mixture of mackinawite, greigite, or pyrite with minor iron hydroxide (cf. Sawlowicz, 1993, 2000; Ariztegui and Dobson, 1996). They also bear comparison with framboids found in fossil hydrothermal chimneys (Larter *et al.*, 1981; Boyce *et al.*, 1983). Framboids are produced as aggregates of magnetic iron sulfides (generally ferromagnetic greigite) in far-from-equilibrium conditions (Wilkin and Barnes, 1997; Sawlowicz, 2000). Note that this experiment was run at 50°C, with the standard reagent concentrations specified in the Methods section.

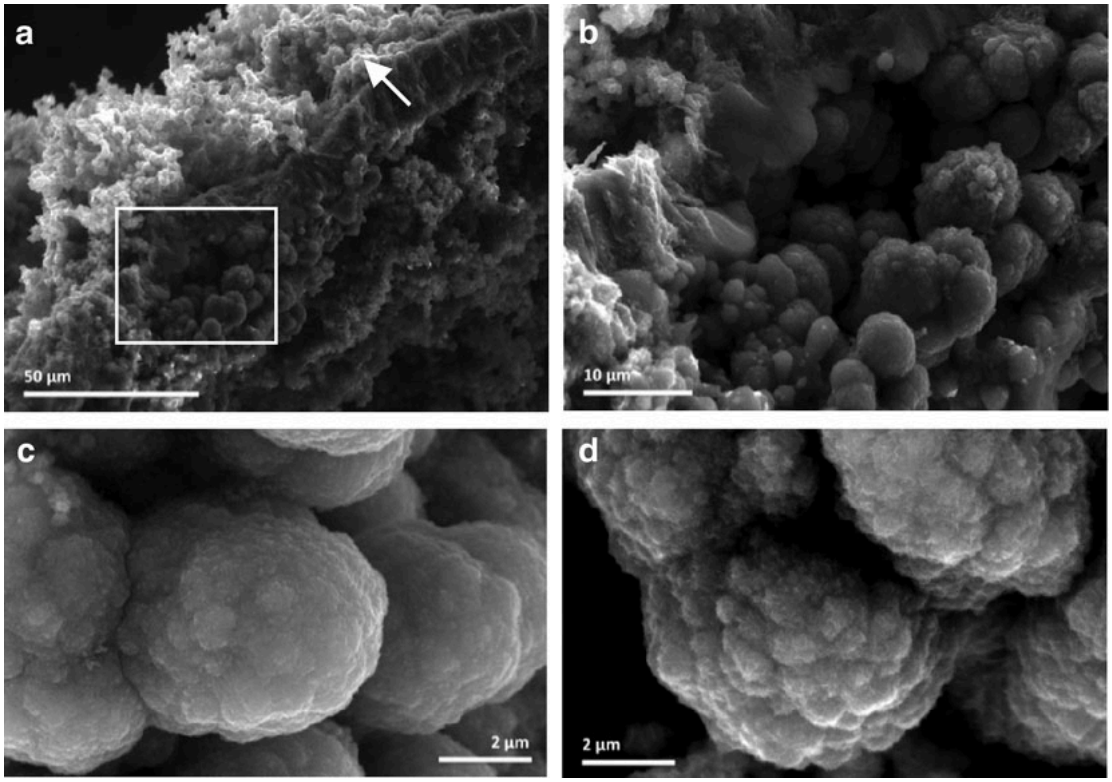

Figure III-4. ESEM micrographs of the flanged walls to iron sulfide/hydroxide chimneys produced when 5 millimolar alkaline sulfide solution is injected into a slightly acidic 10 millimolar iron (II) chloride solution. Experiments were conducted at a rate of 7.2 mL/h with a peristaltic pump. Micrographs (a) and (b) are from separate experiments. Both exhibit flange growth normal to the apparent growth axis with a periodicity (wavelength) of ~4 μm. The exterior flanges are composed of iron hydroxide flocculent (Fe/S = 5.42 ± 0.48 for the mean of three EDX analyses). The polarity of growth in (b) might indicate the direction of diffusive flow.

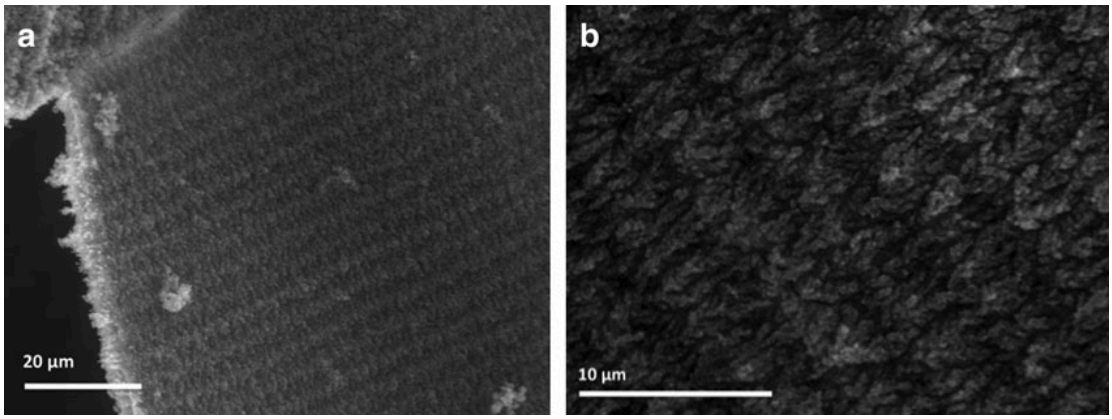

Figure III-5. Series of frames (top) captured from video of separate experiments with varying injection solution pH (i.e., sodium sulfide solution). Notice the increasing bulbous appearance and eventual deterioration of the FeS precipitate as pH is lowered and the lack of chimney formation that occurs at pH 8.03. Above pH 11 the exterior membrane surfaces comprise green rust (iron oxyhydroxides), and chimneys are characteristically taller and often branched. The graph (bottom) shows the ESEM–energy dispersive X-ray spectroscopy (EDX) analytical results for iron:sulfur atomic ratios of multiple analyses per chimney cross section and multiple chimneys at the various pHs. Note that this experiment was run under ambient laboratory conditions with reactant concentrations specified in the Methods section. For a scale of reference, the stainless steel tubing possesses an outer diameter of 1/16 inch (1.59 mm) (3 mm scale bar). Color images available online at www.liebertonline.com/ast.

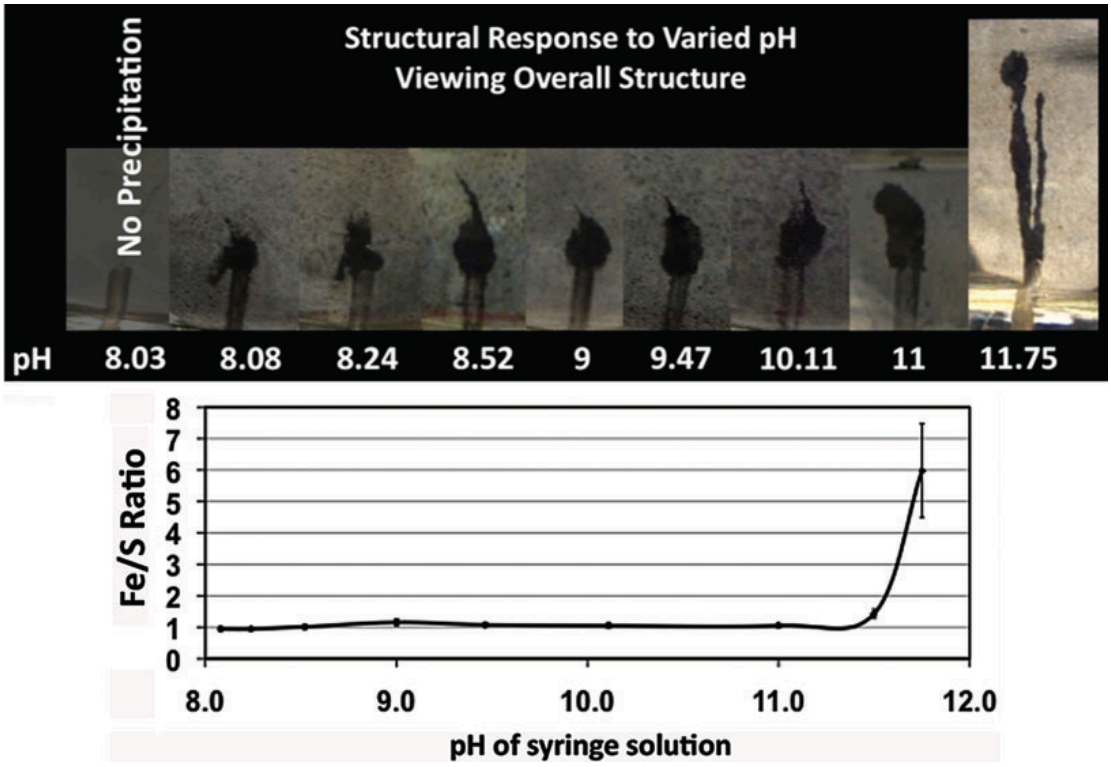

Figure III-6. Series of frames (top) captured from video of separate experiments involving various concentrations of sodium orthosilicate added to the sodium sulfide solution at an unadjusted pH of ~11.7 and injected into a solution of iron (II) chloride. The left-hand data point here is equivalent to right-hand data point in Fig. III-5. The precipitate structures become more bulbous with increasing sodium orthosilicate concentrations. The graph (bottom) of ESEM-EDX analyses of iron:sulfur atomic ratio indicates that the highest sulfur content relative to iron is found in these structures when the concentration of sodium orthosilicate in the sodium sulfide injection solution is ~7.15 millimoles/liter. For a scale of reference, the stainless steel tubing possesses an outer diameter of 1/16 inch (1.59 mm) (3 mm scale bar). Color images available online at www.liebertonline.com/ast.

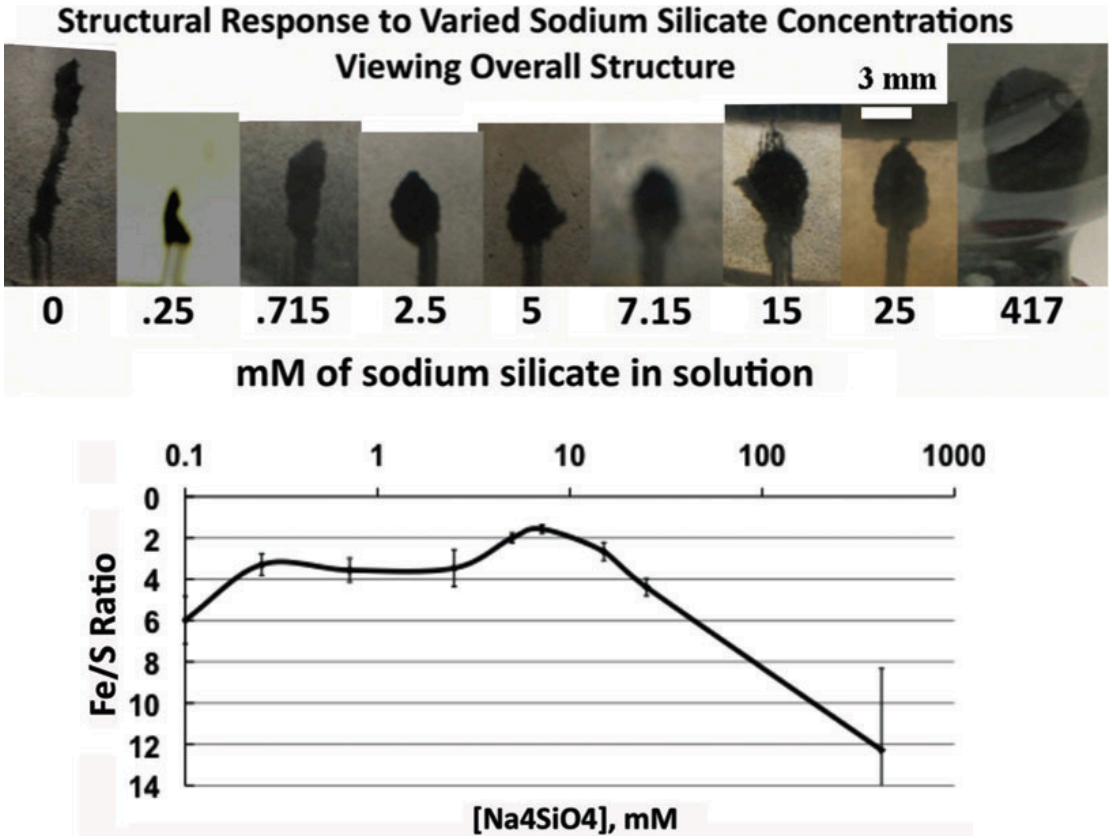

Figure III-7. X-ray diffraction spectra of a precipitate formed via the injection of 2.0 millimolar sodium orthosilicate and 10.0 millimolar of sodium sulfide solution into a receptacle solution of 10 millimolar iron (II) chloride at STP. The main mineral phase was found to be mackinawite. The two strong peaks at ~32° and ~46° are associated with unknown minerals that may be forms of ferrous silicate (cf. Bourdoiseau *et al.*, 2008; Rémazeilles *et al.*, 2010). All solutions contain 600 millimoles/liter sodium chloride. Color images available online at www.liebertonline.com/ast.

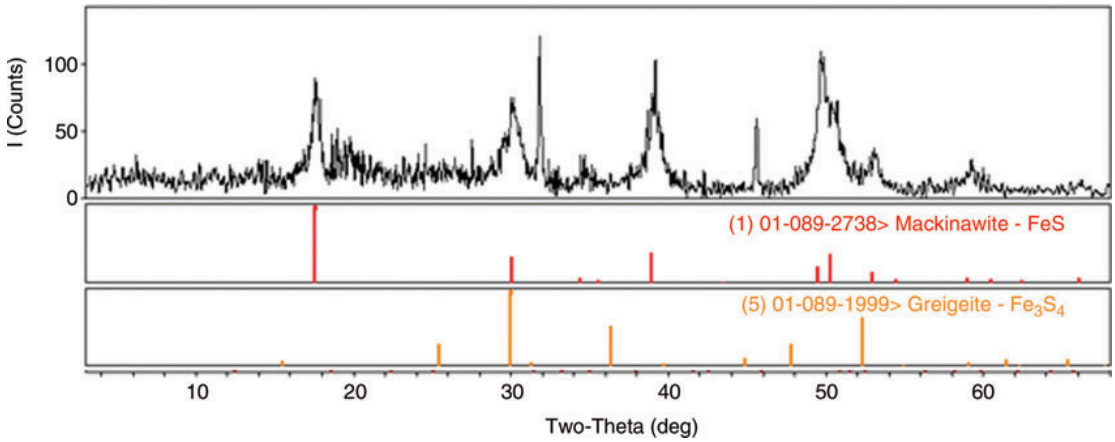

Figure III-8. Raman spectrographic analysis shows evidence for partially oxidized mackinawite (iron (III)-containing mackinawite) in iron sulfide chimney grown at 70°C. The small shoulder peak at ~309 cm^{-1} and the broad hump centered around ~354 cm^{-1} are similar to the spectral peaks identified by Bourdoiseau *et al.* (2008) as representing partial oxidation of iron (II) in mackinawite to iron (III). The partial oxidation of iron (II) is demonstrated to lead to the formation of greigite (Rickard *et al.*, 2001, and see Fig. III-9). Color images available online at www.liebertonline.com/ast.

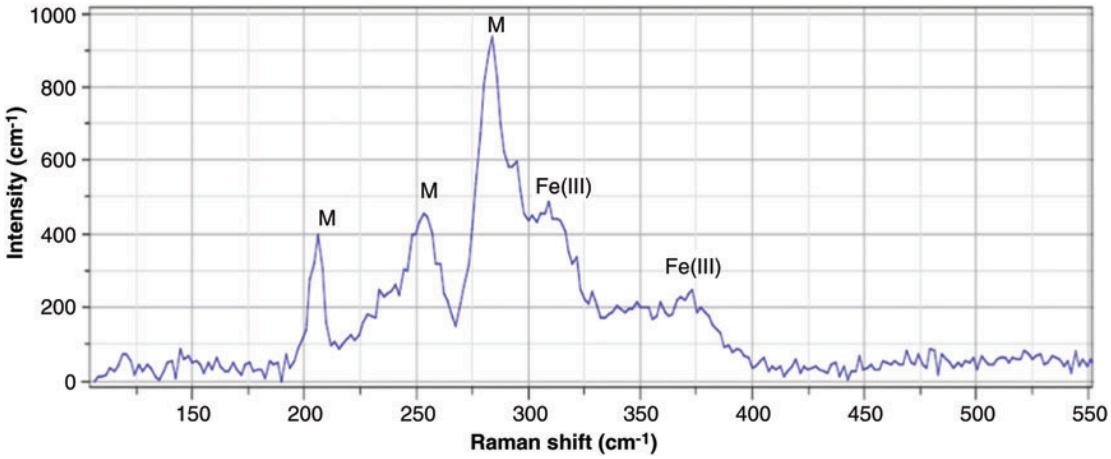

Figure III-9. Raman spectrographic analysis shows evidence for greigite and native sulfur in iron sulfide chimneys grown at 70°C. Greigite is expected at higher temperatures through the loss of iron to solution, and the native sulfur is possibly produced by the same process, though we cannot rule out the production of sulfur by oxidation occurring during transfer of the sample to the Raman system. The large greigite peak around 350 cm^{-1} is separated into two bands occurring at ~351 and ~352 cm^{-1}, closely resembling the greigite Raman spectrum of Rémazeilles *et al.* (2010, and see Wei and Osseo-Asare, 1995; Benning *et al.*, 2000; Rickard *et al.*, 2001.) Color images available online at www.liebertonline.com/ast.

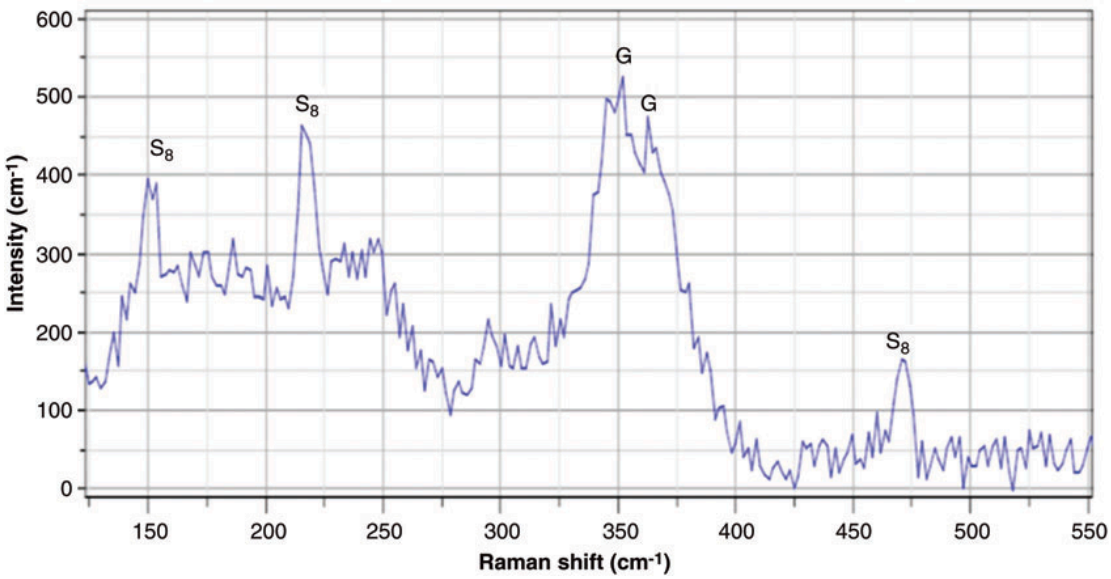

Figure III-10. ESEM images of flanged walls on ferrous sulfide/hydroxide chimneys grown by the injection of a 5 millimolar alkaline sodium sulfide (pH ~11.7) solution bearing 100 micromolar pentameric peptides into a 10 millimolar slightly acidic iron (II) chloride solution. The chimneys were produced at an injection rate of 7.2 mL/h, and the different pentameric peptides are identified below the ball-and-stick illustrations. All three peptide experiments formed flanged walls that had a similar periodicity (wavelength) of ~4 µm. The three peptides gave structures topographically unique from one another as judged by ESEM. All solutions contained 600 millimolar sodium chloride and no sodium orthosilicate. Ball-and-stick images produced with BALLView 1.4.

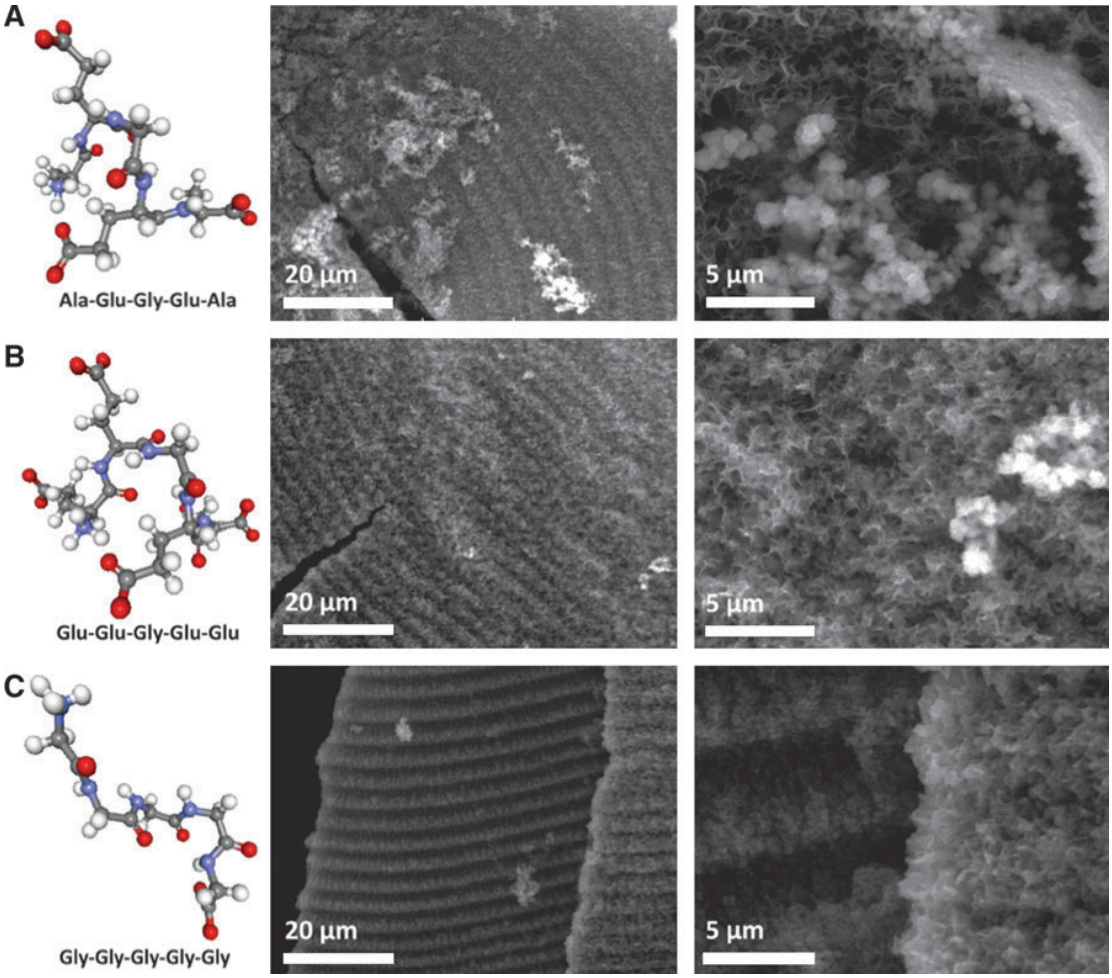

Figure III-11. Composite selection of micrographs illustrating the regular flanges that comprise ferrous hydroxide microdendrites (see Fig. III-2d for detail) on the exterior of an iron sulfide–bearing membrane (left), a cross section (middle), and framboidal iron sulfides from the interior of a chimney (right). We speculate that flange growth results from the escape of alkaline solution through the membrane along subcompartments oriented normal to growth. Where this solution meets the ferrous iron, ferrous hydroxide is precipitated as ribs, also normal to growth. A counterflow of protons down-gradient to the alkaline interior takes place in the neighboring subcompartments. Platelets of ferrous minerals are spontaneously precipitated at the interface of the two solutions. This is where we imagine the potential exists for carbon dioxide reduction/hydrogenation under the higher pressures obtaining early in the history of wet, rocky worlds—an idea amenable to testing through microfluidics.

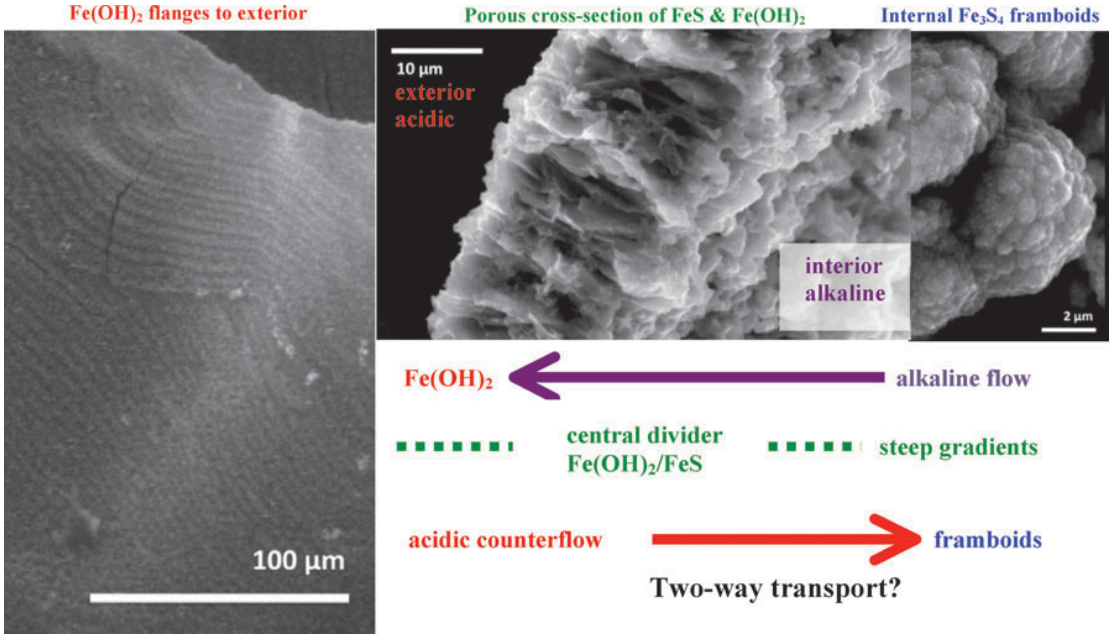

IV. Differential growth of and nanoscale TiO_2 accumulation in *Tetrahymena thermophile* by direct feeding versus trophic transfer from *Pseudomonas aeruginosa*

Applied and Environmental Microbiology, Volume 78, Number 18, pp. 5616-5624 (September 2013).

Randall E. Mielke[1,2], John H. Priester[1], Rebecca A. Werlin[3], Jeff Gelb[4], Allison M. Horst[1], Eduardo Orias[3], Patricia A. Holden[1]

[1] Bren School of Environmental Science and Management, Earth Research Institute, UC Center for the Environmental Implications of Nanotechnology (UC CEIN), University of California, Santa Barbara, CA 93106-5131; [2] Jet Propulsion Laboratory, California Institute of Technology – NASA, Planetary Science, Pasadena, CA 91109-8099; [3] Department of Molecular, Cellular and Developmental Biology, University of California, Santa Barbara, CA, 93106-9625; [4] Xradia Corporation, Pleasanton, CA, USA

* Corresponding author. Email: holden@bren.ucsb.edu

ABSTACT

Nanoscale titanium dioxide (TiO_2) is increasingly used in consumer goods and is entering waste streams, thereby exposing and potentially affecting environmental microbes. Protozoans could either take up TiO_2 directly from water and sediments or acquire TiO_2 during bactivory (ingestion of bacteria) of TiO_2-encrusted bacteria. Here, the route of exposure of the ciliated protozoan *Tetrahymena thermophila* to TiO_2 was varied and the growth of, and uptake and accumulation of TiO_2 by, *T. thermophila* were measured. While TiO_2 did not affect *T. thermophila* swimming or cellular morphology, direct TiO_2 exposure in rich growth medium resulted in a lower population yield. When TiO_2 exposure was by bactivory of *Pseudomonas aeruginosa*, the *T. thermophila* population yield and growth rate were lower than those that occurred during the bactivory of non-TiO_2-encrusted bacteria. Regardless of the feeding mode, *T. thermophila* cells internalized TiO_2 into their food vacuoles. Biomagnification of TiO_2 was not observed; this was attributed to the observation that TiO_2 appeared to be unable to cross the food vacuole membrane and enter the cytoplasm. Nevertheless, our findings imply that TiO_2 could be transferred into higher trophic levels within food webs and that the food web could be affected by the decreased growth rate and yield of organisms near the base of the web.

1. INTRODUCTION

With the increased production and use of manufactured nanomaterials, there are concerns regarding their environmental buildup and possible ecological impacts (Klaine *et al.*, 2008; Lawton, 2008). One highly produced nanomaterial is nanoscale titanium dioxide (TiO_2), which is found in a wide range of impermanent consumer products such as household paints (Kaegi *et al.*, 2008; Weir *et al.*, 2012), cosmetics (Nohynek *et al.*, 2010), medicinal ointments (Choksi *et al.*, 2010), and food products (Philips *et al.*, 1997). On the basis of the projected increase in its production (Robichaud *et al.*, 2009), manufactured TiO_2 will increasingly enter the environment, where it could impact ecosystem health (Boxall *et al.*, 2007), including food web interactions between protozoan predators and bacterial prey that are important in nutrient cycling (Klaine *et al.*, 2008).

Many manufactured nanomaterials (Suresh *et al.*, 2013), including TiO2 (Mileyeva-Biebesheimer *et al.*, 2010) and either cadmium telluride (CdTe) (Dumas *et al.*, 2009) or cadmium selenide (CdSe) (Priester *et al.*, 2009) quantum dots (QDs), have been shown to impact bacterial cell membranes and interfere with bacterial population growth (Dumas *et al.*, 2009; Priester *et al.*, 2009). In experiments with planktonic *Pseudomonas aeruginosa* growing in the presence of CdSe QDs, cell membranes were disrupted by reactive oxygen species, resulting in QDs entering cells (Kloepfer *et al.*, 2003; Priester *et al.*, 2009; Werlin *et al.*, 2011). In a trophic-transfer experiment, we showed that intracellular CdSe QDs in *P. aeruginosa* prey were

transferred into the ciliated protozoan predator *Tetrahymena thermophila* and biomagnified in the process (Werlin *et al.*, 2011). In another investigation, carbon nanotubes were directly ingested by these protozoans, which interfered with bactivory (ingestion of bacteria) (Ghafari *et al.*, 2008), but trophic transfer was not studied. Thus, at least two scenarios of protozoan exposure to manufactured nanomaterials have been reported: protozoan predation upon bacteria with already internalized nanomaterials and direct ingestion of nanomaterials from the aqueous environment.

A third, potentially common, scenario for nanomaterial exposure to protozoans is via ingestion of nanomaterials-coated bacteria. While there are various potential nanomaterial impacts on bacteria according to nanomaterial properties size, as well as exposure conditions (Suresh *et al.*, 2013), many nanomaterials such as TiO_2 are observed to adsorb to cell membranes, e.g. of *Escherichia coli* (Mileyeva-Biebesheimer *et al.*, 2010) and *P. aeruginosa* (Horst *et al.*, 2010). In fact, since nanomaterials are often larger than typical bacterial cell wall openings (Demchick *et al.*, 1996), external envelope adsorption may be the prevalent mode of manufactured nanomaterial association with bacteria. Given this likelihood, questions arise concerning protozoan predation of such bacteria, i.e., if it occurs and whether bacterially sorbed nanomaterials, including TiO_2, can be transferred into protozoans during bactivory of nanomaterial-encrusted bacteria. Information about the trophic transfer of bacterially adsorbed TiO_2, with possible TiO_2 biomagnification in protozoa, will provide a better understanding of the potential impacts of manufactured TiO_2 on base food web interactions.

In this study, we investigated (i) whether TiO_2 that is adsorbed to *P. aeruginosa* is transferred to *T. thermophila* during protozoan bactivory and (ii) the possible effects on protozoan growth. The condition of *T. thermophila* grown with TiO_2-encrusted *P. aeruginosa* is compared to that of direct uptake of TiO_2, i.e. by *T. thermophila* grown in bacteria-free, nutrient-rich medium that is amended with TiO_2.

2. MATERIALS and METHODS

2.1. Strains, media, and nanomaterials. The bacterial strain used in this study was *P. aeruginosa* PG201, a Gram-negative organism studied previously (Horst *et al.*, 2010; Priester *et al.*, 2009; Werlin *et al.*, 2011), and maintained at -80°C. As described before (Werlin *et al.*, 2011), the protozoan strain was *T. thermophila* SB210E. The medium used for *P. aeruginosa* cultivation was Luria Bertani (LB) broth or agar. The media used for *T. thermophila* cultivation was either super-nutrient-rich medium (1% SSP [1% proteose peptone, 0.1% yeast extract, 0.2% dextrose, 75 μM Fe EDTA]) for growth experiments involving direct TiO_2 exposure or starvation medium (Dryl's medium [2 mM sodium citrate, 2 mM $NaH_2PO_4 \cdot H_2O$, 1 mM Na_2HPO_4, 1.5 mM $CaCl_2$, pH 7.4) for trophic-transfer experiments.

The nanomaterial was dry powder industrial P25 Aeroxide TiO_2 (Evonik, Parsippany, NJ) (75% anatase and 25% rutile) (Ohno *et al.*, 2001) which was stored in the dark at room temperature prior to usage. As described by Horst *et al.* (2010), the industrial TiO_2 used in these experiments is highly heterogeneous, with equivalent

particle diameters ranging from 6.4 to 73.8 nm, where 75% of the particles are between 15 to 60 nm (average diameter, 37.5 nm). The electrophoretic mobility (zeta potential) of this TiO_2 varies with aqueous chemistry (Keller *et al.*, 2010) and in LB medium is -17.9 mV (Horst *et al.*, 2010). All other chemicals were reagent grade or better (Sigma Chemical or Fisher Scientific). Nanopure water (pH 6.9, 18.2 MΩ-cm) was used to prepare media and nanomaterial suspensions.

2.2. Preparation of *P. aeruginosa* and *T. thermophila* inocula. The bacterial inoculum was initially streaked from frozen stock (-80°C, preserved in 70% LB plus 30% [vol/vol] glycerol) onto LB agar and cultivated in the dark (12 h, 30°C). Following incubation, several discrete colonies were dispersed into 4 mL of LB broth to serve as the liquid inoculum.

T. thermophila cells maintained axenically by passaging every three weeks in nutrient medium at room temperature were inoculated into standard (10 cm by 15 mm) sterile plastic petri dishes containing 10 mL SSP and grown in a humidity chamber without shaking (17 h, 30ºC), similarly to before (Werlin *et al.*, 2011). After reaching mid to late exponential phase, the culture was centrifuged (1,470 × g, 40 s). The cell pellet was washed once with Dryl's medium, and cells were resuspended to a concentration of ca. 650,000 cells mL^{-1} in 10 mL Dryl's medium in petri dishes and then starved (17 h, 30°C) in humidity chambers. The starved *T. thermophila* cells were centrifuged, washed in Dryl's medium, and resuspended into either SSP or

Dryl's medium for growth experiments, including trophic-transfer studies (Dryl's medium only).

2.3. *P. aeruginosa* cultivation in liquid medium. *P. aeruginosa* was cultured in LB broth to determine the effects of TiO_2 exposure on growth and the amount of TiO_2 adsorbed to the bacteria; identical *P. aeruginosa* cultivation conditions were used to generate prey for trophic-transfer experiments. Cultivation was performed similarly to before (Horst *et al.*, 2010), i.e., in the dark in 96-well plates (flat-bottomed polystyrene with clear bottom and sides; Corning Incorporated) with 200 μL of LB broth (with or without 0.1 mg TiO_2 mL^{-1}) per well and inoculated with exponential-phase *P. aeruginosa*. For the TiO_2 treatments, dry TiO_2 powder was preweighed, added to sterile LB broth, vortexed (10 min), dispensed into wells, and inoculation with *P. aeruginosa*. As before, TiO_2 handled in this way initially formed large agglomerates that dispersed during *P. aeruginosa* population growth because of the adsorption of TiO_2 onto *P. aeruginosa* surfaces (Horst *et al.*, 2010). Each treatment (including uninoculated controls) was prepared in triplicate. The multiwell plates were incubated (30°C, 200 rpm) in a Synergy HT Multi-Mode microplate reader (Biotek Instruments, Winooski, VT) equipped with a xenon lamp set to measure optical density at 600 nm (OD_{600}) regularly over time.

P. aeruginosa cultures for use in *T. thermophila* feeding (trophic-transfer) experiments were prepared in glass flasks containing 400 mL of LB broth with or

without 0.1 mg TiO_2 mL^{-1} and 25 µL of *P. aeruginosa* inoculum. The flasks were incubated in the dark at 30°C while shaking at 200 rpm until the OD_{600} reached 0.4 (ca. 10 h). The flask contents were dispensed (40-mL aliquots) into 10 50-mL tubes for centrifugation (12,000 × *g*, 10 min), and the supernatants discarded. Each pellet was washed once with Dryl's medium to remove LB medium constituents and resuspended in 20 mL of sterile Dryl's medium. The washed cells for each treatment were combined, and triplicate (60-mL) aliquots from each flask were transferred into separate, sterile glass flasks from which 1 mL was removed for fixation and cell counting. The experiment was repeated identically to provide *P. aeruginosa* cells for imaging by environmental scanning electron microscopy (ESEM). The remaining cell suspensions, which, according to the above steps, consisted of a washed 2× concentration of the harvested culture, were used for *T thermophila* feeding experiments. It was determined, by assessing the initial mass of TiO_2 administered to the *P. aeruginosa* culture versus the TiO_2 observed to be sorbed onto these bacteria (by ESEM; see the IV-supplemental material), that all of the TiO_2 administered was sorbed to the bacteria at the start of the trophic-transfer experiment. Thus, there was no need to separate unbound TiO_2 from bacterially sorbed TiO_2 during culture washing.

2.4. *T. thermophila* growth without *P. aeruginosa* prey. *T. thermophila* cells were cultivated in either SSP or Dryl's medium in the absence of *P. aeruginosa*

prey to determine the effects of direct TiO_2 exposure on *T. thermophila* growth rates and yields. In the control cultures (without TiO_2), starved *T. thermophila* cells were suspended in 12 mL of either Dryl's or SSP medium in petri dishes. Where used, TiO_2 was first sonicated (10 W, 20 min, Branson 8210; Branson, Danbury, CT) and diluted to a final concentration of 0.10 mg mL^{-1} in 12 mL of either Dryl's or SSP medium, and then *T. thermophila* inocula were dispensed into the TiO_2 suspensions. In the control and TiO_2 treatments, the starting culture represented a 100× dilution of starved inocula to 6,500 cells mL^{-1}. Each inoculated culture (i.e. each medium with or without TiO_2) was established in triplicate. Abiotic controls consisted of uninoculated medium, with or without TiO_2. *T. thermophila* cells were cultured in the dark at 30°C in a humidity chamber without agitation. The cultures were sampled over time for cell counting and observation of live-cell characteristics under a dissecting microscope. Cultivation was repeated within 1 day as described above but with enough replicates to allow for sacrificing of entire cultures at 2, 8, 16, and 22 h for use in Nomarski and electron microscopy.

2.5. *T. thermophila* growth with *P. aeruginosa* prey. *T. thermophila* cells were cultured in Dryl's medium with *P. aeruginosa* to determine growth rates and yields when bacterial prey, with or without preadsorbed TiO_2, was the only food source. In the control *T. thermophila* growth experiment, control *P. aeruginosa* cells (cultured without TiO_2 for 10 h) were suspended in Dryl's medium as described

above. Starved *T. thermophila* cells were added to achieve a final density of ca. 6,500 cells mL^{-1} as before (Werlin *et al.*, 2011). The trophic-transfer and control growth experiments were conducted identically, except that *P. aeruginosa* cells used in trophic-transfer studies had presorbed TiO_2. Six individual replicate experiments were prepared—three each for the control and trophic-transfer experiments. All other cultivation conditions and approaches, including additional experimental replication for microscopy, were identical to the procedures used for *T. thermophila* cultured in SSP medium (without *P. aeruginosa*).

2.6. Cell counts by light microcopy. *P. aeruginosa* cells for counting were fixed with glutaraldehyde (2.5%, vol/vol) and stored at 4°C briefly (less than 24 h). Fixed cells were then stained with SYBR gold (Life Technologies, Carlsbad, CA) and counted using epifluorescence microscopy (Nikon E800, ×1,000 total magnification) as described before (Priester *et al.*, 2009).

T. thermophila population growth was assessed for all of the cultures (with or without, *P. aeruginosa* prey or TiO_2) by counting the cells in a 100-µL sample (fixed with 5 µL formaldehyde) periodically (2, 4, 8, 16, and 22 h) using a hemocytometer. Duplicate counts were averaged for each time point. For differential interference contrast (Nomarski) imaging of *T. thermophila* morphology, 1.5 mL of each *T. thermophila* culture was fixed with glutaraldehyde to a final concentration of ~2.5% (vol/vol). An aliquot (50 µL) was imaged at 200× magnification by Nomarski bright-

field microscopy. *T. thermophila* cells were also observed periodically during population growth for overall morphology and swimming behavior (without fixing) with a dissecting microscope.

2.7. Electron microscopy and X-ray microanalysis. Electron microscopy was used to image TiO_2 on *P. aeruginosa* and within *T. thermophila cells*. TiO_2 uptake into *T. thermophila* cells was quantified by digitally analyzing electron micrographs. This, in turn, allowed calculations of TiO_2 bioconcentration and biomagnification.

Imaging by ESEM was used to confirm that TiO_2 was adsorbing to *P. aeruginosa* cell membranes as described before (Horst *et al.*, 2010). The washed bacteria were imaged directly on a carbon-coated aluminum stub with a FEI Co. XL30 field emission gun (FEG) environmental scanning electron microscope (Philips Electron Optics, Eindhoven, The Netherlands) at a 20-kV accelerating voltage with a gaseous secondary electron detector in the wet mode (4 torr) and a 10.3-mm working distance. This method had been independently confirmed previously (by cryoscanning electron microscopy and by dynamic light scattering of *P. aeruginosa* cells) to reliably enable visualizing *P. aeruginosa* cells retaining a tightly adsorbed TiO_2 coating on cellular outer membranes (Horst *et al.*, 2010).

Imaging by scanning transmission electron microscopy (STEM) was used for high magnification observations of *T. thermophila*, including internalized TiO_2. To

prepare *T. thermophila* cells for STEM imaging and analysis, 10 mL of each *T. thermophila* culture was fixed with glutaraldehyde to a final concentration of ~2.5% (vol/vol) and then refrigerated (4°C) until embedding. The 10-mL fixed samples were prepared for embedding by centrifugation (10,000× g, 10 min), followed by three sequential washings with 500 μL nanopure water. The cell pellet was combined with 50 μL of 2% Noble agar and extruded as an agar worm; this was followed by optional staining (1 h) with 2% OsO_4 (Werlin *et al.*, 2011). Both stained and unstained specimens were prepared. The stained and unstained specimens were then sequentially dehydrated with 25%, 50%, 75%, and 2× 100% ethanol at intervals of 15 min. The dehydrated samples were infused with 1:1 ethanol/acetone and 100% acetone at 15-min intervals, followed by a final 8-h infusion of 1:1 acetone/resin at 4°C. The specimen agar worms were transferred into molds with 100% Eponate 12 resin and dried (60°C, 24 h) (Werlin *et al.*, 2011). The samples in resin blocks were sectioned with an ultramicrotome with a 45° Diatome diamond knife. The ultrathin sections (60 nm) were deposited on Formvar-coated 200-mesh copper grids (Werlin *et al.*, 2011). Imaging was performed using a FEI XL30 FEG environmental scanning electron microscope (Philips Electron Optics, Eindhoven, The Netherlands) at 30-kV accelerating voltage with a STEM detector in high-vacuum mode and at an ~6.7-mm working distance. All images were dark field with minimal digital postprocessing.

ESEM was also used to evaluate TiO_2 distribution within the *T. thermophila* cultured in trophic-transfer experiments. Selective embedded samples were thick sectioned (5 μm) and deposited onto sticky carbon dots (Ted Pella, Redding, CA)

adhering to 100% silicon slides (1 by 1 cm; Electron Microscopy Sciences, Hatfield, PA) (Kirk *et al.*, 2009). The thick sections were imaged by ESEM (as described above) in the wet mode (4 torr) and at a 10.3-mm working distance at a 20-kV accelerating voltage with a backscattering secondary electron detector.

To confirm the presence and location of elemental titanium (Ti) in thick sections, energy dispersive X-ray spectroscopy (EDS) of selected areas of either 1-μm^2 (ESEM) or 100 nm^2 (STEM, data not included) areas was performed with an X-ray spectrometer (15 s at 25.6 μS) with a sapphire Super Ultra-Thin Window (EDAX, Inc.) on an FEI Nano600 FEG microscope (Werlin *et al.*, 2011). Genesis analytical software (EDAX, Inc.) was used in conventional atomic number, absorption, and fluorescence (ZAF) correction mode to analyze the spectra (Werlin *et al.*, 2011), i.e., to obtain atomic mass percentages for titanium along with additional elements (C, O, Si, P, S, Cl, K, Ca) (Douglas *et al.*, 2008).

2.8. X-ray microscopy. X-ray microscopy was used to visualize the TiO_2 metal (Ti) distribution in *T. thermophila* cells. A resin-embedded thick section (50 μm) of *T. thermophila* cells (harvested after 22 h of growth on TiO_2-encrusted *P. aeruginosa*) was mounted to a thin wire for imaging using an Xradia UltraXRM-L200 3-D (Xradia, Inc., Pleasanton, CA) microscope with a quasimonochromatic operating photon energy of 8 keV, configured with a 65-μm isotropic field of view at a 150-nm spatial resolution (Priester *et al.*, 2012). The Zernike phase-contrast imaging mode

was used to enhance the visualization of TiO_2 within *T. thermophila* food vacuoles (Tkachuk *et al.*, 2007). A tomography series was created from transmission X-ray images collected at 0.2º steps across a 180º rotation range with a 4-min integration time per image. The Xradia XMReconstructor software package was used to reconstruct the tomography series into a stack of tomograms corresponding to virtual slices inside the specimen by the filtered back projection reconstruction technique. The Xradia XM3DViewer software assembled these tomograms into various renderings to visualize the area imaged in both planar and three-dimensional (3D) volumetric formats.

2.9. Calculation of TiO_2 mass adsorbed to *P. aeruginosa*. The mass of TiO_2 adsorbed to *P. aeruginosa* cells was calculated by assuming, and then confirming via ESEM images, that all of the TiO_2 administered became adsorbed to *P. aeruginosa* bacterial cells during growth. The mass of TiO_2 per *P. aeruginosa* cell was divided by the calculated cell volume and the dry cell mass to estimate the volume- and mass-based concentrations of TiO_2 delivered with prey cells during *T. thermophila* predation of TiO_2-encrusted *P. aeruginosa* (see the IV-supplemental material). The volumetric concentration of TiO_2 on *P. aeruginosa* was used to calculate the biomagnification factor (BMF) associated with TiO_2 trophic transfer from *P. aeruginosa* into *T. thermophila*. Note that since the TiO_2 nanoparticles administered here greatly exceed the size of typical bacterial cell envelope openings

(Demchick *et al*, 1997) and since TiO_2 thus was only extracellularly adsorbed onto *P. aeruginosa* cells, there was no basis for the calculation of a bioconcentration factor (BCF) for *P. aeruginosa* uptake of TiO_2.

2.10. Quantitative analysis of *T. thermophila* food vacuoles. For *T. thermophila* cells grown either directly with TiO_2 (SSP medium) or with TiO_2-encrusted *P. aeruginosa* (in Dryl's medium), *T. thermophila* food vacuole geometries and the amounts of TiO_2 that accumulated in food vacuoles were measured by quantitative analysis of STEM images. The image measurements, made using the Measurement Tool in Adobe Photoshop, were of the food vacuole diameters and areas and also the areas in the food vacuoles that were TiO_2 dense as evidenced by image brightness. Between three and eight *T. thermophila* cells, and between 9 and 23 food vacuoles were analyzed at each time point. The number of visible food vacuoles per cell varied, as this depended on the plane of the section created when specimens embedded in random orientations were microtomed for STEM imaging. At each time point, the diameter of up to seven randomly selected food vacuoles were measured for each image. Because the food vacuoles appeared to be circular, the area of each was then calculated assuming circular geometry. The areas of the same food vacuoles were then measured directly in Adobe Photoshop with the Area Measurement Tool. The directly measured areas were compared to the calculated areas to determine if the

assumption of circular geometry, and thus spherical geometry for volume calculations, was legitimate.

With the Area Select and Measurement Tools in Photoshop, the area of TiO_2 filling within each of the same food vacuoles was measured as described above after adjusting the image brightness to retain only the bright, electron-dense (TiO_2-enriched) regions of each food vacuole. The total measured bright area was typically irregularly shaped and often consisted of multiple irregular sub-areas. Still, the total measured area was converted to a circular geometry so that a volume could be calculated by assuming spherical geometry. The assumption of spherical geometry is justified by the observation that, in sections of many cells at random angles, food vacuoles always showed a near circular cross section. The equivalent diameter (D_{ti}; see Fig. IV-S1 in the IV-supplemental material) of a circle whose area was equivalent to the measured area, A_{Ti} (Figure IV-S1), was calculated by using the equation of a circle. Relating the equations for a circle and a sphere to one another, the volume of TiO_2 filling was calculated as $V = 4/3\ r\ A_{Ti}$, where radius r equals $D_{Ti} / 2$. The volume calculation thus required the assumption that the TiO_2 in food vacuoles propagated depthwise into and out of the plane of the imaged embedded specimen section. Since this assumption would likely generate an overestimate of TiO_2 in the food vacuoles, calculations of bioconcentration and biomagnification were also likely overestimates. The mass of TiO_2 per food vacuole was also calculated by multiplying the TiO_2 volume for each food vacuole by the TiO_2 density of 3.97 g cm^{-3} (Horst *et al.*, 2010). The mass of TiO_2 per *T. thermophila* cell was estimated by assuming that there were

seven TiO_2-containing food vacuoles (at all sampling points) per cell, on the basis of a 3D X-ray volume rendering (see Movie IV-S1 in the supplemental material; not included in the PhD dissertation). The *T. thermophila* cellular concentration of TiO_2 was then estimated assuming a constant cell volume of 7,042 μm^3, as measured before (Werlin *et al.*, 2011). These measured and calculated variables are summarized in Table IV-S1 and shown as a graphical scheme in Fig. IV-S1 in the supplemental material.

2.11. Bioconcentration and biomagnification calculations. BCFs of TiO_2 in *T. thermophila* cells grown in SSP medium were calculated at 2, 8, 16, and 22 h by dividing the cellular TiO_2 concentration by the TiO_2 concentration in the medium. There were two key assumptions in making the *T. thermophila* BCF calculations. The first was that TiO_2 in *T. thermophila* cells was only within the food vacuoles. This was confirmed by inspection of STEM images and EDS data acquired in *T. thermophila* cytoplasm external to the food vacuoles. The second was that the medium TiO_2 concentration was decreased from the initial concentration by the amount of TiO_2 accumulated in *T. thermophila* population at each time point.

The BMFs at 2, 8, 16, and 22 h for *T. thermophila* cells feeding on TiO_2-encrusted *P. aeruginosa* were calculated by dividing the *T. thermophila* cellular TiO_2 mass concentration by the *P. aeruginosa* cellular TiO_2 mass concentration, where

both cellular mass concentrations were on a dry cell mass basis (Arnot *et al.*, 2006; Luoma and Rainbow 2008).

2.12. Quantitative assessment of TiO_2 within *T. thermophila* populations. The amounts of TiO_2 within whole *T. thermophila* populations at each time point were calculated by combining the *T. thermophila* cell concentrations with the TiO_2 masses in food vacuoles (and therefore *T. thermophila* cells) that were measured by quantitative image analysis. Mass values were calculated at each time point by multiplying the TiO_2 mass per *T. thermophila* cell by the population size (the number of *T. thermophila* cells per milliliter of culture) and by 12 mL (culture volume in *T. thermophila* growth experiments). Percentages were calculated at each time point by dividing the masses by the total TiO_2 administered in the 12 mL of *T. thermophila* culture medium (1.2×10^9 pg for SSP, 2.16×10^9 pg for Dryl's medium plus TiO_2-encrusted *P. aeruginosa*) and then multiplying each fraction by 100.

2.12. Additional data and statistical analyses. Exponential growth rate constants for *P. aeruginosa* and *T. thermophila* cells were calculated from the slopes of the best-fit (by linear regression) lines through log-transformed OD_{600} (*P. aeruginosa*) or cell count (*T. thermophila*) time course data for each replicate in each growth experiment with Microsoft Excel 2010 software. Statistical analyses of the

replicate results were performed with SPSS 12.0.1 (SPSS Inc., Chicago, IL) or Microsoft Excel 2010 software. Means were compared by the Student *t* test or by one-way analysis of variance.

3. RESULTS

3.1. Growth and morphology of *P. aeruginosa*. Planktonic *P. aeruginosa* grew exponentially, with or without TiO_2 (see Fig. IV-S2 in the IV-supplemental material). The specific growth rates averaged 0.97 ± 0.11 h^{-1} and 0.97 ± 0.06 h^{-1} in the control and TiO_2 treatments, respectively; these values did not significantly differ (*t* test, P = 0.50), which indicated that TiO_2 was not growth inhibitory and did not interfere with OD_{600} measurements. ESEM micrographs of *P. aeruginosa* cells cultivated with TiO_2 showed extracellular bright accumulations on the cells, confirming adsorption of electron-dense Ti onto their cell membranes (see Fig. IV-SM3 in the IV-supplemental material).

3.2. *T. thermophila* growth and motility. *T. thermophila* cells grew rapidly in rich (SSP) medium with or without TiO_2 (Fig. IV-1). Exponential growth occurred over 16 h; the associated *T. thermophila* specific growth rate averaged 0.26 ± 0.003 h^{-1} and was the same with or without TiO_2 (P = 0.17). The maximum cell counts (22 h; Fig. IV-1) were approximately 19% lower when TiO_2 was present than

in the control, and the difference was significant (P=0.00). As expected, there was no growth in Dryl's medium in the absence of *P. aeruginosa* as prey, with or without TiO_2 (data not shown).

By staining and direct counting, the initial concentration of *P. aeruginosa* cells in *T. thermophila* trophic-transfer experiments was 3.6×10^9 mL^{-1}. The growth of the *T. thermophila* predator population was exponential over 22 h (Fig. IV-1; see Fig. IV-S4 in the IV-supplemental material), and the associated specific growth rate for protozoans consuming control prey (i.e. no adsorbed TiO_2) averaged 0.14 ± 0.00 h^{-1} (n=3). This specific growth rate was 7% higher than the average specific growth rate of the protozoans eating prey that had preadsorbed TiO_2 (0.13 ± 0.00 h^{-1}, n=3), and the difference between the two treatments was significant (P=0.03). Growth of *T. thermophila* with TiO_2-encrusted *P. aeruginosa* resulted in a 45% reduction in the 22-h protozoan cell count compared to that of *T. thermophila* with control *P. aeruginosa* (P=0.00; Fig. IV-1). As expected, growth of *T. thermophila* in Dryl's medium when *P. aeruginosa* prey was the exclusive food source was slower than in SSP, with and without TiO_2 (P = 0.00) and by approximately 81% without TiO_2 (P=0.00) and by approximately 89% with TiO_2 (P=0.00) than that in rich (SSP) medium (no bacteria). When considering the initial counts of *P. aeruginosa* prey (4.3×10^{10} cells, i.e., 3.6×10^9 cells mL^{-1} in 12 mL; see the IV-supplemental material) and assuming a yield of 2×10^{-5} *T. thermophila* cells per *P. aeruginosa* cell as described before (Werlin *et al.*, 2011), the maximum expected *T. thermophila* population size was 8.6×10^5 cells per culture or 7.2×10^4 cells mL^{-1}. This is a slightly higher *T. thermophila* cell

concentration than that measured in this experiment at 22 h (Fig. IV-1), suggesting that the *T. thermophila* populations in this trophic-transfer experiment were likely in late exponential phase by 22 h.

Light and Nomarski microscopy of control *T. thermophila* cells grown in SSP showed normal, vigorously swimming cells. Observations of the protozoans frown in the trophic-transfer experiments with *P. aeruginosa* showed physically normal *T. thermophila* cells swimming comparatively slower than cells growing in SSP. The swimming characteristics, grazing behavior, and physical appearance of *T. thermophila* cells remained similar throughout the 22 h experiment in all of the treatments. Thus, no obvious signs of TiO2-induced morbidity of *T. thermophila* cells were observed under light microscopy in any of the treatments.

3.3. *T. thermophila* uptake of TiO_2 from rich medium. For *T. thermophila* grown in SSP medium with TiO_2, the bright white spots in the unstained specimen STEM images show the presence of TiO_2 in food vacuoles at all of the time points, although there are temporal variations in TiO_2 accumulation (Fig. IV-2). The 2- and 8-h samples showed abundant TiO_2 accumulations in food vacuoles (see Fig. IV-S5 in the supplemental material). The 16- and 22-h samples showed smaller amounts of TiO_2 in food vacuoles (Fig. IV-2e and g). These trends are supported by the data obtained via quantitative image analysis (Fig. IV-3a; Table IV-S2 in IV-supplemental material). The TiO_2 available for consumption in the medium

surrounding *T. thermophila* cells was apparent at 22 h (upper left corner, Fig. IV-2g) and also at 16 h (not shown). Consistent with the images of food vacuoles over time (Fig. IV-2), the calculated food vacuole volumes increased between 2 and 8 h, decreased at 16 h, and then increased again at 22 h (Fig. IV-3a; see Table IV-S2). The TiO_2 mass per *T. thermophila* cell was highest at 2 h then decreased until 16 to 22 h (Fig. IV-3a, see Table IV-S4). The percent filling of food vacuoles by TiO_2 declined in a similar pattern (Fig. IV-3a). Still, although the overall TiO_2 mass per *T. thermophila* cell declined over time (Fig. IV-3a, see Table IV-S4), the total TiO_2 in the *T. thermophila* population increased over time while the population size grew (Fig. IV-4). The final TiO_2 mass within the entire population was 0.42 mg (Fig. IV-4, top), which was ca. 35% of the total initial TiO_2 mass administered (Figure IV-4, bottom).

3.4. *T. thermophila* uptake of TiO_2 from *P. aeruginosa* prey. STEM images, acquired at 2, 8, 16, and 22 h, of unstained samples of *T. thermophila* grown exclusively by feeding on TiO_2-encrusted *P. aeruginosa* in Dryl's medium showed increasing amounts of TiO_2 in food vacuoles over time (Fig. IV-2). Normal digestion of *P. aeruginosa* cells in *T. thermophila* was indicated by the few observable *P. aeruginosa* cells in food vacuoles. Greater TiO_2 amounts, with still fewer undigested *P. aeruginosa* cells in food vacuoles were observed at 16 h than at earlier time points (Fig. IV-2f). ESEM imaging showed TiO_2 bound to *P. aeruginosa* cell membranes

within a *T. thermophila* food vacuole at 16 h (see Fig. IV-S6 in the IV-supplemental material); control (i.e. not TiO_2 exposed) treatments did not exhibit this brightness (not shown). The EDS spectrum (see Fig. IV-S6) confirmed the presence of titanium. At 22 h, most food vacuoles appeared to be filled with TiO_2, and there were very few undigested *P. aeruginosa* cells (Fig. IV-2h). The X-ray microscopy images of a thick section of a *T. thermophila* cell cultured to 22 h with TiO_2-encrusted *P. aeruginosa* cells as prey show, consistent with the STEM image (Fig. IV-2h), food vacuoles filled with TiO_2 mainly near the oral apparatus (see Fig. IV-S7 and Movie IV-S1 in the supplemental material). Nomarski images at 22 h also show numerous dark food vacuoles, illustrating that they contained TiO_2 (see Fig. IV-S8).

The volume fraction of $nTiO_2$ in food vacuoles varied with time when *T. thermophila* grown in SSP with TiO_2 was compared with *T. thermophila* grown with TiO_2-encrusted *P. aeruginosa* (Fig. IV-3). Initially (2 h), the food vacuoles of *T. thermophila* that were fed TiO_2-encrusted *P. aeruginosa* contained little TiO_2 (Fig. IV-3b; see Table IV-S3). Over time, however, the amount increased (Fig. IV-3b; see Table IV-S3). Essentially, the food vacuoles-filling patterns were reversed for *T. thermophila* grown in TiO_2-amended SSP and *T. thermophila* grown with TiO_2-encrusted *P. aeruginosa* (Fig. IV-3; see Tables IV-S2 versus IV-S3).

The average FV volume decreased rather consistently between 2 and 22 h for *T. thermophila* cells feeding exclusively on TiO_2-encrusted *P. aeruginosa* (Fig. IV-3b; see Table IV-S3), while the volume percent of food vacuoles filled with TiO_2

increased (Fig. IV-3b). The calculated mass of TiO_2 per *T. thermophila* cell increased between 2 and 16 h for *T. thermophila* feeding on TiO_2-encrusted *P. aeruginosa* but then dropped at 22 h to less than half of the 16 h value (Fig. IV-3b; see Table IV-S5). Although *T. thermophila* population growth still appeared to be exponential between 16 and 22 h (Fig. IV-1; see Fig. IV-S4), the total TiO_2 in this predatory *T. thermophila* population peaked at 16 h and was 0.06 mg at 22 h (Fig. IV-4, top). This final mass of TiO_2 in the *T. thermophila* population represented less than 3% of the starting TiO_2 mass associated with *P. aeruginosa*-encrusted cells (Fig. IV-4, bottom).

3.5. Quantitative assessment of TiO_2 bioconcentration and biomagnification. The mass of TiO_2 adsorbed per *P. aeruginosa* cell was determined to be 0.06 pg (see Section IV-1.2 of IV-supplemental material). On a dry cell mass basis and on a cell volume basis, this is equivalent to 0.33 pg TiO_2/pg of TiO_2-encrusted dry *P. aeruginosa* cells and 0.00015 mg TiO_2 mL^{-1} of *P. aeruginosa* cells, respectively. All of the TiO_2 administered in the trophic-transfer growth medium was adsorbed to *P. aeruginosa* cells (see the IV-supplemental material).

For *T. thermophila* grown in rich medium with TiO_2, the cellular mass concentration of TiO_2 (Fig. IV-3; see Table IV-S4) declined from 2 to 22 h. During the growth time course, the cellular TiO_2 made up 5% or less of the *T. thermophila* cell mass (see Table IV-S4). The *T. thermophila* BCFs, calculated by dividing the *T. thermophila* cellular TiO_2 mass concentration by the initial SSP medium TiO_2

concentration were 142, 78, 40, and 98 at 2, 8, 16, and 22 h, respectively (see Table IV-S4). By these BCFs, TiO_2 bioconcentrated in *T. thermophila* cells apparently only in the food vacuoles (Fig. IV-2) and not in the growth medium. However, its bioconcentration varied over time (see Table IV-S4), as evidenced by the initially TiO_2-enriched then TiO_2-depleted and enriched-again food vacuoles over time (Fig. IV-2 and IV-3a; see Table IV-S2).

In *T. thermophila* grown by predation of TiO_2-encrusted *P. aeruginosa*, the *T. thermophila* cellular mass concentration of TiO_2 (Fig. IV-3b; see Table IV-S5) increased from 2 and 8 h to 16 h and then decreased at 22 h. In the 2- to 22-h growth period, the TiO_2 mass per *T. thermophila* cell was up to 5% of the *T. thermophila* mass (see Table IV-S5). When taking into account the cellular concentration of TiO_2 on TiO_2-encrusted *P. aeruginosa* prey (0.06 pg of TiO_2/pg TiO_2-encrused *P. aeruginosa* cells; see the IV-supplemental material), the BMF was much less than 1, i.e., with a low of 0.003 at 2 h and a high of 0.16 at 16 h (see Table IV-S5). Thus, TiO_2 was far more concentrated on *P. aeruginosa* cells than in *T. thermophila* cells. The low BMFs are partly explained by the volumetric dilution of initially bacterially associated TiO_2 into much larger protozoan cells (i.e., 7,042 μm^3 for *T. thermophila*, versus 0.4 μm^3 for a bare *P. aeruginosa* cell; see Section IV-S1.3 of the IV-supplemental material) and also by the observation that TiO_2 stayed within food vacuoles and was not distributed into the *T. thermophila* cytoplasm (Fig. IV-2). The localization of ingested TiO_2 to food vacuoles within *T. thermophila* also limited biomagnification, as food vacuoles ultimately excrete their contents into the medium.

Assuming that the yield of *T. thermophila* from predation upon control *P. aeruginosa* was ca. 2 x 10^{-5} protozoans per *P. aeruginosa* cell, as described before (Werlin *et al.*, 2011), the maximum potential mass of TiO_2 in the *T. thermophila* population would be (1.95 x 10^5 *T. thermophila* cells) × (2 x 10^5 *P. aeruginosa* cells / *T. thermophila* cell) x (0.06 pg of TiO_2/*P. aeruginosa* cell) = 0.23 x 10^{10} pg or 2.33 mg TiO_2. This maximum potential TiO_2 mass delivered into the *T. thermophila* population after 22 h of predation of TiO_2-encrusted *P. aeruginosa* is very close to the total TiO_2 initially associated with *P. aeruginosa* in the trophic-transfer experiment (2.6 mg; see Section IV-2 of the IV-supplemental material). Clearly, since a much smaller mass of TiO_2 was in the *T. thermophila* population by 22 h (0.06 mg, Fig. IV-S4), ingestion of TiO_2 via predation of TiO_2-encrusted *P. aeruginosa* had to have been accompanied by extensive TiO_2 excretion from *T. thermophila* food vacuoles. Thus, although food vacuoles were smaller and more TiO_2 filled over time (Fig. IV-3b), which may have contributed to a lower growth rate (Fig. IV-1), TiO_2 biomagnification did not occur in predatory *T. thermophila*, owing to localization of TiO_2 limited to *T. thermophila* food vacuoles, a cellular volumetric dilution effect, and ongoing excretion of TiO_2 back into the medium.

4. DISCUSSION

Given the prevalence and increasing use of nanoscale TiO_2 in consumer goods (Robichaub *et al.*, 2009), it is potentially concerning that nanoscale TiO_2 –a relatively insoluble manufactured nanomaterial—could accumulate in the environment, where microbial processes contributing to nutrient cycling could be impacted. Concentrations of nanoscale titanium were recently reported to be up to 6% in aquatic sediments near the outlet of a major wastewater treatment plant outfall (Luo *et al.*, 2011). In this present study, a model protozoan, *T. thermophila*, was exposed to lower concentrations of TiO_2 via one of two routes: direct ingestion from surrounding aqueous medium or predation of TiO_2-encrusted bacterial prey, in this case, *P. aeruginosa* that had previously been shown to extracellularly adsorb TiO_2 (Horst *et al.* 2010). The results showed that the effects of TiO_2 on *T. thermophila* could vary with exposure route.

Protozoans could be exposed to nanoscale TiO_2 in the environment via either medium or prey, and our results suggest TiO_2 uptake in either case. Protozoans accumulate nutrients by swimming through the water column and grazing along the solid-water interface (Güde *et al.*, 1979), feeding on bacteria, inert materials, and other dead or decaying debris small enough to enter the oral apparatus (Pernthaler *et al.*, 2005; Sherr *et al.*, 2002). Here, TiO_2 was ingested indiscriminately by *T. thermophila*. This was evidenced by observation that the amount of nanomaterial taken up was quantitatively similar to the mass expected on the basis of the numbers

of bacteria in the food vacuoles. For example, an 8-h food vacuole shows around 10 bacterial cells (Fig. IV-2d). This number of cells would have carried approximately 0.6 pg of TiO_2 (10 cells, each with 0.06 pg TiO_2; see Section IV-1 of the IV-supplemental material) into the food vacuole, which is comparatively very close to the average mass of TiO_2 per food vacuole (0.9 pg; see Table IV-S3). This indicates that there was no preferential feeding, e.g., of sparsely versus heavily coated *P. aeruginosa* cells. While there are prior examples of preferential feeding by protozoa, including an acidophilic protozoan that preferentially consumed *Acidithiobacillus ferrooxidans* over *Leptospirillum ferrooxidans* (Johnson *et al.*, 1995; McGinness *et al.*, 1992) and marine protozoa that preferentially grazed on larger allochthonous bacteria even within a larger population of small autochthonous bacteria (Menon *et al.*, 1996), other results are more similar to ours, i.e., showing predator-prey behavior with bacterially sorbed or free-floating particles and no preferential feeding with either inert beads (Boenigk *et al*., 2001) or CdSe ZnS-capped QD nanoparticles (Holbrook *et al.*, 2008).

In a prior study conducted similarly, the trophic transfer of CdSe QDs resulted in significant toxicity to *T. thermophila* at the cellular and population levels, owing to the inherent chemical toxicity of the nanomaterials and the translocation of the QDs past food vacuoles and into the *T. thermophila* cytoplasm (Werlin *et al.*, 2011). In contrast, there were no obvious toxic cellular effects (as indicated by normal *T. thermophila* morphology and motility) of nanoscale TiO_2. Rather, effects were restricted to population growth. While the exact mechanism was not elucidated in this

study, TiO_2 uptake into food vacuoles could displace nutrients and thereby create a nutrient-limiting condition that has an effect at the population scale, i.e., slightly slowing population growth for predatory *T. thermophila* exclusively fed TiO_2-encrusted *P. aeruginosa*. A consequence of this occurrence in nature could be a negative effect on the predator-prey equilibrium, which has inherent ecosystem level implications. This consideration would not have been predicted by the lack of observed toxicity to individual cells.

The potential for nanomaterial uptake into organisms and enhanced transfer of nanomaterials in food chains, i.e., bioaccumulation and biomagnification, is also of interest in the ecotoxicology of nanomaterials (Werlin *et al.,* 2011; Hou *et al.*, 2013). In a prior study, Cd associated with CdSe QDs was biomagnified during trophic transfer from *P. aeruginosa* to *T. thermophila* (Werlin *et al.*, 2011), suggesting that bacteria with their bioconcentrated nanomaterials could initiate biomagnification at the base of food webs. Nanomaterial uptake into bacteria has been demonstrated for gold (Deplanche *et al.*, 2008), silver (Sondi *et al.*, 2004), cerium dioxide (CeO2) (Limbach *et al.*, 2008), and CdSe QDs (Priester *et al.*, 2009), as well as clays and other nanomaterials that tend to aggregate in nature (Lead *et al.*, 1997; Guo *et al.*, 2007). However, here, while *T. thermophila* fed upon TiO_2-encrused *P. aeruginosa* and thereby ingested TiO_2, there was no quantitative biomagnification. In an analogous study of zebrafish that were ingesting TiO_2 either directly or by predation upon TiO_2-contaminated daphnids, the BCFs and BMFs were in the ranges of those reported here (Zhu *et al.*, 2010). In this study, since TiO_2 in *T. thermophila* cells was

confined within food vacuoles, there was little opportunity for nanoscale TiO_2 to be magnified in these protozoans. With other nontoxic nanoscale metals, biomagnification does not occur since the predator-prey interactions facilitate metal recycling. For example, many iron-encrusted microbial communities are continually being grazed on by protozoa (Gillan *et al.*, 2004; Gillan *et al.*, 1997) and the iron is ultimately utilized in protozoan and bacterial processes (Chase *et al.*, 1997; Wilson *et al.*, 1998) as an alternate Fe source that increases productivity and nitrogen uptake in food webs (Kudo *et al.*, 2009; Christaki *et al.*, 2008; Vogel *et al.*, 2009). Protozoa also engulf manganese-encrusted bacteria, which contributes to the geochemical cycling of Mn during normal protozoan bacterial digestion (Zeiner *et al.*, 2006). Bioaccumulated thallium adsorbed to bacteria that are preyed upon by protozoa contributes to geochemical cycling through the oxidation of thermodynamically stable Tl(I) to more abundant Tl(III) (Twining *et al.*, 2003). Here, the rather insoluble (Keller *et al.*, 2010) TiO_2 nanomaterial was ingested and egested, as was the protozoan's food, and thus a greater proportion of the overall TiO_2 in the cultures was within the protozoans as their population size increased. Still, although biomagnification did not occur in our study, TiO_2 uptake was not beneficial to *T. thermophila* and in fact was slightly harmful on the population scale.

The ever-increasing use of manufactured TiO_2 increases the potential for population level impacts on organisms at the lowest trophic levels, which are fundamental to the overall health of ecosystems. Here, TiO_2 adsorbed to *P. aeruginosa* prey, which is a likely common association of manufactured

nanomaterials with bacteria, was ingested along with *P. aeruginosa* during *T. thermophila* predation. In both regimens of TiO_2 intake (trophic transfer and directly via medium) by *T. thermophila*, the main effects were the presence of TiO_2 in the *T. thermophila* population and a reduced population growth rate and yield. An implication is that, by their uptake into and growth effects on microbial food chains, nanomaterials could impact higher trophic levels irrespective of biomagnification.

ACKNOWLEDGEMENTS

This research was funded primarily by the National Science Foundation and the Environmental Protection Agency under Cooperative Agreement Number DBI-0830117. Any opinions, findings, and conclusions or recommendations expressed in this material are ours and do not necessarily reflect the views of either the National Science Foundation or the Environmental Protection Agency. This work has not been subjected to Environmental Protection Agency review, and no official endorsement should be inferred.

ESEM and STEM were partly performed in the Micro-Environmental Imaging and Analysis Facility at the University of California Santa Barbara (www.bren.ucsb.edu/facilities/MEIAF/) under National Science Foundation awards BES-9977772 and DBI-0216480. Funding to E.O. was provided by National Science Foundation award MCB-1025069.

FIGURES

Figure IV-1. Growth curves of *T. thermophila* cultured in rich (SSP) medium without bacterial prey (open symbols, dashed lines) or in Dryl's medium with bacterial prey (closed symbols, solid lines). Triangles (Δ, ▲) and circles (○, ●) represent control (without TiO_2) and treatments with TiO_2, respectively. Each point is the average of three independent replicates. Standard error bars are smaller than the symbols and thus not visible. The inset graph shows the individual replicate growth curves for the six Dryl's medium (with prey) cultures. The symbols in the inset represent the same treatments as in the main graph.

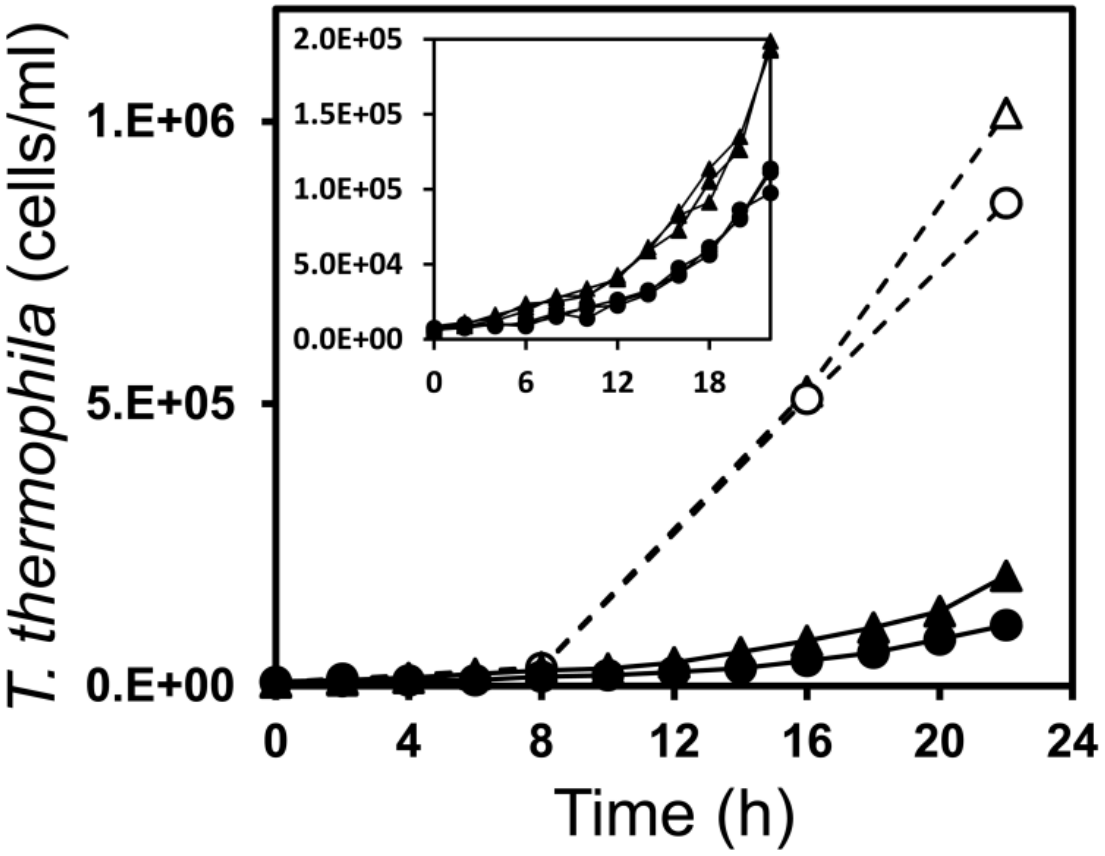

Figure IV-2. Dark-field STEM micrographs of unstained thin sections of *T. thermophila* cells grown in rich medium (SSP) in the presence of TiO_2 (0.1 mg ml/L) without (w/o) bacteria (left column) or in Dryl's medium with (w) TiO_2-encrusted *P. aeruginosa* prey (right column). *T. thermophila* cells are shown after 2 h (a, b), 8 h (c, d), 16 h (e, f), and 22 h (g, h) of growth, where 16 and 22 h were during rapid growth (Fig. IV-1). Food vacuoles (FV) are indicated. The brighter spots are indicative of higher-molecular-weight elements, in this case, Ti associated with TiO_2. Scale bars, 2 μm.

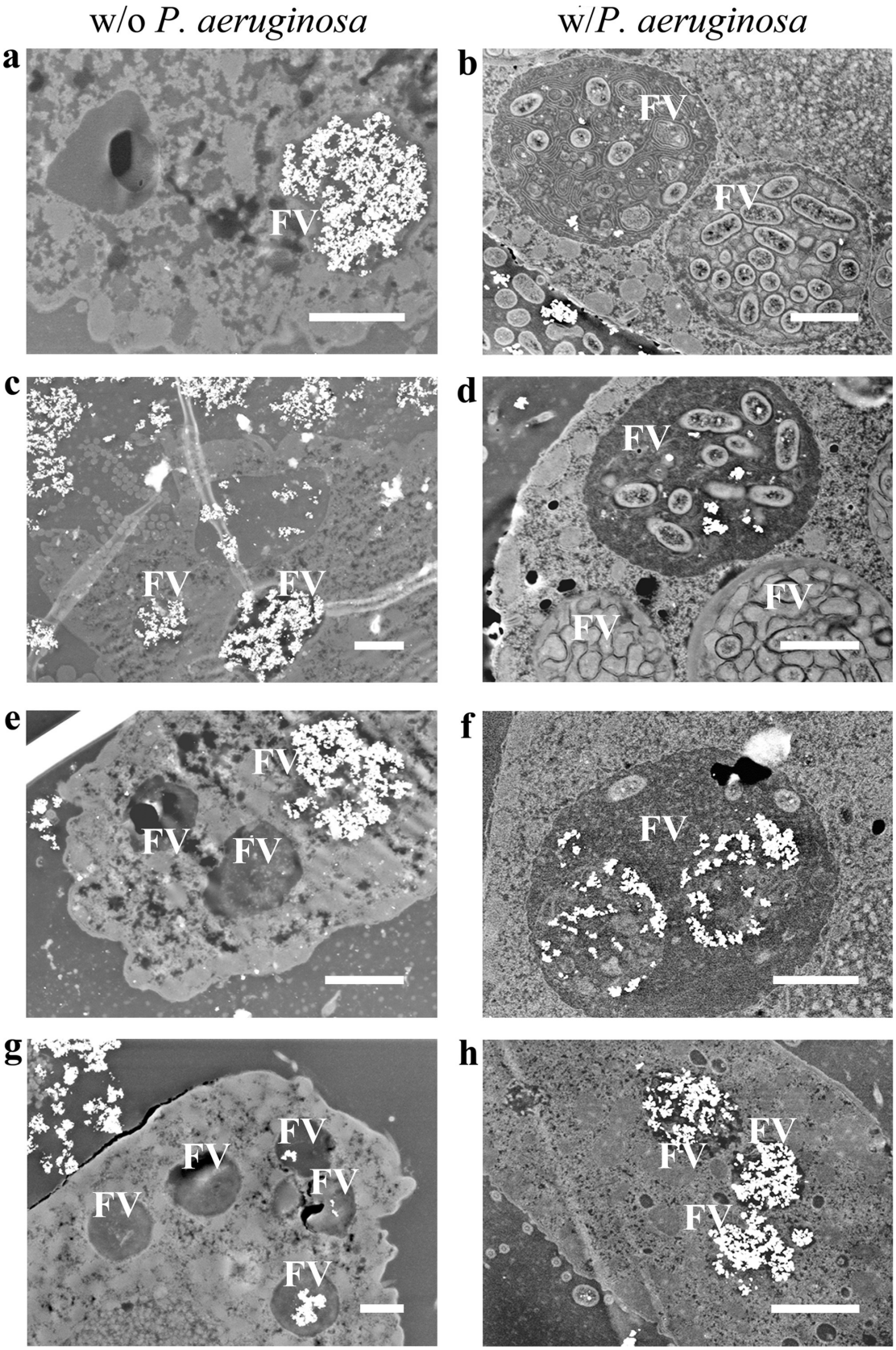
w/o *P. aeruginosa*
w/*P. aeruginosa*
a
b
c
d
e
f
g
h
FV

Figure IV-3. Time course during *T. thermophila* growth (Fig. IV-1) of mean food vacuole (FV) volume (○, dashed lines), measured average percent food vacuole volume filled with TiO2 (◊, dotted lines), and TiO_2 mass per *T. thermophila* cell (●, solid lines). (a) *T. thermophila* grown in rich (SSP) medium with 0.1 mg ml/L TiO_2 but without *P. aeruginosa* bacterial prey. (b) *T. thermophila* grown by feeding exclusively on TiO_2-encrusted *P. aeruginosa* cells. The patterns are consistent with those observed in electron micrographs (Fig. IV-2). The plotted values are tabulated in Tables IV-S2 to IV-S5 in the supplemental material.

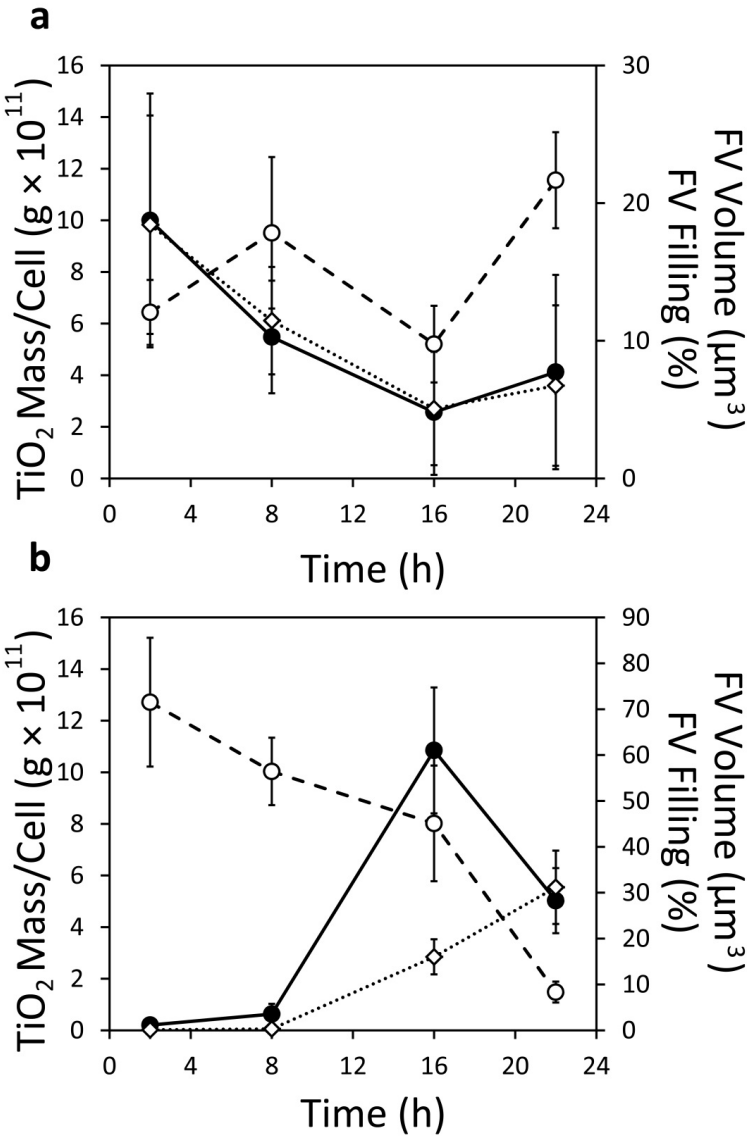

Figure IV-4. Total TiO_2 mass (a) and percentage of total administered TiO_2 (b) within whole *T. thermophila* populations at each time point during growth. Dashed line (○), SSP-grown population; solid line (●), population grown in Dryl's medium with *P. aeruginosa*. Points are average values (n = 3). Error bars are the result of propagating errors according to standard methods.

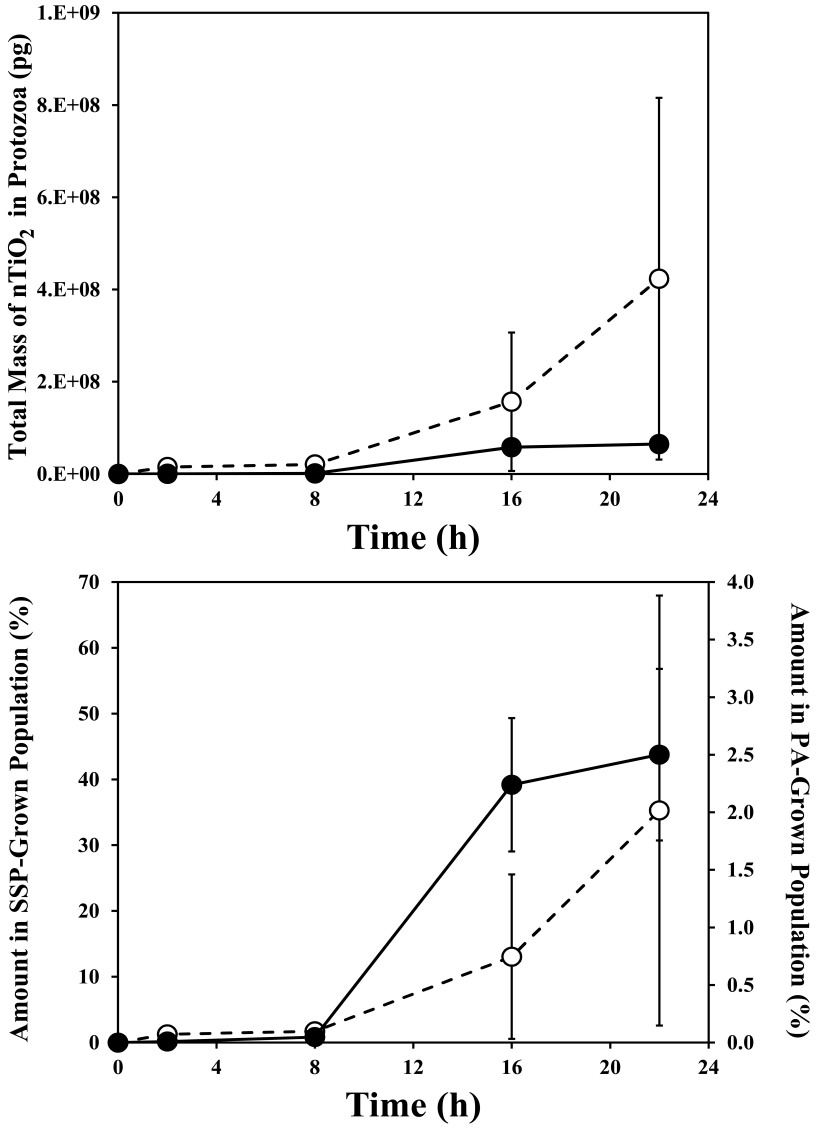

5. SUPPLEMENTAL MATERIAL

5.1. Estimation of the average amount of TiO_2 adsorbed to *P. aeruginosa*.

5.1.1. Background. We previously showed that TiO_2 (P25 Aeroxide, Evonik) sorbs rapidly and extensively to *P. aeruginosa* in LB medium (Horst *et al.*, 2010). In that prior study, environmental scanning electron microscopy (ESEM) images and dynamic light scattering (DLS) measurements of *P. aeruginosa* cell hydrodynamic diameter revealed an increase in apparent "cell size" with TiO_2 adsorption, which encrusts the bacterial cells (Horst *et al.*, 2010). Here, knowing the amount of TiO_2 added to the *P. aeruginosa* culture initially, and the final *P. aeruginosa* cell counts at harvest, the mass of TiO_2 per cell was calculated. This was then used to calculate the concentration of TiO_2 adsorbed to *P. aeruginosa*, since the concentration of TiO_2 delivered with prey was relevant in the trophic transfer experiment in this study. The estimate was then used when calculating the Biomagnification Factor (BMF) for *T. thermophila*, as per the Methods.

5.1.2. Amount nanoscale TiO_2 adsorbed onto *P. aeruginosa* cells, as confirmed by ESEM images. One type of measure (ESEM) was used to confirm that $nTiO_2$ was adsorbed onto cells. Sample ESEM images (Fig. IV-S3) of *P. aeruginosa* cells (harvested at 0.4 OD_{600}, after cultivation at 30 °C, in LB broth amended with 0.1 mg mL^{-1} of nanoscale TiO_2) show cells with patchily-adsorbed

TiO_2. No TiO_2 was observed to have settled in the culture flask, and thus all TiO_2 apparently became fully suspended, wherein it adsorbed to exponential-phase *P. aeruginosa* cells as carefully documented before (Horst *et al.*, 2010). We estimate the average possible amount of TiO_2 per *P. aeruginosa* cell at harvest by dividing the TiO_2 concentration in the growth medium by the *P. aeruginosa* cell concentration at harvest:

$[(0.1 \text{ mg } TiO_2 \text{ mL}^{-1}) / (1.8 \times 10^9 \text{ cells mL}^{-1})] \times (10^9 \text{ pg / mg})$ = **0.06 pg TiO_2 per PA cell**

To assess if this TiO_2 mass per cell reconciles with ESEM images (Figure IV-S3), we calculate the number of particles in 0.06 pg, then considered how this number of particles would be distributed onto a cell surface. First, since the as-synthesized TiO_2 is somewhat heterogeneously-sized (as per the IV-Methods, 75% is between 15 to 60 nm), we assume an average TiO_2 particle diameter of 37.5 nm, or 3.75×10^{-6} cm. Assuming that each particle is spherical, the volume per particle is:

$(4/3) \times (\pi) \times [(3.75 \times 10^{-6}/2)^3] = 2.76 \times 10^{-17} \text{ cm}^3$

As per the IV-Methods, the density of TiO_2 is = 3.97 g/cm^3

Therefore, the mass of one TiO_2 particle = $(3.97 \text{ g/cm}^3) \times (2.76 \times 10^{-17} \text{ cm}^3) = 1.096 \times 10^{-16}$ g

Then, the number of TiO_2 particles per cell is, approximately:

$(1 \text{ particle}/1.096 \times 10^{-16} \text{ g}) \times (0.06 \text{ pg } TiO_2/\text{cell}) \times (1 \text{ g}/10^{12} \text{ pg}) = 547$

Next, to compare this particle number loading per cell to the ESEM images (Figure IV-S3), we first calculate the cell surface area, assuming a cylindrical geometry. Bare (no TiO_2) *P. aeruginosa* dimensions were assumed to be as before: length = 1.4 μm, and diameter = 0.6 μm, using images of *P. aeruginosa* acquired in Werlin *et al.* (2011). The surface area of a cylinder of these dimensions is:

$\{2 \times [\pi \times (0.6/2)^2]\} + [2 \times \pi \times 1.4 \times (0.6/2)] = 3.2 \ \mu m^2$

Then, we project the surface area of 547 individual TiO_2 (37.5 nm or 0.0375 μm diameter, as above) nanoparticles onto this cell surface area, and calculate the expected % cell surface that is covered by the nanoparticles:

projected circular surface area of one 0.0375 μm particle: $\pi \times (0.0375/2)^2 = 0.0011 \ \mu m^2$

The total, for 547 particles, is then: $547 \times 0.0011 = 0.60 \ \mu m^2$

This total projected particle surface area, as a percentage of cell surface area is:

$(0.60 / 3.2) \times 100 = 19\%$

This percentage is within mid-range for a packing density of nanoscale TiO_2 onto abiotic surfaces, according to Yum *et al.* (2005). Given the apparently "open" structure of the sorbed material on cells (Figure IV-S3) which would be expected with a ca. 20% packing density, the assumption that all TiO_2 administered sorbed onto harvested *P. aeruginosa* cells is deemed to be consistent with ESEM observations and thus reasonable.

5.1.3. Volume- and mass-basis concentration of nanoscale TiO_2 per *P. aeruginosa* cell. The volume of a bare *P. aeruginosa* cell is calculated to be 0.40 μm^3, assuming cylindrical geometry and the dimensions above. Dividing the (also above) calculated mass of nanoscale TiO_2 per *P. aeruginosa* cell by this volume per cell yields 0.15 pg μm^{-3} or **1.5×10^{-4} mg mL^{-1}**. As per Werlin *et al.* (2011), the dry mass of bare *P. aeruginosa* is 0.12 pg, under the conditions of growth that are similar to this study. Adding the TiO_2 mass per cell to this dry *P. aeruginosa* cell mass, the mass of a TiO2-encrusted *P. aeruginosa* is 0.18 pg. Dividing the mass above (of estimated TiO_2 per cell) by this estimated mass of TiO_2-encrusted cell yields **0.33 pg TiO_2 per pg dry TiO_2-encrusted PA cell**.

5.2. Mass of TiO_2 delivered with *P. aeruginosa* in the trophic transfer experiment. As per the IV-Methods, the trophic transfer *T. thermophila* growth experiment involved first re-suspending *P. aeruginosa* in 12 mL Dryl's medium to a starting cell density of ca. 3.6×10^9 bacterial cells mL^{-1}. Thus, there were ca. 4.3 ×

10^{10} *P. aeruginosa* cells initially in a *T. thermophila* culture. Assuming the above mass of TiO_2 per *P. aeruginosa* cell (0.06 pg TiO_2 per *P. aeruginosa* cell), then initially 2.6×10^9 pg of TiO_2 is delivered into the trophic transfer experiment. This is equivalent to 2.6 mg, and thus **0.0026 g TiO_2 was delivered per 12 mL culture which rounds out to 0.0002 g mL^{-1}, or 0.2 mg mL^{-1}.** The latter assumes that all TiO_2 delivered with TiO_2-encrusted *P. aeruginosa* cells is distributed evenly throughout the culture, which is not the case as the TiO_2 is tightly adsorbed to *P. aeruginosa* (Horst *et al.*, 2010). Still, this calculation provides an upper bound estimate of the equivalent volumetric concentration of TiO_2 if all of it were available from *P. aeruginosa* during *T. thermophila* growth in the trophic transfer experiment, and also conveys that more TiO_2 was delivered per *T. thermophila* culture during the trophic transfer experiment than during the growth experiment in SSP (rich medium).

SUPPLEMENTAL MATERIALS FIGURES

Table IV-S1. Tabulation of the methods used to measure and calculate characteristics of *T. thermophila*, including food vacuole (FV) sizes, FV filling with TiO_2, and TiO_2 mass and mass concentration per *T. thermophila* cell. The measurement approaches, using quantitative analysis of STEM images, are described in the IV-Methods; results are tabulated in Tables IV-S2 through IV-S5, and described in the main manuscript.

Item	Measured[1]	Calculated[2]	Calculation Notes[3]
1	FV diameter (L)		N/A
2	FV area (L^2)		N/A
3		FV area (L^2)	Diameter (Item 1) is used to calculate FV area, assuming a circular geometry. Items 2 and 3 are then compared statistically to assess agreement between measured, and calculated, areas and thus to test if circular FV geometry assumption holds.
4		FV volume (L^3)	Spherical FV geometry assumed, based on Items 2 and 3 values not being significantly different ($P \geq 0.15$) for FV areas within STEM sections cut at random angles.
5	FV area (L^2) filled by TiO_2 agglomerate		N/A
6		Radius (L) of a circle whose area is equivalent to the measured area of TiO_2 agglomerate in each FV	For each FV, Item 5 value is equated to the area of a circle, A, where $A = \pi r^2$; r (the radius of a circle with area equivalent to Item 5) is calculated from measured A
7		TiO_2 volume in each FV (L^3)	For each FV, Item 6 is used to calculate the volume of a spherical agglomerate, where $V = 4/3\ \pi r^3$.
8		TiO_2 mass in each FV (M)	For each FV, Item 7 multiplied by assumed density of TiO_2 of 3.97×10^{-12} g μm^{-3} (Horst *et al.*, 2010)
9		TiO_2 mass per TT cell (M)	Item 8 is multiplied by the number of TiO_2-containing FVs per cell (assumed to be 7), where the latter quantity was observed in whole *T. thermophila* X-ray micrographs (example in Fig. IV-6, main manuscript, Movie IV-S1, herein).
10		TiO_2 concentration per TT cell ($M\ L^{-3}$)	Divides Item 9 by 7042 μm^3, the volume of a cell measured previously (Werlin *et al.*, 2011).

[1]Measured from replicate STEM images, as per IV-Methods. Generic dimensions are indicated: L = length, L^2 = area

[2]Calculated from Measured values, in some cases using assumptions as stated in the IV-Methods and in the Calculation Notes herein. Generic dimension additionally indicated: M = mass

[3] N/A = not applicable (for Measured characteristics)

Table IV-SM2. Characteristics of individual food vacuoles (FVs) over time, during TT growth in rich medium (SSP) without PA, and with $nTiO_2$. Shown are the total number of FVs measured (across the number of individual TT cells shown), and the means, plus or minus standard error of the mean, of measured and calculated FV characteristics. In the table, "Meas." indicates that the characteristic was measured directly from electron micrographs, as per the Methods. "Calc." indicates that the characteristic was calculated from measurements with stated assumptions herein and as per the Methods. Table IV-SM1 summarizes Measured versus Calculated characteristics.

Time (h)	No. FVs Meas.[a]	No. TT Cells[a]	Meas. Diameter (μm)	Meas. Area (μm^2)	Calc. Area (μm^2)[b]	Calc. Volume (μm^3)[c]	Meas. $nTiO_2$ Area (μm^2)	Calculated Fill Radius (μm)[d]	Calc. $nTiO_2$ Vol. (μm^3)[e]	Calc. $nTiO_2$ mass (pg)[f]
2	11	3	2.72 ± 0.19	6.93 ± 1.11	6.08 ± 0.82	12.06 ± 2.36	2.07 ± 0.87	0.60 ± 0.17	3.6 ± 1.8	14.3 ± 7.0
8	13	4	2.88 ± 0.31	7.77 ± 1.71	7.41 ± 1.51	17.84 ± 5.50	1.49 ± 0.48	0.55 ± 0.12	2.0 ± 0.8	7.8 ± 3.1
16	9	3	2.38 ± 0.30	4.47 ± 1.18	5.04 ± 1.10	9.76 ± 2.78	0.64 ± 0.52	0.27 ± 0.13	0.9 ± 0.9	3.7 ± 3.5
22	13	3	3.32 ± 0.21	7.66 ± 0.74	9.03 ± 1.03	21.66 ± 3.49	0.80 ± 0.63	0.27 ± 0.12	1.5 ± 1.4	5.9 ± 5.4

[a] As per the Methods.

[b] As per the Methods, the Calc. Area assumed circular FVs cross-sections, and used the Meas. Diameter to test the assumption of circularity. Meas. and Calc. areas did not significantly differ (T – test; all $P \geq 0.15$) at each time point, indicating that, together with the near circularity of observed cross-sections of FVs sectioned at random angles, the food vacuoles could be approximated as spheres, and that the measured diameters are suitable for calculating the volume.

[c] As per the Methods, the Calc. Volume assumed spherical geometry, and used the Meas. Diameter in the calculation.

[d] As per the Methods, the Meas. $nTiO_2$ Area was the total area of $nTiO_2$ measured, using the Measurement Tool in Adobe Photoshop, from the STEM images of FVs. The Calculated Fill Radius is the radius of a circle whose area is equivalent to the Meas. $nTiO_2$ Area. This Radius was used to calculate the Calc. $nTiO_2$ Vol. (next column to the right), i.e. the volume of the sphere resulting when that circle with its Radius is propagated into three dimensions. The Calculated Fill Radius is equal to ½ of D_{Ti} in Figure IV-SM1.

[e] As per the Methods, the calculated $nTiO_2$ volume is derived using the Calculated Fill Radius in the equation for the volume of a sphere.

[f] As per the Methods, the Calc. $nTiO_2$ mass in individual FVs is derived by multiplying the Calc. $nTiO_2$ Vol. by the density of $nTiO_2$ which is assumed to be 3.97×10^{-12} g μm^{-3} (Kalyanasundaram *et al.*, 1998; Yum *et al.*, 2005).

Table IV-SM3: Characteristics of individual food vacuoles (FVs) over time, during TT growth in starvation medium with $nTiO_2$-encrusted PA. Shown are the total number of FVs measured (across several individual TT cells), and the means, plus or minus standard error of the mean, of measured and calculated FV characteristics. In the table, "Meas." indicates that the characteristic was measured directly from electron micrographs, as per the Methods. "Calc." indicates that the characteristic was calculated from measurements with stated assumptions herein and as per the Methods. Table IV-SM1 summarizes Measured versus Calculated characteristics.

Time (h)	No. FVs Meas.[a]	No. TT Cells[a]	Meas. Diameter (μm)	Meas. Area (μm^2)	Calc. Area (μm^2)[b]	Calc. Volume (μm^3)[c]	Meas. $nTiO_2$ Area (μm^2)	Calculated Fill Radius (μm)[d]	Calc. $nTiO_2$ Vol. (μm^3)[e]	Calc. $nTiO_2$ mass (pg)[f]
2	18	4	4.76 ± 0.34	22.84 ± 2.73	19.40 ± 2.60	71.52 ± 14.04	0.16 ± 0.05	0.18 ± 0.03	0.1 ± 0.0	0.3 ± 0.2
8	23	8	4.47 ± 0.26	15.21 ± 1.72	16.85 ± 1.66	56.43 ± 7.35	0.30 ± 0.12	0.25 ± 0.04	0.2 ± 0.1	0.9 ± 0.6
16	16	7	4.05 ± 0.31	14.46 ± 2.54	13.99 ± 2.40	45.10 ± 12.61	2.74 ± 0.44	0.88 ± 0.08	3.9 ± 0.9	15.5 ± 3.5
22	10	4	2.35 ± 0.21	5.22 ± 0.89	4.64 ± 0.84	8.33 ± 2.28	1.67 ± 0.30	0.69 ± 0.08	1.8 ± 0.5	7.2 ± 1.8

[a] As per the Methods.

[b] As per the Methods, the Calc. Area assumed circular FVs cross-sections, and used the Meas. Diameter to test the assumption of circularity. Meas. and Calc. areas did not significantly differ (T – test; all $P \geq 0.15$) at each time point, indicating that, together with the near circularity of observed cross-sections of FVs sectioned at random angles, the food vacuoles could be approximated as spheres, and that the measured diameters are suitable for calculating the volume.

[c] As per the Methods, the Calc. Volume assumed spherical geometry, and used the Meas. Diameter in the calculation.

[d] As per the Methods, the Meas. $nTiO_2$ Area was the total area of $nTiO_2$ measured, using the Measurement Tool in Adobe Photoshop, from the STEM images of FVs. The Calculated Fill Radius is the radius of a circle whose area is equivalent to the Meas. $nTiO_2$ Area. This Radius was used to calculate the Calc. $nTiO_2$ Vol. (next column to the right), i.e. the volume of the sphere resulting when that circle with its Radius is propagated into three dimensions. The Calculated Fill Radius is equal to ½ of D_{Ti} in Figure IV-SM1.

[e] As per the Methods, the calculated $nTiO_2$ volume is derived using the Calculated Fill Radius in the equation for the volume of a sphere.

[f] As per the Methods, the Calc. $nTiO_2$ mass in individual FVs is derived by multiplying the Calc. $nTiO_2$ Vol. by the density of $nTiO_2$ which is assumed to be 3.97×10^{-12} g μm^{-3} (Kalyanasundaram *et al.*, 1998; Yum *et al.*, 2005).

Table IV-S4: Calculated values of TiO_2 volume- and mass-based concentrations in *T. thermophila* cells, and calculated values of Bioconcentration Factor (BCF) for the *T. thermophila* growth condition of rich medium with TiO_2.

Time (h)	TiO_2 Mass per *T. thermophila* cell (pg)[a]	Cellular Volumetric TiO_2 Concentration (mg mL^{-1})[b]	Cellular Mass-Based TiO_2 Concentration (pg pg^{-1})[c]	BCF[d]
2	99.94 ± 49.17	14.19 ± 6.98	0.05 ± 0.02	142 ± 70
8	54.80 ± 21.84	7.78 ± 3.10	0.03 ± 0.01	78 ± 31
16	25.66 ± 24.30	3.64 ± 3.45	0.01 ± 0.01	40 ± 38
22	41.22 ± 37.66	5.85 ± 5.35	0.02 ± 0.02	98 ± 89

[a] Calculated by multiplying the values of TiO_2 mass per FV (values in the far right column of Table IV-S1), multiplied by 7 FV per *T. thermophila* cell, where the latter quantity was observed in whole-cell X-ray micrographs (example in Fig. IV-S7, and Movie IV-S1, herein).
[b] Calculated by dividing the TiO_2 mass per *T. thermophila* cell by the previously determined (Werlin *et al.*, 2011) *T. thermophila* cell volume (7042 μm^3).
[c] Calculated by assuming the *T. thermophila* dry cell mass (in the absence of TiO_2) is 1860 pg, as before (Werlin *et al.*, 2011), then adding to this the mass of TiO_2 per cell, then dividing the mass of TiO_2 per cell (2nd column from the left) by this total mass (*T. thermophila* cell plus mass of TiO_2 per *T. thermophila* cell).
[d] Bioconcentration factor (BCF), calculated by dividing the *T. thermophila* Cellular Volumetric TiO_2 Concentration (3rd column from the left) by the TiO_2 concentration in growth medium, which was initially 0.10 mg TiO_2 mL^{-1}. The BCF calculation for each time point accounted for the change in TiO_2 accumulation in *T. thermophila* food vacuoles.

Table IV-S5: Calculated values of TiO_2 volume- and mass-based concentrations in *T. thermophila* cells, and calculated values of Biomagnification Factor (BMF) for the *T. thermophila* growth condition of Dryl's medium with TiO_2-encrusted *P. aeruginosa* as the food source.

Time (h)	TiO_2 Mass per *T. thermophila* cell (pg)[a]	Cellular Volumetric TiO_2 Concentration (mg mL^{-1})[b]	Cellular Mass TiO_2 Concentration (pg pg^{-1})[c]	BMF[d]
2	2.04 ± 1.11	0.29 ± 0.16	0.001 ± 0.001	0.003 ± 0.002
8	6.31 ± 3.98	0.90 ± 0.57	0.003 ± 0.002	0.01 ± 0.02
16	108.48 ± 24.38	15.40 ± 3.46	0.053 ± 0.011	0.16 ± 0.03
22	50.26 ± 12.61	7.14 ± 1.80	0.026 ± 0.006	0.08 ± 0.02

[a] Calculated by multiplying the values of TiO_2 mass per FV (values in the far right column of Table IV-S2), multiplied by 7 FV per *T. thermophila* cell, where the latter quantity was observed in whole-cell X-ray micrographs (example in Fig. IV-7, and Movie IV-S1, herein).
[b] Calculated by dividing the TiO_2 mass per *T. thermophilic* cell by the previously determined (Werlin *et al.*, 2011) *T.* thermophila cell volume (7042 μm^3).
[c] Calculated by assuming that the *T. thermophila* dry cell mass (in the absence of TiO_2) is 1860 pg, as before (Werlin *et al.*, 2011), then adding to this the mass of TiO_2 per cell, then dividing the mass of TiO_2 per cell (2nd column from the left) by this total mass (*T. thermopila* cell plus mass of TiO_2 per *T. thermophila* cell).
[d] Biomagnification factor (BMF), calculated by dividing the *T. thermophila* Cellular Mass-Based TiO_2 Concentration (4th column from the left) by 0.33 pg TiO_2 per pg dry TiO_2-encrusted *P. aeruginosa* cell (as above, this IV-supplemental material, section IV-5.1).

Figure IV-S1. Schematic/flow diagram and sample calculations for the *T. thermophila* trophic transfer experiment. TiO_2-exposed *P. aeruginosa* cells were fed to *T. thermophila* (a), resulting in food vacuole (FV) filling by TiO_2-encrusted bacteria. TiO_2 in FVs was clearly visible in STEM micrographs of *T. thermophila*, and the FV and TiO_2 areas (A_v and A_{Ti}, respectively) were measured for each FV (b). The diameter (D_{Ti}) of a circle, whose area (A_{Ti}) was equivalent to the measured TiO_2 area within the FV, was calculated (c). The calculated diameter D_{Ti} derived from the circular area was then used to calculate the spherical volume ($Vol._{Ti}$) of TiO_2 in the FV (c). The volume percent FV filling was calculated by dividing $Vol._{Ti}$ into the FV volume ($Vol._v$), then multiplying by 100 (d). The mass of TiO_2 contained in each FV (d) was calculated by multiplying $Vol._{Ti}$ by the density of TiO_2 (3.97×10^{-12} g μm^{-3}).

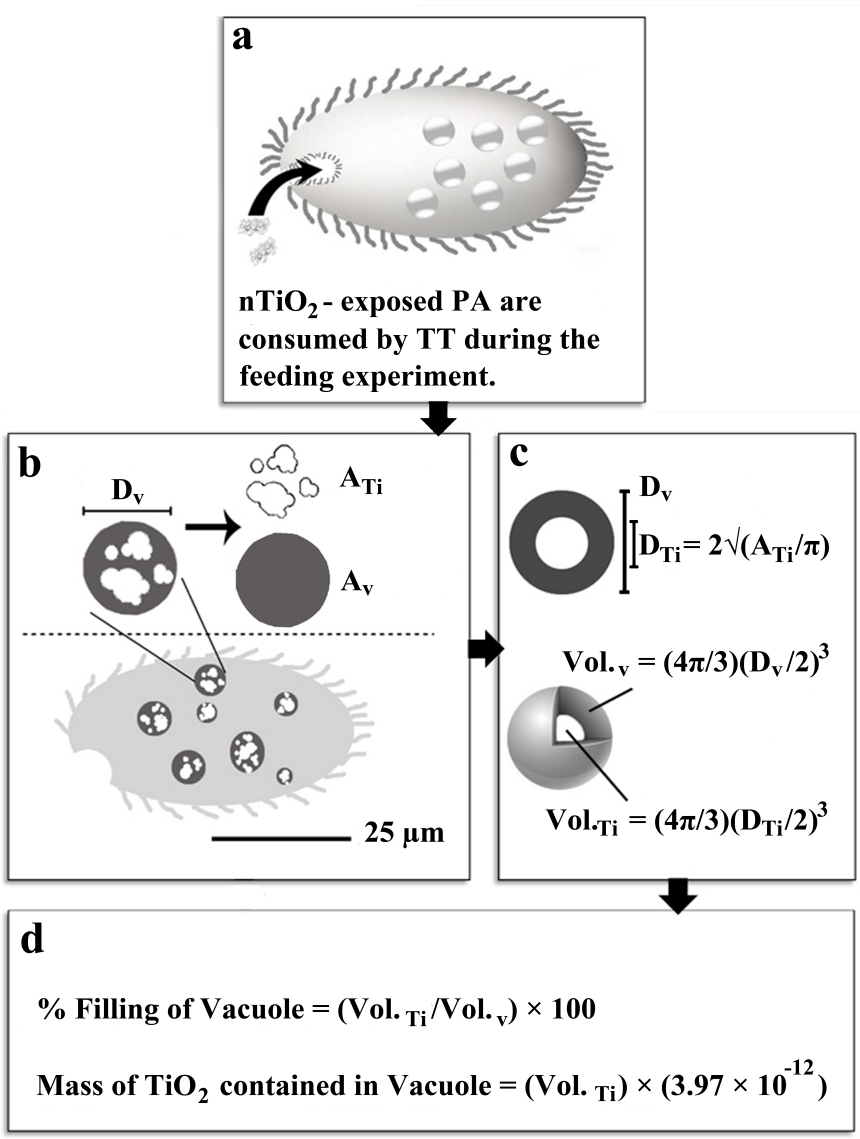

Figure IV-S2. Growth curves for planktonic *P. aeruginosa* in the absence (○) or presence (▲) of nanoscale TiO_2 (0.1 mg ml^{-1}). Mean optical density (OD_{600}; n = 3) is plotted. Error bars represent the standard errors of the means, but are not visible due to their low values.

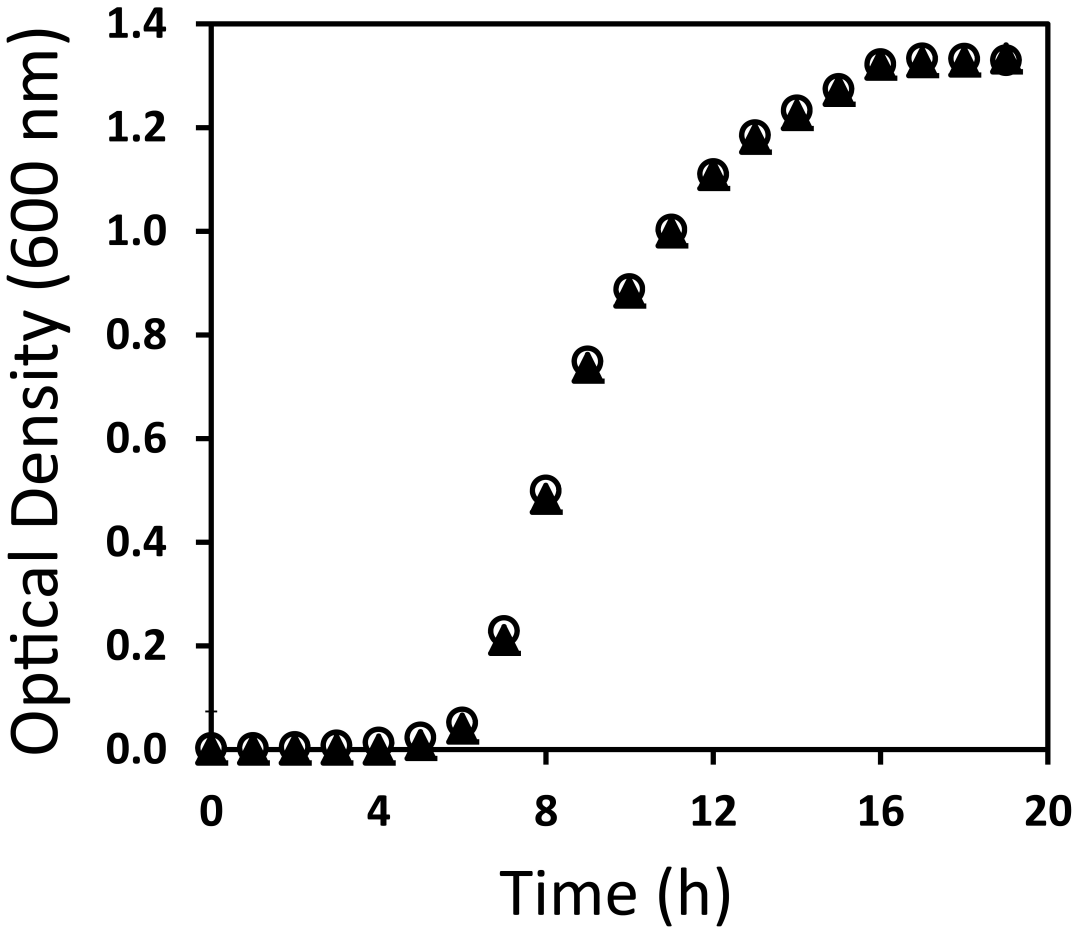

Figure IV-S3. Representative ESEM micrographs of nanoscale TiO_2-encrusted *P. aeruginosa*. Arrows indicate individual cells. The scale bar in each image represents 2 μm.

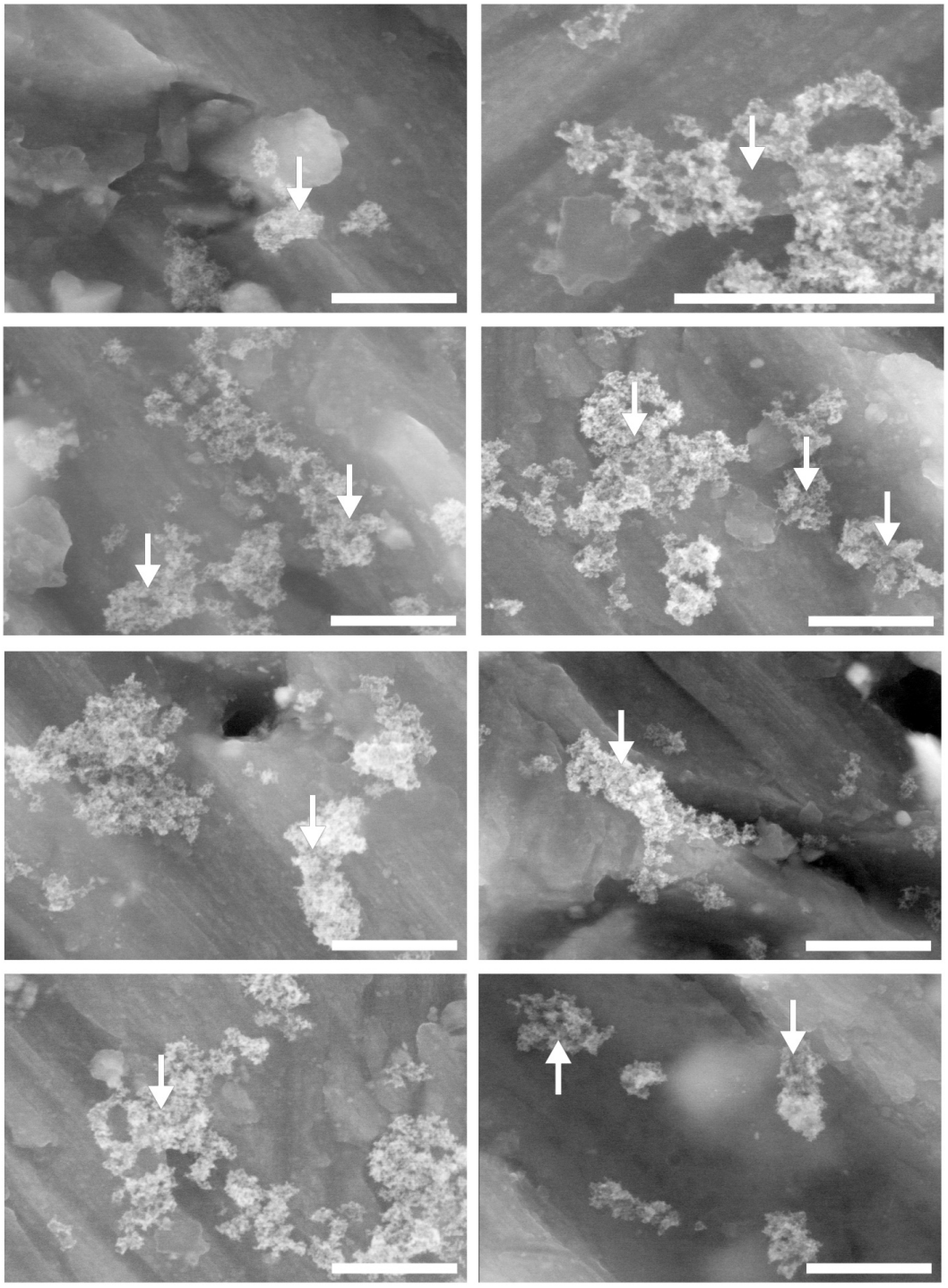

Figure IV-S4. Linearity of natural log-transformed *T. thermophila* cell counts (mL^{-1}) over 22 hours of growth in Dryls' medium with *P. aerginosa* as the exclusive food source. Symbols are as per Figure IV-1 in the main manuscript, where filled triangles are the averaged triplicate measures for the treatment with control *P. aeruginosa* (no TiO_2), and filled circles are the averaged triplicate measures for the treatment w/ TiO_2 pre-adsorbed to *P. aeruginosa* before feeding to *T. thermophila* as prey. Regression lines are calculated from the average data (n=3) at each time point, within each data series. Slopes of the regression lines are the specific growth rates (h^{-1}), as reported in the main manuscript. Error bars are not shown, but the low variation is indicated by overlapping growth curves in the Figure IV-1 inset. Note that, in the calculation of specific growth rates (see main manuscript, IV-Methods) slopes of individual lines of regression from individual replicate growth curves were calculated, then the slopes averaged to compute mean specific growth rate constants.

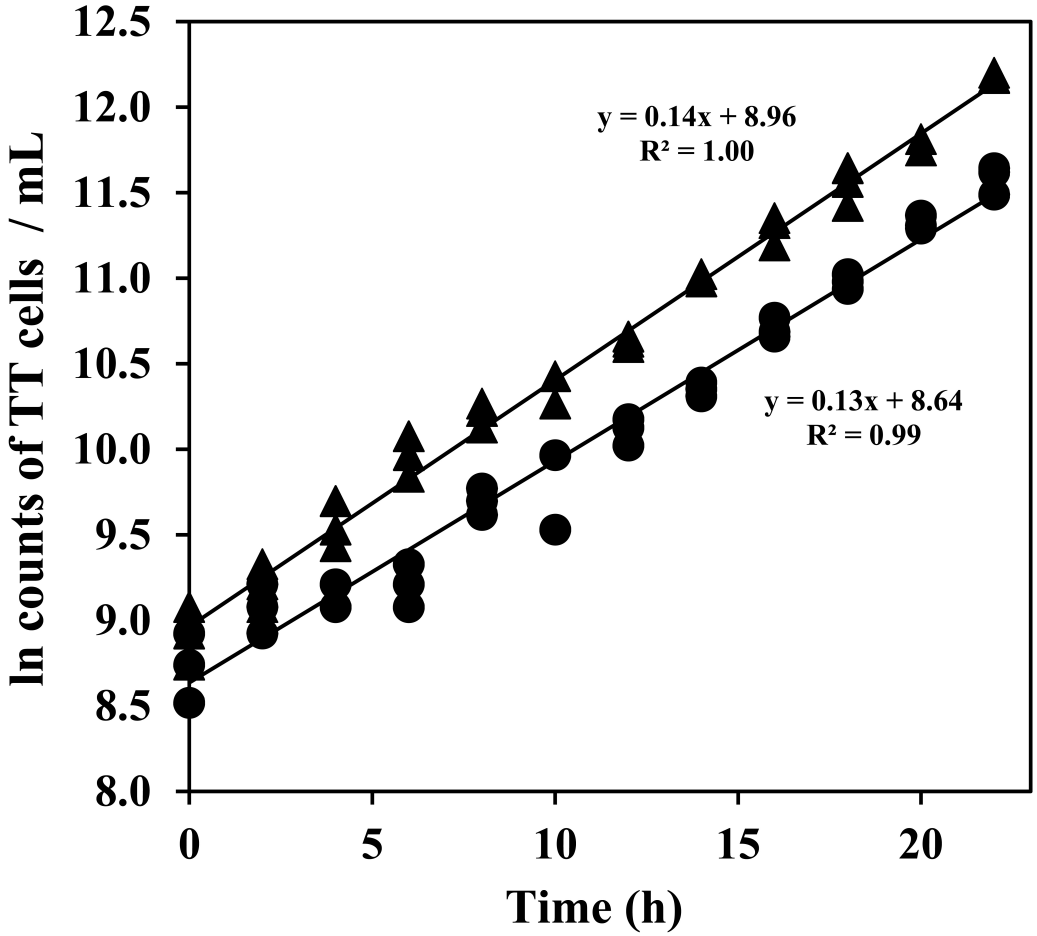

Figure IV-S5. Dark field STEM micrograph of an unstained thin section of embedded *T. thermophila* culture grown in rich (SSP) medium with TiO_2 for 2 h. There are no *T. thermophila* cells in the image, which is expected given the early stage in the population growth (Figure IV-1). Rich medium components are visible as gray microspheres (arrow). The bright spots are TiO_2 agglomerates.

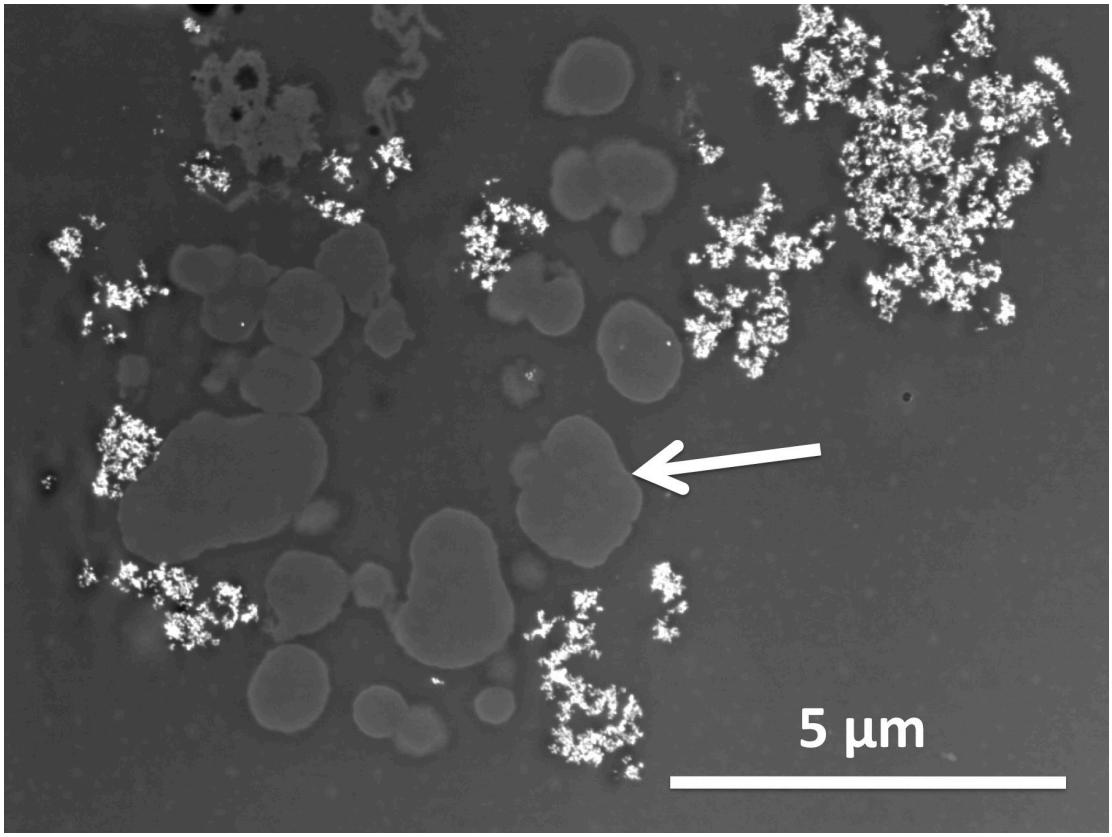

Figure IV-S6. Electron micrograph acquired by backscatter detection (BSD) of a single 16-h *T. thermophila* food vacuole (FV, a), with an associated X-ray microanalysis spectra (b, by energy dispersive spectrometry or EDS). The food vacuole (a) contains *P. aeruginosa* cells that were TiO_2-encrusted when fed as prey for *T. thermophila* growth in minimal (Dryl's) medium (Figure IV-1). The spectrum (b) was collected from one region (white square) shown in (a). The black arrow in (b) is above the Ti peak of the spectrum, confirming the presence of Ti. The brightness of the *P. aeruginosa* cells in the image is atomic weight-dependent, illustrating that these cells are coated with non-agglomerated TiO_2. Agglomerates separate from *P. aeruginosa* cells are evidenced by bright white speckles (bottom right).

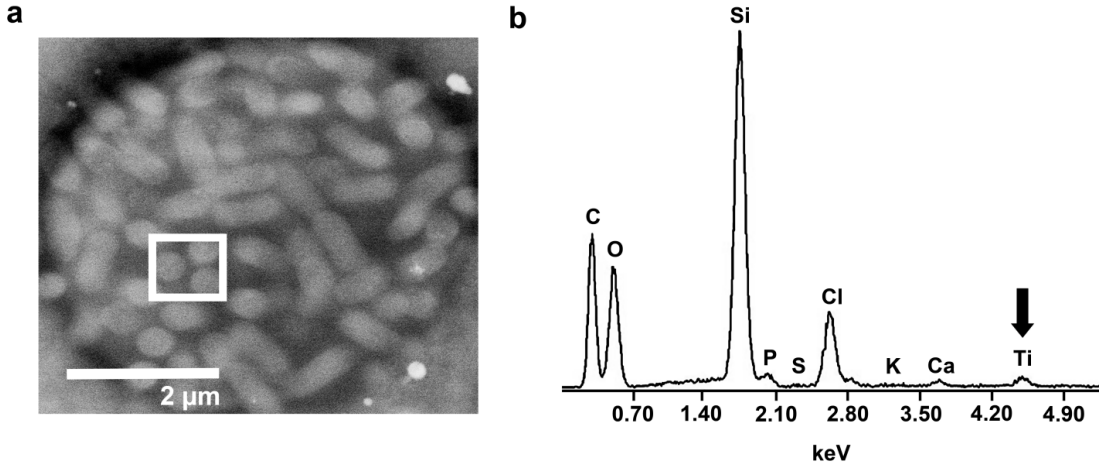

Figure IV-S7. Artificial color X-ray microscope image of a whole *T. thermophila* protozoan cell, harvested from a population grown for 22 h in minimal (Dryl's) medium with TiO_2-encrusted *P. aeruginosa* bacteria as prey. TiO_2 filled food vacuoles (FV) are visible in the anterior region of the cell. The scale bar represents 25 µm. Thin sections of such FVs are shown in high magnification in Figure IV-2h.

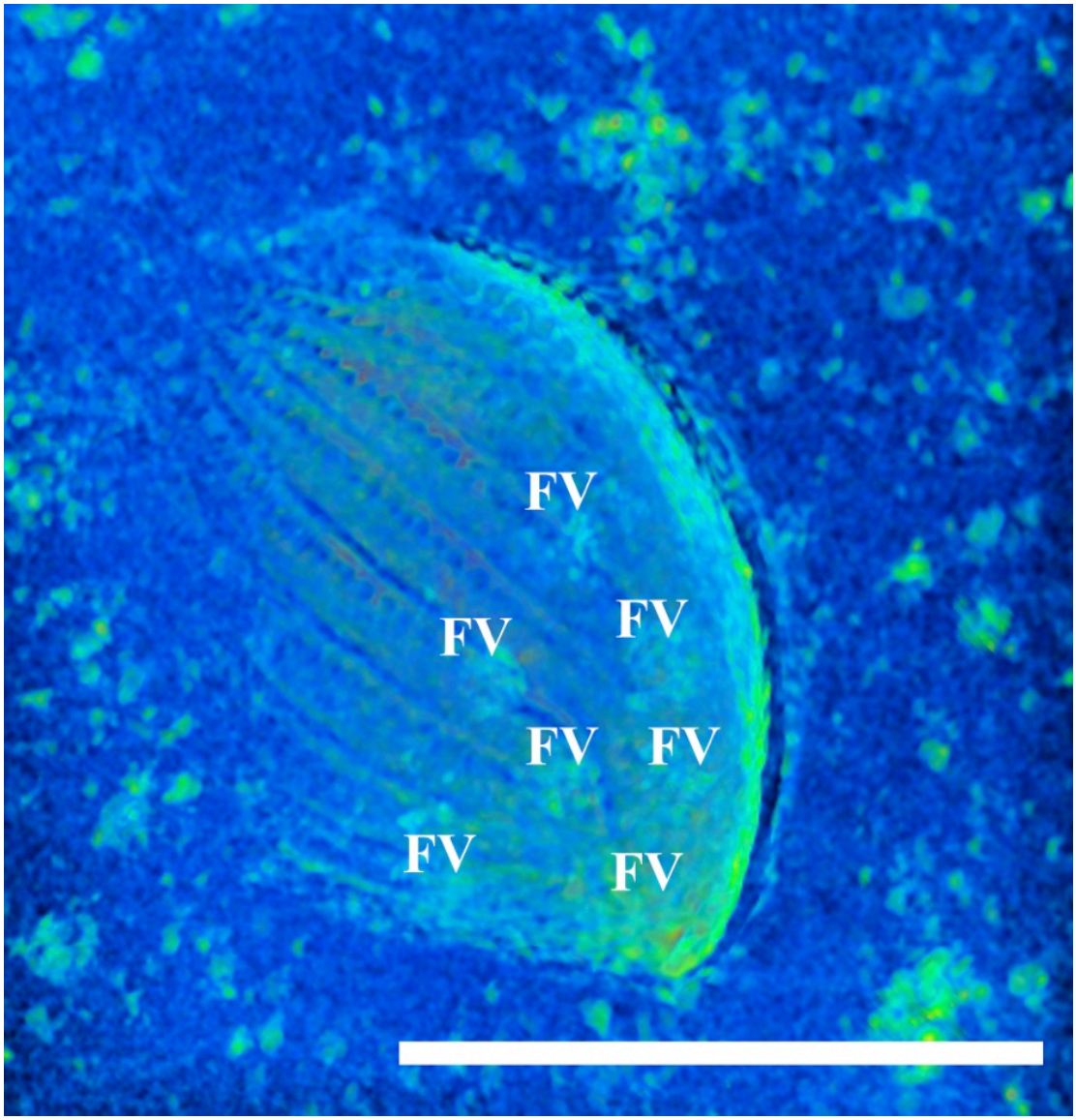

Figure IV-S8. Nomarski images of *T. thermophila* cells cultured in Dryl's medium with TiO_2-encrusted *P. aeruginosa* after 0 h (a) and 22 h (b). Extracellular TiO_2 agglomerates (stars) and *P. aeruginosa* cells (triangles) are visible. The oral apparatus is well outlined in one cell (thin arrow). At 22 h, TiO_2-filled food vacuoles (thick arrows) are also visible (b). *T. thermophila* in these 22-h cultures showed normal motility.

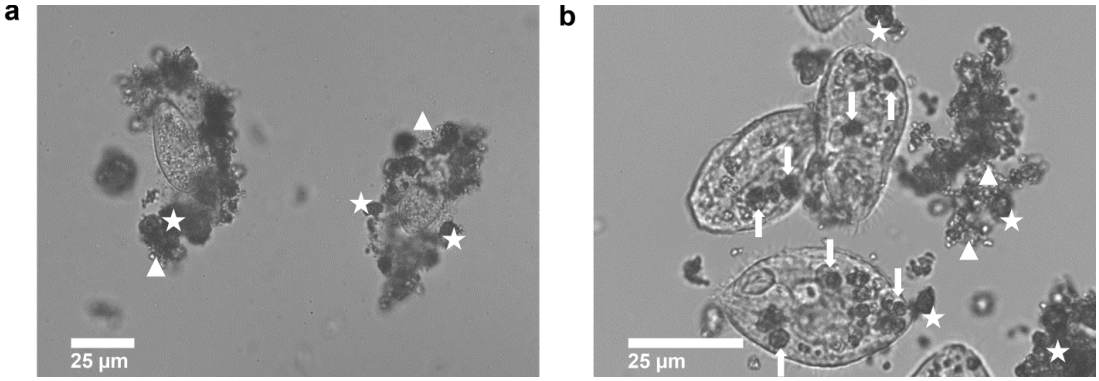

Movie IV-S1.

http://www.bren.ucsb.edu/~holden/AEM_SI_2013_movie/UXRM029_UCSB_Protozoa_TiO2NP_VRT.mpg

3D volume rendering of X-ray microscopy reconstruction of *T. thermophila* grown for 22 hours with TiO_2-encrusted *P. aeruginosa* as prey. This volume rendering is represented by the 2D virtual slice in Figure IV-S7 in this IV-supplemental material.

V. Dark-field Scanning Transmission Electron Microscopy – Energy Dispersive X-ray Spectroscopic (STEM-EDS) analysis of manufactured nanomaterial alterations

ABSTRACT

The potential release of nanomaterials (NMs) from electronic waste is an ongoing threat to water and ecosystems, where the use of cell phones, televisions and other electronic devices is commonplace. The intentional, or unintentional, disposal of electronic wastes may well have dire consequences to current ecosystems. Organismal exposure in the environment to electronic waste is either via direct uptake of NM-sized fragments from water or sediment reservoirs by the release of the dissolved NMs component salts, or via trophic transfer through protozoan bactivory of bacteria with internalized NMs. However, most NM hazard assessments are performed by exposing organisms to neat 'as-synthesized' NMs when in fact, uptake of NMs into the cells results in biological processing that can affect both toxicity, and storage within biota. To reveal the spatial distribution of cell-associated NMs by conventional chemical analytical approaches (i.e. by inductively coupled plasma spectroscopy or ICP) is not possible due to its capability to only quantify total elemental masses. This need for innovative scientific approaches looking at cell-associated NMs is further developed in the following research. Here, the fundamental research is performed by Electron

Microscopy (EM) and Energy Dispersive x-ray Spectroscopy (EDS) to analyze the location and composition of NMs in and on minimally impacted cells.

Dark field - Scanning Transmission Electron Microscopy (STEM) along with EDS was used to evaluate the environmental weathering of NMs, (i) including both cadmium selenide (CdSe), and cadmium telluride (CdTe) quantum dots (QDs), when exposed to an environmental bacteria, *Pseudomonas aeruginosa* (PA). (ii) Chemical experiments exposed PA to Cd^{+2} and SeO_3^{-2} salts to determine the composition of NMs that formed in the PA cytoplasm. (iii) Trophically transferred CdSe QDs, initially internalized by PA, were consumed through bactivory by *Tetrahymena thermophila* (TT) were located throughout the TT organelles.

The PA QD studies showed Se-enriched CdSe QDs present in the cytoplasm, while Te-enriched CdTe QDs were associated with the PA cell wall, and the QDs present in the cytoplasm for CdTe QDs and associated with the cell wall for the CdSe QDs studies had similar elemental composition as the starting QDs, respectively. The NMs observed in the PA cytoplasm, for the salt experiments, have a similar CdSe atomic ratio as the manufactured CdSe QDs. The trophically transferred QDs present in TT organelles were Cd-enriched. STEM-EDS analyses of QDs located in resin-embedded bacteria and protozoa show that the local environmental conditions, along with the journey to reach the final resident location, results in the weathering of the QDs' elemental composition.

1. INTRODUCTION

A study of heavy metal contamination to the environment using nanomaterial imaging and analysis inside targeted bacteria and protozoa. Since the 1950's, research has been conducted regarding the production of electronic devices using cadmium-X (X = sulfur, selenium, tellurium) mineral nanostructures, including CdSe solid-state image storage devices (Nicoll 1958), CdX semiconductors (Eichkorn and Ahlrichs, 1998), CdX television screens (Firth *et al.*, 2004), and CdX thin films for carbon dioxide detection (Patel *et al.*, 2006). These now-aging electronic devices, and the increased consumer demand for CdX devices, have resulted in the potential for CdX nanomaterial (NM) contamination from the improper disposal of electronic waste (Pollmann *et al.*, 2006; Wong *et al.*, 2007).

Electronic waste is comprised of discarded devices having electronic chips, electrical motors, and any devices with illuminating touch screens such as cell phones, televisions (including flat screens), and MP3 players. Such electronic waste is often improperly disposed of at unauthorized sites (i.e. the side of the road or even in normal garbage dumps), where it poses the greatest threat to the environment from weathering, and the subsequent release of toxic heavy metals (Bondarenko *et al.*, 2010) and other persistent organic pollutants (Wong *et al.*, 2007). The heavy metals released into the soil and groundwater due to weathering, could include cadmium, selenium, tellurium, and many other contaminants, which are used in product manufacturing.

The abilities of microorganisms to process (Lies *et al.,* 2005) and form NMs (Bazylinski and Frankel, 2004; Pages *et al.,* 2008) are well established. Cadmium selenide (CdSe) QDs are used in ever-increasing amounts in electronic devices (Pollmann *et al*., 2006; Wong *et al*., 2007) and are known to weather, or chemically degrade, at extreme pHs releasing toxic cadmium ions (Mahendra *et al.*, 2008). The weathering of cadmium ions can only occur on surfaces that are in direct contact with the environmental medium, predominately water, but moist soil also provides the perfect conditions which hasten the degradation of electronic waste. The surface area, as compared to the volume of a NM, becomes larger as the volume gets smaller. The surface area is inversely proportional to the volume leading to the conclusion that as NM weather they will have more intimate interaction with cellular materials that will lead to possible increased biochemical interactions. These interactions will alter the surface atomic composition of NMs that currently can't be monitored with conventional chemical analytical approaches, such as ICP, and protozoan organelle chemical isolation techniques can cause damage to the NM surfaces. There is a great need for the development of an evaluation technique in order to better monitor chemical weathering of NMs. Here, fundamental research is developed to directly reveal the spatial distribution that influences toxicity in the immediate area and give the NM elemental composition. That is key in understanding physical and chemical barriers for future reaction, and also identifying those instances, which have previously occurred, through the use of EM techniques and the EDS analytical approach. Such evaluative techniques could influence the design of new electronic

devices that would weather less severely under environmental conditions, resulting in a decreasing quantity of released toxic chemicals into the environment.

Cleanup of such electronic waste is costly. The cleanup of heavy metal contaminated soils by using bacteria showed remarkable amounts of heavy metal accumulation by *Bacillus* cells isolated from uranium mine tailings (Pollmann *et al*., 2006). Little is currently known about the actual crystalline structure of cell-associated metals, including NM inclusions formed during metal accumulation in bacteria (Schüler & Frankel 1999; Bazylinski & Frankel 2004). The use of metal-accumulating bacteria for cleanup of electronic waste is one application driving the development of better approaches to enable visualization and analyses of 'nano' sized materials within cells at atomic levels.

Bulk analysis by various methods, including inductively coupled plasma mass spectroscopy (ICP-MS), is used to quantify the heavy metals released into solution during QD dissolution experiments (Priester *et al.*, 2009). The weathering products and the dispersed CdSe QDs have been shown to be toxic to PA due to increased cellular levels of Reactive Oxygen Species (ROS) (Cho *et al.*, 2007; Priester *et al.*, 2009; Aruguete *et al.*, 2010; Werlin *et al.*, 2011). The ROS generation produced extensive membrane damage, which was revealed by dark-field Scanning Transmission Electron Microscopy (STEM). Further, simultaneous Energy Dispersive x-ray Spectroscopy (EDS) showed the presence of QDs within the cytoplasm and within protozoan organelles (Priester *et al.*, 2009; Werlin *et al.*, 2011).

The extent of QD weathering in these locations was not fully addressed in the previous research and that has motivated the continued research into developing a STEM-EDS evaluation approach, which could simultaneously resolve the physical location, and elemental composition of weathered QDs in cells. The use of the STEM-EDS evaluation approach will allow researchers to focus on elemental changes to a single QD in order to better understand biochemical impacts within various cellular compartments and also organelle internal environments related to QD atomic composition.

Electron microscopy uses an electron beam to image biological, geological, and chemical samples that are smaller than those which can be imaged with the standard optical light microscope. While Leo Szilárd patented the Electron Microscope (EM) concept in 1931, Julius Ruska designed the first EM (Ruska 1993). The first EM had only 400 times magnification and gave only slightly better resolution than the then typical optical microscopes of the early 1930's. Modern day EMs can reach two million times magnification and are critical tools for use in scientific research and are used within all schools of study. Imaging NMs with EM is a perfect approach for addressing where NMs reside in bacteria, and for identifying which specific organelles NMs are able to penetrate in the higher trophic-level organisms (Priester *et al.*, 2009; Clarke *et al.*, 2010; Werlin *et al.*, 2011). The dark-field STEM-EDS technique that was used for imaging and analysis of the NMs elemental composition has shown that the semiconductor NMs, or QD NMs, were internalized by several bacteria, including *Pseudomonas aeruginosa* (PA), *Bacillus*

subtilus, and *Escherichia coli* (Kloepfer *et al.*, 2005; Dumas *et al.*, 2009; Priester *et al.*, 2009).

Our research uses STEM to investigate the weathering of QDs (CdSe & CdTe) by *Pseudomonas aeruginosa* (PA) during 24 continuous hours of exposure. Imaging by STEM is coincided with EDS analyses that will generate the atomic percentages for single QDs statistically grouped into the selected regions of a specimen. Our STEM-EDS analysis was conducted at low-accelerating voltages to reduce the destruction of embedded biological specimens due to heating from the electron beam, and to minimize excess x-ray signals from multiple electron strikes on a single atom as received at the EDS detector. The reduction of background x-ray noise is critical when analyzing a 100 nm^2-selected area of a 60 nm ultra-thin resin-embedded sample, using the standard preparation for biological specimens with associated NMs (Priester *et al.*, 2009; Clarke *et al.*, 2010; Werlin *et al.*, 2011). Our finding will help to show that low accelerating voltages of this particular STEM-EDS system generates x-ray signals from QDs at varied elemental composition when present in different location within a bacterial cell and protozoan organelles. The unique ability to analyze and interpret atomic composition of QDs will provide a better understanding of the localized environmental weathering of QDs as associated with the bacterial cell wall, QDs that were internalized by bacteria, and the weathering affects QD when located in protozoan organelles.

2. MATERIALS and METHODS

2.1. Strains, media, and nanomaterials. The bacterial strain used was *Pseudomonas aeruginosa* PG201 (PA). This strain was studied previously (Priester *et al.*, 2009; Werlin *et al.*, 2011) and is a Gram-negative organism that can survive in elevated concentrations of heavy metals, making it an ideal organism for use in these experiments. Luria Bertani (LB) broth was used for the culture medium during the initial PA growth and exposure studies. *Tetrahymena thermophila* (TT) SB210E was the bacterivore protozoan strain used in this experiment, as it was before in Werlin *et al.* (2011). The starvation medium (Dryl's buffer: 2 mM sodium citrate, 2 mM $NaH_2PO_4 \bullet H_2O$, 1 mM Na_2HPO_4, 1.5 mM $CaCl_2$, pH 7.4) was used for the exposure in the PA TT trophic-transfer study (Werlin *et al.*, 2011).

The manufactured NMs used in these experiments were Cadmium selenide (CdSe) and Cadmium telluride (CdTe) Quantum Dots (QD). The CdSe QDs were prepared, as described by Rogach *et al.* (2000), which yields fully dispersed red (peak emission of 600 – 650 nm), citrate-stabilized "bare" QDs (mean dia. 5 nm) in water. The CdTe QDs (emission peak 590 nm; diameter 3.5) were prepared, as described by Kloper *et al.* (2007), and synthesized in octadecene, originally stabilized in toluene, and were borate buffer-stabilized until use. Because of the instability of dispersed CdTe QDs, the particles were re-dispersed and rinsed right before their use in an experiment, as described in Dumas *et al.* (2009).

The QD suspensions were stored in the dark at room temperature. Preparation of QDs, before their use in experiments, involved removing excess cadmium ions in solution by dialysis of QDs for 24 h with Spectra/Por 1, flat-width 10-mm membranes (MW cutoff 10,000; Fisher Scientific, Hampton, NH) as before (Priester *et al.*, 2009), against 4 mM sodium citrate for CdSe QDs and 40 mM borate buffer for CdTe QDs. All other chemicals were reagent grade or better (Sigma Chemical or Fisher Scientific). Nanopure water (pH 6.9, 18.2 MΩ-cm) was used throughout the process.

2.2. Preparation of bacterial and protozoan inocula. The preparations of the cells, and the experiments to generate some of the biological specimens were conducted within a prior study (Werlin *et al.*, 2011). The methods are briefly summarized. Bacteria from frozen stock (-80°C) were streaked onto LB agar plates, and 18-hour colonies were dispersed into a LB broth for aerobic cultivation (30°C) to an optical density (OD_{600}) of 1.0. Cells were washed and then re-suspended in either LB broth (for QD weathering and control salt experiments) or in Dryl's buffer (for the trophic-transfer experiment).

Frozen stock protozoan cells were grown to a mid- to late- exponential phase, then washed (Dryl's) and resuspended into Dryl's medium for starvation. After the cells were starved, the cells were centrifuged and washed again with Dryl's medium before a final dilution of protozoan cells, with Dryl's medium used for the trophic transfer studies, as described in Werlin *et al.* (2011).

2.3. Bacterial cultivation in aqueous media with QDs, cadmium, or selenite salts. Bacteria were cultured with QDs over an extended period of time to evaluate the QDs alteration (weathering) that occurred in the bacterial cytoplasm, and to determine where QDs were localized within the bacteria, as previously discussed in Werlin *et al.* (2011). The sample preparation methods are briefly summarized. Additional salt experiments used cadmium acetate (Cd^{+2}) and sodium selenite (SeO_3^{-2}) to evaluate if metal accumulations formed within PA show similar weathering as the manufactured CdSe QDs within those cells, as described above.

Growth was performed in the dark in order to determine the non-photocatalytic effects of QDs on PA cells contaminated with 0.075 mg mL^{-1} total cadmium equivalence of either CdSe QDs (Priester *et al.*, 2009), or CdTe QDs (Dumas *et al.*, 2009). Abiotic control experiments (without bacterial inoculation) were conducted for both QDs. The salt experiments were conducted in 10 mL sterile centrifuge tubes with PA exposed to 0.075 mg mL^{-1} cadmium acetate ($Cd(CH_3CO_2)^2$) (Cd^{+2} equivalence) and 200 mg mL^{-1} sodium selenite (Na_2SeO_3) (Se^{-2} equivalence) in LB broth (7.5 mL) under aerobic conditions (30°C, shaking at 200 rpm) in triplicate (Priester *et al.*, 2009). All experiments were periodically sacrificed (4, 12, 16, 24 h), fixed with glutaraldehyde (~2.5% vol/vol), and immediately refrigerated (4°C) until embedding as described in Priester *et al*. (2009).

For the TT trophic-transfer experiments, PA cells were grown with 0.075 mg mL^{-1} CdSe QDs (Cd^{+2} equivalence) in LB broth in the dark until the optical density (OD_{600}) reached 0.1 as fully described in Werlin *et al.* (2011). The CdSe QD contaminated PA cells were centrifuged, washed once with Dryl's medium, and re-suspended in Dryl's medium for use in trophic-transfer experiments.

2.4. Protozoan growth with QD contaminated bacterial prey. The preparations of cells and the experiments to generate some of the biological specimens were conducted within a prior study (Werlin *et al.*, 2011). The methods are briefly summarized herein. PA cells contaminated with CdSe QDs in Dryl's medium were inoculated with TT cells and incubated in a humidity chamber without agitation. Sampling involved sacrificing replicates at time intervals (4, 12, 16, 24 h), then fixing with glutaraldehyde, and immediately refrigerating until embedding as described in Werlin *et al*. (2011).

2.5. Specimen preparation, and electron microscopy and x-ray microanalysis. STEM was used to image QDs at high magnification when associated with bacteria and inside protozoans, for specimens generated using the resin embedding process previously described (Priester *et al.*, 2009; Clarke *et al.*, 2010; Werlin *et al.*, 2011). The embedding process, STEM imaging, and energy

dispersive x-ray spectroscopic (EDS) methods will be briefly summarized herein. QDs associated with the PA cell wall, in the PA cytoplasm, and QDs accumulated inside various protozoan organelles were analyzed by STEM–EDS. As described below, the EDS-generated atomic ratios for (cadmium: selenium) or (cadmium: tellurium) are used to indicate the QD weathering during the experimental exposure time period.

The glutaraldehyde-fixed samples of PA cells grown with with QDs, cadmium and selenium salts, and the PA prey used during the trophic-transfer study with TT, were initially centrifuged and rinsed with nanopure water to remove the excess glutaraldehyde from the medium surrounding the cells. Washed, fixed samples were extruded into Noble agar worm structures (Kloepfer *et al.*, 2003) as before, to aid in discovering cells during embedded specimen sectioning (Werlin *et al.*, 2011). Sub-samples from each experiment were stained with 2% osmium tetraoxide (OsO_4) (vol/vol H_2O, 4°C, 1 h), rinsed with nanopure water (3x), followed by 2% uranyl acetate (UA) (vol/vol H_2O, 4°C, 1 h) for cellular ultrastructure imaging; unstained sub-samples were reserved for STEM-EDS imaging and analyses. The stained agar worms were rinsed with nanopure water to remove excess stain after the last staining technique in order to insure proper dehydration (25%, 50%, 75%, 2X 100% ethanol) and infusion (50% ethanol: 50% acetone, 100% acetone, 50% acetone: 50% resin) of the Eponate 12 resin throughout the worm. The agar worms were then placed in 100% resin blocks and oven dried at 60°C for 12 h. The resin embedded sample blocks were thin-sectioned using a microtome to generate 60 nm ultra-thin sections

that were deposited onto 200-mesh copper formvar coated TEM grids (Werlin *et al.*, 2011).

Imaging by dark field - STEM was used for high magnification observations of internalized QDs in both PA and TT cells and organelles. An FEI XL30 FEG ESEM (Philips Electron Optics, Eindoven, The Netherlands) at 30 kV accelerating voltage with a STEM detector, under high vacuum mode and a ~6.7 mm working distance was used for imaging. All images were dark field-STEM with minimal post-digital processing.

To confirm the presence and location of elemental cadmium (Cd), selenium (Se), and tellurium (Te) in ultra-thin sections, EDS was performed on selected 100 nm^2 areas at a 100,000 × magnification. The EDS attached to an FEI Nano600 FEG microscope equipped with a STEM detector using a 6.0 nm working distance was as described in Werlin *et al.* (2011). EDS analyses were done on random PA cells and randomly selected QDs located within TT organelles. For each thin section of an experimental sampling time point, a maximum of three EDS analyses per field of view, and a total of 15 EDS analyses per thin section, were performed to insure random selection of EDS sampling locations. The Genesis analytical software (EDAX, Inc.) was used to analyze the EDS spectra (ZAF mode) and to obtain the Cd, Se, and Te percentages, and the analyses also included the elements of Si, P, S, Cl, K, Ca (Douglas *et al.*, 2008).

2.6. Quantitative assessment of theoretical EDS spectral penetration depth for specific minerals.

Scientific understanding from EM images of NM-biological spatial relationships is greatly improved when elemental composition of a single NM is detectable and analyzable using an energy dispersive x-ray spectrometer (EDS). EDS analyzes x-rays generated from the atoms in a specific sample. The x-rays form when an electron is initially dislodged from an atomic shell by an excitation electron, either a primary electron from the EM gun (backscattering x-rays) or a secondary electron source of electrons ping-ponging inside the crystal matrix (secondary x-rays). The electron hole fills with a higher energy level shell electron that releases excess energy in the form of photons of light or x-rays. These x-rays can be counted and analyzed to determine the atomic percentages of selected areas of a sample (Goldstein 2003). The theory as it stands shows that EDS x-rays are generated from teardrop shapes that are correlated to specific depths whose size decreases as the crystalline structure molecular weight increases. This x-ray teardrop depth profile can be as large as millimeters for biological samples and micrometers for minerals with greater molecular weight atoms (Goldstein 2003). The expected x-ray interaction volume can be calculated using the nomogram for x-ray spatial resolution (μm) (Goldstein 2003):

$$\text{Resolution} = 0.231\ (E_0^{3/2} - E_c^{3/2})/\ \rho$$

In the above relationship, E_0 is the accelerating voltage (in keV), E_c is the critical excitation voltage for elements to be analyzed (keV), and ρ is the mean sample

density. For example, when calculating the calcium atom's x-ray-depth profile (E_c=3.690 keV) (JOEL Excitation Tables 2013) we use a biofilm with a volumetric density of 1.065 g cm^{-3} (Peyton 1996) at the accelerating voltages of 30 keV and 100 keV, resulting in calculated x-ray spatial resolution values of (34.1 μm) and (215 μm), respectively. Calculations of the x-ray spatial resolution for CdSe QDs with a density of ρ=5.816 g/cm^{-3} at the accelerating voltages of 30 keV and 100 keV produced calculated x-ray spatial resolution values of (6.5 μm Se; 6.3 μm Cd) and (39.7 μm Se; 39.6 μm Cd), respectively. To determine the analytical area below the incident electron source (Goldstein 2003), we use Castaing's formula (Goldstein 2013):

$$z_m = 0.033\ (E_0^{1.7} - E_c^{1.7})/\ (A\ /\ \rho * Z)$$

In the above relationship, z_m is the calculated penetration distance into the surface of a sample, E_0 is the accelerating voltage (in keV), E_c is the critical excitation voltage for elements to be analyzed (keV), and ρ is the mean sample density. For example, calculating the penetration distance for CdSe QDs with a density of ρ=5.186 g/cm^{-3} at the accelerating voltages of 30 keV and 100 keV, we find calculated penetration distance values of (4.3 μm Se; 4.2 μm Cd) and (33.1 μm Se; 33.3 μm Cd), respectively (JOEL Excitation Tables 2013). Both estimations of depth for the x-ray source by EDS detection are many magnitudes greater than the diameter of a 5 nm CdSe QD, indicating that x-rays from a NM will be generated from x-rays escaping the crystal in direct alignment to the EDS detector window. The physical alignment of

the EDS detector on the FEI Co. Nano600 SEM instrument is at 35° above the plane of the STEM detector in a 45° orientation from y = zero (FEI Build paperwork). The STEM detector is an aluminum constructed box with the STEM detector window located on the bottom surface of the box, making it improbable that x-rays escaping below the TEM grid into the box will ever reach the EDS detector. Given all of the physical limitations described above, understanding the fraction of x-rays reaching the EDS detector window during interpretation of EDS atomic percentages is critical in understanding the exact location of x-ray generation within a single NMs' multiple-shelled or -layered tetrahedral construction.

2.7. Quantitative assessment of EDS spectra to analyze quantum dot weathering. In samples containing bacteria, QDs in three distinct locations were investigated:

1. QDs not associated with cells (either originally internalized by PA but released with cell death or dislodged from PA cell wall during the experimental process),
2. QDs associated with the PA cell wall (outer membrane and cytoplasmic membrane) and,
3. QDs located in the PA interior (cytoplasm).

Each of these sampled regions was analyzed separately.

The following calculations were used to determine the specific number of Cd or Se atoms present in an ideal ~8.5 nm CdSe QD. The innermost core for a CdSe QD could be a $(CdSe)_6$ complex with an exterior first cage or shell with $(CdSe)_{28}$ as described (for Figure 4b in Kasuya *et al.* 2004). Since each additional shell will be generated by the addition of a Cd or Se centered tetrahedral, we can estimate how many shells are present in the ~8.5 nm CdSe crystal.

Table V-1 was generated in Excel using fundamental chemical principles to ultimately determine how many Cd or Se atoms make up each of the 11 shells around the core required to generate an ~8.5 nm CdSe crystal. A brief description of calculation in Table V-1 follows:

1. CdSe core with the 1st shell of (CdSe) has a diameter of (Kasuya *et al.* 2004; Figure 4b):

   = 1.460 nm (Core + 1st shell)

2. 2nd shell consists of CdSe tetrahedral structures ($CdSe_4$ and $SeCd_4$ depending the outer most elemental composition) from all facets: Diameter of CdSe Tetrahedral length is 0.3548 nm extends in all directions (multiplied by 2) (Figure 13 from Rosenthal *et al.*, 2007):

   = 1.45 nm (core + 1st shell) + 2 * 0.3548 nm (CdSe tetra length)

= 2.160 nm (2nd shell diameter)

3. 3rd shell is continuation as described in #2 above:

   = 2.160 nm (2nd shell diameter) + 2 * 0.3548 nm (CdSe tetra length)

   = 2.869 nm (3rd shell diameter)

4. From the diameter of each shell the volume can be calculated:

   Volume = 4/3 * ((π) * ((diameter / 2)^3))) = 1.33 * ((3.14) * ((1.450/2)^3)))

   1st core volume = 1.595 nm^3

5. From the density (ρ) of CdSe QDs of 5.816 g cm^{-3} (5.82 x 10^{-21} g nm^{-3}) the mass of CdSe can be calculated:

   Mass of CdSe = Volume of core * ρ = 1.595 nm^3 * 5.82 x 10^{-21} g nm^{-3}

   1st core mass CdSe = 9.279 x 10^{-21} g of CdSe

6. For every CdSe QD, the applicable bulk analysis shows a ~1: 1 (Cd:Se) ratio of atoms in a single wurzite crystal (Rosenthal *et al.*, 2007). Since the weight percents of Cd and Se are 58.8 and 41.3%, respectively, we can

calculate the mass of Cd and Se atoms present in each shell of a CdSe ideal crystal:

Number of Cd (or Se) = 0.588 * total mass for Cd or 0.413 * total mass Se

Cd mass = 0.588 g Cd/g CdSe * 9.279×10^{-21} g of CdSe

1st core Cd mass = 5.453×10^{-21} g Cd

1st core Se mass = 3.831×10^{-21} g Se

7. Determining the number of CdSe molecules in each shell is by calculating the quotient of the mass of CdSe and the molecular weight to generate moles of CdSe, that can be multiplied by Avogadro's number (6.02×10^{23} molecule/mole):

molecules of CdSe = 1st core mass * mol weight CdSe * Avogadro's #

1st core = 9.279×10^{-21} g of CdSe ÷ 191.27 g/mole = 4.851×10^{-23} mole

4.851×10^{-23} mole * 6.02×10^{23} molecule/mole = 29.2 molecule CdSe

1st core = 29 molecules of CdSe, which is slightly less than what was determined by Kasuya *et al.* (2004) who reported 28 CdSe molecules within the shell and a 6 molecule CdSe core. Kasuya *et al.* (2004) found the crystalline core structure is not in a perfect tetrahedral orientation resulting in an extremely rigid core that is unique to these CdSe crystal structures.

8. From the above approximation of CdSe molecules present in each shell, the theoretical QD will have a definitive number of Cd and Se atoms in each shell and within the interior core structure.

   For example, the largest calculated QD has an ~8.5 nm diameter and consists of a total of 5,981 CdSe molecules, which results in 1,369 molecules of CdSe in the outer shell with a CdSe core of 4,611 molecules (Table V-1).

The next step is to theoretically examine the QD weathering percentages and their relationships to the EDS-generated Cd:Se atomic ratios for biologically-weathering QDs with the diameters equal to calculated shell diameters (Table V-2 & Figure V-1; CdSe QDs ~5 nm dia have 6 shells + core). Limiting weathering of a QD to only the outermost shell atoms would theoretically result in equal amounts of Cd and Se atoms located on the outer-most surface of an ideal QD (Rosenthal *et al.*, 2007). Investigating an ~8.55 nm QD, the 11th shell was calculated to have 1,369 molecules of CdSe with a core of 4,611 molecules of CdSe; when 50% weathering occurs of only Se atoms from the outer shell, 1,369 atoms of Cd and the remaining 684.5 atoms of Se occupy the 11th shell. This produces a Cd:Se atomic ratio of 1,369:684.5 or 2:1 (Table V-2). When x-rays are generated for STEM-EDS from only surface-exposed atoms of the external shell, we could assume at locations of a

weathered Se atom will reveal 1 or 3 Cd atom(s) that were previously tetrahedrally covalently bound to the Se but still considered Cd atoms residing in the exterior shell (Figure V-1).

To determine if the interior core shell atoms' x-rays have influenced the atomic ratio generated from EDS, we theoretically examined the weathering percentage of the 11th shell for an ~8.55 nm CdSe QD and included 100% of the x-ray influence from atoms in the 10th shell (7.84 nm) on the theoretical atomic ratio for Cd: Se generated from EDS analyses (Table V-3 and Figure V-2). The weathering of the surface atoms would produce a Cd: Se atomic ratio of above 2 for the extreme weathering case of 70% of the Se atoms, which were removed. For shell 11, with 1,349 CdSe molecules in the outermost shell and a central core with 4,611 CdSe molecules, and since we have equal numbers of Cd as Se atoms, then there are 1,349 atoms of Cd and 1,369 atoms of Se located in the 11th shell. If there is 70% weathering of the Se atoms there will be 1,369 atoms of Cd and 410 atoms of Se resulting in x-rays being produced in the following ratio:

= 1,369 (shell 11) Cd + 1,142 (shell 10) Cd /

/410 (shell 11; weathered) Se + 1,142 (shell 10) Se

= 2,511 Cd atoms / 1,552 Se atoms = 1.618 Cd:Se

Note that the above is the atomic ratio of 7.84 nm (100%) & 8.55 nm (70%) in circle (Table V-3).

The diagramed CdSe QD shows 11 shells of an ~8.55 nm size QD (not to scale) (Figure V-2). The red shell, in this case shell 6 (5.00 nm QD), illustrates that the EDS x-ray signal is being generated from atoms in shell 6 and the adjacent shell of atoms in green (shell 5, 4.29 nm). This results in a Cd:Se atomic ratio up to only 2.36 with 100% weathering of all Se atoms from the surface. This is an unlikely theoretical model since the experimental EDS analyses produce Cd: Se atomic ratios up to 2.8 and even some of the analyses are above a 4.0 Cd: Se atomic ratio (Table V-3). The CdSe atomic ratio theoretically calculated for x-rays generated from only the outer most shell produce possible atomic ratios as high as 100 Cd: Se (Table V-2). Since the atomic ratios up to 100 are extremely high and the atomic ratios calculated by the first two shells influencing the EDS spectra were too low, then some percentage of the second inner shell must play a critical role in generating the experimental EDS observed in these studies.

Evaluating the percentage of the second shell influence on EDS analysis will be limited to 25% for demonstration (Table V-4 and Figure V-3). For 70% weathering of the outer shell of a ~5.0 nm QD, the theoretical Cd: Se atomic ratio would be 2.46 Cd: Se (core). What is promising about this theoretical model is the ability to reach 4.0 Cd: Se atomic ratios when 80 to 90% weathering has occurred (red zones; 2.0 to 4.0 green zone).

2.8. Additional Data and Statistical Analyses. EDS spectra-generated data sets that include atomic ratios with values above and below 1.0 cannot be included in statistical analysis without the following adjustment of the data sets central datum. The following example will use real data to evaluate the required data adjustment in order to insure that the statistical analysis results are true for this type of data. The first calculations and statistics are completed on unadjusted original two data sets as follows. Two data sets of Cd: Se atomic ratios that include values below 1.0 as decimal numbers, the means and standard error are 1.49(891) ± 0.51(765) (n=50) for whole mounted control CdSe QDs and 1.36(806) ± 0.86(319) (n=40) for QDs in PA cytoplasm (24 h) (Figure V-4; column 1 & 2). The student T-test for whole mounted QDs versus QDs in PA cytoplasm was statistically different (P=0.38). EDS analyses replicates above 1.0 Cd:Se atomic ratio for whole mounted QDs was 41 (n=50) and 22 (n=40) replicated for QDs in PA cytoplasm.

The second step is to adjust the atomic ratio data by correctly accounting for the range of data below 1.0 for same CdSe data sets as above. The atomic ratio values below 1.0 for Cd: Se can be inverted to generate the Se: Cd atomic ratios with values greater than 1.0, but will extend below the 1.0 datum of Cd: Se. The 1.0 datum allows for the visualization of the true range of EDS analyses for CdSe QDs (Figure V-4; column 3 & 4). The range observed for Cd: Se and Se: Cd are extending in opposite directions from the central datum of 1.0. The data is adjusted by changing the central datum to 5.0 to obtain all positive numbers that can be analyzed in order to determine the mean, the standard error, and are evaluated further by student T-Test.

The repositioning of the central datum 1.0 is accomplished by the addition of 4.0 to the Cd: Se data above 1.0, resulting in an adjusted central datum which is then increased to 5.0 (Figure V-4; column 5 where Cd: Se 1.59 is adjusted to 5.59). The original Cd: Se data below 1.0 is inverted, as shown above, to the Se: Cd data before the following calculation can be accomplished. The Se: Cd data is subtracted from 2.0 (Figure V-4; red, where Se: Cd 1.61 is adjusted to a 0.39 value), this produces the value above the old Cd: Se 1.0 datum. The adjusted value is subsequently added to 4.0 so as to reach the new central datum of 5.0 (Figure V-5; green, 0.39 + 4.0 → 4.39), which is located 0.61 above this data. The mean and standard error for the data adjusted to a new central datum of 5, are 5.49(619) ± 0.52(120) (n=50) for whole mounted CdSe QDs and 5.26(397) ± 0.98(246) (n=40) for PA QDs in cytoplasm (24 h) (Figure V-4; column 7 & 8, respectively) and by subtracting the 4.0 from each value you have the real calculated value for Cd: Se atomic ratio 1.49(619) ± 0.52(120) (n=50) and 1.26(397) ± 0.98(246) (n=40) respectively. The student T-test resulted in a greater statistical difference between data sets of P=0.15 for whole mounted QDs versus QDs in PA cytoplasm.

The two data sets were specifically chosen to illustrate that as the number of replicate spanning across the central datum or range below 1.0, they will propagate greater analytical error using conventional analysis, and this clearly illustrates the STEM-EDS atomic ratio generated data requires these few additional mathematical steps to insure accurate and precise analysis of this type of data. Following the datum adjustment, all statistical analyses of the replicate results were performed with

Microsoft Excel 2000 software. The student T-test compared means. Where applicable, standard errors were obtained and propagated according to standard methods (Taylor 1997).

3. RESULTS and INTERPRETATION

3.1. QD weathering by bacteria. The ability to view bacterial cells with associated NMs is limited to electron microscopy techniques that can image through resin embedded specimens, only when ultra-thin sections are used. Thin sections from designated time points during the contamination of bacteria with CdSe QD were sacrificed and fixed immediately during the 24 h growth period (Figure V-5). During the initial 24 h contamination period PA cell wall destruction is evident, as shown in Priester *et al.* (2009). Some of the imaged PA cells show QDs entering the bacterial cells without the destructive results (Figure V-5) observed in other selective bacterial cells (Figure V-6), that showed various degrees of cellular degradation over the 24 h exposure time.

PA cells contaminated with CdSe QDs for 24 h, the cytoplasm appears to be "cleared", progressively from the interior to the plasma membrane structure (Figure V-5), which was not observed in control PA cells (data not shown). The PA cells that had intact cell walls and internalized QDs were analyzed by EDS at a small selected area in order to minimize stray x-rays from the surrounding materials. The STEM-EDS atomic ratios were analyzed from individual EDS spectra generated for CdSe QDs starting material, PA cytoplasm (at locations of bright dots in Figure V-4), PA cell wall (bright dots in Figure V-4), and for locations of bright dots (Figure V-4) not directly associated with PA cells (Figure V-5). A total of ~ 50 EDS analyses were

acquired for each of the three specific regions, around or in cells, for each time point. The replicate (n=x) is for the number of replicates for the atomic ratios expressed as either Cd: Se or Se: Cd.

The Cd: Se and Se: Cd calculated values for CdSe-internalized by PA were maintained in determining appropriate atomic ratio placement in a graph to visually maintain similar spacing for Cd-enriched (pink region, Cd-QDs) or Se-enriched (green region, Se-QDs) QDs (Figure V-7). The EDS analyses with atomic percentage for only Cd or only Se are indicated in the lower (n=x) in the respective Cd (pink, upper) region or Se (green, lower) region. These EDS results could be from CdSe QDs with selenium concentrations below the detectable level or are bright cellular locations where only cadmium is present and vice versa for bright spots with only Se having an analyzed atomic percentage. For easy communication the Below Detection "BD" designation will be identified as "QD" when an atomic ratio is calculated, and when only Cd or Se was present in the EDS analyses.

The CdSe QD starting material (SM) has an atomic ratio spread from 2.8 Cd:Se to 1.3 Se:Cd with no EDS analyses showing only Cd or Se being analyzed for the 50 EDS replicates (Figure V-7). The CdSe QD SM was shown to have 41 EDS replicates with Cd:Se above 1.0 indicating cadmium (Cd)-enriched QDs. These results show that 82% of the 50 EDS replicates were Cd-enriched QDs with only 9 replicates in the green region, indicating selenium (Se)-enriched QDs (Figure V-7). The Se-enriched QDs are calculated to have Se: Cd atomic ratio above 1.0, because

this is where Se atomic percentage is higher than the Cd atomic percentage for a single EDS analysis. The broadest atomic ratio spread is observed in the 4 h sample for cytoplasm-associated QDs (4.9 Cd: Se to 3.2 Se: Cd) where 56% are Cd-enriched QDs. The 4 h cell wall-associated QDs had a similar atomic ratio spread, except for a few outliers, as the QD SM, but had a reduced number of Cd-enriched QDs (68%).

The PA CdSe 12 h sample had slightly lower cytoplasm-associated Cd-enriched QDs (53%) and an atomic ratio spread of Cd: Se (3.1) to Se: Cd (2.7) (Figure V-7). The 12 h cell wall-associated Cd-enriched QDs (84%) with Cd: Se atomic ratio reaching 4.2 to a Se: Cd of 2.2. The PA CdSe 24 h sample resulted in the cytoplasm-associated QDs having a 50: 50 percentage split for Cd-enriched QDs and Se-enriched QDs and a larger Se-enriched QDs atomic ratio spread (Cd: Se 4.3; Se: Cd 2.7) (Figure V-7 and V-8). The cell wall QDs however remained similar to the QD starting material with 78% Cd-enriched QDs and a slight Cd: Se atomic ratio (2.8) shift toward Cd-enriched QDs. These results show the weathering of QDs located in the cytoplasm become Se-enriched QDs (Figure V-7 and V-8, cytoplasm-associated Cd-enriched QDs: 82% SM-QDs; 56% 4h-QDs; 53% 12h-QDs; 50% 24h-QDs). The QDs associated with the cell wall after 24 h have similar Cd: Se atomic ratios as the starting QDs, which could imply that minimal weathering is occurring on QDs associated with the PA cell wall. The different extent of weathering would indicate the biochemical environment inside the cytoplasm is causing more CdSe QD weathering than the cell wall-associated QDs. These EDS results could be from CdSe QDs with Se concentrations below the detectable level or are bright cellular locations

where only Cd is present, and vice versa for bright spots with only Se having an analyzed atomic percentage. The CdSe QDs located in the medium was only observed a few times in the 4 h sample and no CdSe QDs were observed in the 12 h or 24 h samples.

STEM electron micrographs of CdTe QD-contaminated PA cells during the first 24 h were generated (Figure V-9). The PA cytoplasm has a distinct separation from cell wall structures starting at the 8 h (Figure V-7E). The STEM-EDS analyses were generated for CdTe QDs (filled circle) starting material, PA cytoplasm-associated QDs (diamond), PA cell wall-associated QDs (triangle), and QDs located away from PA cells (black-filled circle) (Figure V-9). A total of ~50 EDS analyses were acquired for each of the three specific region for each time point. The replicate (n=x) is for the number of replicates for either Cd: Te or Te: Cd. Cd: Te and Te: Cd calculated values were maintained in determining appropriate atomic ratio placement in the graph to visually maintain similar spacing for Cd-enriched (pink region) QDs or Te-enriched (green region) QDs. The EDS analyses with an atomic percentage for only Cd or only Se are indicated in the lower (n=x) within the respective Cd (pink, upper) region or Se (green, lower) region. These EDS results could be from CdTe QDs with Te concentrations below the detectable level or are bright cellular locations, where only Cd is present and vice versa for bright spots with only Te having an analyzed atomic percentage.

The CdTe QD starting material has an atomic ratio spread from 2.7 Cd: Te to 1.8 Te: Cd with no EDS analyses showing only Cd or Te being calculated for the 50 EDS analyses (Figure V-9). The CdTe QDs were shown to have 52% Cd-enriched QDs from the 50 EDS analyses, and of those 24 EDS analyses indicating Te-enriched QDs in the lower green region (Figure V-9). Te-enriched QDs are where the Te atomic percentage is higher than the calculated Cd atomic percentage for a single EDS analysis. The atomic ratio spread observed in the 4 h sample for cytoplasm-associated QDs (2.3 Cd: Te to 1.8 Te: Cd) where 50% are Cd-enriched QDs. The 4 h cell wall-associated QDs had a similar atomic ratio spread as the QD starting material, but had a reduced number of Cd-enriched QDs (33%). The PA with internalized-CdTe 8 h sample had cytoplasm-associated Cd-enriched QDs (39%) and a broader atomic ratio spread of Cd: Te (3.3) to Te: Cd (3.7). The 8 h cell wall-associated Cd-enriched QDs (34%) had Cd: Te atomic ratios reaching 2.3 and for Te: Cd of 3.9 (Figure V-7 and V-9).

The PA CdTe 24 h sample resulted in the cytoplasm QDs having a 58: 42 percentage split for Cd-enriched QDs and Te-enriched QDs, and a broader atomic ratio spread (Cd: Te 3.0; Te: Cd 2.6) as compared to the CdTe QD starting material (Figure V-8). The 24 h cell wall-associated QDs were shown to shift towards a Te-enriched QD compared to the CdTe QD starting material with 18% Cd-enriched QDs and a slight Cd: Te (2.7) atomic ratio shift toward Te-enriched QDs. These results show that the weathering of QDs located in the cytoplasm became Te-enriched QDs by 8 h but after 24 h they are more Cd-enriched QDs (Figure V-9), Cytoplasm-

associated Cd-enriched QDs (Figure V-7: 52% SM-QDs; 50% 4 h-QDs; 39% 8 h-QDs; 58% 24 h-QDs) from the CdTe-internalized by Pa studies show slight changes at 8 h but became more Cd-enriched by 24 h. The QDs associated with the cell wall, after 24 h, have Cd: Te atomic ratios that are similarly spread as compared to the QD starting material, but a shift in EDS analysis of Te-QDs would indicate that weathering is occurring on QDs associated with the PA cell wall (Figure V-7, Cell wall-associated Cd-enriched QDs: 52% SM-QDs; 33% 4 h-QDs; 34% 8 h-QDs; 18% 24 h-QDs). The different extent of weathering would indicate that the biochemical environment outside, near the cell wall, is causing more CdTe QD weathering than for the cytoplasm-associated QDs. The CdTe QDs located in the medium were only observed a few times in the 24 h sample and no CdTe QDs were observed in the 4 h or 8 h samples.

3.2. Quantification of bacterial formed QD by STEM-EDS. The results for PA with internalized-CdSe QD produced atomic ratios in the range of 5:1 Cd: Se to 3:1 Se: Cd suggest that the STEM-EDS spectra at 30 kV accelerating voltage is greater in atomic ratio span from the manufactured CdSe QDs. This atomic ratio span seems to indicate the variation in atomic composition when compared with unweathered or chemically unaltered manufactured CdSe QDs. Chemical etching of QDs was experimentally shown to occur during the first 24 h in de-ionized water at approximately 30% by weight (Priester *et al.* 2009) of the initial 0.075 mg mL^{-1}. The

Cd(II) concentrations from the loss of Cd atoms on the exterior surfaces for a ~5.0 nm CdSe QDs is a 36% loss of the total Cd mass from the single CdSe QD (Table V-1). These results could indicate the stabilization of Se surfaces has occurred under the experimental conditions during the subsequent release of Cd into the solution.

The analysis by low-accelerating voltage – STEM-EDS of PA and QDs is used to evaluate the percentage of the weathering for specific elements from a single QD. The CdSe QDs were above shown to have been weathered more extensively in the PA cytoplasm, and CdTe are surprisingly minimally weathered in the same PA cytoplasmic environment. These results show that CdSe QDs present in the PA cytoplasm will be Se-enriched on the surfaces due to the loss of Cd by cytoplasmic weathering. The CdTe QDs on the PA cell wall are Te-enriched compared to cytoplasm QDs. These results for CdTe QDs associated with the PA cytoplasm will be Te-enriched on the surfaces due to the loss of Cd by cytoplasmic weathering.

The previous studies looked at STEM-EDS of quantum dots that were used to contaminate a PA cultures. The following study will determine if the addition of the dissolved salts of cadmium (Cd^{+2}) and selenite (SeO_3^{-2}) ions will produce precipitates similar in form and Cd: Se atomic composition as observed in the PA cytoplasm. The cells were grown with either 0.075 mg mL^{-1} Cd^{+2} only and 0.075 mg mL^{-1} Cd^{+2} with 0.20 mg mL^{-1} SeO_3^{-2} in LB broth for 24 h.

STEM-EDS analyses were generated for the salts contamination studies with PA growth (Figure V-11). The PA specimens grown in the presence of Cd^{+2}

produced bright spots that were analyzed and shown to contain cadmium (data not included) and the STEM images (Figure V-10) also show bright spots along the outer and cytoplasmic membrane. Additional bright spots were located in the cytoplasm but most were contained within the PA periplasmic space. The PA Cd^{+2} and SeO_3^{-2} study showed similar bright spots and 50% of the EDS analyses resulted in Cd:Se atomic ratios similar to the manufactured CdSe QDs. The bright spots were located in the cytoplasm (diamond), bound to the PA cell membrane (triangle); QDs (circle) not associated with PA could also be detected (Figure V-11). The EDS analyses were performed on a large number of bright spots, with only cadmium or selenium present in the EDS analytical results. These results could be interpreted as QDs having only one of the elements present on the surface and precipitates constructed of only Cd or Se or, alternatively QDs with the opposing element (Cd or Se) below the detection limit of the EDS system. There were ~50 EDS replicates for each region except for media QDs.

3.3. Quantification of QD weathering by protozoa with STEM-EDS.

The ability to view into a protozoan cell and investigate how NMs are being accommodated is important in understanding the microbial eukaryotic localization and fate of NMs, and in studying trophic-transfer of base microbial food chains (Werlin *et al.*, 2011; Mielke *et al.*, 2013). The scientific instrument used for this task is the STEM that allows a glimpse in time at the internal structures and the relative

localization of NMs inside the organism. EDS allows for the analysis of the elemental composition of NMs in protozoans cells (Werlin *et al.*, 2011), but using accelerating voltages above 100 kV can quickly destroy the NMs and the sample. Using a lower accelerating voltage (30 kV) does not immediately destroy the resin embedded sample but allows for analysis of weathering of CdSe QDs. Additionally, the STEM-EDS technique is ideal for investigating QDs that are easily destroyed by the chemical methods used when isolating protozoan organelles (i.e. mitochondria).

The STEM-EDS analyses of TT that were fed QDs-contaminated for 8 h shows the presence of QDs along the TT cell outer membrane which could be either from QDs damaging the eukaryotic membrane and entering from the medium, or from the QDs being transported during protozoans digesting food from the food vacuoles (FVs) (Figure V-11). The QDs have similar CdSe atomic ratio ranges as the starting material QDs shown as the red dot-line-dot ( ). When comparing all QDs in 8 h TT organelles to the starting material QDs, the average CdSe atomic ratio is 1.5 ± 0.5 for starting material QDs and 1.9 ± 0.8 Cd: Se atomic ratio (ρ= 5.5 x 10^{-3}, n=50) for the TT organelles. Investigating the 24 h TT cells fed PA contaminated with CdSe QDs, resulted in CdSe QDs being analyzed in all organelles as the 8 h sample with similar Cd:Se atomic ratio range (Figure V-12). Comparing all QDs in 24 h TT organelles to the starting material QDs, the average CdSe atomic ratio is 1.5 ± 0.5 for starting material QDs and 1.8 ± 0.8 Cd: Se atomic ratio (ρ= 1.9 x 10^{-2}, n=39) for TT organelles. The difference between 8 hour and 24 hour QDs Cd: Se atomic ratio was significant (ρ= 0.8) indicating that overall the QDs are losing Cd and

becoming Se-enriched QDs, which is closer to what the starting material QDs originate in analysis. This is an indication that the Se has been stripped off the QDs within the TT cell.

3.4. Evaluation of x-rays generation depth profile. The experimental results for contamination studies using CdSe and CdTe QDs show atomic ratios that span across limited parameters for the low-accelerating voltage dark-field STEM-EDS analytical results. The starting QDs have different atomic ratio extremes with few outliers. The Cd: Se atomic ratios have a span from Cd: Se 2.8 to Se: Cd 1.3. The Cd: Te atomic ratio spans from Cd: Te 2.8 to Te: Cd 1.8. The span of atomic ratios is an indication of the numbers of atoms that were excited by the electron beam and the resulting x-rays that had the potential escape velocity and direction to reach the EDS window.

When considering the 50 replicate EDS analyses, the CdSe QDs are 82% Cd-enriched QDs, while the CdTe QDs have Cd- enriched QDs only 52% of the time (Figure V-7). The most predominant trends are the CdSe QDs reduction in Cd-enriched QDs to 50% in the PA cytoplasm, even after 4 h of exposure and the CdTe QDs reduction of Cd-enriched QDs occurs when associated with the PA cell wall. The bulk composition of both QDs is 1:1 for their respective elements (Rosenthal *et al.* 2007) and would indicate that EDS atomic ratios should be closer to 1:1 in the NMs size range. The variation in atomic ratio could be the result of how the QD is

positioned and the orientation of its facet if it is facing the detector. For most CdSe QDs, the crystal structure is Wurtzite. The Wurtzite crystal lattices have surfaces or facets, which are either cadmium rich or Se rich (Rosenthal *et al*. 2007). The CdTe QDs predominately have a cubic, zinc blended crystal structure, with surface composition depending on the amount of terminal atoms present.

To better understand where the x-rays are generated from, in a theoretical CdSe QD, we first need to evaluate the ideal QD structure and estimate atomic ratios that could be generated under the following conditions:

1. When x-rays are generated from only the outer most shell of the CdSe crystal. The weathering of the surface atoms would produce a Cd: Se 2:1 if 50% of the Se atoms were removed (Table V-2 and Figure V-1).
2. When x-rays are generated from the outer two shells and only weathering is occurring on the surface shell. The influence of the inner atom is evident, in that only above 70% weathering produces CdSe atomic ratios above 2 for the smaller QDs (Table V-3 and Figure V-2).
3. When x-rays are generated from the outer three shells and only weathering is occurring on the surface shell. A trend is starting to emerge, that as the shells increase in number there is a greater influence towards a Cd:Se (1:1) atomic ratio. Data not shown.
4. X-rays generated from consecutively deeper shells for the ideal ~8.5 nm and any weathering is only occurring on the surface atoms. Again the deeper shells

atomic composition determines the possible atomic ratios generated. Only weathering above 50% could produce atomic ratios above 2 for only surface atoms. Data not shown.

5. X-rays generated from complete inner shells and the core, with weathering occurring at the different possible diameter CdSe QDs. Only the smallest QDs (below 3 shells) could be weathered enough to generate CdSe atomic ratios above 2.

When considering the possible ideal inner shells atomic composition, influence and percentage of weathering that could occur produce a second inner shell influence at 25% and weathering on the surface atoms. This generated a possible answer that takes into account the specific facet facing the EDS detector and weather of the surface atoms (Table V-4 and Figure V-3).

4. DISCUSSION

The characterization of CdSe QD toxicity to contaminated planktonic *Pseudomonas aeruginosa* (PA) is compared to cadmium (Cd) salt toxicity in a study by Priester *et al*. (2009). It is shown in the QD study that Cd was internalized (0.15±0.02 pg/cell) and bioconcentrated to 4,460 times higher than the administered dose in the medium. The Se was shown to have intracellular concentrations of 0.08±0.01 pg per cell. A weak x-ray diffraction (XRD) peak was found that was consistent with the dominant peak for intact CdSe QDs, suggesting at least some cell-

associated QDs were intact. The dark-field - STEM images had nano-sized particles that were of a similar size range to the CdSe QDs 5-8 nm. Priester *et al.* (2009) also used XANES to trace the QDs' integrity by Se oxidation state. The presence of Se(0) in the cytoplasm, along with Se(II) confirmed the above findings by XRD and STEM that CdSe QDs have entered the bacterial cell. In a prior study using different bacteria, the direct evidence that intact QDs became intracellular was shown by Kloepfer *et al*. (2005), using high resolution - TEM in order to confirm distinct crystal lattice structures of intact or possibly partially weathered QDs. The presence of internalized QDs was established but the exact extent of QD degradation was not addressed in the above-mentioned publications, nor in a subsequent study by Werlin *et al*. (2011). The Werlin *et al*. (2011) did use STEM imaging and EDS to show the presence of Cd and Se in locations with bright nano-sized particles that had a similar Cd: Se atomic ratio as the starting QD NMs. The Cd: Se atomic ratios of QDs internalized into the cytoplasm by *Tetrahymena thermophila* (TT) were statistically similar to ratios for QDs in TT food vacuoles (FV), but further EDS analysis of QD weathering in the organelles was not investigated by Werlin *et al.* (2011).

Experimentally, during the first 4 h after contamination with QDs, the PA bacteria internalized whole QDs into the cytoplasm for both QD types (CdSe and CdTe). The PA cytoplasm Cd:Se atomic ratio varied considerably in elemental composition for the CdSe QDs, while the CdTe showed minimal weathering when compared to the QD starting materials. By 24 h, the cytoplasm QD contained Se-enriched CdSe QDs and the cell wall-associated CdTe QDs study were Te-enriched

CdTe QDs when compared to the CdTe QD starting material. Additionally at 24 h, STEM-EDS analyses revealed many bright spots assumed to be QDs, but resulted in only Se, Te or Cd being detected in various locations in the cytoplasm or associated with the cell wall. The EDS results including only one element could be regions where break down products are being hyper-accumulated and possibly formed into subsequent mineral aggregates. The real power of the low-accelerating voltage STEM-EDS is not in being able to generate large quantities of analyses of single QDs, but it can prove that these atomic ratio results show the chemical etching of QDs, or weathering, that is occurring on the immediate QD.

All of the above information is generated with a single make and model of EDS instrumentation, i.e. the EDAX Inc. spectrometer using the Genesis (EDAX Inc.) software by a ZAF method. This ZAF method factors in atomic mass (Z), adsorption (A), and fluorescence (F) when specific elements are included into the analytical criteria. The following discussion will verify that the atomic ratios produced by the low-accelerating voltage STEM-EDS system are related to the physical dimensions of an ideal CdSe QD. Rosenthal *et al*. (2007) constructed a 3-D rendering of a CdSe QD and identified facets that would be cadmium rich (001)' and selenium rich (001). The terminal atoms would make these surfaces chemically different, as identified as dangling bonds (Rosenthal *et al.*, 2007). These single element-rich facets are chemically different, but EDS signals are generated from these surface atoms and from atoms included throughout the crystal's shells. The depth of penetration of primary electrons is assumed to be in the micron level as defined by a

Monte Carlo electron trajectory simulation and as illustrated by Casino (by Hovington *et al.*, 1997). We can then assume that there are adequate electron penetrations to cause electron orbital ejection that results in the x-ray photon being emitted from atoms deeper in the mineral surface when an elelctron fills the hole. Nanocrystals are so small that the x-ray signal generated is assumed to be from the complete crystal, as it faces the EDS detector. The CdSe QDs have a Wurtzite crystal structure with a stoichiometry of 1:1 for Cd: Se and the EDS analyses should produce analytical results close to this value. However, rarely are the results for EDS and bulk analysis (ICP-OES) relatively close to each other. The Kleopfer *et al*. (2005) EDS finding for CdSe QDs showed an atomic ratio for Cd: Se of 1.56±0.57 with a spread of 1.2:1 to 1.8:1 for n=100 replicates. The TEM-EDS analysis was done at 100 keV accelerating voltage and a selective area of 8.8 nm x 8.8 nm. The higher accelerating voltage (100 keV) uses more electrons for generating x-rays than the low-accelerating voltage (30 keV) STEM-EDS system. While this theoretical model presented in this chapter asserts that x-rays are generated from the surface layer atoms, direct experimental evidence, perhaps by STEM-EDS of NMs with atomic layer shell configurations, would be needed to further test this concept. Otherwise, the published literature doesn't support the x-rays would derive from the surface layer but rather from the complete NM.

The use of instrumentation by researchers is driving the scientific world into the 21st century, and electron microscopy is on the leading edge of that technology. The STEM includes a simple detector that, when used within conventional SEMs,

make it possible to image through thin-sectioned samples. The analytical instrumentation developed for EDS to generate atomic percentages of a selected area has also improved dramatically. The new STEM-EDS systems have decreased the required working distance of the x-ray window by about 50%, and at the reduced accelerating voltage has enable the analysis of the surface alteration of minerals in the nanometer size range. From this research, we hope to open a new and expanded study of using a 30 kV accelerating voltage – STEM EDS system. Analyses of NMs atomic composition will be beneficial in understanding how QDs, both the CdSe and CdTe, are weathered differently in the *Pseudomonas aeruginosa* (PA) cytoplasm, as compared to those associated with the PA cell wall.

Future research will include more EDS analyses on additional environmentally relevant bacterial strains, and aid in determining the extent of weathering that occurs on QDs located in the cytoplasm and the QDs associated with the cell wall. I presently have several bacteria (*Bacillus subtilis*, *Escherichia coli* and *Staphylococcus epidermidis*) contaminated with QDs (CdSe, CdTe and CdSe/ZnS), preserved in resin for similar STEM-EDS analyses as described above for PA. The analysis of these bacteria would help to understand the possible differences between Gram-positive and Gram-negative weathering of QDs during the first 48 hours.

ACKNOWLEDGEMENTS

This research was primarily funded by the National Science Foundation (NSF) and the Environmental Protection Agency (EPA) under Cooperative Agreement Number DBI-0830117. Any opinions, findings, and conclusions or recommendations expressed in this material are those of the author(s) and do not necessarily reflect the views of either the NSF or the EPA. This work has not been subjected to EPA review, and no official endorsement should be inferred. Peter K. Stoimenov at UCSB made the CdSe QDs. Valery Ozenne at McGill University made the CdTe QDs. Environmental scanning and scanning transmission electron microscopy were partly performed in the Micro-Environmental Imaging and Analysis Facility at University of California Santa Barbara (www.bren.ucsb.edu/facilities/**MEIAF**/) under NSF awards # BES-9977772 and # DBI-0216480.

FIGURES

Table V-1. The central core and first shell have a diameter of 1.450 nm (Kasuya et al. 2004) and is built on by the addition of tetrahedral structures (0.3548 nm total height). The addition of 11 shells to the central core will develop a ~8.5 nm CdSe QD. The shells elemental content can be calculated through the volume and density of CdSe. The enumeration of Cd and Se atoms present in each shell will allow further investigation into understanding the influence of weathering surface atoms in the STEM-EDS analyses. This table was generated with Microsoft Excel.

				density				weight %				
109.5			4	5.816	g/cm3			0.588	112.41	Cd		
Bond length	0.266	(1)	3.14	5.82E-21	g/nm3			0.413	78.96	Se		
19.5	0.0888		6.02E+23	(5) 191.27	g/mol			Total			unweathered QDs	
Tetra length	0.3548	QDs Diameter	volume sphere	g CdSe	g Cd	g Se	mol CdSe	molecules CdSe	surface CdSe	core CdSe	cadmium	selenide
3.548	1 core 1	1.450	(4) 1.595	9.279E-21	5.453E-21	3.831E-21	4.851E-23	(7) 29.22	22	6	22.0	22.0
3.193	2 shell	(2) 2.160	5.271	3.066E-20	1.802E-20	1.266E-20	1.603E-22	96.52	67.3	29.2	67.3	67.3
2.838	3 shell	(3) 2.869	12.361	7.189E-20	4.225E-20	2.968E-20	3.759E-22	226.35	129.8	96.5	129.8	129.8
2.484	4 shell	3.579	23.988	1.395E-19	8.199E-20	5.759E-20	7.294E-22	439.26	212.9	226.4	212.9	212.9
2.129	5 shell	4.288	41.273	2.400E-19	1.411E-19	9.909E-20	1.255E-21	755.78	316.5	439.3	316.5	316.5
1.774	6 shell	4.998	65.338	3.800E-19	2.233E-19	1.569E-19	1.987E-21	1196.45	440.7	755.8	440.7	440.7
1.419	7 shell	5.708	97.306	5.659E-19	3.326E-19	2.336E-19	2.959E-21	1781.83	585.4	1196.5	585.4	585.4
1.064	8 shell	6.417	138.298	8.043E-19	4.727E-19	3.320E-19	4.205E-21	2532.47	750.6	1781.8	750.6	750.6
0.710	9 shell	7.127	189.436	1.102E-18	6.475E-19	4.548E-19	5.760E-21	3468.89	936.4	2532.5	936.4	936.4
0.355	10 shell	7.836	251.842	1.465E-18	8.608E-19	6.047E-19	7.658E-21	4611.65	1142.8	3468.9	1142.8	1142.8
0.01	11 shell	8.546	326.638	1.900E-18	1.116E-18	7.842E-19	9.932E-21	5981.30	1369.6	(8) 4611.7	1369.6	1369.6
Depth of penetration			=4/3*((3.14)*((D17/2)^3))									
		10 shell + 2x tetra lenth		=E18*F3								=$K18
		equal to 11 shell		Vol*Density	=F19*J2						=$K19	surface Se
					g*%weight	=F20*J3				=J20-K20	surface Cd	
						g*%weight	=F21/F4		=J21-J20	total CdSe-surface CdSe		
							g*MW	=I22*E4	shell 11- shell 10			
								mol*Avogadros #				

Table D1. The central core and first shell has a diameter of 1.450 nm (Kasuya *et al.* 2004) and is built on by addition of tetrahedral structures (0.3548 nm total height). The addition of 11 shells to the central core will develop a ~8.5 nm CdSe QD. The shells elemental content can be calculated through the volume and density of CdSe. The enumeration of Cd and Se atoms present in each shell will allow further investigation into understanding the influence of weathering surface atoms the STEM-EDS analyses. This table was generated with Microsoft Excel.

1) Diameter of shell
2) 1.45 nm (core + 1st shell) + 2 * 0.3548 nm (CdSe tetra length) = **2.160 nm** (2nd shell diameter)
3) 2.160 nm (2nd shell diameter) + 2 * 0.3548 nm (CdSe tetra length) = **2.869 nm** (3rd shell diameter)
4) Volume = 4/3 * ((π) * ((diameter / 2)^3))) = 1.33 * ((3.14) * ((1.450/2)^3))) = 1st core volume = **1.595 nm^3**
5) Mass of CdSe = Volume of core * ρ = 1.595 nm^3 * 5.82 x 10^{-21} g nm^{-3} = 1st core mass CdSe = **9.279 x 10^{-21} g of CdSe**
7) molecules of CdSe = 1st core mass * mol weight CdSe * Avogadro's #
= 9.279 x 10^{-21} g of CdSe * 191.27 g/mol * 6.02 x 10^{23} mol/g = 1st core = **29 molecules of CdSe**
8) The largest calculated QD has a 8.5 nm diameter and consists of a total of 5,981 CdSe molecules which results in 1,369 molecules of CdSe in the outer shell with a CdSe core of 4,611 molecules

Table V-2. Predicted atomic ratios (Cd: Se or Se: Cd) in EDS of CdSe QDs on the basis of all x-rays generated from the outermost shell of a weathered QD. The weathering of the surface atoms would produce a Cd: Se atomic ratio of 2:1 if 50% of the Se atoms were removed. For shell 11 with 1,349 CdSe molecules in the outer most shell, and a central core with 4,611 CdSe molecules, and since we have equal numbers of Cd as Se atoms, there are 1,349 atoms of Cd and 1,369 atoms of Se located in the 11th shell. If there is 50% weathering of the Se atoms there will be 1,369 atoms of Cd and 684.5 atoms of Se producing a x-ray atomic ratio of 1,369/684.5 = 2.0 Cd: Se.

	Cd weathering		Se/Cd Atomic Ratio				Se weathering		Cd/Se Atomic Ratio												
QD diameter	0.01	0.05	0.1	0.15	0.2	0.25	0.3	0.35	0.4	0.45	0.5	0.55	0.6	0.65	0.7	0.75	0.8	0.85	0.9	0.95	0.99
	99%	95%	90%	85%	80%	75%	70%	65%	60%	55%	50%	45%	40%	35%	30%	25%	20%	15%	10%	5%	1%
1.45	100.00	20.00	10.00	6.67	5.00	4.00	3.33	2.86	2.50	2.22	2.00	1.82	1.67	1.54	1.43	1.33	1.25	1.18	1.11	1.05	1.01
2.16	100.00	20.00	10.00	6.67	5.00	4.00	3.33	2.86	2.50	2.22	2.00	1.82	1.67	1.54	1.43	1.33	1.25	1.18	1.11	1.05	1.01
2.87	100.00	20.00	10.00	6.67	5.00	4.00	3.33	2.86	2.50	2.22	2.00	1.82	1.67	1.54	1.43	1.33	1.25	1.18	1.11	1.05	1.01
3.58	100.00	20.00	10.00	6.67	5.00	4.00	3.33	2.86	2.50	2.22	2.00	1.82	1.67	1.54	1.43	1.33	1.25	1.18	1.11	1.05	1.01
4.29	100.00	20.00	10.00	6.67	5.00	4.00	3.33	2.86	2.50	2.22	2.00	1.82	1.67	1.54	1.43	1.33	1.25	1.18	1.11	1.05	1.01
5.00	100.00	20.00	10.00	6.67	5.00	4.00	3.33	2.86	2.50	2.22	2.00	1.82	1.67	1.54	1.43	1.33	1.25	1.18	1.11	1.05	1.01
5.71	100.00	20.00	10.00	6.67	5.00	4.00	3.33	2.86	2.50	2.22	2.00	1.82	1.67	1.54	1.43	1.33	1.25	1.18	1.11	1.05	1.01
6.42	100.00	20.00	10.00	6.67	5.00	4.00	3.33	2.86	2.50	2.22	2.00	1.82	1.67	1.54	1.43	1.33	1.25	1.18	1.11	1.05	1.01
7.13	100.00	20.00	10.00	6.67	5.00	4.00	3.33	2.86	2.50	2.22	2.00	1.82	1.67	1.54	1.43	1.33	1.25	1.18	1.11	1.05	1.01
7.84	100.00	20.00	10.00	6.67	5.00	4.00	3.33	2.86	2.50	2.22	2.00	1.82	1.67	1.54	1.43	1.33	1.25	1.18	1.11	1.05	1.01
8.55	100.00	20.00	10.00	6.67	5.00	4.00	3.33	2.86	2.50	2.22	2.00	1.82	1.67	1.54	1.43	1.33	1.25	1.18	1.11	1.05	1.01

Figure V-1. Diagramed CdSe QD that shows the 11 shells of an ~8.55 nm size (not to scale). The red shell, in this case shell 11, illustrates that the EDS x-ray signal is only being generated by atoms in the outermost shell of an ~8.55 nm QD. This results in a Cd: Se atomic ratio of 2.0 for all size QDs and it is unlikely that none of the atoms from the interior core of the QDs will influence the EDS analytical results.

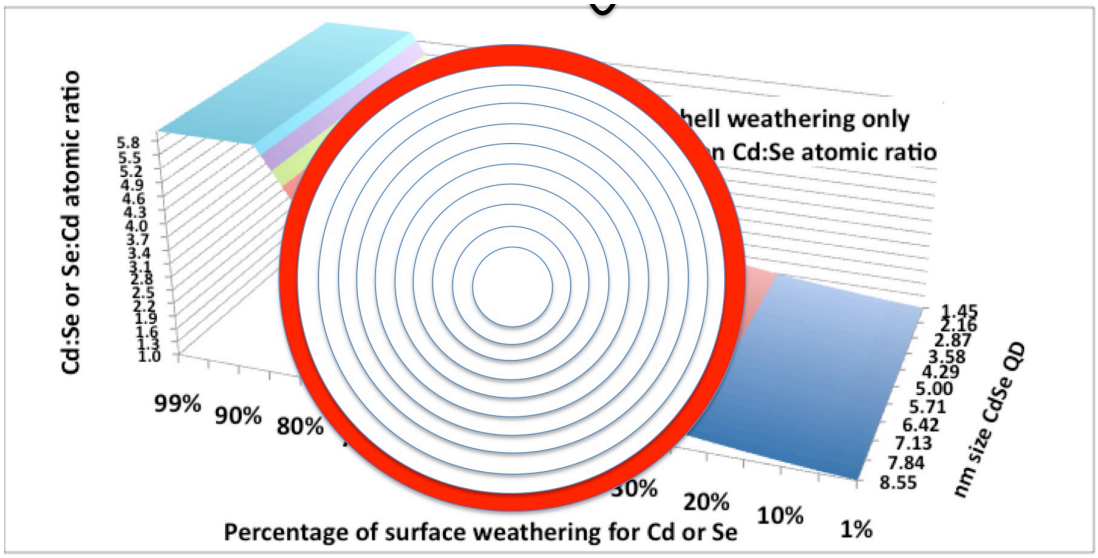

Table V-3. When x-rays are generated from only the two outer most shell CdSe molecules of the CdSe crystal, and only weathering is occurring on the outer shell Cd or Se atoms. The weathering of the surface atoms would produce a Cd: Se atomic ratio of above 2, for the extreme weathering of 70% of the Se atoms removed. For shell 11 with 1,349 CdSe molecules in the outer most shell, and a central core with 4,611 CdSe molecules, then since we have equal numbers of Cd as Se atoms, there are 1,349 atoms of Cd and 1,369 atoms of Se located in the 11th shell. If there is 70% weathering of the Se atoms, there will be 1,369 atoms of Cd and 410 atoms of Se, resulting in x-rays being produced from;

= 1,369 (shell 11) Cd + 1,142 (shell 10) Cd /

/410 (shell 11; weathered) Se + 1,142 (shell 10) Se

= 2,511 Cd atoms / 1,552 Se atoms = 1.618 Cd: Se atomic ratio

(These are the atomic ratios of 7.84 & 8.55 (70%) in circles)

	Cd weathering	Se/Cd Atomic Ratio					Se weathering	Cd/Se Atomic Ratio													
QD diameter	0.01	0.05	0.1	0.15	0.2	0.25	0.3	0.35	0.4	0.45	0.5	0.55	0.6	0.65	0.7	0.75	0.8	0.85	0.9	0.95	0.99
weathered	99%	95%	90%	85%	80%	75%	70%	65%	60%	55%	50%	45%	40%	35%	30%	25%	20%	15%	10%	5%	1%
1.45	4.50	3.94	3.41	3.01	2.69	2.43	2.22	2.04	1.89	1.76	1.65	1.55	1.46	1.38	1.31	1.24	1.19	1.13	1.09	1.04	1.01
2.16	3.94	3.52	3.11	2.78	2.52	2.30	2.12	1.96	1.83	1.71	1.60	1.51	1.43	1.36	1.29	1.23	1.18	1.13	1.08	1.04	1.01
2.87	2.87	2.67	2.46	2.27	2.11	1.98	1.86	1.75	1.65	1.57	1.49	1.42	1.36	1.30	1.25	1.20	1.15	1.11	1.07	1.03	1.01
3.58	2.6	2.44	2.27	2.12	1.99	1.87	1.77	1.68	1.59	1.52	1.45	1.39	1.33	1.28	1.23	1.18	1.14	1.10	1.07	1.03	1.01
4.29	2.45	2.31	2.16	2.03	1.92	1.81	1.72	1.64	1.56	1.49	1.43	1.37	1.31	1.26	1.22	1.18	1.14	1.10	1.06	1.03	1.01
5.00	2.36	2.24	2.10	1.98	1.87	1.77	1.69	1.61	1.54	1.47	1.41	1.35	1.30	1.26	1.21	1.17	1.13	1.10	1.06	1.03	1.01
5.71	2.30	2.18	2.06	1.94	1.84	1.75	1.66	1.59	1.52	1.46	1.40	1.35	1.30	1.25	1.21	1.17	1.13	1.09	1.06	1.03	1.01
6.42	2.25	2.14	2.02	1.91	1.82	1.73	1.65	1.58	1.51	1.45	1.39	1.34	1.29	1.24	1.20	1.16	1.13	1.09	1.06	1.03	1.01
7.13	2.22	2.12	2.00	1.89	1.80	1.71	1.64	1.56	1.50	1.44	1.38	1.33	1.29	1.24	1.20	1.16	1.12	1.09	1.06	1.03	1.01
7.84	2.19	2.07	1.96	1.86	1.77	1.69	1.62	1.55	1.49	1.43	1.37	1.33	1.28	1.24	1.20	1.16	1.12	1.09	1.06	1.03	1.01
8.55	2.17	2.07	1.96	1.86	1.77	1.69	1.62	1.55	1.49	1.43	1.37	1.33	1.28	1.24	1.20	1.16	1.12	1.09	1.06	1.03	1.01

Figure V-2. Diagramed CdSe QD that shows the 11 shells of an ~8.55 nm size (not to scale). The red shell, in this case shell 6 (5.00 nm QD), illustrates that the EDS x-ray signal is being generated from atoms in shell 6 and the adjacent shell of atoms in green (shell 5 4.29 nm). This results in a Cd: Se atomic ratio up to only 2.36 with 100% weathering of all Se atoms from the surface. This is an unlikely theoretical model since the experimental EDS analyses produce Cd: Se atomic ratios up to 2.8 and even some of the analyses are as much as 4.0:1.0 Cd: Se atomic ratio.

	Cd weathering		Se/Cd Atomic Ratio				Se weathering		Cd/Se Atomic Ratio												
QD diameter	0.01	0.05	0.1	0.15	0.2	0.25	0.3	0.35	0.4	0.45	0.5	0.55	0.6	0.65	0.7	0.75	0.8	0.85	0.9	0.95	0.99
weathered	99%	95%	90%	85%	80%	75%	70%	65%	60%	55%	50%	45%	40%	35%	30%	25%	20%	15%	10%	5%	1%
1.450	4.50	3.94	3.41	3.01	2.69	2.43	2.22	2.04	1.89	1.76	1.65	1.55	1.46	1.38	1.31	1.24	1.19	1.13	1.09	1.04	1.01
2.160	3.94	3.52	3.11	2.78	2.52	2.30	2.12	1.96	1.83	1.71	1.60	1.51	1.43	1.36	1.29	1.23	1.18	1.13	1.08	1.04	1.01
2.869	2.87	2.67	2.46	2.27	2.11	1.98	1.86	1.75	1.65	1.57	1.49	1.42	1.36	1.30	1.25	1.20	1.15	1.11	1.07	1.03	1.01
3.579	2.6	2.44	2.27	2.12	1.99	1.87	1.77	1.68	1.59	1.52	1.45	1.39	1.33	1.28	1.23	1.18	1.14	1.10	1.07	1.03	1.01
4.288	2.45	2.31	2.16	2.03	1.92	1.81	1.72	1.64	1.56	1.49	1.43	1.37	1.31	1.26	1.22	1.18	1.14	1.10	1.06	1.03	1.01
4.998	2.36	2.24	2.10	1.98	1.87	1.77	1.69	1.61	1.54	1.47	1.41	1.35	1.30	1.26	1.21	1.17	1.13	1.10	1.06	1.03	1.01
5.708	2.30	2.18	2.06	1.94	1.84	1.75	1.66	1.59	1.52	1.46	1.40	1.35	1.30	1.25	1.21	1.17	1.13	1.09	1.06	1.03	1.01
6.417	2.25	2.14	2.02	1.91	1.82	1.73	1.65	1.58	1.51	1.45	1.39	1.34	1.29	1.24	1.20	1.16	1.13	1.09	1.06	1.03	1.01
7.127	2.22	2.12	2.00	1.89	1.80	1.71	1.64	1.56	1.50	1.44	1.38	1.33	1.29	1.24	1.20	1.16	1.12	1.09	1.06	1.03	1.01
7.836	2.19	2.07	1.96	1.86	1.77	1.69	1.62	1.55	1.49	1.43	1.37	1.33	1.28	1.24	1.20	1.16	1.12	1.09	1.06	1.03	1.01
8.546	2.17	2.07	1.96	1.86	1.77	1.69	1.62	1.55	1.49	1.43	1.37	1.33	1.28	1.24	1.20	1.16	1.12	1.09	1.06	1.03	1.01

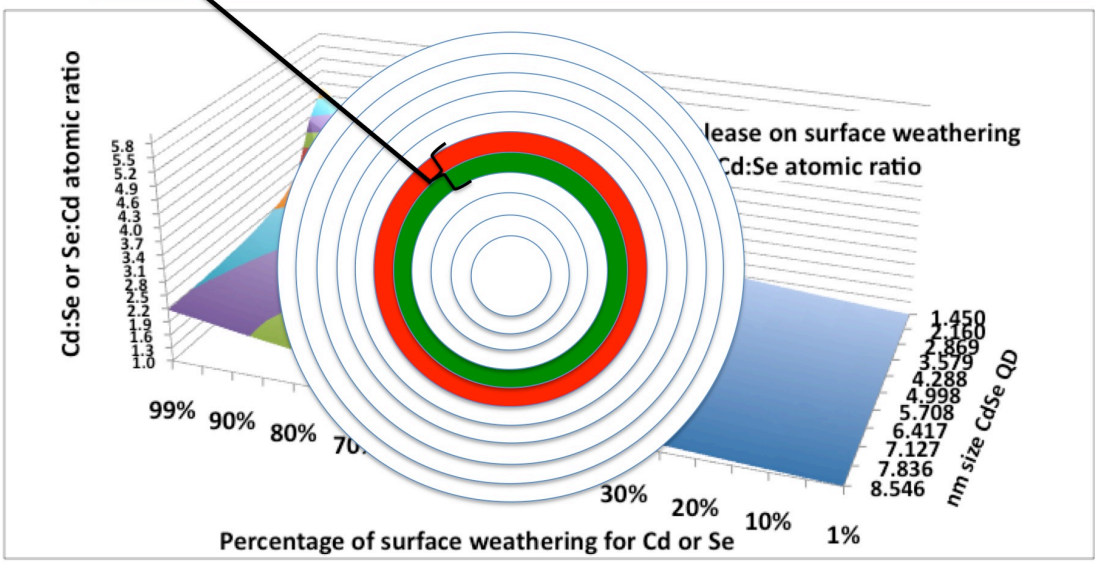

Table V-4. When x-rays are generated from only the outer most shell CdSe molecules and 25% of the adjacent inner shell of the CdSe crystal with only weathering occurring on the outer shell of Cd or Se atoms. The weathering of the surface atoms would produce a Cd: Se atomic ratio of about 2.46 for extreme weathering of 70% of the Se atoms removed for a 5.00 nm QD. The number of atoms influencing the x-ray signal is more in line with the experimental EDS analyses generating the range between Cd: Se 2.8 to Se: Cd 1.3.

25% 1st shell	Cd weathering		Se/Cd Atomic Ratio				Se weathering		Cd/Se Atomic Ratio											
QD diameter	0.01	0.05	0.1	0.15	0.2	0.25	0.3	0.35	0.4	0.45	0.5	0.55	0.6	0.65	0.7	0.75	0.8	0.85	0.9	0.95	0.99
weathered	99%	95%	90%	85%	80%	75%	70%	65%	60%	55%	50%	45%	40%	35%	30%	25%	20%	15%	10%	5%	1%
1.45	13.66	9.04	6.35	4.90	3.98	3.36	2.90	2.55	2.28	2.06	1.88	1.73	1.60	1.49	1.39	1.31	1.23	1.16	1.10	1.05	1.01
2.16	11.79	8.21	5.95	4.67	3.84	3.26	2.83	2.51	2.25	2.03	1.86	1.71	1.59	1.48	1.38	1.30	1.23	1.16	1.10	1.05	1.01
2.87	8.09	6.29	4.92	4.04	3.43	2.98	2.63	2.36	2.13	1.95	1.79	1.66	1.55	1.45	1.36	1.28	1.22	1.15	1.10	1.05	1.01
3.58	7.09	5.69	4.56	3.81	3.27	2.86	2.55	2.29	2.09	1.91	1.77	1.64	1.53	1.44	1.35	1.28	1.21	1.15	1.10	1.05	1.01
4.29	6.56	5.35	4.36	3.67	3.17	2.79	2.50	2.25	2.06	1.89	1.75	1.63	1.52	1.43	1.35	1.27	1.21	1.15	1.09	1.04	1.01
5.00	6.22	5.14	4.22	3.58	3.11	2.75	2.46	2.23	2.04	1.87	1.74	1.62	1.51	1.42	1.34	1.27	1.20	1.15	1.09	1.04	1.01
5.71	5.99	4.99	4.12	3.51	3.06	2.71	2.43	2.21	2.02	1.86	1.73	1.61	1.51	1.42	1.34	1.27	1.20	1.14	1.09	1.04	1.01
6.42	5.83	4.88	4.05	3.46	3.02	2.69	2.41	2.19	2.01	1.85	1.72	1.60	1.50	1.41	1.34	1.26	1.20	1.14	1.09	1.04	1.01
7.13	5.71	4.79	4.00	3.43	3.00	2.67	2.40	2.18	2.00	1.85	1.71	1.60	1.50	1.41	1.33	1.26	1.20	1.14	1.09	1.04	1.01
7.84	5.61	4.73	3.95	3.40	2.98	2.65	2.39	2.17	1.99	1.84	1.71	1.60	1.50	1.41	1.33	1.26	1.20	1.14	1.09	1.04	1.01
8.55	5.53	4.67	3.92	3.37	2.96	2.64	2.38	2.16	1.99	1.84	1.71	1.59	1.49	1.41	1.33	1.26	1.20	1.14	1.09	1.04	1.01

Figure V-3. Diagramed CdSe QD that shows the 11 shells of an ~8.55 nm size (not to scale). The red shell, in this case shell 6 (5.00 nm QD), illustrates that the EDS x-ray signal is being generated from atoms in shell 6 and the adjacent shell of atoms in blue (shell 5, 4.29 nm) is only influencing the EDS with 25% of the shell atoms. This results in a possible Cd: Se atomic ratio of 6.22 when 100% weathering of all Se atoms from the QD surface. The theoretical model is more likely, and fits the experimental EDS analyses that produces Cd: Se atomic ratios over 2.8 when below 80% weathering of Se atom from the surface has occurred.

25% 1st shell	Cd weathering		Se/Cd Atomic Ratio				Se weathering		Cd/Se Atomic Ratio												
QD diameter	0.01	0.05	0.1	0.15	0.2	0.25	0.3	0.35	0.4	0.45	0.5	0.55	0.6	0.65	0.7	0.75	0.8	0.85	0.9	0.95	0.99
weathered	99%	95%	90%	85%	80%	75%	70%	65%	60%	55%	50%	45%	40%	35%	30%	25%	20%	15%	10%	5%	1%
1.45	13.66	9.04	6.35	4.90	3.98	3.36	2.90	2.55	2.28	2.06	1.88	1.73	1.60	1.49	1.39	1.31	1.23	1.16	1.10	1.05	1.01
2.16	11.79	8.21	5.95	4.67	3.84	3.26	2.83	2.51	2.25	2.03	1.86	1.71	1.59	1.48	1.38	1.30	1.23	1.16	1.10	1.05	1.01
2.87	8.09	6.29	4.92	4.04	3.43	2.98	2.63	2.36	2.13	1.95	1.79	1.66	1.55	1.45	1.36	1.28	1.22	1.15	1.10	1.05	1.01
3.58	7.09	5.69	4.56	3.81	3.27	2.86	2.55	2.29	2.09	1.91	1.77	1.64	1.53	1.44	1.35	1.28	1.21	1.15	1.10	1.05	1.01
4.29	6.56	5.35	4.36	3.67	3.17	2.79	2.50	2.25	2.06	1.89	1.75	1.63	1.52	1.43	1.35	1.27	1.21	1.15	1.09	1.04	1.01
5.00	6.22	5.14	4.22	3.58	3.11	2.75	2.46	2.23	2.04	1.87	1.74	1.62	1.51	1.42	1.34	1.27	1.20	1.15	1.09	1.04	1.01
5.71	[illegible]	4.99	4.12	3.51	3.06	2.71	2.43	2.21	2.02	1.86	1.73	1.61	1.51	1.42	1.34	1.27	1.20	1.14	1.09	1.04	1.01
6.42	5.8[illegible]	4.88	4.05	3.46	3.03	2.69	2.41	2.19	2.01	1.85	1.72	1.60	1.50	1.41	1.34	1.26	1.20	1.14	1.09	1.04	1.01
7.13	5.71	4.79	4.00	3.43	3.00	2.67	2.40	2.18	2.00	1.85	1.71	1.60	1.50	1.41	1.33	1.26	1.20	1.14	1.09	1.04	1.01
7.84	5.61	4.73	3.95	3.40	2.98	2.65	2.39	2.17	1.99	1.84	1.71	1.60	1.50	1.41	1.33	1.26	1.20	1.14	1.09	1.04	1.01
8.55	5.53	4.67	3.92	3.37	2.96	2.64	2.38	2.16	1.99	1.84	1.71	1.59	1.49	1.41	1.33	1.26	1.20	1.14	1.09	1.04	1.01

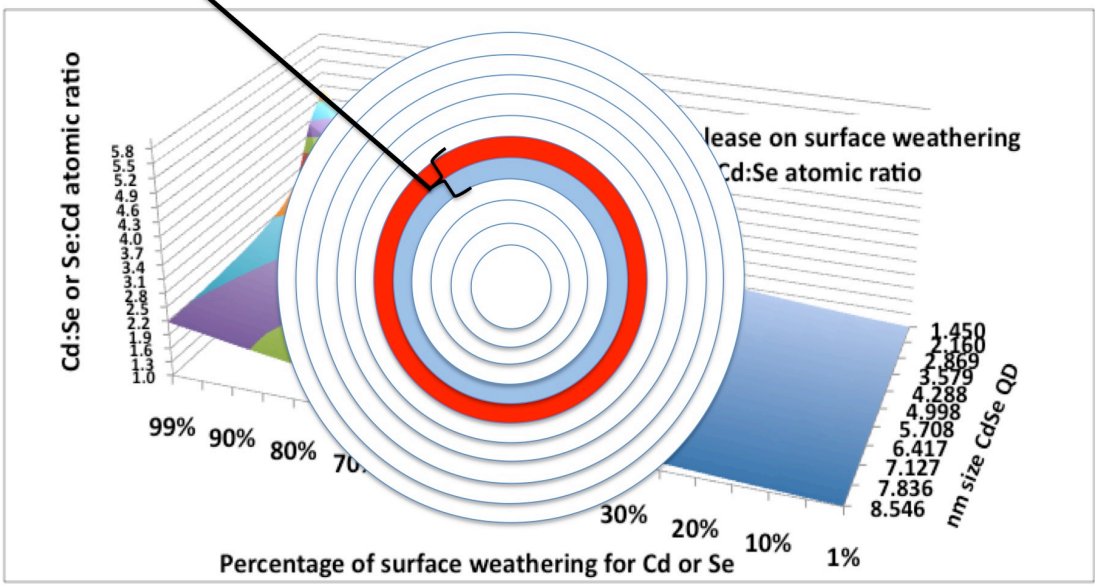

Figure V-4. STEM-EDS analyses of the CdSe QDs starting material used in contamination studies with *Pseudomonas aeruginosa* (PA) bacteria. The QDs starting material uses diamond shapes, and PA cytoplasm uses circles. Column 1 & 2 are from data generated from the Cd and Se atomic percentages in the form of Cd:Se atomic ratios. Values for Cd: Se ratios below 1.0 are squeezed between 0 and 1. Column 3 & 4 are the same data set, except values of Cd: Se below 1.0 were calculated to Se: Cd atomic ratios that are above 1.0 but from central datum in opposite direction. Column 5 illustrates the datum change from 1.0 to 5.0 with the addition of 4 to the calculated Cd: Se atomic ratio. Column 6 illustrates the datum change for Se: Cd where the initial Se: Cd is subtracted from 2 followed by the addition of 4. Column 7 and 8 are the same data with the datum adjusted by 4 to allow for further statistical analysis to properly interpret total range spread that is observed in evaluation of atomic ratios that span below 1.0 for two element calculated atomic ratio values.

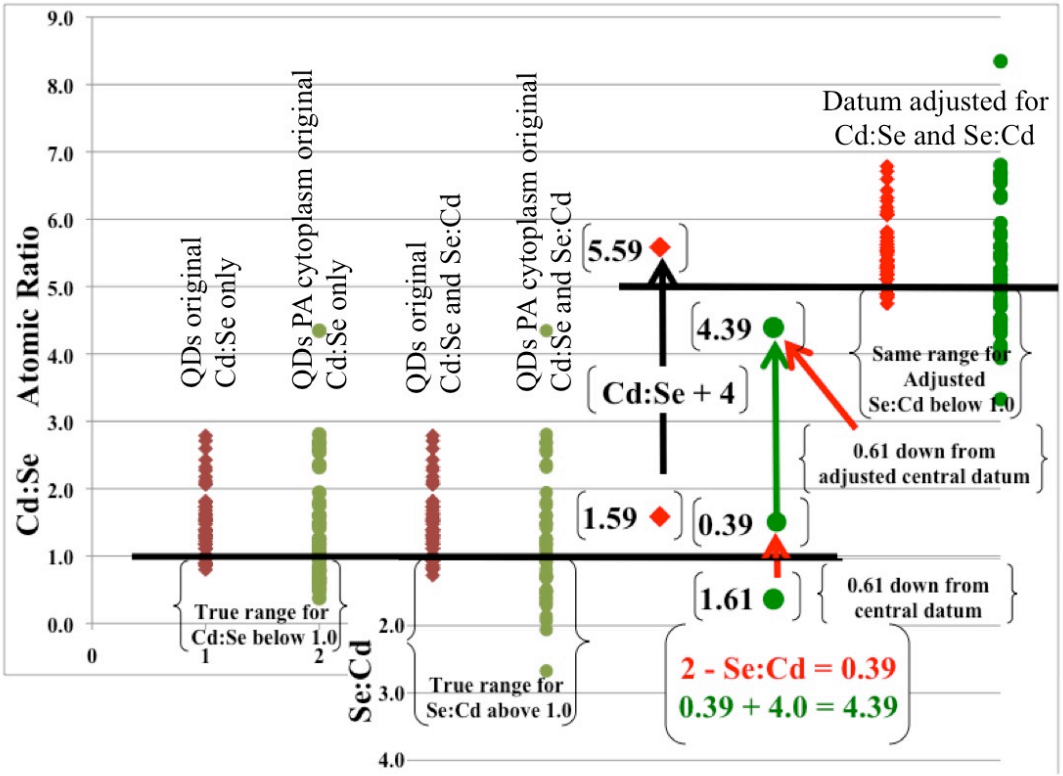

Figure V-5. PA contaminated with CdSe Quantum Dots for 24 hours. The STEM images show the progression of the cell's internal structural deformation (white star). The CdSe QDs are located in the PA cytoplasm, and associated with the PA cell wall (white arrows). The dark-field STEM imaging technique is atomic mass dependent and produces a brighter contrast where larger atomic masses of CdSe QDs are located.

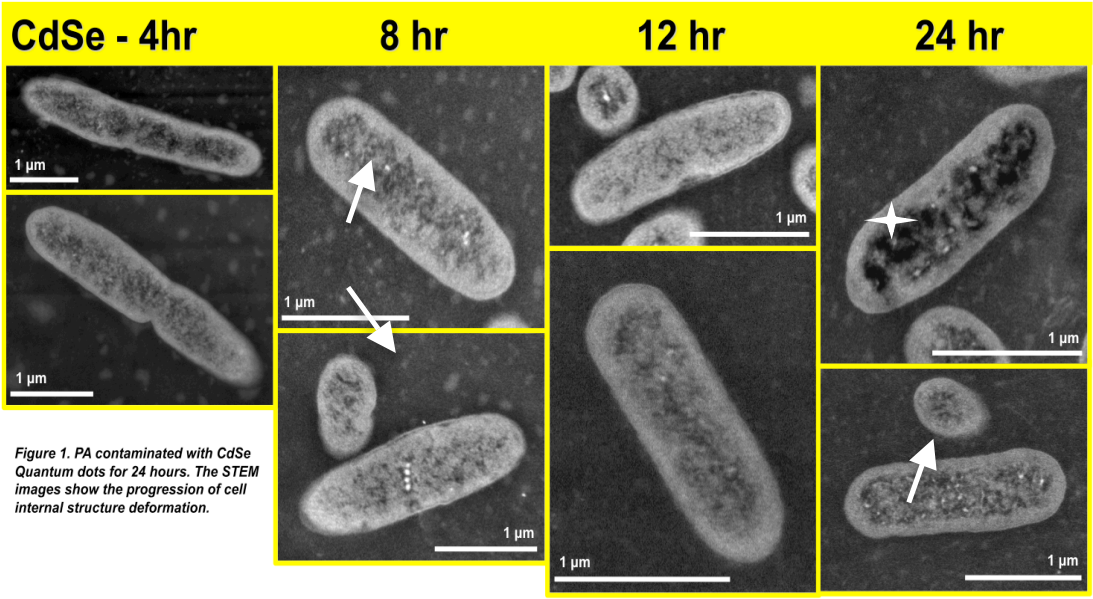

Figure V-6. PA contaminated with CdSe and CdTe QDs for 24 hours. The STEM images show the destruction of cell wall integrity from as early as 4 hour for both QDs (A - CdSe, B - CdTe). The 8 hour sample shows increased destruction of PA cells (C – CdSe, E – CdTe). The dead cells become prevalent in the 12 hour CdSe sample (E – CdSe) and by 24 hour regions will have very few viable looking PA cells (F – CdTe, G – CdSe).

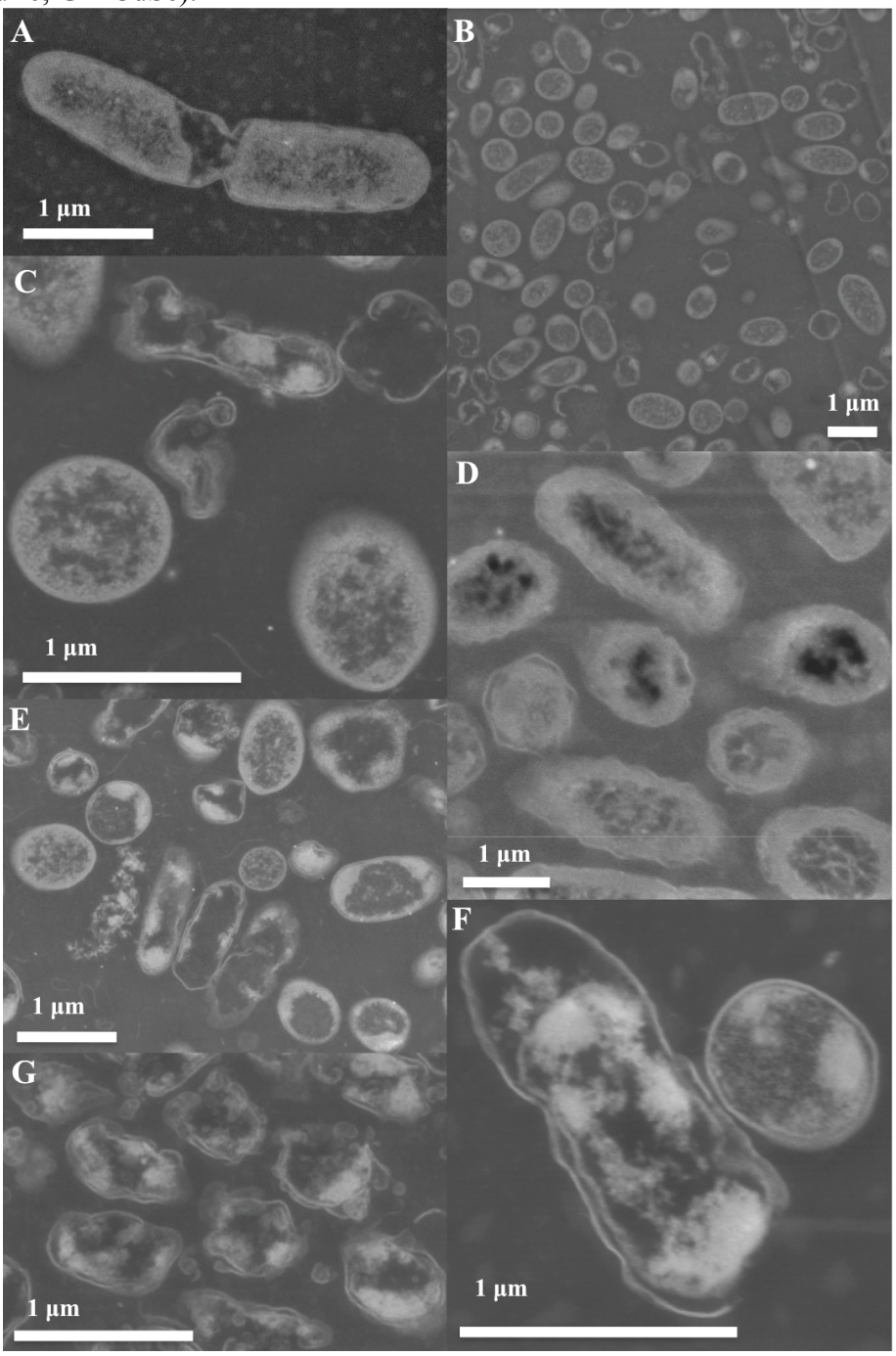

Figure V-7. STEM-EDS analyses for CdSe QDs (filled circle) starting material, PA cytoplasm-associated QDs (diamond), PA cell wall-associated QDs (triangle), and QDs located away from PA cells (blue-filled circle). A total of ~ 50 EDS analyses were acquired for each of the three specific region for each time point. The replicate (n=x) is for the number of replicates for either Cd: Se or Se: Cd. Whole numbers were maintained in determining appropriate atomic ratio placement in graph to visually maintain similar spacing for Cd-enriched (pink region) or Se-enriched (green region) QDs. The EDS analyses that calculated atomic percentages for only Cd, or only Se, are indicated by the lower (n=x) in the respective Cd (pink) region or Se (green) region. These EDS results could be from CdSe QDs with selenium concentrations below the detectable level, or are bright cellular locations where only cadmium is present and vice-versa for bright spots, with only Se having a calculated atomic percentage.

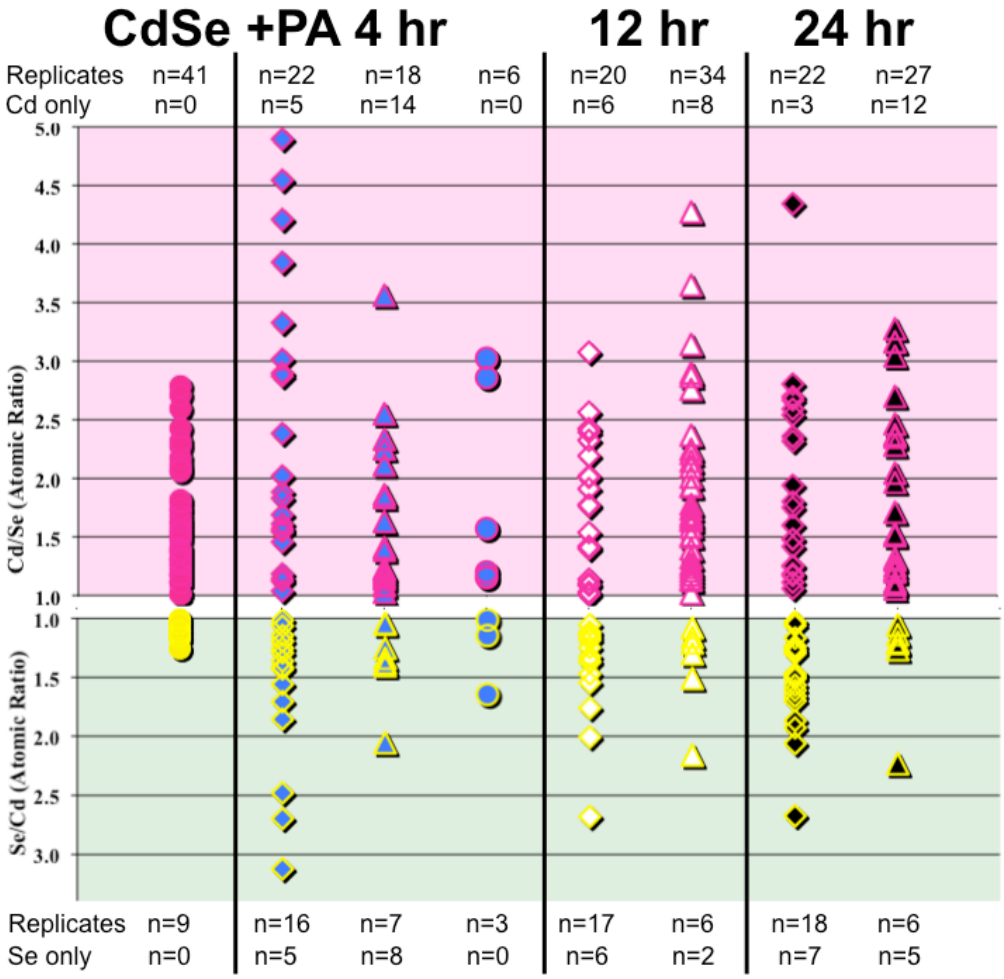

Figure V-8. STEM-EDS analyses were taken of QDs located in PA cytoplasm, QDs associated with PA cell wall, and QDs outside PA in the medium. The starting material (SM-QDs) QDs was also analyzed to determine how weathering of QDs progressed during the 24 h contamination study. A total of ~50 EDS replicates were determined to be either Cd-enriched QDs, or Se-enriched QDs, by the respective Cd: Se (<1.0) or Cd: Se (>1.0; Se: Cd greater than 1). The SM-CdSe QDs resulted in 82% showing Cd-enriched QDs and SM-CdTe QDs had 52% of the EDS analyses showing Cd-enriched QDs. The PA CdSe QD study had Cd-enriched QDs in the cytoplasm being reduced to 50%, showing that the QDs were becoming Se-enriched QDs. The PA CdTe QD study showed the Cd-enriched QDs associated with the PA cell wall was reduced to 18% indicating the trend toward Se-enriched QDs.

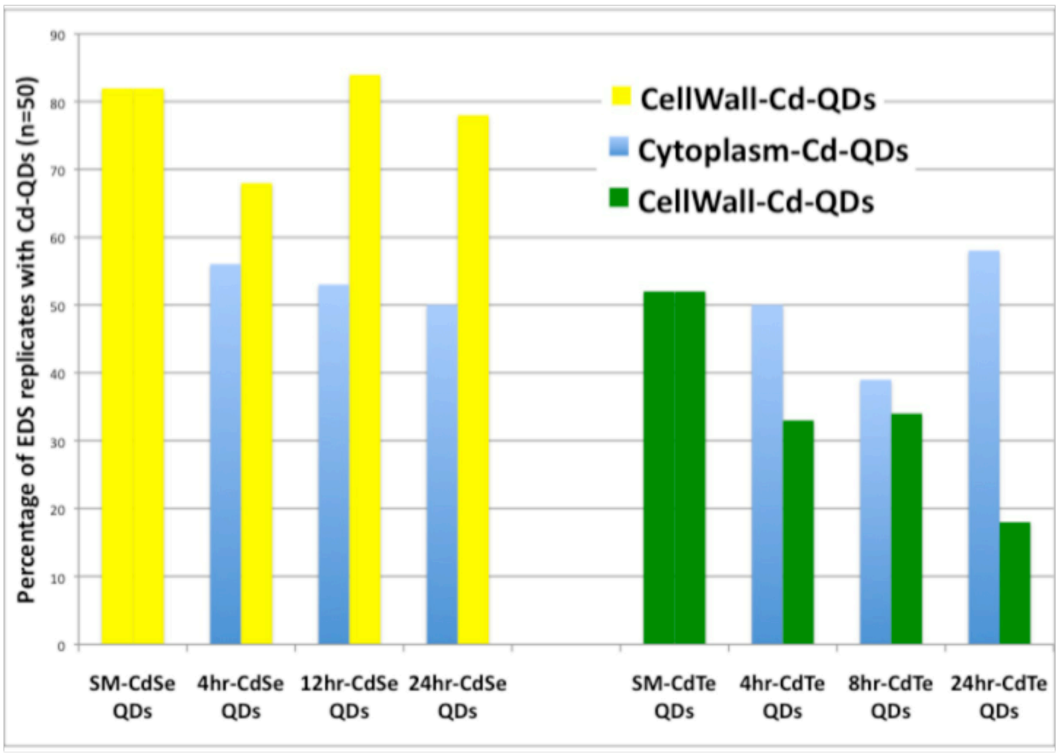

Figure V-9. PA contaminated with CdTe Quantum dots for 24 h. The STEM images show the progression of cell internal structural deformation (white star). The CdTe QDs are located in the PA cytoplasm and associated with the PA cell wall (white arrows). The dark-field STEM imaging technique is atomic mass dependent that produces brighter contrast where larger atomic masses of CdTe QDs are located.

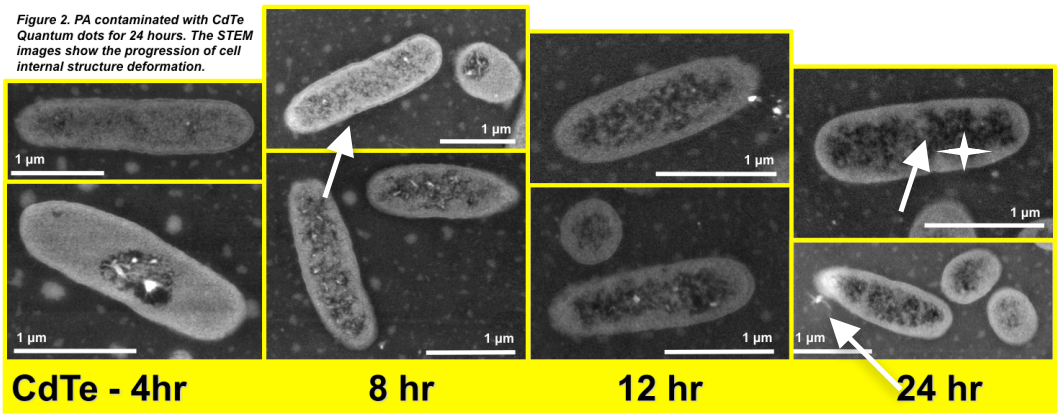

Figure V-10. STEM-EDS analyses for CdTe QDs (filled circle) starting material, PA cytoplasm-associated QDs (diamond), PA cell wall-associated QDs (triangle), and QDs located away from PA cells (black-filled circle). A total of ~50 EDS analyses were acquired for each of the three specific regions for each time point. The replicate (n=x) is for the number of replicates for either Cd: Te or Te: Cd. Values above one were maintained in determining appropriate atomic ratio placement in the graph, to visually maintain similar spacing for Cd-enriched (pink region) or Te-enriched (green region) QDs. The EDS analyses that calculated atomic percentage for only Cd or only Te are indicated by the lower (n=x) in the respective Cd (pink) region or Te (green) region. These EDS results could be from CdTe QDs with tellurium concentrations below the detectable level or are bright cellular locations, where only cadmium is present, and vice-versa for bright spots with only Te having a calculated atomic percentage.

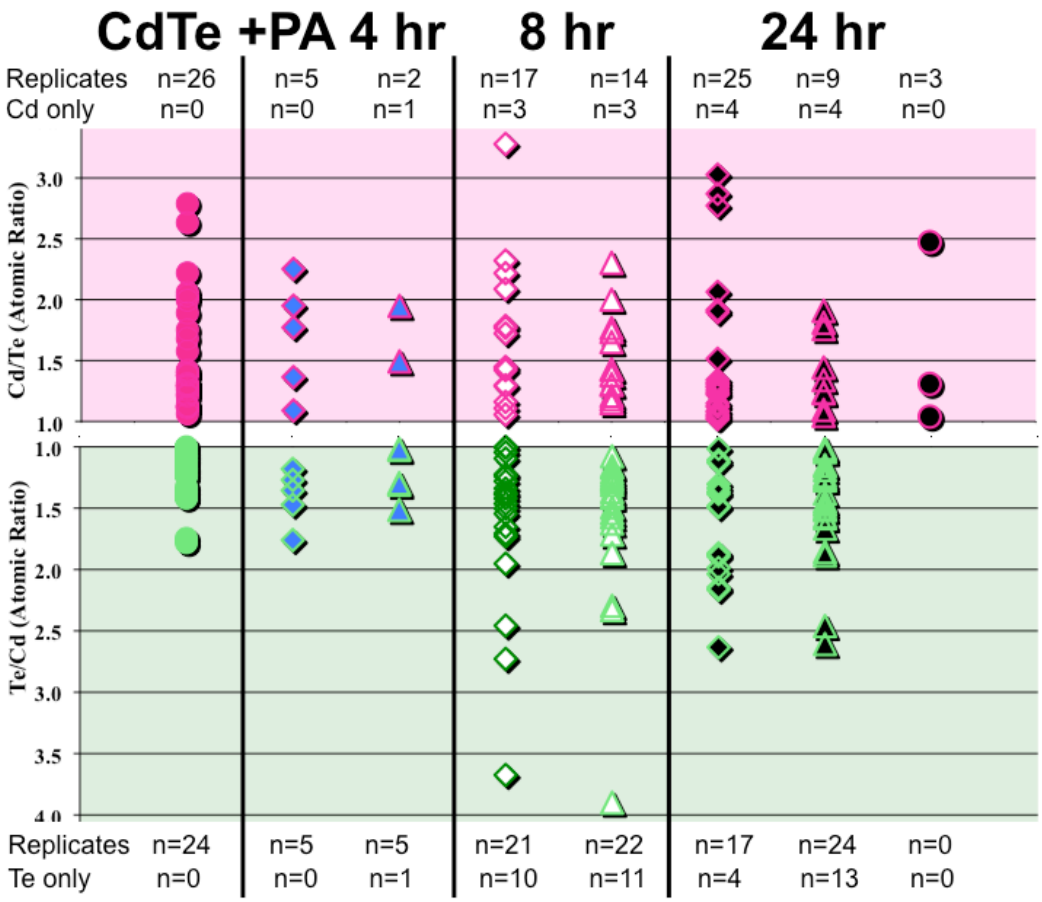

Figure V-11. PA contaminated with 0.075 mg mL^{-1} Cd^{+2}, 0.075 mg mL^{-1} Cd^{+2} and 0.2 mg mL^{-1} SeO_3^{-2} in LB broth for 24 h. The STEM images show Cd^{+2} bright spots within the periplasmic space cell. The Cd^{+2} and SeO_3^{-2} contaminated PA STEM images show distinct bright spots located in the cytoplasm and associated with the PA cell wall. The scale bars are 1 µm for all images.

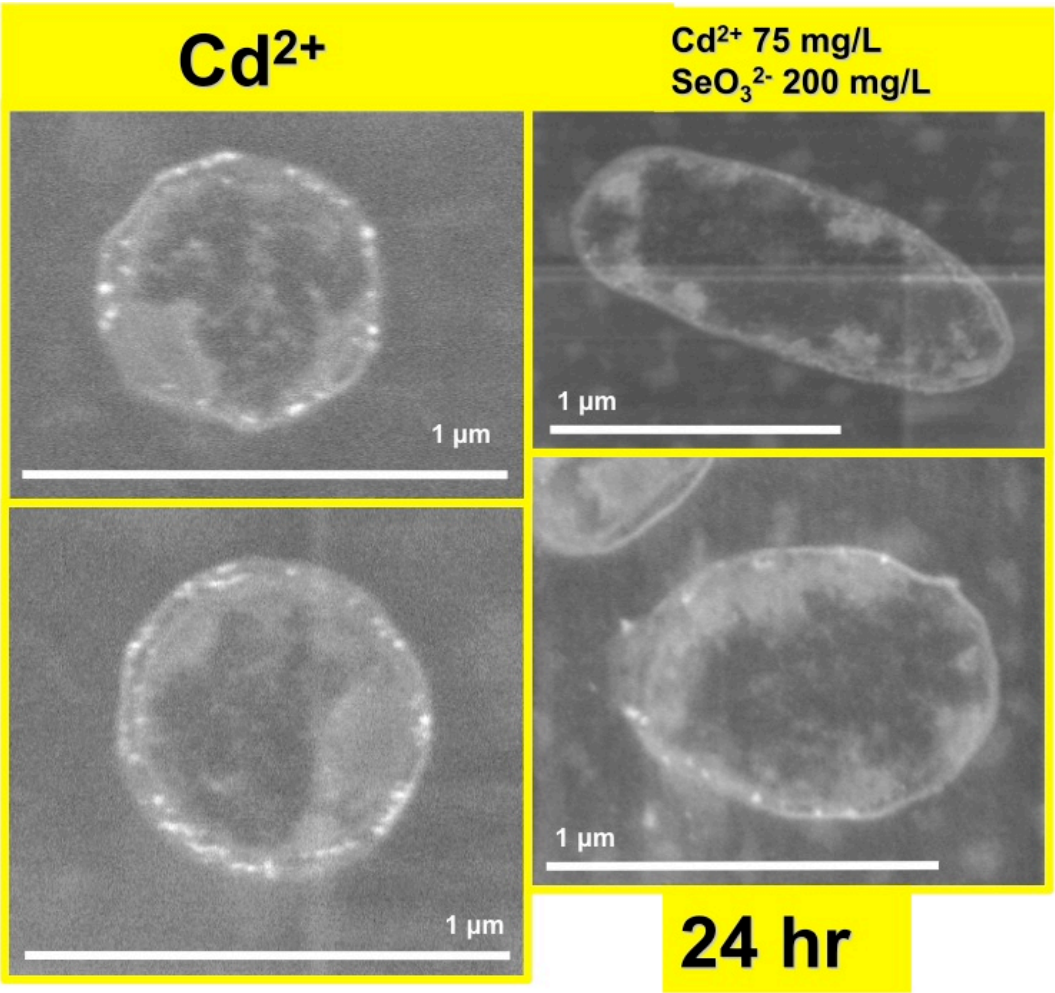

Figure V-12. STEM-EDS analyses were taken of QDs located in PA cytoplasm, QDs associated with PA cell wall and QDs outside PA in the medium. The starting material (SM-QDs) QDs was also analyzed to determine how weathering of QDs progress during the 24 h contamination study. A total of ~50 EDS replicates were determined to be either Cd-enriched QDs or Se-enriched QDs by the respective Cd: Se (<1.0) or Cd: Se (>1.0; Se: Cd greater than 1). The SM-CdSe QDs resulted in 82% showing Cd-enriched QDs and SM-CdTe QDs had 52% of the EDS analyses showing Cd-enriched QDs. The PA Cd^{+2} and SeO_3^{-2} salt study had Cd-enriched QDs in the cytoplasm being 50% showing the QDs were becoming Se-enriched QDs. The QDs associated with the PA cell wall had 16 analyses resulting in Cd-enriched CdSe QD and 20 that showed only Cd, which could have indicated that either Cd-enriched QDs where Se is below the detection limit, or a build up of Cd^{+2} ions.

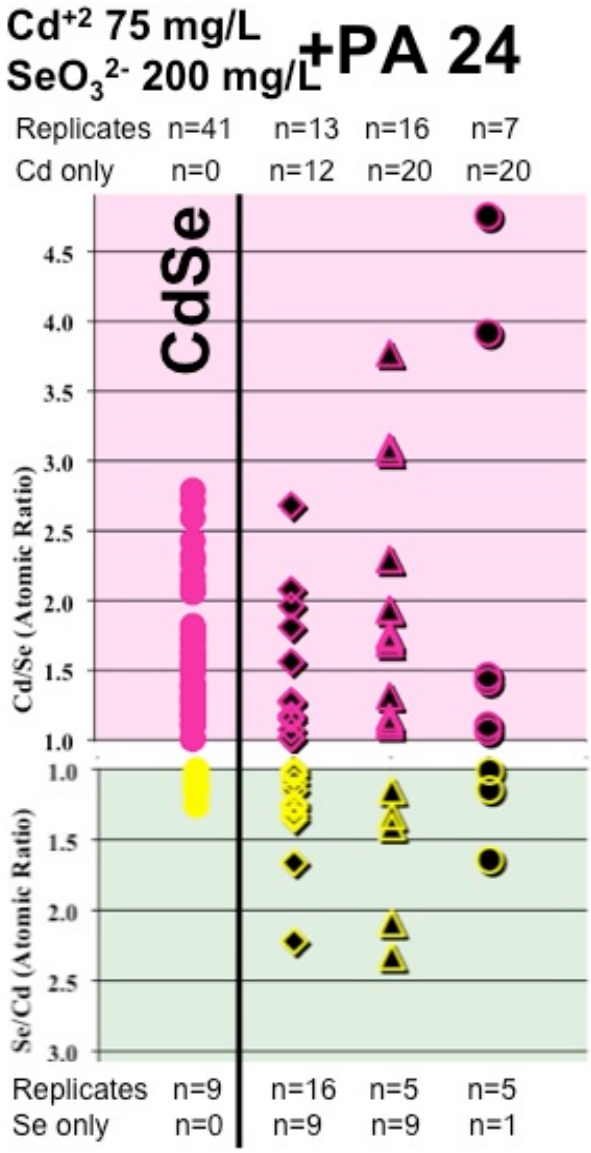

Figure V-13. STEM-EDS analyses were taken of QDs located in TT contaminated with CdSe QDs PA after 8 h contamination. The TT cell membrane had 10 replicates of CdSe atomic ratios similar to the starting materials QDs (Figure V-2). The TT cellular organelles show the presence of CdSe QDs located throughout the TT cell.

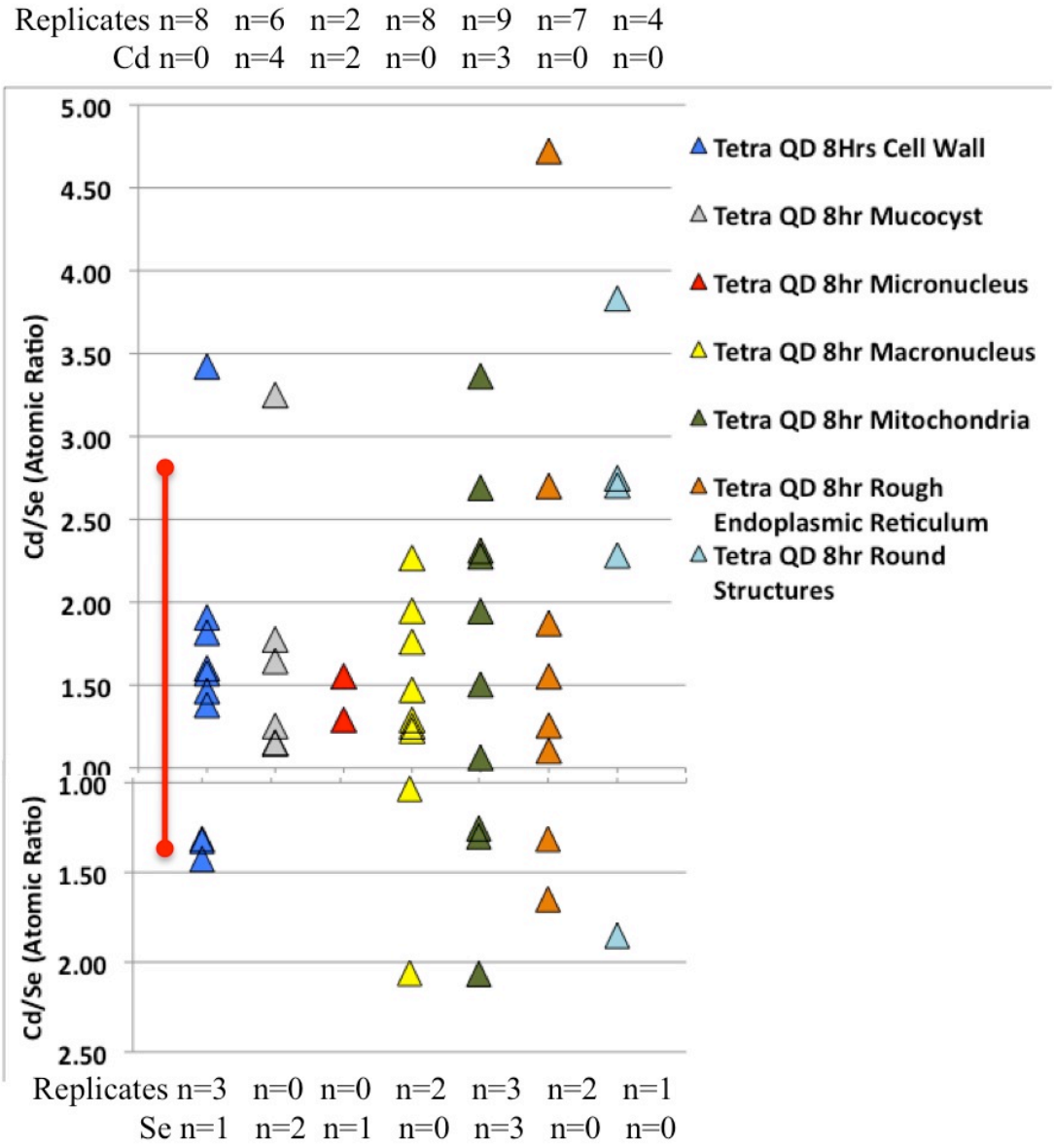

Figure V-14. STEM-EDS analyses were taken of QDs located in TT contaminated with CdSe QDs PA after 24 h contamination. The TT cell membrane had 9 replicates of CdSe atomic ratios similar to the starting materials QDs (Figure V-2). The TT cellular organelles show the presence of CdSe QDs located throughout the TT cell. The greatest potential use of STEM-EDS is determining how the QDs are weathering in the different chemical environments that are present in the different TT organelles.

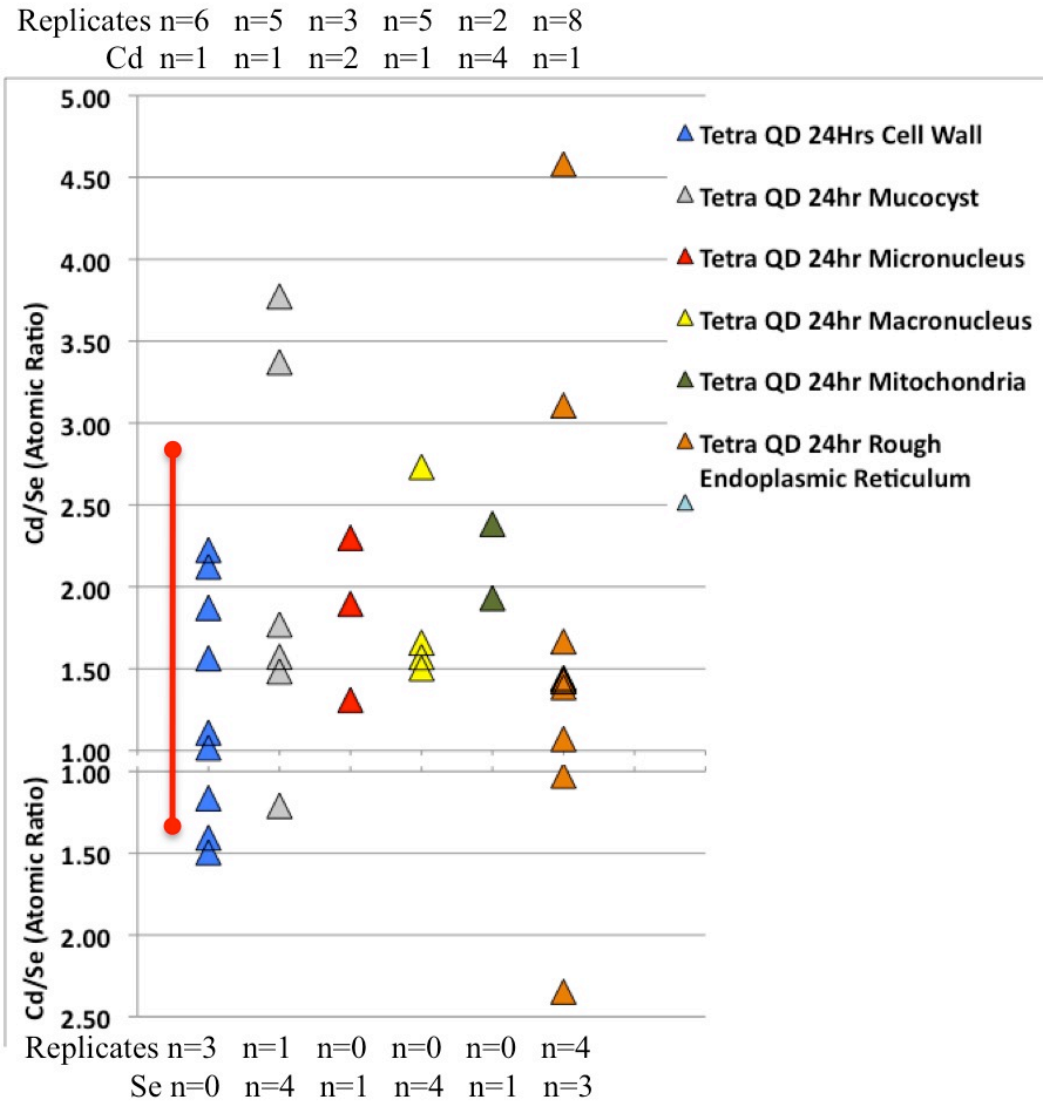

CONCLUSION

Nanomaterials in the environment, both natural and man-made, may contribute to the emergence of life on a different planet and the destruction of all life on this planet. Through this dissertation research, there have been great advances in showing that nanomaterials (NMs) can be degraded through serpentization as well as the chemical etching power of hydrogen and carbon dioxide gas at high pressure and moderate temperatures. This physical geological setting is present on a possibly only few of the billion planets in the solar system and it takes only time and water to make what we call life a true reality. Signs of life on Earth for the past ~1.1 billion years are in the form of stromatolites (Allwood 2007) and nanomaterials have co-existed with life on Earth during life's development. But can this reality of life be taken down and destroyed by nano-sized materials in the environment? The answer is simply 'YES'. What man has to do is not manufacture NMs that can destroy life on Earth.

This research has been able to produce iron sulfide NMs and analyze the mineral structure resulting in a chemically highly reactive effluent that produces new iron sulfide 'hydrothermal vent'-like chimney structures. These structures have large surface areas in wall-lined compartments making them ideal locations for the concentration of organic molecules generated from the hydrothermal vent system. These organic molecules are similar to the 5-mer peptides that enhance a periodic wall formation while structurally strengthening the chimney. All of these structures for the emergence of life are directly influenced by the chemistry of the effluent

indicating the ability for life to form in a wide range of environmental conditions that could occur on other planets in the solar system. These chimney structures are based on flow of energy or electrons across a physical barrier and as long as there is a difference in chemical properties across the membrane energy will continue to do work. Over the hundred thousand years they have been in existence, these chimney structures have contributed to the production of the simple organic building blocks needed for the emergence of life on Earth.

Life's emergence can be observed with scientific equipment that can visualize life below the micron-scale and observe how microorganisms interact with the new expansive world. Millimeter size rocks will look like mountain ranges and nanometer size rocks look like a loaf of bread. Using scanning transmission electron microscopy (STEM), we have investigated two distribution methods of nanometer size structures (NMs) from bacteria to higher trophic level organisms. Specifically, we show that CdSe QDs NMs are internalized by bacteria, and $nTiO_2$ NMs are encrusted on bacterial surfaces.

Both distribution methods for NMs were shown to be toxic to some extent to higher trophic level organisms that predominately feed on bacteria. The CdSe QDs contaminated PA caused the death of the TT protozoa, while the $nTiO_2$ encrusted PA slowed TT growth rate. These interpretations were accomplished through image analysis of STEM micrographs, a technique that makes it possible to evaluate NMs' immediate destructive properties and locations within higher trophic level organisms

by bypassing conventional destructive chemical analytical methods that compromise the integrity of the finer organelle structures observed in protozoa.

Image analysis of these organelle structures is limited. The use of EDS to determine the atomic percentages of elements became the next tool used to investigate NM alteration within the different chemical environments of the protozoan organelles. The use of STEM-EDS at low accelerating voltages was essential in analyzing the weathering of CdSe and CdTe QDs by bacteria. The development of this method has shown that PA cytoplasmic space will chemically etch the different QDs in distinctively different ways. The CdSe QDs were stripped of the Cd and became Se-enriched QDs. The CdTe QDs on the other hand did not chemically weather in the cytoplasmic space but did weather when associated with the PA cell wall, where CdSe QDs showed little surface weathering in similar locations. This very interesting weathering phenomenon will require further investigation to truly understand how the cytoplasm and cell wall chemical environments will weather different QDs.

The STEM-EDS was also useful in evaluating the presence of CdSe QDs that were formed in the cytoplasm of PA cells from the introduction of Cd^{+2} and SeO_3^{-2} salts in LB medium. The CdSe mineral structure was maintained throughout the crystal producing similar EDS atomic percentages as those produced from the analysis of manufactured CdSe QDs. The biologically produced CdSe QDs is formed by the reduction of the Se atom to its elemental charge. This redox reaction can only

be accomplished biologically or under reducing conditions not generally associated with LB broth. This study further enhances the use of the EDS technique in evaluating nanometer size structures, allowing us a greater degree of certainty in our interpretation of NM elemental composition.

The STEM-EDS method was also used to further investigate QD distribution in protozoan organelles during contamination studies that fed TT a CdSe QD PA diet. We observed the bioaccumulation of QDs throughout the TT cell and organelles. The range of CdSe atomic ratio was similar to the starting material QDs and only by looking at larger EDS replicates did a trend start to appear. The QDs in the organelles and associated with the TT cell were being stripped of the Se atoms and becoming statistically Cd-enriched QDs when compared to the starting material QDs. This weathering pattern is opposite to the pattern observed in the bacterial cell cytoplasm. The true understanding of why Se is selectively etched off the QD is still needs to be further investigated, and any interpretation at this time would be at best conjecture.

What has emerged through this research is the great benefit of STEM imaging of NMs and the EDS analytical advantages of using low accelerating voltages that do not obliterate NMs during the analysis process. The ability to investigate micron size entities at high magnification makes it possible to study the most elemental biological and chemical structures on our planet, leading to the promise of utilizing these techniques on worlds beyond our solar system.

REFERENCES

Abrajano, T. A., N. C. Sturchio, B. M. Kennedy, G. L. Lyon, K. Muehlenbachs, and J. K. Bohlke. Geochemistry of reduced gas related to serpentinization of the Zambales ophiolite, Philippines. *Applied Geochemistry,* 5:625–630 (1990).

Abramov, O. and S. J. Mojzsis. Microbial habitability of the Hadean Earth during the late heavy bombardment. *Nature,* 459:419–422 (2009).

Adams, M. W. W. The evolutionary significance of the metabolism of tungsten by microorganisms growing at 100C. In thermophiles: the keys to molecular evolution and the origin of life? edited by J. Wiegel and M. W. W. Adams, Taylor and Francis, London and Philadelphia, pp 325–338 (1998).

Allen, J. F. Redox homeostasis in the emergence of life. On the constant internal environment of nascent living cells. *The Journal of Cosmology,* 10:3362–3373 (2010).

Allen, D. E. and W. E. Seyfried. Serpentinization and heat generation: constraints from Lost City and Rainbow hydrothermal systems. *Geochimica et Cosmochimica Acta,* 68:1347–1354 (2004).

Allwood, A. C., M. R. Walter, I. W. Burch, and B. S. Kamber. 3.43 billion-year-old stromatolite reef from the Pilbara Craton of Western Australia: Ecosystem-

scale insights to early life on Earth. *Precambrian Research*, 158:198-227 (2007).

Ariztegui, D., and J. Dobson. Magnetic investigations of framboidal greigite formation: a record of anthropogenic environmental changes in eutrophic Lake St Moritz, Switzerland. *The Holocene,* 6:235–241 (1996).

Arnot, J. A., and F. Gobas. A review of bioconcentration factor (BCF) and bioaccumulation factor (BAF) assessments for organic chemicals in aquatic organisms. *Environmental Reviews* 14:257-297 (2006).

Aruguete, D. M., J. S. Guest, W. W. Yu, N. G. Love, and M. F. Hochella Jr. Interaction of CdSe/CdS core-shell quantum dots and *Pseudomonas aeruginosa*. *Environmental Chemistry,* 7:28–35 (2010).

Baaske, P., F. Weinert, S. Duhr, K. Lemke, M. J. Russell, and D. Braun. Extreme accumulation of nucleotides in simulated hydrothermal pore systems. *Proceedings of the National Academy Science of the USA*, 104:9346–9351 (2007).

Bahcall, J. N., M. H. Pinsonneault, and S. Basu. Solar models: current epoch and time dependences, neutrinos, and helioseismological properties. *Astrophysics Journal,* 555:990–1012 (2001).

Bähr, G., A. Ayalon, F. D. Rompf, and P. Hirsch-Ayalon. Discrimination between the permeation of H^+ and OH^- ions in precipitation membranes. *Journal of Membrane Science,* 20:103–111 (1984).

Baltscheffsky, M., A. Schultz, and H. Baltscheffsky. H^+-PPases: a tightly membrane-bound family. *Federation of European Biochemical Societies Letters,* 457:527–533 (1999).

Banks, D. A. A fossil hydrothermal worm assemblage from the Tynagh lead-zinc deposit in Ireland. *Nature,* 313:128–131 (1985).

Barge, L. M., M. J. Russell, and I. Kanik. Precipitation patterns of iron minerals in a chemical gradient: a laboratory analog to hydrothermal environments on the early Earth [abstract 1099]. In *42nd Lunar and Planetary Science Conference*, Lunar and Planetary Institute, Houston (2011).

Barnes, S. J. Introduction to nickel sulfide orebodies and komatiites of the Black Swan area, Yilgarn Craton, Western Australia. *Mineralium Deposita,* 39:679–683 (2004).

Barnes, I., J. B. Rapp, and J. R. O'Neil. Metamorphic assemblages and the direction of flow of metamorphic fluids in four instances of serpentinization. *Contribution to Mineral Petrology,* 35:263–276 (1972).

Baymann, F., E. Lebrun, M. Brugna, B. Schoepp-Cothenet, M. T. Giudici-Orticoni, and W. Nitschke. The redox protein construction kit: prelist

universal common ancestor evolution of energy-conserving enzymes. *Philosophical Transactions of the Royal Society London B: Biological Sciences,* 358:267–274 (2003).

Bazylinski, D. A., and R. Frankel. Magnetosome formation in prokaryotes. *Microbiology: Nature Reviews,* 2:217-230 (2004).

Beinert, H., R. H. Holm, and E. Münck. Iron-sulfur clusters: nature's modular, multipurpose structures. *Science,* 277:653–659 (1997).

Bekker, A., M. E. Barley, M. L. Fiorentini, O. J. Rouxel, D. Rumble, and S. W. Beresford. Atmospheric sulfur in Archean komatiite-hosted nickel deposits. *Science,* 326:1086–1089 (2009).

Benning, L. G., T. Rick, R. T. Wilkin, and H. L. Barnes. Reaction pathways in the Fe–S system below 100°C. *Chemical Geology,* 167:25–51 (2000).

Berg, I. A., D. Kockelkorn, W. H. Ramos-Vera, R. F. Say, J. Zarzycki, M. Hügler, B. E. Alber, and G. Fuchs. Autotrophic carbon fixation in archaea. *National Reviews Microbiology,* 8:447–460 (2010).

Boenigk, J., C. Matz, K. Jurgens, and H. Arndt. Confusing selective feeding with differential digestion in bacterivorous nanoflagellates. *Journal Eukaryote Microbiology,* 48:425-432 (2001).

Bonatti, E., E. C. Simmons, D. Breger, P. R. Hamlyn, and J. Lawrence. Ultramafic rock/seawater interaction in the oceanic crust: Mg-silicate

(sepiolite) deposit from the Indian Ocean floor. *Earth Planet Science Letters,* 62:229–238 (1983).

Bondarenko, O., P. K. S. M. Rahman, T. J. Rahman, A. Kahru, and A. Ivask. Effects of rhamnolipids from *Pseudomonas aeruginosa* DS10-129 on luminescent bacteria: toxicity and modulation of cadmium bioavailability. *Microbial Ecology,* 59:3:588-600 (2010).

Bounama, C., S. Franck, and W. von Bloh. The fate of the Earth's ocean. *Hydrology and Earth System Sciences,* 5:569–575 (2001).

Bourdoiseau, J-A., M. Jeannin, R. Sabot, C. Rémazeilles, and P. Refait. Characterisation of mackinawite by Raman spectroscopy: effects of crystallisation, drying and oxidation. Corrosion Science 50:3247–3255 (2008).

Bourdoiseau, J-A., M. Jeannin, C. Rémazeilles, R. Sabot, and P. Refait. The transformation of mackinawite into greigite studied by Raman spectroscopy. *Journal of Raman Spectroscopy,* 42:496–504 (2010).

Boxall, A. B., K. Tiede, and Q. Chaudhry. Engineered nanomaterials in soils and water: how do they behave and could they pose a risk to human health? *Nanomedicine,* 2:919-927 (2007).

Boyce, A. J., M. L. Coleman, and M. J. Russell. Formation of fossil hydrothermal chimneys and mounds from Silvermines, Ireland. *Nature,* 306:545–550 (1983).

Bratbak, G. Bacterial biovolume and biomass estimations. *Applied Environmental Microbiology,* 49:1488-1493 (1985).

Braterman, P. S., A. G. Cairns-Smith, and R. A. Sloper. Photo-oxidation of hydrated Fe^{2+}—significance for banded iron formations. *Nature,* 303:163–164 (1983).

Brooks, D. J., J. R. Fresco, A. M. Lesk, and M. Singh. Evolution of amino acid frequencies in proteins over deep time: inferred order of introduction of amino acids into the genetic code. *Molecular Biology Evolution,* 19:1645–1655 (2002).

Budin, R., J. Bruckner, and J. W. Szostak. Formation of protocell-like vesicles in a thermal diffusion column. *Journal of American Chemistry Society*, 131:9628–9629 (2009).

Cairns-Smith, A. G. Genetic Takeover and the Mineral Origins of Life, Cambridge University Press, Cambridge (1982).

Canuto, V. M., J. S. Levine, T. R. Augustsson, and C. L. Imhoff. UV radiation from the young Sun and oxygen and ozone levels in the prebiological palaeoatmosphere. *Nature,* 296:816–820 (1982).

Cartwright, J., J. García-Ruiz, M. Novella, and F. Otálora. Formation of chemical gardens. *Journal of Colloid Interface Science,* 256:351–359 (2002).

Castro, I. A., M. Motizuki, H. Murai, M. C. Chiu, and R. S. S. F. Silva. Effect of anticaking agent addition and headspace reduction in the powdered-drink mix sensory stability. *Journal of Food Quality,* 29:3:203-215 (2006).

Charlou, J. L., L. P. Donval, C. Konn, H. Ondreas, Y. Fouquet, P. Jean-Baptiste, and E. Fourré. High production and fluxes of H_2 and CH_4 and evidence of abiotic hydrocarbon synthesis by serpentinization in ultramafic-hosted hydrothermal systems on the Mid-Atlantic Ridge. In Diversity of Hydrothermal Systems on Slow Spreading Ocean Ridges, edited by P. Rona, C. Devey, J. Dyment, and B. Murton, AGU Geophysical Monograph 188, American Geophysical Union, Washington DC (2010).

Chase, Z., and N. M. Price. Metabolic consequences of iron deficiency in heterotrophic marine protozoa. *Limnology Oceanography,* 42:1673-1684 (1997).

Cho S. J., D. Maysinger, M. Jain, B. Röder, S. Hackbarth, and F. M. Winnik. Long-term exposure to CdTe quantum dots causes functional Impairments in Live Cells. *Langmuir,* 23:1974–80 (2007).

Choksi, A. N., T. Poonawalla, and M. G. Wilkerson. Nanoparticles: a closer look at their dermal effects. *Journal of Drugs in Dermatology,* 9:475-481 (2010).

Christaki, U., I. Obernosterer, F. Van Wambeke, M. Veldhuis, N. Garcia, and P. Catala. Microbial food web structure in a naturally iron-fertilized area in the

Southern Ocean (Kerguelen Plateau). *Deep-Sea Research Part Ii-Topical Studies in Oceanography,* 55:706-719 (2008).

Clarke, S., R. E. Mielke, A. Aneal, P. A. Holden, and J. L. Nadeau. Bacterial and mineral elements in an Arctic biofilm: a correlative study using fluorescence and electron microscopy. *Microscopy & Microanalysis,* 16:2:99133, 1-13 (2010).

Corliss, J. B. On the creation of living cells in submarine hot spring flow reactors: attractors and bifurcations in the natural hierarchy dissipative systems. *Origin of Life Evolution Biosphere,* 19:381–382 (1986).

Cox, H. A., R. Hodyss, and J. L. Beauchamp. Cluster-phase reactions: gas-phase phosphorylation of peptides and model compounds with triphosphate anions. *Journal of American Chemistry Society,* 127:4084–4090 (2005).

da Silva, F. J. J. R., and R. J. P. Williams. The biological chemistry of the elements, Clarendon Press, Oxford (1991).

Davis, B. K. Molecular evolution before the origin of species. *Progress in Biophysics and Molecular Biology,* 79:77–133 (2002).

Delacour, A., G. L. Früh-Green, and S. M. Bernasconi. Sulfur mineralogy and geochemistry of serpentinites and gabbros of the Atlantis Massif (IODP Site U1309). *Geochimica et Cosmochimica Acta,* 72:5111–5127 (2008).

Demchick, P., and A. L. Koch. The permeability of the wall fabric of *Escherichia coli* and *Bacillus subtilis*. *Journal of Bacteriology,* 178:768-773 (1996).

Deplanche, K., and L. E. Macaskie. Biorecovery of gold by *Escherichia coli* and *Desulfovibrio desulfuricans*. *Biotechnology Bioengineering,* 99:1055-1064 (2008).

de Zwart, I. I., S. J. Meade, and A. J. Pratt. Biomimetic phosphoryl transfer catalysed by iron(II)-mineral precipitates. *Geochimica et Cosmochimica Acta,* 68:4093–4098 (2004).

Dobbek, H., V. Svetlitchnyi, L. Gremer, R. Huber, and O. Meyer. Crystal structure of a carbon monoxide dehydrogenase reveals a [Ni-4Fe-5S] cluster. *Science,* 293:1281–1285 (2001).

Douglas, S., W. Abbey, R. Mielke, P. Conrad, and I. Kanik. Textural and mineralogical biosignatures in an unusual microbialite from Death Valley, California. *Icarus,* 193:620-636 (2008).

Douville, E., J. L. Charlou, E. H. Oelkers, P. Bienvenu, C. F. J. Colon, J.P. Donval, Y. Fouquet, D. Prieur, and P. Appriou. The rainbow vent fluids (368140N, MAR): the influence of ultramafic rocks and phase separation on trace metal content in Mid-Atlantic Ridge hydrothermal fluids. *Chemical Geology,* 184:37–48 (2002).

Ducluzeau, A-L., R. van Lis, S. Duval, B. Schoepp-Cothenet, M. J. Russell, and W. Nitschke. Was nitric oxide the first strongly oxidizing terminal electron sink? *Trends in Biochemistry Sciences,* 34:9–15 (2009).

Dumas, E. M., V. Ozenne, R. E. Mielke, and J. L. Nadeau. Toxicity of CdTe quantum dots in bacterial strains. *Institute of Electrical and Electronics Engineers Transactions in NanoBiosciences,* 8:58-64 (2009).

Emmanuel, S., and B. Berkowitz. Suppression and stimulation of seafloor hydrothermal convection by exothermic mineral hydration. *Earth and Planetary Science Letters,* 243:657–668 (2006).

Eck, R. V., and M. O. Dayhoff. Evolution of the structure of ferredoxin based on living relics of primitive amino acid sequences. *Science,* 152:363–366 (1966).

Eichkorn, K., and R. Ahlrichs. Cadmium selenide semiconductor nanocrystals: a theoretical study. *Chemical Physics Letters,* 288:2-4:235-242 (1998).

Elkins-Tanton, L. T. Linked magma ocean solidification and atmospheric growth for Earth and Mars. *Earth and Planetary Science Letters,* 271:181–191 (2008).

Emmanuel, S. and B. Berkowitz. An experimental analogue for convection and phase separation in hydrothermal systems. *Journal of Geophysical Research,* 111:0148-0227 (2006).

Fallick, A. E., J. H. Ashton, A. J. Boyce, R. M. Ellam, and M. J. Russell. Bacteria were responsible for the magnitude of the world-class hydrothermal base-metal orebody at Navan, Ireland. *Economic Geology,* 96:885–890 (2001).

Fallick, A. E., M. Ilich, and M. J. Russell. A stable isotope study of the magnesite deposits associated with the Alpinetype ultramafic rocks of Yugoslavia. *Economic Geology,* 86:847–861 (1991).

Ferris, F. G., T. R. Jack, and B. J. Bramhill. Corrosion products associated with attached bacteria at an oil field water injection plant. *Canadian Journal of Microbiology,* 38:1320–1324 (1992).

Filtness, M. J., I. B. Butler, and D. Rickard. The origin of life: the properties of iron sulphide membranes. *Transactions of the Institution of Mining and Metallurgy, Section B: Applied Earth Science*, 112:171–172 (2003).

Firth, A. V., S. W. Haggat, P. K. Khann, S. J. Williams, J. W. Allen, S. W. Magennis, D. W. Samuel, and D. J. Cole-Hamilton. Production and luminescent properties of CdSe and CdS nanoparticle– polymer composites. *Journal of Luminescence,* 109:3-4:163–172 (2004).

Fouquet, Y., A. Wafik, P. Cambon, C. Mevel, G. Meyer, and P. Gente. Tectonic setting and mineralogical and geochemical zonation in the Snake Pit sulfide deposit (Mid- Atlantic Ridge at 23_N). *Economic Geology,* 88:2018–2036 (1993).

Foustoukos, D. I., I. P. Savov, and D. R. Janecky. Chemical and isotopic constraints on water/rock interactions at the Lost City hydrothermal field, 308N Mid-Atlantic Ridge. *Geochimica et Cosmochimica Acta,* 72:5457–5474 (2008).

Früh-Green, G. L., D. S. Kelley, F. M. Benasoni, J. A. Karson, K. A. Ludwig, D. A. Butterfield, C. Boschi, and G. Proskurowski. 30,000 years of hydrothermal activity at the Lost City vent field. *Science,* 301:495–498 (2003).

Fuchs, G. Alternative pathways of autotrophic CO_2 fixation. In Autotrophic Bacteria, edited by H.G. Schlegel and B. Bowen, Science Technology, Madison, WI, pp 365–382 (1989).

Gao, X., Y. Liu, Y. M. Cai, and Y. F. Zhao. a-amino acid behaves differently from b or c amino acids as treated by metaphosphate. *Amino Acids,* 34:47–53 (2008).

Gautason, B., H. T. Valtysson, H. Einarsson, A. Eythorsdottir, E. Bogason, and S. A. Steingrimsson. Arnarnesstrytur: a recently discovered active shallow marine hydrothermal system in Eyjafjördur, Iceland [abstract OS21C-02]. In *Eos Transactions AGU*, Vol. 86, Fall Meeting Supplement, American Geophysical Union, Washington DC (2005).

Ghafari, P., C. H. St-Denis, M. E. Power, X. Jin, V. Tsou, H. S. Mandal, N. C. Bols, and X. Tang. Impact of carbon nanotubes on the ingestion and digestion of bacteria by ciliated protozoa. *Nature Nanotechnology,* 3:347-351 (2008).

Gillan, D. C., and C. DeRidder. Morphology of a ferric iron-encrusted biofilm forming on the shell of a burrowing bivalve (Mollusca). *Aquatic Microbiology Ecology,* 12:1-10 (1997).

Gillan, D. C., J. Ribesse, and C. de Ridder. The iron-encrusted microbial community of *Urothoe poseidonis* (Crustacea, Amphipoda). *Journal of Sea Research,* 52:21-32 (2004).

Goldstein, J., D. Newbury, D. Joy, C. Lyman, P. Echlin, E. Lifshin, L. Sawyer, and J. Michael. Scanning electron microscopy and x-ray microanalysis. ISBN: 0-306-47292-9. Third Edition (2003).

Gottschalk, F., and B. Nowack. The release of engineered nanomaterials to the environment. *Journal of Environmental Monitoring,* 13:1145-1155 (2011).

Güde, H. Grazing by protozoa as selection factor for activated-sludge bacteria. *Microbial Ecology,* 5:225-237 (1979).

Guo, L., and P. H. Santschi. Ultrafiltration and its applications to sampling and characterisation of aquatic colloids, p. 159-221. *In* K. J. Wilkinson and J. R.

Lead (ed.), Environmental Colloids and Particles: Behaviour, Separation and Characterisation. John Wiley & Sons, Ltd, West Sussex (2007).

Hagan, W. J., A. Parker, A. Steuerwald, and M. Hathaway. Phosphate solubility and the cyanate-mediated synthesis of pyrophosphate. *Origin of Life Evolution Biosphere,* 37:113–122 (2007).

Hall, D. O., R. Cammack, and K. K. Rao. Role for ferredoxins in the origin of life and biological evolution. *Nature,* 233:136–138 (1971).

Hand, K. P., R. W. Carlson, and C. F. Chyba. Energy, chemical disequilibrium, and geological constraints on Europa. *Astrobiology,* 7:1006–1022 (2007).

Hand, K. P., C. F. Chyba, J. C. Priscu, R. W. Carlson, and K. H. Nealson. Astrobiology and the potential for life on Europa. In *Europa,* edited by R. Pappalardo, W. McKinnon, and K. Khurana, University of Arizona Press, Tucson, AZ, pp 589–629 (2010).

Harford, C., and B. Sarkar. Amino terminal Cu(II) and Ni(II) binding ATCUN motif of proteins and peptides. *Accounts of Chemical Research,* 30:123–130 (1999).

Haydon, N., S. E. McGlynn, and O. Robus. Speculation on quantum mechanics and the operation of life giving catalysts. *Origin of Life Evolution Biosphere,* 41:1:35-50 (2010).

Hennet, R. J-C., N. G. Holm, and M. H. Engel. Abiotic synthesis of amino acids under hydrothermal conditions and the origin of life: a perpetual phenomenon? *Naturwissenschaften,* 79:361–365 (1992).

Hoke, K. R., N. Cobb, F. A. Armstrong, and R. Hille. Electrochemical studies of arsenite oxidase: an unusual example of a highly cooperative two-electron molybdenum center. *Biochemistry,* 43:1667–1674 (2004).

Holbrook, R. D., K. E. Murphy, J. B. Morrow, and K. D. Cole. Trophic transfer of nanoparticles in a simplified invertebrate food web. *Nature Nanotechnology,* 3:352-355 (2008).

Houlé, M. G., C. M. Lesher, S. Préfontaine, J. A. Ayer, B. R. Berger, V. Taranovic, P. C. Davis, and B. Atkinson. Stratigraphy and physical volcanology of komatiites and Associated Ni-Cu-(PGE) mineralization in the western Abitibi Greenstone Belt, Timmins area, Ontario: a field trip for the 11th International Platinum Symposium, Open File Report 6255, Ontario Geological Survey, Mines and Minerals Division, Sudbury, ON, Canada (2010).

Horst, A. M., A. C. Neal, R. E. Mielke, P. R. Sislian, W. H. Suh, L. Mädler, G. D. Stucky, and P. A. Holden. Dispersion of TiO_2 nanoparticle agglomerates by *Pseudomonas aeruginosa*. *Applied Environmental Microbiology,* 76:7292-7298 (2010).

Hou, W. C., P. Westerhoff, and J. D. Posner. Biological accumulation of engineered nanomaterials: a review of current knowledge. *Environmental Science-Processes & Impacts*, 15:103-122 (2013).

Hovington P., D. Drouin, and R. Gauvin. CASINO : A new era of Monte Carlo code in C language for the electron beam interaction—Part I: Description of the program. *Scanning,* 19:1–14 (1997).

Huber, C., and G. Wächtershäuser. Activated acetic acid by carbon fixation on (Fe,Ni)S under primordial conditions. *Science,* 276:245–247 (1997).

Huber, C., and G. Wächtershäuser. Primordial reductive amination revisited. *Tetrahedron Letters,* 44:1695–1697 (2003).

Hunt, J. P. Porphyry copper deposits. *Economic Geology Monograph,* 8:192–206 (1991).

Izawa, M. R. M., H. W. Nesbitt, N. D. MacRae, and E. L. Hoffman. Composition and evolution of the early oceans: evidence from the Tagish Lake meteorite. *Earth Planetary Science Letters,* 298:443–449 **(**2010).

Jacobs, D. E., R. P. Clickner, J. Y. Zhou, S. M. Viet, D. A. Marker, J. W. Rogers, D. C. Zeldin, P. Broene, and W. Friedman. The prevalence of lead-based paint hazard in U.S. housing. *Environmental Health Perspectives,* 110:10: A599–606 (2002).

Jeol Excitation Table. http://www.unamur.be/universite/services/microscopie/sme-documents/Energy-20table-20for-20EDS-20analysis-1.pdf (2013).

Jeong, J-H., N. Goldenfeld, and J. A. Dantzig. Phase field model for three-dimensional dendritic growth with fluid flow. *Physics Review E of Statistical, Nonlinear, and Soft Matter Physics,* 64:4:1-14 (2001).

Johnson, D. B. Acidophilic microbial communities: candidates for bioremediation of acidic mine effluents. *International Biodeterioration Biodegradation,* 35:41-58 (1995).

Kaegi, R., A. Ulrich, B. Sinnet, R. Vonbank, A. Wichser, S. Zuleeg, H. Simmler, S. Brunner, H. Vonmont, M. Burkhardt, and M. Boller. Synthetic TiO_2 nanoparticle emission from exterior facades into the aquatic environment. *Environmental Pollution,* 156:233-239 (2008).

Kalyanasundaram, K., and M. Grätzel. Applications of functionalized transition metal complexes in photonic and optoelectronic devices. *Coordination Chemistry Reviews,* 177:347-414 (1998).

Kasting, J. F., D. H. Eggler, and S. P. Raeburn. Mantle redox evolution and the oxidation state of the Archean atmosphere. *Journal of Geology,* 101:245–257 (1993).

Kasuya, A., R. Sivamohan, Y. A. Barnakov, I. M. Dmitruk, T. Nirasawa, V. R. Romanyuk, V. Kumar, S. V. Mamykin, K. Tohji, B. Jeyadevan, K. Shinoda,

T. Kudo, O. Terasaki, Z. Liu, R. V. Belosludov, V. Sundararajan, and Y. Kawazoe. Ultrastable nanoparticles of CdSe revealed from mass spectrometry. *Nature Materials,* 3:2:99-102 (2004).

Kehew, A. E. Applied Chemical Hydrogeology, Prentice-Hall, Upper Saddle River, NJ (2001).

Kell, D.B. On the functional proton current pathway of electron transport phosphorylation: an electrodic view. *Biochimica et Biophysica Acta,* 549:55–99 (1979).

Keller, A. A., H. T. Wang, D. X. Zhou, H. S. Lenihan, G. Cherr, B. J. Cardinale, R. Miller, and Z. X. Ji. Stability and aggregation of metal oxide nanoparticles in natural aqueous matrices. *Environmental Science and Technology,* 44:1962-1967 (2010).

Kelley, D. S., J. A. Karson, D. K. Blackman, G. L. Früh-Green, D. A. Butterfield, M. D. Lilley, E. J. Olson, M. O. Schrenk, K. K. Roe, G. T. Lebon, P. Rivizzigno, and the AT3-60 Shipboard Party. An off-axis hydrothermal vent field near the Mid-Atlantic Ridge at 30_N. *Nature,* 412:145–149 (2001).

Kelley, D. S., J. A. Karson, G. L. Früh-Green, D. R. Yoerger, T. M. Shank, D. A. Butterfield, J. M. Hayes, M. O. Schrenk, E. J. Olson, G. Proskurowski, M. Jakuba, A. Bradley, B. Larson, K. Ludwig, D. Glickson, K. Buckman, A. S. Bradley, W. J. Brazelton, K. Roe, M. J. Elend, A. Delacour, S. M.

Bernasconi, M. D. Lilley, J. A. Baross, R. E. Summons, and S. P. Sylva. A serpentinite-hosted ecosystem: the Lost City hydrothermal field. *Science,* 307:1428–1434 (2005).

Kirk, S., J. Skepper, and A. M. Donald. Application of environmental scanning electron microscopy to determine biological surface structure. *Journal of Microscopy-Oxford,* 233:205-224 (2009).

Klaine, S. J., P. J. J. Alvarez, G. E. Batley, T. F. Fernandes, R. D. Handy, D. Y. Lyon, S. Mahendra, M. J. McLaughlin, and J. R. Lead. Nanomaterials in the environment: behavior, fate, bioavailability, and effects. *Environmental Toxicology Chemistry,* 27:1825-1851 (2008).

Kloepfer, J. A., R. E. Mielke, and J. L. Nadeau. Uptake of CdSe and CdSe/ZnS quantum dots into bacteria via purine-dependent mechanisms. *Applied and Environmental Microbiology,* 71:5:2548-2557 (2005).

Kloepfer, J. A., R. E. Mielke, M. S. Wong, K. H. Nealson, G. Stucky, and J. L. Nadeau. Quantum dots as strain- and metabolism-specific microbiological labels. *Applied Environmental Microbiology,* 69:4205-4213 (2003).

Kloper, V., R. Osovsky, J. Kolny-Olesiak, A. Sashchiuk, and E. Lifshitz. The growth of colloidal cadmium telluride nanocrystal quantum dots in the presence of Cd-0 nanoparticles. *Journal of Physical Chemistry C*, 111:10336-10341 (2007).

Knauth, L. P. and D. R. Lowe. High Archean climatic temperature inferred from oxygen isotope geochemistry of cherts in the 3.5 Ga Swaziland Supergroup, South Africa. *Geology Society of American Bulletin,* 115:566–580 (2003).

Köhler, B., A. Singer, and P. Stoffers. Biogenic nontronite from marine white smokers chimneys. *Clays and Clay Minerals,* 42:6:689-701 **(**1994).

Konn, C., J. L. Charlou, J. P. Donval, N. G. Holm, F. Dehairs, and S. Bouillon. Hydrocarbons and oxidized organic compounds in hydrothermal fluids from Rainbow and Lost City ultramafic-hosted vents. *Chemical Geology,* 258:299–314 (2009).

Koonin, E. V. An RNA-making reactor for the origin of life. *Proceeds from National Academy of Science in USA,* 104:9105–9106 (2007).

Koonin, E. V. and W. Martin. On the origin of genomes and cells within inorganic compartments. *Trends Genetics,* 21:647–654 (2005).

Koski, R. A., I. R. Jonasson, D. C. Kadko, V. K. Smith, and F. L. Wong. Compositions, growth mechanisms, and temporal relations of hydrothermal sulfide-sulfate-silica chimneys at the northern cleft segment, Juan de Fuca Ridge. *Journal of Geophysical Research Solid Earth,* 99B:4813–4832 (1994).

Krueger F. R., and J. Kissel. First direct chemical analysis of interstellar dust. Sterne und Weltraum 39:326-329 (2000).

Krupp, R. E. Phase relations and phase transformations between the low-temperature iron sulfides mackinawite, greigite, and smythite. *European Journal of Mineralogy,* 6:265–278 (1994).

Kudo, I., Y. Noiri, W. P. Cochlan, K. Suzuki, T. Aramaki, T. Ono, and Y. Nojiri. Primary productivity, bacterial productivity and nitrogen uptake in response to iron enrichment during the SEEDS II. *Deep-Sea Research Part Ii-Topical Studies in Oceanography,* 56:2755-2766 (2009).

Kump, L. R., and W. E. Seyfried. Hydrothermal Fe fluxes during the Precambrian: effect of low oceanic sulfate concentrations and low hydrostatic pressure on the composition of black smokers. *Earth and Planetary Science Letters,* 235:654–662 (2005).

Kwon, K. D., K. Refson, S. Bone, R. Qiao, W-L. Yang, Z. Liu, and G. Sposito. Magnetic ordering in tetragonal FeS: evidence for strong itinerant spin fluctuations. *Physics Reviews B Condensed Matter Material Physics,* 83:6:1-7 (2011).

Lambert, J. B., G. Lu, S. R. Singer, and V. M. Kolb. Silicate complexes of sugars in aqueous solution. *Journal of American Chemical Society,* 126:9611–9625 (2004).

Lambert, J. B., S. A. Gurusamy-Thangavelu, and M. Ma. The silicate-mediated formose reaction: bottom-up synthesis of sugar silicates. *Science,* 327:984–986 (2010).

Lane, N., J. F. Allen, and W. Martin. How did LUCA make a living? Chemiosmosis in the origin of life. *Bioessays,* 32:271–280 (2010).

Larter, R. C. L., A. J. Boyce, and M. J. Russell. Hydrothermal pyrite chimneys from the Ballynoe baryte deposit, Silvermines, County Tipperary, Ireland. *Mineralium Deposita,* 16:309–318 (1981).

Lawton, J. Novel Materials in the Environment: The case of nanotechnology. *Royal Commission on Environmental Pollution* (2008).

Lead, J. R., W. Davison, J. Hamilton-Taylor, and J. Buffle. Characterizing colloidal material in natural waters. *Aquatic Geochemistry,* 3:213-232 (1997).

Leduc, S. The Mechanism of Life, Rebman Ltd., London (1911).

Lennie, A. R., S. A. T. Redfern, P. E. Champness, C. P. Stoddart, P. F. Schofield, and D. J. Vaughan. Transformation of mackinawite to greigite: an in situ X-ray powder diffraction and transmission electron microscope study. *American Mineralogist,* 82:302–309 (1997).

Lesher, C. M., and W. E. Stone. Exploration geochemistry of komatiites. In trace element geochemistry of volcanic rocks: applications for massive sulphide

exploration, short course Notes Vol. 12, edited by D.A. Wyman, Geological Society of Canada, St. John's, Canada, pp 153–204 (1997).

Lévy, B. Laplace-Beltrami Eigenfunctions: towards an algorithm that ''understands'' geometry. In SMI 2006. *IEEE International Conference on Shape Modeling and Applications, Institute of Electrical and Electronics Engineers (IEEE),* New York, doi:10.1109/SMI.2006.21 (2006).

Lies, D. P., M. E. Hernandez, A. Kappler, R. E. Mielke, J. A. Gralnick, D. K. Newman. *Shewanella oneidensis* MR-1 uses overlapping pathways for iron reduction at a distance and by direct contact under conditions relevant for biofilms. *Applied and Environmental Microbiology,* 71:8:4414-4426 (2005).

Limbach, L. K., R. Bereiter, E. Mueller, R. Krebs, R. Gaelli, and W. J. Stark. Removal of oxide nanoparticles in a model wastewater treatment plant: influence of agglomeration and surfactants on clearing efficiency. *Environmental Science and Technology,* 42:5828-5833 (2008).

Ljungdahl, L. G. The acetyl-CoA pathway and the chemiosmotic generation of ATP during acetogenesis, In *Acetogenesis*, edited by H.L. Drake, Chapman and Hall, New York, pp 63–87 (1994).

Lowell, R. P., and P. A. Rona. Seafloor hydrothermal systems driven by the serpentinization of peridotite. *Geophysical Research Letters,* 29:11:26-1-26-4 (2002).

Ludwig, K. A., D. S. Kelley, D. A. Butterfield, B. K. Nelson, and G. L. Früh-Green. Formation and evolution of carbonate chimneys at the Lost City Hydrothermal Field. *Geochimica et Cosmochimica Acta,* 70:3625–3645 (2006).

Ludwig, K. A., D. S. Kelley, C. Shen, H. Cheng, and R. L. Edwards. U/Th geochronology of carbonate chimneys at the Lost City hydrothermal field [abstract V51B-1487]. In *Eos Transactions AGU*, Vol. 86, Fall Meeting Supplement, American Geophysical Union, Washington DC (2005).

Luo, Z. X., Z. H. Wang, Q. Z. Li, Q. K. Pan, C. Z. Yan, and F. Liu. Spatial distribution, electron microscopy analysis of titanium and its correlation to heavy metals: occurrence and sources of titanium nanomaterials in surface sediments from Xiamen Bay, China. *Journal of Environmental Monitoring,* 13:1046-1052 (2011).

Luoma, S. N., and P. S. Rainbow. Metal contamination in aquatic environments: science and lateral management. Cambridge University Press, Cambridge (2008).

Macleod, G., C. McKeown, A. J. Hall, and M. J. Russell. Hydrothermal and oceanic pH conditions of possible relevance to the origin of life. *Origin of Life Evolution Biosphere,* 24:19–41 (1994).

Maden, B. E. H. Tetrahydrofolate and tetrahydromethanopterin compared: functionally distinct carriers in C1 metabolism. *Biochemical Journal,* 350:609–629 (2000).

Mahendra, S., H. G. Zhu, V. L. Colvin, and P. J. Alvarez. Quantum dot weathering results in microbial toxicity. *Environmental Science & Technology,* 42:9424-9430 (2008).

Marteinsson, V. T., J. K Kristjánsson, H. Kristmannsdóttir, M. Dahlkvist, K. Sæmundsson, M. Hannington, S. K. Pétursdóttir, A. Geptner, and P. Stoffers. Discovery of giant submarine smectite cones on the seafloor in Eyjafjordur, Northern Iceland, and a novel thermal microbial habitat. *Applied and Environmental Microbiology,* 67:827–833 (2001).

Martin, W., J. Baross, D. Kelley, and M. J. Russell. Hydrothermal vents and the origin of life. *National Review of Microbiology,* 6:805–814 (2008).

Martin, W., and M. J. Russell. On the origin of cells: an hypothesis for the evolutionary transitions from abiotic geochemistry to chemoautorophic prokaryotes, and from prokaryotes to nucleated cells. *Philosophical Transaction Review Society London B Biological Sciences,* 358:27–85 (2003).

Martin, W., and M. J. Russell. On the origin of biochemistry at an alkaline hydrothermal vent. *Philosophical Transaction Review Society London B Biological Sciences,* 362:1887–1925 (2007).

Martin, R. S., T. A. Mather, and D. M. Pyle. Volcanic emissions and the early Earth atmosphere. *Geochimica et Cosmochimica Acta,* 71:3673–3685 (2007).

Martin, W., J. Baross, D. Kelley, and M. J. Russell. Hydrothermal vents and the origin of life. *National Review of Microbiology,* 6:805–814 (2008).

Mast, C. B., and D. Braun. Thermal trap for DNA replication. *Physics Review Letters,* 104, doi:10.1103/PhysRevLett.104.188102 (2010).

Maynard, A. D., and E. Michelson. The nanotechnology consumer products inventory; PEN: Washington, DC (2007).

McGlynn, S. E., D. W. Mulder, E. M. Shepard, J. B. Broderick, and J. W. Peters. Hydrogenase cluster biosynthesis: organometallic chemistry nature's way. *Dalton Transactions,* 4274– 4285 (2009).

McGinness, S., and D. B. Johnson. Grazing of acidophilic bacteria by a flagellated protozoan. *Microbial Ecology,* 23:75-86 (1992).

McNulty G. S. Production of titanium dioxide. Plenary lecture. NORM V International Conference. Sevilla, Spain, v.pl.3.eu-norm.org/index.pdf (2007).

Menon, P., S. Becquevort, G. Billen, and P. Servais. Kinetics of flagellate grazing in the presence of two types of bacterial prey. *Microbial Ecology,* 31:89-101 (1996).

Michalkova, A., Y. Kholod, D. Kosenkov, L. Gorb, and J. Leszczynski. Viability of pyrite pulled metabolism in the 'iron-sulfur world' theory: quantum chemical assessment. *Geochimica et Cosmochimica Acta,* 75:1933–1941 (2011).

Mielke, R. E., K. J. Robinson, L. M. White, S. E. McGlynn, K. McEachem, R. Bhartia, I. Kanik, and M. J. Russell. Iron-sulfide-bearing chimneys as potential energy traps at life's emergence. *Astrobiology,* 11:10:1-18 (2011).

Mielke, R. E., M. J. Russell, P. R. Wilson, S. McGlynn, M. Coleman, R. Kidd, and I. Kanik. Design, fabrication and test of a hydrothermal reactor for origin-of-life experiments. *Astrobiology,* 10:799–810 (2010).

Mileyeva-Biebesheimer, O. N., A. Zaky, and C. L. Gruden. Assessing the impact of titanium dioxide and zinc oxide nanoparticles on bacteria using a fluorescent-based cell membrane integrity assay. *Environmental Engineering Science,* 27:329-335 (2010).

Milner-White, E. J., and M. J. Russell. Predicting the conformations of peptides and proteins in early evolution. *Biology Direct,* 3:3:1-9 (2008).

Milner-White, E. J., and M. J. Russell. Polyphosphatepeptide synergy and the organic takeover at the emergence of life. *The Journal of Cosmology,* 10:3217–3229 (2010).

Mitchell, P. (1961). Coupling of phosphorylation to electron and hydrogen transfer by a chemi-osmotic type of mechanism. *Nature,* 191:4784:144–148.

Mitra-Delmotte, G., and A. N. Mitra. Magnetism, FeS colloids, and origins of life. In *The legacy of Alladi Ramakrishnan in the mathematical sciences,* edited by K. Alladi, J.R. Klauder, and C.R. Rao, Springer, New York, pp 529–564 (2010).

Mojzsis, S. J., G. Arrhenius, K. D. McKeegan, T. M. Harrison, A. P. Nutman, and C. R. L. Friend. Evidence for life on Earth before 3,800 million years ago. *Nature,* 384:55–59 (1996).

Mueller, N. C., and B. Nowack. Nanoparticles for remediation: Solving big problems with little particles. *Elements,* 6:395-400 (2010).

Neal, C., and G. Stanger. Calcium and magnesium hydroxide precipitation from alkaline groundwater in Oman, and their significance to the process of serpentinization. *Mineralogical Magazine,* 48:237–241 (1984).

Nicoll, F. H. A hysteresis effect in photoconductive cadmium selenide and its use in a solid-state image storage device. *IEEE Transactions on Electron Devices,* 5:2:115-115 (1958).

Nitschke, W., and M. J. Russell. Hydrothermal focusing of chemical and chemiosmotic energy, supported by delivery of catalytic Fe, Ni, Mo/W, Co, S

and Se, forced life to emerge. *Journal of Molecular Evolution,* 69:481–496 (2009).

Nitschke, W., and M. J. Russell. Just like the Universe the emergence of life had high enthalpy and low entropy beginnings. *Journal of Cosmology,* 10:3200–3216 (2010).

Nitschke, W. and M. J. Russell. Redox bifurcations: mechanisms and importance to life now, and at its origin. *BioEssays,* 34:DOI 10.1002/bies.201100134 (2011).

Nohynek, G. J., E. Antignac, T. Re, and H. Toutain. Safety assessment of personal care products/cosmetics and their ingredients. *Toxicology and Applied Pharmacology,* 243:239-259 (2010).

Ohfuji, H., and D. Rickard. Experimental syntheses of framboids—a review. *Earth-Science Reviews,* 71:147–170 (2005).

Ohno, T., K. Sarukawa, K. Tokieda, and M. Matsumura. Morphology of a TiO_2 photocatalyst (Degussa, P-25) consisting of anatase and rutile crystalline phases. *Journal of Catalysis,* 203:82-86 (2001).

Pagano, J. J., T. Bánsági, and O. Steinbock. Bubble templated and flow-controlled synthesis of macroscopic silica tubes supporting zinc oxide nanostructures. *Angewandte Chemie International Edition, English,* 120:10048–10051 (2008).

Pages, D., J. Rose, S. Conrod, S. Cuine, P. Carrier, T. Heulin, and W. Achouak. Heavy metal tolerance in *Stenotrophomonas maltophilia*. *PLOS One,* 2:1539 (2008).

Palandri, J., and M. H. Reed. Geochemical models of metasomatism in ultramafic systems: serpentinization, rodingitization, and sea floor carbonate chimney precipitation. *Geochimica et Cosmochimica Acta,* 68:1115–1133 (2004).

Patel, N. G., C. J. Panchal, and K. K. Makhija. Use of cadmium selenide thin films as a carbon dioxide gas sensor. *Crystal Research and Technology,* 29:7:1013–1020 (2006).

Pernthaler, J. Predation on prokaryotes in the water column and its ecological implications. *Nature Reviews Microbiology,* 3:537-546 (2005).

Peyton, B. M. Effects of shear stress and substrate loading rate on *Pseudomonas aeruginosa* biofilm thickness and density. *Water Research*, 30:1:29-36 (1996).

Phillips, L. G., and D. M. Barbano. The influence of fat substitutes based on protein and titanium dioxide on the sensory properties of lowfat milks. *Journal Dairy Science,* 80:2726-2731 (1997).

Pollmann, K., J. Raff, M. Merroun, K. Fahmy, and S. Selenska-Pobell. Metal binding by bacteria from uranium mining waste piles and its technological applications. *Biotechnology Advances,* 24:1:58-68 (2006).

Postberg, F., J. Schmidt, J. Hillier, S. Kempf, and R. Srama. A salt-water reservoir as the source of a compositionally stratified plume on Enceladus. *Nature,* 474:620–622 (2011).

Priester, J. H., Y. Ge, R. E. Mielke, A. M. Horst, S. C. Moritz, K. Espinosa, J. Gelb, S. L. Walker, R. M. Nisbet, Y-J. An, J. P. Schimel, R. G. Palmer, J. A. Hernandez-Viezcas, L. Zhao, J. L. Gardea-Torresdey, and P. A. Holden. Soybean susceptibility to manufactured nanomaterials with evidence for food quality and soil fertility interruption. *Proceedings of the National Academy of Sciences,* 109:E2451-E2456 (2012).

Priester, J. H., P. K. Stoimenov, R. E. Mielke, S. M. Webb, C. Ehrhardt, J. P. Zhang, G. D. Stucky, and P. A. Holden. Effects of soluble cadmium salts versus CdSe quantum dots on the growth of planktonic *Pseudomonas aeruginosa*. *Environmental Science and Technology,* 43:2589-2594 (2009).

Proskurowski, G., M. D. Lilley, D. S. Kelley, and E. J. Olson. Low temperature volatile production at the Lost City Hydrothermal Field, evidence from a hydrogen stable isotope geothermometer. *Chemical Geology,* 229:331–343 (2006).

Proskurowski, G., M. D. Lilley, J. S. Seewald, G. L. Früh-Green, E. J. Olson, J. E. Lupton, S. P. Sylva, and D. S. Kelley. Abiogenic hydrocarbon production at Lost City hydrothermal field. *Science,* 319:604–607 (2008).

Rabinowitz, J., R. Flores, R. Krebsback, and G. Rogers. Peptide formation in the presence of linear or cyclic polyphosphates. *Nature,* 224:795–796 (1969).

Rabone, J., Y-F. Yue, S. Y. Chong, K. C. Stylianou, J. Bacsa, D. Bradshaw, G. R. Darling, N. G. Berry, Y. Z. Khimyak, A. Y. Ganin, P. Wiper, J. B. Claridge, and M. J. Rosseinsky. An adaptable peptide-based porous material. *Science,* 329:1053–1057 (2010).

Rémazeilles, C., M. Saheb, D. Neff, E. Guilminot, K. Tran, J-A. Bourdoiseau, R. Sabot, M. Jeannin, H. Matthiesen, P. Dillmann, and P. Refait. Microbiologically influenced corrosion of archaeological artefacts: characterisation of iron(II) sulfides by Raman spectroscopy. *Journal of Raman Spectroscopy,* 41:1425–1433 (2010).

Rickard, D., and G. W. Luther. Chemistry of iron sulfides. *Chemical Reviews,* 107:514–562 (2007).

Rickard, D., R. Knott, R. Duckworth, and B. Murton. Organ pipes, beehive diffusers and chimneys at the Broken Spur hydrothermal sulphide deposits. *Mineralogist Magazine,* 58A:774–775 (1994).

Rickard, D., I. B. Butler, and A. Olroyd. A novel iron sulphide switch and its implications for Earth and planetary science. Earth Planetary Science Letters, 189:85–91 (2001).

Rico, C. M., S. Majumdar, M. Duarte-Gardea, J. R. Peralta-Videa, and J. L. Gardea-Torresdey. Interaction of nanoparticles with edible plants and their possible implications in the food chain. *Journal Agricultural Food Chemistry,* 59:3485–3498 (2011).

Robichaud, C. O., A. E. Uyar, M. R. Darby, L. G. Zucker, and M. R. Wiesner. Estimates of upper bounds and trends in nano-TiO_2 production as a basis for exposure assessment. *Environmental Science and Technology,* 43:4227-4233 (2009).

Rogach, A. L., D. Nagesha, J. W. Ostrander, M. Giersig, and N. A. Kotov. "Raisin bun"-type composite spheres of silica and semiconductor nanocrystals. *Chemistry of Materials,* 12:9:2676-2685 (2000).

Rosenthal, S. J., J. McBride, S. J. Pennycook, and L. C. Feldman. Synthesis, surface studies, composition and structural characterization of CdSe, core/shell and biologically active nanocrystals. *Surface Science Reports,* 62:111-157 (2007).

Rosing, M. T. 13C-depleted carbon microparticles in > 3700-Ma sea-floor sedimentary rocks from west Greenland. *Science,* 283:674–676 (1999).

Rothery, R. A., G. J. Workun, and J. H. Weiner. The prokaryotic complex iron–sulfur molybdoenzyme family. *Biochimica et Biophysica Acta,* 1778:1897–1929 (2008).

Royal Commission Report. Novel materials in the environment: the case of nanotechnology. *Royal Commission on Environmental Pollution*, TSO (2008).

Ruska, E. Nobel Lectures, Physics 1981-1990, Editor-in-Charge Tore Frängsmyr, Editor Gösta Ekspång, World Scientific Publishing Co., Singapore (1993).

Russell, M. J. Downward-excavating hydrothermal cells and Irish-type ore deposits: importance of an underlying thick Caledonian Prism. *Transactions of the Institution of Mining and Metallurgy. Section B: Applied Earth Science,* 89:B168–B171 (1978).

Russell, M. J., R. M. Daniel, A. J. Hall, and J. Sherringham. A hydrothermally precipitated catalytic iron sulphide membrane as a first step toward life. *Journal of Molecular Evolution,* 39:231–243 (1994).

Russell, M. J., and A. J. Hall. The emergence of life from iron monosulphide bubbles at a submarine hydrothermal redox and pH front. *Journal of Geology Society London,* 154:377–402 (1997).

Russell, M. J., and A. J. Hall. From geochemistry to biochemistry: chemiosmotic coupling and transition element clusters in the onset of life and photosynthesis. *The Geochemical News,* No. 113, October 6–12 (2002).

Russell, M. J., and A. J. Hall. The onset and early evolution of life. In evolution of aarly Earth's atmosphere, hydrosphere, and biosphere—constraints from ore

deposits, Geological Society of America Memoir 198, edited by S. Kesler and H. Ohmoto, Geological Society of America, Boulder, CO, pp 1–32 (2006).

Russell, M. J., A. J. Hall, A. G. Cairns-Smith, and P. S. Braterman. Submarine hot springs and the origin of life. *Nature,* 336:117 (1988).

Russell, M. J., A. J. Hall, and W. Martin. Serpentinization as a source of energy at the origin of life. *Geobiology,* 8:5:355-71 (2010).

Russell, M. J., A. J. Hall, and D. Turner. In vitro growth of iron sulphide chimneys: possible culture chambers for origin-of-life experiments. *Terra Nova,* 1:238–241 (1989).

Russell, M. J., and I. Kanik. Why does life start, what does it do, where will it be, and how might we find it? *The Journal of Cosmology,* 5:1008–1039 (2010).

Russell, M. J., and W. Martin. The rocky roots of the acetyl- CoA pathway. *Trends in Biochemistry Sciences,* 29:358–363 (2004).

Russell, M. J., and H. Skauli. A history of theoretical developments in carbonate-hosted base metal deposits and a new tri-level enthalpy classification. *Economic Geology Monograph,* 8:96–116 (1991).

Sadiq, I. M., N. Chandrasekaran, and A. Mukherjee. Studies on effect of TiO_2 nanoparticles on growth and membrane permeability of *Escherichia coli*, *Pseudomonas aeruginosa*, and *Bacillus subtilis*. *Current Nanoscience,* 6:381-387 (2010).

Salisbury, M. H. Leg 195 Shipboard Scientific Party Site 1200. In Proceedings of the Ocean Drilling Program, Initial Reports, Vol. 195, Ocean Drilling Program, College Station, TX. Available online at http://www-odp.tamu.edu/publications/ 195_IR/195TOC.HTM (2002).

Sawlowicz, Z. Pyrite framboids and their development: a new conceptual mechanism. *Geologische Rundschau,* 82:148–156 (1993).

Sawlowicz, Z. Framboids: from their origin to application. Prace Mineralogiczne 88:1–80 (2000).

Say, R. F., and G. Fuchs. Fructose 1,6-bisphosphate aldolase/ phosphatase may be an ancestral gluconeogenic enzyme. *Nature,* 464:1077–1081 (2010).

Schoonen, M. A. A., Y. Xu, and J. Bebie. Energetics and kinetics of the prebiotic synthesis of simple organic and amino acids with the FeS-H_2/FeS_2 redox couple as reductant. *Origin of Life Evolution Biosphere,* 29:5–32 (1999).

Schrödinger, E. What is life? The physical aspects of the living cell, Cambridge University Press, Cambridge (1944).

Schüler, D., and R. B. Frankel. Bacterial magnetosomes: microbiology, biomineralization and biotechnological applications. *Applied Microbiological Biotechnology,* 52:4:464-473 (1999).

Seewald, J. S., M. Y. Zolotov, and T. McCollom. Experimental investigation of single carbon compounds under hydrothermal conditions. *Geochimica et Cosmochimica Acta,* 70:446–460 (2006).

Sherr, E. B., and B. F. Sherr. Significance of predation by protists in aquatic microbial food webs. *Antonie van Leeuwenhoek International Journal G,* 81:293-308 (2002).

Shibuya, T., T. Komiya, K. Nakamura, K. Takai, and S. Maruyama. Highly alkaline, high-temperature hydrothermal fluids in the early Archean ocean. *Precambrian Research,* 182:230–238 (2010).

Shock, E., and P. Canovas. The potential for abiotic organic synthesis and biosynthesis at seafloor hydrothermal systems. *Geofluids,* 10:161–192 (2010).

Shock, E. L. Stability of peptides in high-temperature aqueous solutions. *Geochimica et Cosmochimica Acta,* 56:3481–3491 (1992).

Sievers, A., M. Beringer, M. V. Rodnina, and R. Wolfenden. The ribosome as an entropy trap. *Proceeds of National Academy of Science in USA,* 101:7897–7901 (2004).

Sikes, C. S., M. L. Yeung, and A. P. Wheeler. Inhibition of calcium carbonate and phosphate crystallization by peptides enriched in aspartic acid and phosphoserine. In *surface reactive peptides and polymers*, ACS Symposium

Series Vol. 444, American Chemical Society, Washington DC, pp 50–71 (1991).

Silverman, D. C., D. J. Kalota, and F. S. Stover. Effect of pH on corrosion inhibition of steel by polyaspartic acid. *Corrosion,* 51:818–826 (1995).

Simoncini, E., A. Kleidon, and E. Gallori. The emergence of life: thermodynamics of chemical free energy generation in off-axis hydrothermal vent systems and its consequences for compartmentalization and life's origins. *The Journal of Cosmology,* 10:3325–3344 (2010).

Smirnov, A., D. Hausner, R. Laffers, D. R. Strongin, and M. A. A. Schoonen. Abiotic ammonium formation in the presence of Ni-Fe metals and alloys and its implications for the Hadean nitrogen cycle. *Geochemica Transactions,* 9:5 (2008).

Sondi, I., and B. Salopek-Sondi. Silver nanoparticles as antimicrobial agent: a case study on *E. coli* as a model for Gram-negative bacteria. *Journal of Colloid Interface Science,* 275:177-182 (2004).

Stockbridge, R. B., C. A. Lewis, Y. Yuan, and R. Wolfenden. Impact of temperature on the time required for the establishment of primordial biochemistry, and for the evolution of enzymes. *Proceeds to National Academy of Science in USA,* 107:22102– 22105 (2010).

Stone, D. A., and R. E. Goldstein. Tubular precipitation and redox gradients on a bubbling template. *Proceeds to National Academy of Science in USA,* 101:11537–11541 (2004).

Suresh, A. K., D. A. Pelletier, and M. J. Doktycz. Relating nanomaterial properties and microbial toxicity. *Nanoscale,* 5:463-474 (2013).

Tarduno, J. A., R. D. Cottrell, M. K. Watkeys, A. Hofmann, P. V. Doubrovine, E. E. Mamajek, D. Liu, D. G. Sibeck, L. P. Neukirch, and Y. Usui. Geodynamo, solar wind, and magnetopause 3.4 to 3.45 billion years ago. *Science,* 37:1238– 1240 (2010).

Taylor, J.R. An introduction to error analysis: the study of uncertainties in physical measurements 2nd ed. University Science Books, Sausalito, CA (1997).

Tkachuk, A., F. Duewer, H. Cui, M. Feser, S. Wang, and W. Yun. X-ray computed tomography in zernike phase contrast mode at 8 keV with 50-nm resolution using Cu rotating anode X-ray source. *Zeitschrift für Kristallographie,* 222:650-655 (2007).

Torrance, G. M., D. P. Leader, D. R. Gilbert, and E. J. Milner-White. A novel main chain motif in proteins bridged by cationic groups: the niche. *Journal of Molecular Biology,* 385:1076–1086 (2009).

Tóth, Á., D. Horváth, R. Smith, J. R. McMahan, and J. Maselko. Phase diagram of precipitation morphologies in the $Cu^{2+}(PO_3)_4$ system. *Journal of Physical Chemistry C Nanomaterial Interfaces,* 111: 14762–14767 (2007).

Traube, M. Experimente zur Theorie der Zellenbildung und Endosmose. Archiv fër Anatomie. *Physiologie und wissenschaftliche Medicin,* 1867:87–165 (1867).

Turcotte, D. L., J. L. Cisne, and J. C. Nordmann. On the evolution of the lunar orbit. *Icarus,* 30:254–266 (1977).

Twining, B. S., M. R. Twiss, and N. S. Fisher. Oxidation of thallium by freshwater plankton communities. *Environmental Science and Technology,* 37:2720-2726 (2003).

Vance, S., J. Harnmeijer, J. Kimura, H. Hussmann, B. Demartin, and J. M. Brown. Hydrothermal systems in small ocean planets. *Astrobiology,* 7:987–1005 (2007).

Vaughan, D. J., and J. R. Craig. Mineral Chemistry of Metal Sulfides. Cambridge University Press, Cambridge (1978).

Villota, R., and J. G. Hawkes. Food Applications and the Toxicological and Nutritional Implications of Amorphous-Silicon Dioxide. *CRC Critical Reviews in Food Science and Nutrition,* 23:4:289-321 (1986).

Vogel, C., and N. S. Fisher. Trophic transfer of Fe, Zn and Am from marine bacteria to a planktonic ciliate. *Marine Ecology-Progress Series,* 384:61-68 (2009).

Volbeda, A., and J. C. Fontecilla-Camps. Catalytic nickel– iron–sulfur clusters: from minerals to enzymes. *In topics in organometallic chemistry*, Vol. 17, edited by G. Simmonneaux, Springer, Berlin, pp 57–82 (2006).

Wächtershäuser, G. From volcanic origins of chemoautotrophic life to Bacteria, Archaea and Eukarya. *Philosophical Transactions in Research Society London B Biological Sciences,* 361:1787–1808 (2006).

Walker, J. C. G. Carbon dioxide on the early Earth. *Origin of Life Evolution Biosphere,* 16:117–127 (1985).

Watson, J. D., and E. J. Milner-White. A novel main-chain anion-binding site in proteins: the nest. A particular combination of u,w values in successive residues gives rise to anion binding sites that occur commonly and are found often at functionally important regions. *Journal of Molecular Biology,* 315:171–182 (2002).

Wei, D., and K. Osseo-Asare. Formation of iron monosulphide: a spectrophotometric study of the reaction between ferrous and sulphide ions in aqueous solutions. *Journal of Colloid Interface Science,* 174:273–282 (1995).

Weir, A., P. Westerhoff, L. Fabricius, K. Hristovski, and N. von Goetz. Titanium dioxide nanoparticles in food and personal care products. *Environmental Science Technology,* 46:2242-2250 (2012).

Werlin, R., J. H. Priester, R. E. Mielke, S. Krämer, S. Jackson, P. K. Stoimenov, G. D. Stucky, G. N. Cherr, E. Orias, and P. A. Holden. Biomagnification of cadmium selenide quantum dots in a simple experimental microbial food chain. *Nature Nanotechnology,* 6:65-71 (2011).

Wetzel, L. R., and E. L. Shock. Distinguishing ultramafic from basalt-hosted submarine hydrothermal systems by comparing calculated vent fluid compositions. *Journal of Geophysical Research,* 105:8319–8340 (2000).

Wiebe, R., and V. L. Gaddy. The solubility of hydrogen in water at 0, 50, 75 and 1008 from 25 to 1000 atmospheres. *Journal of American Chemical Society,* 56:76–79 (1934).

Wilkin, R. T., and H. L. Barnes. Formation processes of framboidal pyrite. *Geochimica et Cosmochimica Acta,* 61:323–339 (1997).

Wilson, M. E., and B. E. Britigan. Iron acquisition by parasitic protozoa. *Parasitology Today,* 14:348-353 (1998).

Wong, M. H., S. C. Wu, W. J. Deng, X. Z. Yu, Q. Luo, A. O. W. Leung, C. S. C. Wong, W. J. Luksemburg, and A. S. Wong. Export of toxic chemicals – A review of the case of uncontrolled electronic-waste recycling. *Environmental Pollution,* 149:2:131-140 (2007).

Wood, B. J., L. T. Bryndzia, and K. E. Johnson. Mantle oxidation state and its relation to tectonic environment and fluid speciation. *Science,* 248:337–345 (1990).

Wood, B. J., M. J. Walter, and J. Wade. Accretion of the Earth and segregation of its core. *Nature,* 441:825–833 (2006).

Yamagata, Y., and K. Inomata. Condensation of glycylglycine to oligoglycines with trimetaphosphate in aqueous solution II: catalytic effect of magnesium ion. *Origin of Life Evolution Biosphere,* 27:339–344 (1997).

Yamagata, Y., H. Wanatabe, M. Saitoh, and T. Namba. Volcanic production of polyphosphates and its relevance to prebiotic evolution. *Nature,* 352:516–519 (1991).

Yamanaka, J., K. Inomata, and Y. Yamagata. Condensation of oligoglycines with trimeta- and tetrametaphosphate in aqueous solutions. *Origin of Life Evolution Biosphere,* 18:165–178 (1988).

Yarus, M. Getting past the RNA world: the initial Darwinian ancestor. In RNA World IV, edited by T. Cech, R. Gesteland, and J. Atkins, Cold Spring Harbor Perspectives in Biology, Cold Spring Harbor Laboratory Press, Woodbury, NY, doi:10.1101/cshperspect.a003590 (2010).

Yum, J. H., S. S. Kim, D. Y. Kim, and Y. E. Sung. Electrophoretically deposited TiO_2 photo-electrodes for use in flexible dye-sensitized solar cells. *Journal of Photochemical Photobiology A: Chemistry.* 173:1-6 (2005).

Zedef, V., M. J. Russell, A. J. Hall, and A. E. Fallick. Genesis of vein-stockwork and sedimentary magnesite and hydromagnesite deposits in the ultramafic terranes of southwestern Turkey: a stable isotope study. *Economical Geology,* 95:429–446 (2000).

Zeiner, C. A., L. W. Lion, M. L. Shuler, W. C. Ghirose, and A. Hay. Cycling of biogenic Mn-oxides in a model microbial predator-prey system. *Geomicrobiology Journal,* 23:37-43 (2006).

Zhu, X. S., J. X. Wang, X. Z. Zhang, Y. Chang, and Y. S. Chen. Trophic transfer of TiO_2 nanoparticles from daphnia to zebrafish in a simplified freshwater food chain. *Chemosphere,* 79:928-933 (2010).